

INFORMATION TO USERS

This manuscript has been reproduced from the microfilm master. UMI films the text directly from the original or copy submitted. Thus, some thesis and dissertation copies are in typewriter face, while others may be from any type of computer printer.

The quality of this reproduction is dependent upon the quality of the copy submitted. Broken or indistinct print, colored or poor quality illustrations and photographs, print bleedthrough, substandard margins, and improper alignment can adversely affect reproduction.

In the unlikely event that the author did not send UMI a complete manuscript and there are missing pages, these will be noted. Also, if unauthorized copyright material had to be removed, a note will indicate the deletion.

Oversize materials (e.g., maps, drawings, charts) are reproduced by sectioning the original, beginning at the upper left-hand corner and continuing from left to right in equal sections with small overlaps. Each original is also photographed in one exposure and is included in reduced form at the back of the book.

Photographs included in the original manuscript have been reproduced xerographically in this copy. Higher quality 6" x 9" black and white photographic prints are available for any photographs or illustrations appearing in this copy for an additional charge. Contact UMI directly to order.

UMI

A Bell & Howell Information Company
300 North Zeeb Road, Ann Arbor MI 48106-1346 USA
313/761-4700 800/521-0600

BAR-TRAPPED EDGE WAVES

By
Karin R. Bryan

SUBMITTED IN PARTIAL FULFILLMENT OF THE
REQUIREMENTS FOR THE DEGREE OF
DOCTOR OF PHILOSOPHY
AT
DALHOUSIE UNIVERSITY
HALIFAX, NOVA SCOTIA
DECEMBER 1996

© Copyright by Karin R. Bryan, 1996



National Library
of Canada

Acquisitions and
Bibliographic Services

395 Wellington Street
Ottawa ON K1A 0N4
Canada

Bibliothèque nationale
du Canada

Acquisitions et
services bibliographiques

395, rue Wellington
Ottawa ON K1A 0N4
Canada

Your file Votre référence

Our file Notre référence

The author has granted a non-exclusive licence allowing the National Library of Canada to reproduce, loan, distribute or sell copies of this thesis in microform, paper or electronic formats.

The author retains ownership of the copyright in this thesis. Neither the thesis nor substantial extracts from it may be printed or otherwise reproduced without the author's permission.

L'auteur a accordé une licence non exclusive permettant à la Bibliothèque nationale du Canada de reproduire, prêter, distribuer ou vendre des copies de cette thèse sous la forme de microfiche/film, de reproduction sur papier ou sur format électronique.

L'auteur conserve la propriété du droit d'auteur qui protège cette thèse. Ni la thèse ni des extraits substantiels de celle-ci ne doivent être imprimés ou autrement reproduits sans son autorisation.

0-612-24733-3

Canada

DALHOUSIE UNIVERSITY

FACULTY OF GRADUATE STUDIES

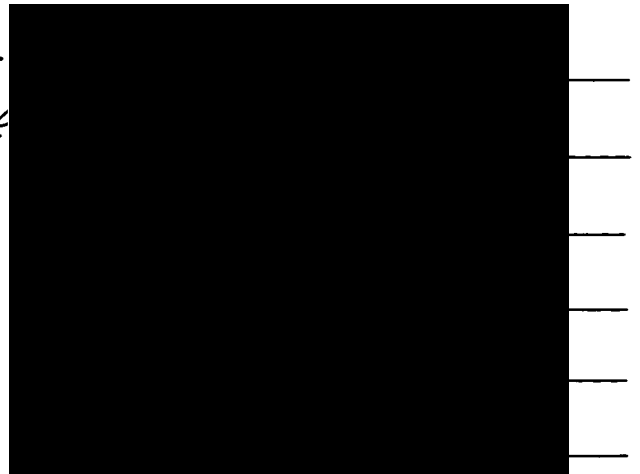
The undersigned hereby certify that they have read and recommend to the Faculty of Graduate Studies for acceptance a thesis entitled "Bar-Trapped Edge Waves"

by Karin Roisin Bryan

in partial fulfillment of the requirements for the degree of Doctor of Philosophy.

Dated: December 3, 1996

External Examiner
Research Supervisor
Examining Committee



DALHOUSIE UNIVERSITY

Date: December 1996

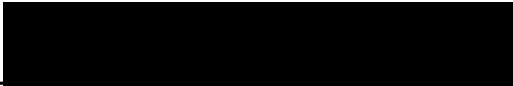
Author: Karin R. Bryan

Title: Bar-Trapped Edge Waves

Department: Oceanography

Degree: Ph.D. Convocation: May Year: 1997

Permission is herewith granted to Dalhousie University to circulate and to have copied for non-commercial purposes, at its discretion, the above title upon the request of individuals or institutions.


Signature of Author

THE AUTHOR RESERVES OTHER PUBLICATION RIGHTS, AND NEITHER THE THESIS NOR EXTENSIVE EXTRACTS FROM IT MAY BE PRINTED OR OTHERWISE REPRODUCED WITHOUT THE AUTHOR'S WRITTEN PERMISSION.

THE AUTHOR ATTESTS THAT PERMISSION HAS BEEN OBTAINED FOR THE USE OF ANY COPYRIGHTED MATERIAL APPEARING IN THIS THESIS (OTHER THAN BRIEF EXCERPTS REQUIRING ONLY PROPER ACKNOWLEDGEMENT IN SCHOLARLY WRITING) AND THAT ALL SUCH USE IS CLEARLY ACKNOWLEDGED.

To Conrad

Contents

List of Figures	viii
List of Symbols	xxi
1 Introduction	1
1.1 Objectives	6
2 Theoretical Basis for Bar Trapping of Edge Waves	8
2.1 Analytic solutions over simple topography	10
2.1.1 Plane beach solutions	12
2.1.2 Simple step-barrred topography	13
2.2 Properties of bar trapped edge waves	21
2.2.1 The kissing modes	21
2.2.2 The non-dispersive property	22
2.3 Numerical solutions for more complex topographies	23
2.4 Cross-shore shapes of bar-trapped edge waves	31
2.5 Bar trapping and longshore currents	32
2.5.1 The longshore current waveguide on plane beaches	34
2.5.2 The combined effect of longshore currents and bars	37
2.6 Summary	43
3 Field Observations of Bar-Trapped Edge Waves	46
3.1 Experimental conditions	48

3.2	Evidence of bar-trapped edge waves during DELILAH	53
3.2.1	Observations from near the bar crest	54
3.2.2	Observations from the outer array	59
3.2.3	Significance levels of spectra estimators	60
3.2.4	Variability of diagonal lines of variance, and edge wave forcing	63
3.2.5	The normalization problem	69
3.2.6	Remarks on optimal observing conditions	73
3.3	Bar-trapped edge waves and effective depth profiles during DELILAH	81
3.3.1	Effective depth profiles during DELILAH	83
3.3.2	Edge wave response to effective depth profiles.	84
3.3.3	The sensitivity of bar-trapped waves to current dominated profiles	87
3.4	Directionality of bar-trapped edge waves during DELILAH	95
3.5	Summary	98
4	Mass Transport by Bar-Trapped Edge Waves	102
4.1	Introduction	102
4.2	Mass transport in a mode 1 edge wave	104
4.2.1	Free surface boundary layer	107
4.2.2	The interior flow and the bottom boundary layer	110
4.2.3	Stokes drift	118
4.3	Mass transport at the top of the boundary layer in bar trapped edge waves	119
4.4	Boundary layer drift during DELILAH	121
4.4.1	Patterns of boundary layer drift due to bar-trapped edge waves	124
4.4.2	Magnitude of boundary layer drift during DELILAH	127
4.5	Conclusions	135
5	Conclusions	138
5.1	Summary of ideas	138

5.2	Related research possibilities	141
A		143
A.1	The maximum likelihood spectral estimator for a longshore array . .	143
A.2	Some simple statistical properties of longshore array data	145
A.3	The relationship between the frequency- wavenumber spectrum and the covariance.	148
A.3.1	Frequency-wavenumber spectrum	148
A.3.2	Cross-spectral matrix	152
A.4	Derivation of the maximum likelihood estimator	153
A.5	The iterative maximum likelihood estimator	160
A.6	Limitations of the iterative maximum likelihood estimator	161
A.6.1	Uni-modal peak	161
A.6.2	Bi-modal peak	164
A.6.3	Random phase	165

List of Figures

2.1	Dispersion diagram for edge waves on a plane beach.	11
2.2	Idealized step-barred geometry for the analytic case.	14
2.3	Dispersion diagram for the step-barred case.	16
2.4	Same as in Figure 2.3, except with phase speed plotted against frequency.	18
2.5	A simple schematic of the cases outlined in Section 2.1.2.	20
2.6	Topographies used in numerical calculations (a) idealized (b) Duck, North Carolina, and (c) Stanhope, Prince Edward Island.	24
2.7	Dispersion diagram from numerical calculations over idealized topography (Figure 2.6a).	25
2.8	Dispersion diagram for Duck, North Carolina, a simple one-bar beach (Figure 2.6b).	26
2.9	Dispersion diagram for Stanhope, Prince Edward Island, a complex three-barred beach system (Figure 2.6c).	27
2.10	Center panel: the same dispersion diagram as given in Figure 2.8. Each of the surrounding panels: sea surface elevation (m), cross shore velocity (m/s) and longshore velocity (m/s) and depth (m) profiles corresponding to each of the solution ranges marked in the center dispersion diagram, assuming $\eta(0) = 1$	29
2.11	A. Idealized longshore current profile on a plane beach (plan view). B. Effective depth profiles for waves travelling against the longshore current for various phase speeds.	36

2.12	A. Idealized longshore current profile on a plane beach (plan view). B. Effective depth profiles for waves travelling with the longshore current for various phase speeds.	38
2.13	Dispersion diagram for edge waves on a plane beach with a longshore current.	39
2.14	Longshore current profile (top), sea surface elevation of a mode 2 edge wave (middle), and bottom profile (bottom) after Schönfeldt (1995).	40
2.15	A. Idealized longshore current profile for a current over a bar, actual depth profile (solid line), effective depth profile, for waves moving with (long dash) and against (short dash) the longshore current. B. Idealized longshore current profile for a current in the trough, and associated effective and actual depth profiles.	42
3.1	A simple schematic of the geometry of the array of current meters and pressure sensors during DELILAH. T	49
3.2	Environmental conditions during DELILAH.	51
3.3	Representative depth profiles during the DELILAH experiment (courtesy of the FRF).	52
3.4	Ratio of the cross-shore component of orbital velocity to the longshore component of orbital velocity at the location of the inner instrument array during DELILAH.	55
3.5	Variance density plotted as a function of frequency and wavenumber of longshore component of orbital velocity from the inner array at DELILAH on October 5, when the array was close to the top of the bar.	56
3.6	A. Variance density along the positive bar-trapped line in Figure 3.5, October 5, plotted against wavenumber.	57

3.7	Dispersion diagram for the same profile as in Figure 2.8, but the grey scale corresponds to the variance of the longshore component of orbital velocity at the location of the array in the trough (A) and seaward of the bar (B).	61
3.8	Variance density plotted as a function of frequency and wavenumber of the longshore component of current data from the outer array taken on October 5, when the array is far from the top of the bar.	62
3.9	Variance density plots of v-component current data taken from the inner array on A. October 10, 22:57 B. October 13, 1:37 C. October 14, 8:39 D. October 18, 6:25 E. October 20, 6:40 F. October 9, 9:19. The leaky wave cut-off is plotted with a black dashed line.	64
3.10	The effect of different normalizations.	70
3.11	The dispersion diagram given in Figure 3.7 renormalized so the amplified waves have a maximum sea surface elevation of one unit anywhere in the cross-shore profile.	71
3.12	Variance density of the longshore component of orbital velocity from the inner array taken when the array is in the trough, on October 16.	74
3.13	Variance density as a function of frequency and wavenumber of the longshore component of orbital velocity from the outer array taken when the array is far from the top of the bar, on October 16.	77
3.14	Variance density as a function of frequency and wavenumber of cross-shore component of orbital velocity from the inner array from the same time as Figures 3.12 and 3.13.	78
3.15	Variance density along the positive bar-trapped line in Figure 3.12.	80

3.16	A.(i) Longshore current profiles at high tide (grey) and low tide (black) from October 7-9. (ii) Effective depth profile for the same times for edge waves travelling against the longshore current and (iii) for waves with the longshore current. (iv) Actual depth profile. B.(i) Eight of the larger longshore current profiles at high tide (grey) and low tide (black) from October 14-20. (ii) Effective depth profiles for edge waves travelling against the longshore current and (iii) with the longshore current. (iv) Actual depth profile.	82
3.17	A. Frequency-wavenumber spectra of the longshore component of orbital velocity from the inner array for three hours over high tide on October 19, starting at 17:36.	85
3.18	Same as Figure 3.17, but for October 13, starting at 13:57	86
3.19	Same as Figure 3.17, but for October 16, starting at 10:20	88
3.20	Six artificial depth profiles created to test the sensitivity of edge waves to small bottom perturbations.	89
3.21	A. Frequency-wavenumber spectrum of the v-component of velocity from the inner array on October 7, over low tide, starting at 14:04. B. Frequency-wavenumber spectrum at high tide on the same day (starting at 19:54). C. The mean longshore current profiles for low tide (black line) and high tide (grey line). D. The actual depth profile (black line) and the effective depth profile at low tide (black dashed line) and at high tide (grey dashed line), for waves travelling with the longshore current.	91

3.22	A. Frequency-wavenumber spectrum of the v-component of velocity from the inner array on October 9, over high tide, starting at 9:19. B. Frequency-wavenumber spectrum at low tide on the same day (starting at 16:03). C. The mean longshore current profiles for low tide (black line) and high tide (grey line). D. The actual depth profile (black line) and the effective depth profile at low tide (black dashed line) and at high tide (grey dashed line), for waves travelling with the longshore current.	92
3.23	A. Mean longshore current profile during the whole experiment (same as in Figure 3.2). B. Cross shore location of the actual (black line) and effective bars for waves travelling with (black dots) and against(grey dots) the longshore current.	94
3.24	Same as Figure 3.17, but for three hours over low tide on October 19, starting at 12:25	96
4.1	A. Depth profile at the location of the v_1 antinode ($x = 43m$) of the longshore drift velocity of a mode 1 edge wave (positive is the direction of wave propagation), $f = 0.018Hz$, slope= 0.015, assuming the net mass flux through the water column is zero. B. The same depth profile of drift, assuming no net second order pressure gradient, note scale difference. C. Cross-shore distribution of longshore drift (assuming no net mass flux) at the surface (z_1), at half the total depth (z_2) and at the top of the boundary layer (z_3). Dashed line is Stokes drift in the inviscid core. D. Cross-shore distribution of the first order cross-shore and longshore component of orbital velocity.	115
4.2	A. Cross-shore distribution of the first order cross-shore and longshore component of orbital velocity of a mode 1 edge wave, $f = 0.018Hz$, $\tan\beta = 0.015$. B. Cross-shore distribution of cross-shore drift at two thirds of the depth (z_1) and one third of the depth (z_2). C. Stream function of the cross-shore drift, z_1 and z_2 are marked.	116

4.3	Each panel shows sea surface elevation at the top, u and v (dashed) components of orbital velocity at the middle top, u and v (dashed) drift at the bottom middle, depth at the bottom, for a mode 0,1,2,3,4 edge wave calculated with the DELILAH (October 16) depth and longshore current profiles.	125
4.4	Each panel shows sea surface elevation at the top, u and v (dashed) components of orbital velocity at the middle top, u and v (dashed) drift at the bottom middle, depth at the bottom, for a mode 2,3,4,5,6 edge wave calculated with the DELILAH (October 16) depth and longshore current profiles.	126
4.5	A-D: Total variance of peaks attributable to bar trapped waves along the diagonal line of variance in Figure 3.12, from October 16, at 4:00, high tide. E-F: percent of total variance of peaks attributable to bar trapped edge waves for the same peaks.	128
4.6	A: ratio of u amplitude to v amplitude (from model results) B-E: Values of cross-shore and longshore orbital velocities projected to locations at the shoreline and over the bar using from model results, which were normalized at the location of the array using the variances in Figure 4.5, from October 16, 4 am, high tide.	129
4.7	Drift velocities calculated using (4.42). The cross-shore shear and the projections of the longshore and cross-shore component of orbital velocity are calculated numerically, and all the first order velocities are normalized at the location of the array by the variance of the longshore component of orbital velocity in Figure 4.5, from October 16, 1990, 4am, high tide. A-B: at the instrument array. C-H: velocities projected to locations on either side of the bar, and on top of the bar.	133
A.1	Time series of the longshore component of orbital velocity from each sensor location on October 16, 1990, 4:00am	146

A.2	Cross correlations of the longshore component of orbital velocity between all sensor combinations on October 16, 1990, 4:00am (same day as Figure 3.12). T	147
A.3	The coherence of the longshore component of orbital velocity between all sensor combinations on October 16, 1990, 4:00am.	149
A.4	Phase of the longshore component of orbital velocity between all sensor combinations on October 16, 1990, 4:00am.	150
A.5	Schematic of the windows that would be derived from several different array geometries of the same number of windows, after Davis and Regier (1977).	156
A.6	The spectral estimate of random noise at each instrument location.	162
A.7	All combinations of wavenumber with which the spectral estimator was tested for its ability to reproduce a bimodal wavenumber spectrum, for the case when only five out of six sensors are working, on October 16, 1990, 4:00am.	163
A.8	The spectral estimate of the longshore component of orbital velocity, from October 16, 1990, 4:00am, when the phases of each signal have been randomized.	166

Abstract

Edge waves are shallow water waves which are trapped along the shoreline waveguide by reflection and refraction. The cross-shore pattern of nodes and antinodes in edge waves has long been hypothesized to have the right lengthscale to explain longshore bars. However, different frequencies and modes have antinodes in different locations, and there is little existing field data to suggest frequency and mode selection. A bar can also provide a local minimum in shallow water wave speed, $C \rightarrow \sqrt{gh_{\text{bar}}}$, (where h is depth), needed to produce a separate waveguide, which can trap and amplify edge waves relative to the shoreline. These trapped solutions have similar shapes over the bar, regardless of frequency or wavenumber. Calculations of drift velocity, in the absence of phase locking, show drift convergence near the top of the bar, at the top of the bottom boundary layer; these bar-trapped waves may cause bar growth. Edge waves react to a longshore current as though it were a change in the bottom topography; the profile will be deeper for edge waves travelling with the current and shallower for edge waves travelling against the current, with the magnitude of the change dependent on the direction and the strength of the current shear relative to the bottom slope. For strong shears, the bottom can be changed to the degree of creating a virtual bar, on which edge waves can also be trapped and amplified. This could be a mechanism for moving a bar, or creating a bar on a plane beach.

These theories were tested using frequency-wavenumber spectra of the longshore component of orbital velocity from observations taken during the DELILAH experiment, October 1990, Duck, N.C.. Continuous, unexplained, diagonal lines of variance have been observed in this data, and similar data from other experiments. Here, these diagonal lines are shown to be evidence of bar-trapped edge waves. These lines not only have the same frequency-wavenumber coordinates as bar-trapped edge waves, but also vary in a predictable manner with changes in the longshore current and depth profile. For example, when the effect of the current was strong enough to remove the effect of the bar in theoretical predictions, the diagonal line of variance disappeared. (The diagonal line reappeared, when this strong current shear moved shoreward into the trough, at high tide). On such days, when the edge wave shape is strongly controlled by current (or for example on a plane beach), the expected affect on topography is unclear because the location of edge wave trapping moves, when the longshore current profile changes with changes the tide. However, on days when the edge wave shape is strongly influenced by the bar, calculations of cross-shore drift, using the DELILAH data to obtain realistic magnitudes, show the drift should allow the bar to grow or maintain itself against gravity and other destructive forces.

List of Symbols

English Letters

a	edge wave amplitude
$A(z')$	Parameter showing the decay of $\overline{u_1 u_1}$ in the boundary layer
$B(z')$	Parameter showing the decay of $\overline{u_1 w_1}$ in the boundary layer
C	Phase speed of edge wave
$C(z')$	Parameter showing the decay of $\overline{v_1 w_1}$ in the boundary layer
DELILAH	Duck Experiment on Low Frequency and Incident Band Longshore and Across-shore Hydrodynamics
$dZ(k, \sigma)$	Frequency representation of variance
$E(k)$	Variance
$E \square$	Expected value
f	Cyclic frequency
F	Forcing
g	Acceleration due to gravity
G	Spatial lag vector in Appendix
h	Depth
h_{min}	Depth of the local minimum in phase speed
h_{bar}	Depth of bar
h_{step}	Depth of step region
h_{trough}	Depth of trough
h_{sea}	Depth of region seaward of bar
h'	Effective depth
$h(k, \sigma)$	Continuous frequency-wavenumber spectrum
$h_N(k, \sigma)$	Random noise spectrum
i	$\sqrt{-1}$
i, j	Indices
IMLE	Iterative maximum likelihood estimator
k	Longshore radial wavenumber
k_x	Cross-shore radial wavenumber
M	Total number of instruments
$M(Y, \sigma)$	Cross correlation function

M_{mn}, M	Cross correlation function
\mathbf{n}	Velocity vector normal to S
n, m	Indices of instrument number in Appendix
N	Total number of instrument lags
$N(x)$	Cross-shore edge wave shape
p_2	Second order pressure
$R(Y, T)$	Covariance
s_N	Variance of random noise
S_{ij}	Radiation stress
S	Free surface
\mathbf{s}	Velocity vector tangential to S in the y - z plane
t	Time
T	Time lag
\hat{T}	Variance estimate for IMLE
\mathbf{t}	Velocity vector tangential to S in the x - z plane
u	Cross-shore orbital velocity
u_{vis}, v_{vis}	Viscous cross-shore and longshore orbital velocity
u_{inv}, v_{inv}	Inviscid cross-shore and longshore orbital velocity
\mathbf{u}	Velocity vector
\mathbf{u}_1	First order velocity vector
\mathbf{u}_2	Second order velocity vector
$\bar{\mathbf{u}}_2$	Second order mean (Eulerian) velocity vector
\mathbf{u}_L	Lagrangian velocity vector
\mathbf{u}_s	Stokes drift vector
U_{zconst}, V_{zconst}	Integration constants
U_o, V_o	amplitude of two dimensional flow in drift calculations
v	Longshore orbital velocity
V	Mean longshore current
w	Vertical orbital velocity
w_n, \mathbf{w}	Complex weights in spectral estimator
$W(k, k_w)$	Window in spectral estimator
x	Cross-shore dimension
x_{min}	Location of the local minimum in phase speed
$X(y, t)$	space-time series of a stochastic process
y	Longshore dimension
Y	Longshore space lag
z	Vertical dimension
z'	$z + h$

Greek Letters

α	Angle of incident wave approach for one wave train
----------	--

β	Bottom slope, also parameter in IMLE in Appendix
γ	Cross shore wave number divided by i , also parameter in IMLE in Appendix
δ	Boundary layer thickness, also used to symbolize Dirac Delta-function in Appendix
Δ	Friction coefficient
ϵ_{ij}	Stress tensor
ϵ	Adjustment parameter for IMLE
ε	Phase of a wave train
η	Sea surface elevation
θ	Angle of incident wave approach
κ	Wavenumber
λ	Cross shore wavelength, also parameter in IMLE in Appendix Also Lagrange multiplier
μ	$\rho\nu$
ν	Kinematic viscosity
ρ	Density
σ	Radial frequency
τ_y	Surface wave stress in the longshore direction
ϕ	$ky - \sigma t$

Other

∇	Gradient
$\ \quad \ $	Magnitude
*	Complex conjugate
\Re	Take the real part
∂	Partial differential
$\hat{\cdot}$	Estimate

Acknowledgments

First and foremost I wish to thank Tony Bowen for the time and effort he has invested in me. Tony has an uncanny ability to see to the root of a problem, and give direction toward a solution, without interfering with my individual approach. The more I learn of Nearshore Oceanography, the more I realize how fortunate I have been to have worked with Tony. I also owe thanks my committee: to Keith Thompson, in particular for the supervision he gave me while Tony was away on sabbatical, to Fred Dobson for reading my thesis in such detail and giving me strong encouragement, and to Paul Hill for giving me advice on the sediment-dynamics application of my thesis. My external, John Trowbridge offered insightful criticisms which improved sections of the thesis. Thanks to Peter Howd for giving access to the DELILAH data which formed the core of my thesis and for providing accommodation during a month long stay at the Duke Marine Laboratory. I appreciate the efforts of the Principle Investigators and the staff at the Federal Research Facility, U.S. Army Corps of Engineers, that went in to the collection of the field data. Support during the first four years of the thesis was provided by NSERC, and during the last four months, by a Dalhousie Graduate Fellowship.

My experience at Dalhousie would be bland without the entertaining input of my office-mate, Michael Dowd, who had the knack of completing problems in a few weeks and passing on all the handy tips. Dan Kelley was always very supportive, and Jacquie Witte was(is) a great buddy. Thanks to the Physical Oceanography students for sitting through all my practice talks. Thanks to the beach people for making field work so much fun (especially Phil MacAulay for trying to talk to me underwater, and Walter Judge for eating as much as me at lunchtime). Jackie Hurst and Steve Matheson were very helpful in solving computer and organizations problems. Finally thanks to all the regular attendees of Thursday Pub, for your companionship over the years.

The approach I have learned at the Department of Oceanography will give me solid basis with which to start my career.

Chapter 1

Introduction

The nearshore environment is characterized by a complex combination of waves and mean currents. However, large-scale spatial patterns of sediment accumulation suggest that flows of similar scale must dominate for sufficiently long times to allow these features to evolve. Though there are a large number of models describing how these features may form, few have demonstrated the necessary predictive skill to determine where and when these features actually occur. In practice, simple parametric descriptions of the beach based on long term observations, for example Wright and Short (1984), have been more successful at predicting such large scale features. However, such descriptions give little insight into the underlying physical processes.

Edge waves, which are discrete-mode waves trapped by refraction and reflection at the shoreline (Eckart, 1951), have long been argued to provide spatially distributed convergences of velocity of the appropriate length scales to explain cusps, longshore sand bars, crescentic sand bars, and other rhythmic features (Bowen and Inman, 1971; Guza and Inman, 1975; Bowen, 1980; Holman and Bowen, 1982). Progressive edge waves or reflected longwaves, both of which are standing in the cross-shore direction, may generate longshore bars at the location of cross-shore nodes or anti-nodes. Standing edge waves have a longshore pattern of nodes and anti-nodes which could cause crescentic bars and cusps. This correlation of length scales and the observation of substantial energy in the low-frequency range of the nearshore spectrum

(Huntley and Bowen, 1975; Huntley, 1976; Guza and Thornton, 1985; Holman and Sallenger, 1985) provides a strong indication that edge waves, or at least cross-shore standing waves, could be energetic enough to generate and maintain major beach features. Unfortunately, in order to allow the resulting topographic features to evolve, it would seem necessary that appropriate waves must be dominant for long periods of time (hours to days). Theoretical arguments exist for the selection of edge wave modes with the right dimensions, for example Symonds and Bowen (1984). However, discrete edge waves are rarely observed in field data, even on beaches with rhythmic topographic features. Though the correct wavelength scales are observed in the field, the nearshore longwave spectra generally seem to be broad banded, and preferential selection of an isolated frequency has rarely been observed (Holman, 1981; Oltman-Shay and Guza, 1987). As a result, the role of edge waves and other longwaves in bar dynamics is still unclear.

Other non-infragravity based arguments for the formation and maintenance of bars exist. Bars may form at the incident wave breakpoint, where seaward of the breakpoint there is a shoreward drift related to wave orbital asymmetry and landward of the break point there is a seaward directed undertow, resulting in a convergence at the bar (i.e. Dally and Dean, 1984). Apart from being difficult to test (Holman and Sallenger, 1993), one of the main problems with this theory is that it requires a very narrow region of breaking. This is generally not the case (Holman and Sallenger, 1993), for example some field evidence shows that the cross-shore scale of a bar was much smaller than the width of the surf zone over the bar (Sallenger *et al.* 1985). Though a positive feedback between the bar and wave breaking is clearly important, the main contender to infragravity wave models, the break point bar model, is also not a completely satisfactory theory of bar formation and growth.

Evidence of edge waves has come from observations at convenient locations such as shoreline run-up data and from arrays located in the trough. However, arrays are rarely located at the bar crest where conditions are turbulent and potentially highly mobile, making data acquisition difficult. On plane beaches and on beaches of simple

monotonic depth variations, the edge wave amplitude is maximum at the shoreline and decreases seaward, so shoreline measurements of edge waves are representative of the edge wave conditions throughout the beach. For complex topographies this is not necessarily the case. Recent numerical calculations show that edge waves can be trapped on bars and longshore currents on beaches (Kirby *et al.*, 1981; Wright *et al.*, 1986, Falques and Iranzo, 1992, Schönfeldt, 1991, Schönfeldt, 1995). This trapping mechanism allows the orbital velocities and sea surface displacement to be severely amplified over the bar relative to their values at the shoreline. Bar-trapped edge waves would not necessarily be evident in observations collected at the shoreline or trough.

The significance of bar trapping is that when the amplification is large, the shapes of the edge wave solutions trapped on the bar are not strongly dependent on mode number, frequency, or longshore wave number. The increased hydrodynamic activity, for example, in the drift velocities associated with bar-trapped edge waves, may be similar for whole ranges of solutions. This raises the possibility of positive feedback in which the trapped modes tend to provide flow patterns which may result in bar maintenance or growth. The bar might then be somewhat resistant to changing wave conditions, bar-trapped waves of similar form existing for all incident wave conditions.

The early results of Kirby *et al.* (1981) and Wright *et al.* (1986) showed the amplification, relative to the shoreline, was a mild change in the edge wave amplitude over the bar. Their main conclusions were that the bar had the ability to attract an edge wave anti-node with implications to the accumulation of sediment on top of the bar. Conversely, Falques and Iranzo (1992) and Schönfeldt (1991) show a few examples in which the amplification can be an order of magnitude larger over the bar than at the shoreline, for the specific geometries they used. Schönfeldt (1995) extends his result for edge waves trapped his geometry to include the effect of a longshore current. Howd *et al.* (1991b) show generally that the effect of a steady longshore current on the edge wave shape is analogous to a change in the depth profile, with the direction of the change dependent on the direction of the longshore

current. Schönfeldt (1995) uses this result to show a case in which a current in the trough increases amplification for edge waves travelling with the longshore current, and reduces amplification for edge waves travelling against the longshore current. He comments that if the mean longshore current profile were such as to change the amplification to a location other than the bar, sediment convergences might cause movement of the bar to this new location. Howd *et al.* (1992) show that a longshore current on a plane beach may cause a bar to form when edge waves travel with the longshore current, though they do not relate this effect directly to amplified edge waves.

Neither Falques and Iranzo (1992), nor Schönfeldt (1991,1995) attempt to generalize their observations. Falques and Iranzo (1992) present the amplification as an aside to a more detail discussion of the effect of longshore current on edge waves. Though strong amplification was evident in one of their numerical runs, they do no more than comment that it is an interesting phenomenon. Of the geometries they experimented on, only one exhibited the amplification. Schönfeldt (1991,1995) shows amplification on the outer bar of a two barred beach, and noted that this occurred when the phase speed approached a constant, $\sqrt{gh_{\text{bar}}}$, where h_{bar} is the depth of the bar. He gave some examples of two different shapes of amplification that occur on the outer bar, but he does not attempt to clearly explain why some shapes are favoured in some instances but not others. He also does not explain the lack of amplification on the inner bar, on the two-barred profile. In the case in which he introduces the effect of a longshore current, for simplicity, he uses a synthetic longshore current profile over the trough, though other longshore current profiles could give significantly different results. These works represent experiments with numerical results on specific geometries with specific longshore current profiles. They served their purpose, in that they introduced the idea that bars can severely change the edge wave solutions, with the interplay between bars and longshore currents being important, and that this amplification may have implications for sediment transport. However it is difficult to gain

an intuitive understanding from the very specific cases they present. A deeper understanding would allow prediction of the conditions under which amplification would occur on other beach profiles, and be of immediate use to nearshore researchers in general. More importantly, very little field evidence has been presented to suggest that these theoretical amplified solutions are significant in practice. Until convincing field evidence is presented, there is no compelling reason for beach studies to include the effect of amplification over bars and longshore currents.

Bar-trapped edge waves should be evident in observations collected near a bar. The question is whether they are dominant relative to the other possible modes. Symonds *et al.* (1982) suggest that a significant component of edge wave forcing is at the location of the bar, where the incident wave heights are close to maximal. Thus energy transfer might occur more easily between the incident waves and these bar-trapped modes (which naturally are most energetic at the bar) than between incident waves and modes which have their greatest maxima at the shore; the bar-trapped wave may be preferentially forced. An edge wave with its greatest maxima at the location of the bar might also experience reduced damping due to bottom friction, as the energetic region of the trapped edge waves is concentrated in deeper water, with relatively small orbital velocities in the shallow water near the shoreline.

The theoretical work of Kirby *et al.* (1981), Wright *et al.* (1986), Schönfeldt (1991, 1995) and Howd *et al.* (1991b, 1992) suggest that bar-trapping of edge waves, may be a mechanism for bar growth, or maintenance against destructive forces (such gravity, or other hydrodynamic patterns), and that the added effect of longshore currents could provide a mechanism for generation of a bar on a plane beach, or the movement or growth of a bar on a barred beach. This preliminary work provides the foundation on which a detailed examination of the theoretical basis for bar-trapping and longshore current trapping of edge waves is developed here. Of course, establishment of bar-trapping as an important hydrodynamic effect in the field of nearshore dynamics requires evidence that these modes exist and are important in field data. The most significant result presented here is the convincing evidence of bar-trapped edge waves

in the longshore component of orbital velocity from an experiment in Duck, N.C.. These observed bar-trapped modes are present under all combinations of depth and longshore current profiles which might lead to bar-trapping, as predicted from the theoretical understanding presented here. These clear field observations allow more realistic analysis of the second order drift patterns induced by these bar trapped solutions than has been attempted in the past for edge waves in general (i.e. Holman and Bowen, 1982). Though establishing that a particular wave is instrumental in causing morphological change is very difficult, demonstrating that bar-trapped edge waves provide the spatially and temporally coherent drift patterns needed to influence topography will go a long way toward this goal.

1.1 Objectives

The main objective of this thesis is to thoroughly investigate bar trapped edge waves both theoretically and in the field, and to examine their significance to the formation, growth and movement of longshore bars. Specifically:

1. To explain physically why edge waves may be trapped and amplified on bars and longshore currents, and from this, to study the shape and dispersive properties of bar-trapped edge waves. Also, to gain insight into the effect on edge wave shape of combining longshore currents and bars.
2. To clearly demonstrate the existence of bar-trapped edge waves in field data. Having accomplished this, to show to what extent, and under what conditions, bar-trapped edge waves dominate over other hydrodynamic processes in the field. Also to investigate the influence of naturally occurring longshore current profiles on the calculated edge wave solutions, and the sensitivity of edge waves in field data to changes in the longshore current profile.
3. Having demonstrated that bar-trapped edge waves are hydrodynamically important, the final objective is show that they provide the spatially and temporally

coherent drift patterns needed to cause enhancement of a bar (or generation or movement of a bar when edge wave is trapped on a longshore current).

These objectives break naturally into three distinct Chapters. The first objective is addressed analytically with a simple solution over step-barrred topography and then numerically with more complex topography and longshore currents in Chapter 2. The second objective is addressed in Chapter 3 using depth profiles, longshore current profiles and frequency-wavenumber spectra of the longshore component of orbital velocity observed during the DELILAH experiment, October 1990, Duck N.C.. (DELILAH stands for Duck Experiment on Low-frequency and Incident-band Longshore and Across-shore Hydrodynamics, an experiment specifically designed to study waves travelling in the longshore direction). The longshore current and depth profiles are needed to calculate theoretical edge wave solutions for comparison with the spectra. In Chapter 4, the third objective is addressed by calculating the Lagrangian drift velocities induced by bar trapped edge waves and normalizing these solutions using the edge wave variance measured during DELILAH.

Chapter 2

Theoretical Basis for Bar Trapping of Edge Waves

Edge waves can be trapped on any feature of the beach which causes a local minimum in the phase speed, for example, changes in depth and mean current speed. On a plane beach, the shoreline acts as a phase speed minimum, so that waves are trapped along the shoreline, and decay exponentially out to sea. Stokes (1849) showed the existence of the lowest (fundamental) mode edge wave which had no zero crossings in the cross-shore profile. Eckart (1951) solved the linear shallow water equations on a plane beach to show that an infinite set of discrete modes (including the Stokes mode) existed, with the mode number corresponding to the number of zero crossings. Ursell (1952) solved the full linear, depth-dependent, equations of motion for edge waves on a plane beach, and showed there was a cut-off frequency at which edge waves could no longer be trapped (the leaky wave cut-off).

Following the work of Eckart and Ursell, researchers experimented with more complex topographies such as exponential beaches (solved analytically by Ball, 1967) and arbitrary depth profile (solved numerically by Holman and Bowen, 1979). The conclusion was that the variable topography could cause some variation in the cross-shore shapes of edge waves, and the dispersion properties of edge waves. Recently the effect of longshore current on edge waves solution has been shown to be similar

to the effect of variable bottom topography (Howd *et al.*, 1991b; Falques and Iranzo, 1992), but the longshore current introduces anisotropy into the edge wave solutions.

When the the bottom topography (or the longshore current) varies to the point of providing a local minimum in the phase speed, such as in the case of a longshore bar, the edge wave cross-shore shapes and dispersion properties can be noticeably different from the plane beach solutions. Longshore bars can attract edge wave anti-nodes, and cause amplification of edge waves over the bar relative to the shoreline (Kirby *et al.*, 1981; Wright *et al.*, 1986; Schönfeldt, 1991; Falques and Iranzo, 1992). Schönfeldt (1995) showed that adding a longshore current could enhance or diminish this effect depending on the direction of the current. Early observations of this bar-trapping effect in numerical calculations focused on small changes in the edge wave solutions over the bar, with no change to the edge wave dispersion properties (Kirby *et al.*, 1981). The more recent results of Schönfeldt (1991) and Falques and Iranzo (1992) showed strong amplification and changes to the dispersion properties, in particular cases. However, very little field evidence demonstrating bar trapping of edge waves exists. As a consequence, the effect of bars on edge waves is still neglected, and researchers have frequently considered the plane beach solution acceptable, even on highly variable topography (i.e. Aagaard and Greenwood, 1994).

In this chapter, the effect of bars and longshore currents as edge wave trapping mechanisms will be examined theoretically, in significantly more detail than Kirby *et al.* (1981), Wright *et al.* (1986), Schönfeldt (1991, 1995) or Falques and Iranzo (1992). Much can be learned about a system from very simple topographies. For example, shallow water solutions have been derived for trapped waves on stepped shelf topography, (Snodgrass *et al.*, 1962; Buchwald and Szoeker, 1973). In a similar way, a simple analytic solution for edge wave modes on idealized step-barrred topography will identify the important parameters causing the amplification and trapping. This simple physical explanations will provided the understanding needed to interpret more complex situations, with many bars and longshore currents. A numerical model, based on Holman and Bowen (1979) and Howd *et al.* (1992) will be used to confirm

these predictions and demonstrate trapping over more complex beach topographies, longshore currents and combinations of both topography and currents.

2.1 Analytic solutions over simple topography

Assuming a wave-like solution travelling along a topography which is of infinite extent in the longshore direction, sea surface elevation η , cross-shore velocity u , and longshore velocity v are the real parts of

$$\begin{aligned}\eta &= \eta(x)e^{i(ky-\sigma t)}, \\ u &= u(x)e^{i(ky-\sigma t)}, \\ v &= v(x)e^{i(ky-\sigma t)}\end{aligned}\tag{2.1}$$

where x is positive in the offshore direction, y is the longshore direction, σ is the radian frequency, and k is the longshore radian wavenumber. The linear, irrotational, inviscid shallow water equations of momentum and continuity are combined, resulting in the edge wave equation

$$\left(\frac{gh\eta_x}{\sigma^2}\right)_x + \left(1 - \frac{k^2gh}{\sigma^2}\right)\eta = 0\tag{2.2}$$

where

$$u = \frac{-ig}{\sigma}\eta_x,\tag{2.3}$$

$$v = \frac{gk}{\sigma}\eta.\tag{2.4}$$

Equation 2.2 is a second-order homogeneous ordinary differential equation. The boundary conditions for the edge wave to be trapped near the shore, are that the sea surface elevation must decay at an infinite distance from the shoreline, and must equal some arbitrary constant at the shoreline.

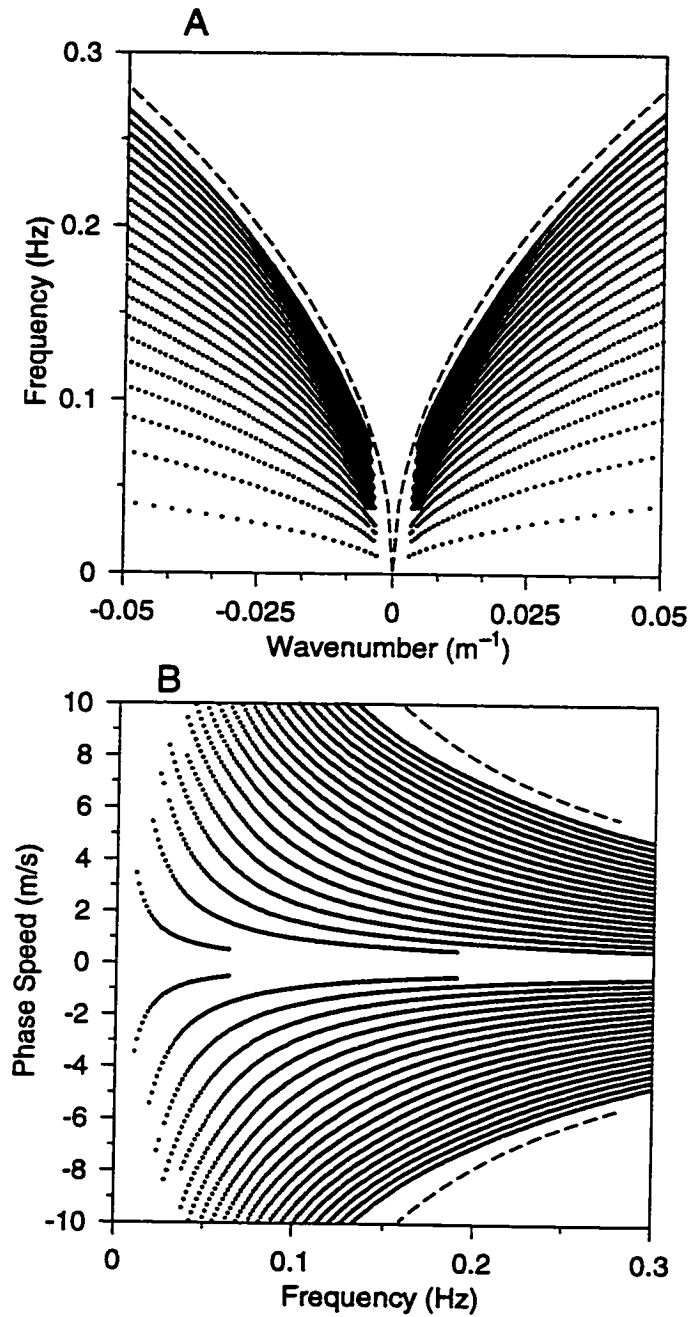


Figure 2.1: Dispersion diagram for edge waves on a plane beach, A. Frequency against wavenumber, B. Phase speed against frequency. The leaky-wave cut-off is marked with a dashed line. Solutions are not shown for the lowest wavenumbers, as the cross shore profiles of these modes extend beyond the seaward limit of the depth profile.

2.1.1 Plane beach solutions

The solutions for edge waves on a plane beach have been well established. Eckart's (1951) solution of (2.2), for edge waves on a plane beach, shows discrete solutions which are sinusoidal near the shore and exponentially decaying out to sea. The sea surface elevation has the form

$$\eta(x) = a_n L_n(2kx) e^{-kx} \quad (2.5)$$

where n is the modal number, β is the slope, a is the amplitude and L_n is a Laguerre polynomial. The frequency and wavenumber must satisfy the dispersion relation

$$\sigma^2 = gk(2n + 1) \tan \beta. \quad (2.6)$$

The dispersion diagram (Figure 2.1) has curves corresponding to different edge wave modes, the mode number being the number of zero crossings in the solutions for sea surface elevation. The cross-shore behaviour of the edge wave solution changes from sinusoidal to exponentially decaying, when the depth equals C^2/g , where C is the phase speed $C = \sigma/k$. At a set phase speed, the lowest modes have the smallest longshore wavenumber and frequency (Figure 2.1). So therefore the discrete combinations of longshore wavenumber and frequency given in the dispersion diagram correspond to the multiple of cross-shore wavelengths of sinusoids which exist shoreward of C^2/g . A small longshore wavenumber corresponds to a low mode, which corresponds to a large cross-shore wavelength or a small cross-shore wavenumber. The slope of the beach governs the spacing between modes; the shallower the slope, the larger the cross-shore dimensions of the wave near the shore. Each combination of wavenumber and frequency falling on any of the modal lines on the dispersion diagram corresponds to a unique cross-shore distribution of sea surface elevation and current.

Also shown on Figure 2.1, with a dashed line, is the leaky wave cut-off (Ursell, 1952). This is the maximum frequency, as a function of wavenumber, for which edge waves are trapped. The leaky wave cut-off is

$$\sigma^2 = gk. \quad (2.7)$$

This is derived from the dispersion relation for edge waves calculated without the shallow water approximation

$$\sigma^2 = gk \sin(2n + 1)\beta, \quad (2.8)$$

considering that sine can be no larger than one (there are no limits on edge waves solutions calculated from the shallow water equations). The leaky wave cut-off is also the maximum wavenumber that the incident waves propagating from deep water can have. This can be shown from Snell's law in which $\sin\alpha/C$ must be conserved as the incident wave shoals, where α is the angle of approach, and C is the phase speed.

The plane beach solutions introduce some of the concepts which also apply to barred beaches. The change from sinusoidal to exponential of the cross-shore shape of the edge wave solutions, depending on depth, suggests that the solutions could be sinusoidal on the bar, but exponential in deeper regions around the bar. Also the sinusoid on the bar could have modes, in the same way as the sinusoid close the shore on a plane beach has different modal shapes.

2.1.2 Simple step-barred topography

Given an idealized step-barred topography, with depth of the water h constant in each region, (Figure 2.2), (2.2) can be solved separately in each of the four regions with constant bathymetry, matching sea surface elevation and mass continuity at each of the three discontinuities at region boundaries, and assuming no cross-shore mass flux at the shoreline. The result is a system of eight equations and eight unknowns (a_j, b_j) governing the shape of the sea surface:

$$\eta_j = a_j \cosh(\gamma_j x) + b_j \sinh(\gamma_j x), \quad (2.9)$$

$j = \text{step, trough, bar, sea}$

where

$$\gamma_j = k \sqrt{1 - \frac{C^2}{gh_j}}, \quad C = \frac{\sigma}{k}. \quad (2.10)$$

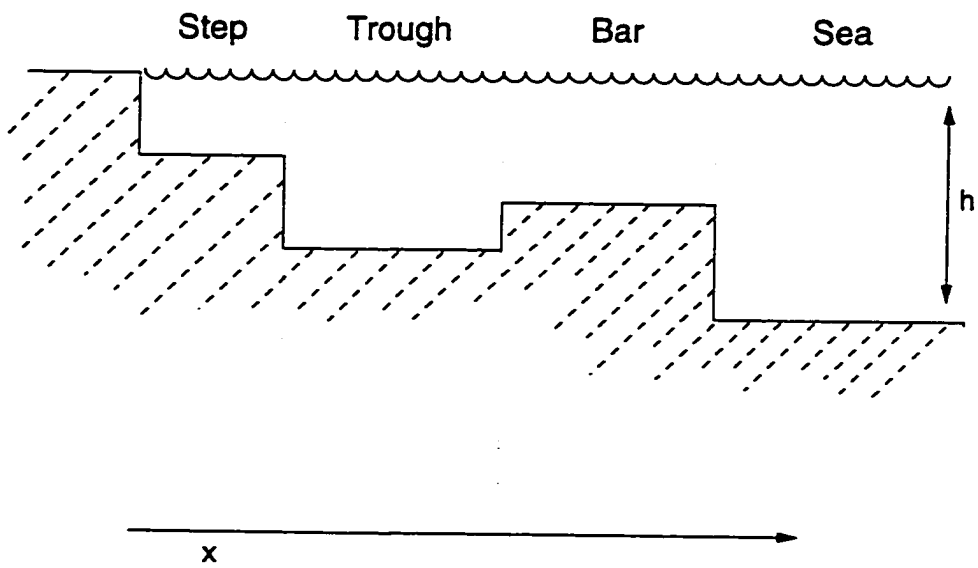


Figure 2.2: Idealized step-barred geometry for the analytic case. Topography is constant in the longshore y direction.

Therefore the solution in each section is either oscillating or exponential, depending on whether γ_j is imaginary or real. In the former case, γ_j/i is the cross-shore wavenumber. Solving the system of linear equations results in a dispersion relation between wave frequency and longshore wavenumber and also in a free variable, which is arbitrarily chosen to be the amplitude at the shoreline (set to 1 for convenience). The dispersion relation (in terms of cyclical frequency and wavenumber) is shown in Figure 2.3 and again in terms of phase speed and frequency in Figure 2.4. The resulting sea surface elevation shapes can be divided into five categories, depending on particular combinations of frequency and phase speed.

1. If the phase speed is smaller than $\sqrt{gh_{\text{step}}}$, then the solutions are exponential in all sections, which makes it impossible to satisfy the matching conditions at the three discontinuities. Thus there are no solutions in this area of the dispersion diagram (Figure 2.4).

2. If the phase speed is smaller than $\sqrt{gh_{\text{bar}}}$ (and $\sqrt{gh_{\text{trough}}}$) but greater than $\sqrt{gh_{\text{step}}}$, then a discrete set of wave-like solutions exist over the step, and exponential solutions exist in all other regions. These oscillating solutions must decay outside of the step region without creating a discontinuity in sea surface elevation. The only multiples of cross-shore wave length (i/γ_{step}) on the step that satisfy this are $\lambda/4 \times (1, 3, 5, 7, \dots)$ corresponding to a 0,1,2,3... mode wave, respectively (where λ is the cross-shore wavenumber). When phase speed approaches $\sqrt{gh_{\text{step}}}$, the term $(1 - C^2/gh_{\text{step}})$ from (2.10) tends to zero. In order to maintain a finite cross-shore wave length, k (from equation 2.10) must approach infinity in this limit, and, consequently, so must frequency (recall $C(= \sigma/k) \rightarrow \sqrt{gh_{\text{step}}}$). This asymptote of frequency and wavenumber occurs anytime the cross-shore wavenumber is restricted to decaying outside of a region.

3. If the phase speed is smaller than $\sqrt{gh_{\text{trough}}}$ (and $\sqrt{gh_{\text{sea}}}$) but greater than $\sqrt{gh_{\text{bar}}}$, then a discrete set of wave-like solutions exist over the step as before, but also, another discrete set of wave-like solutions exist over the bar; the solution remains exponential over the trough. In this case the oscillating solution over the bar must

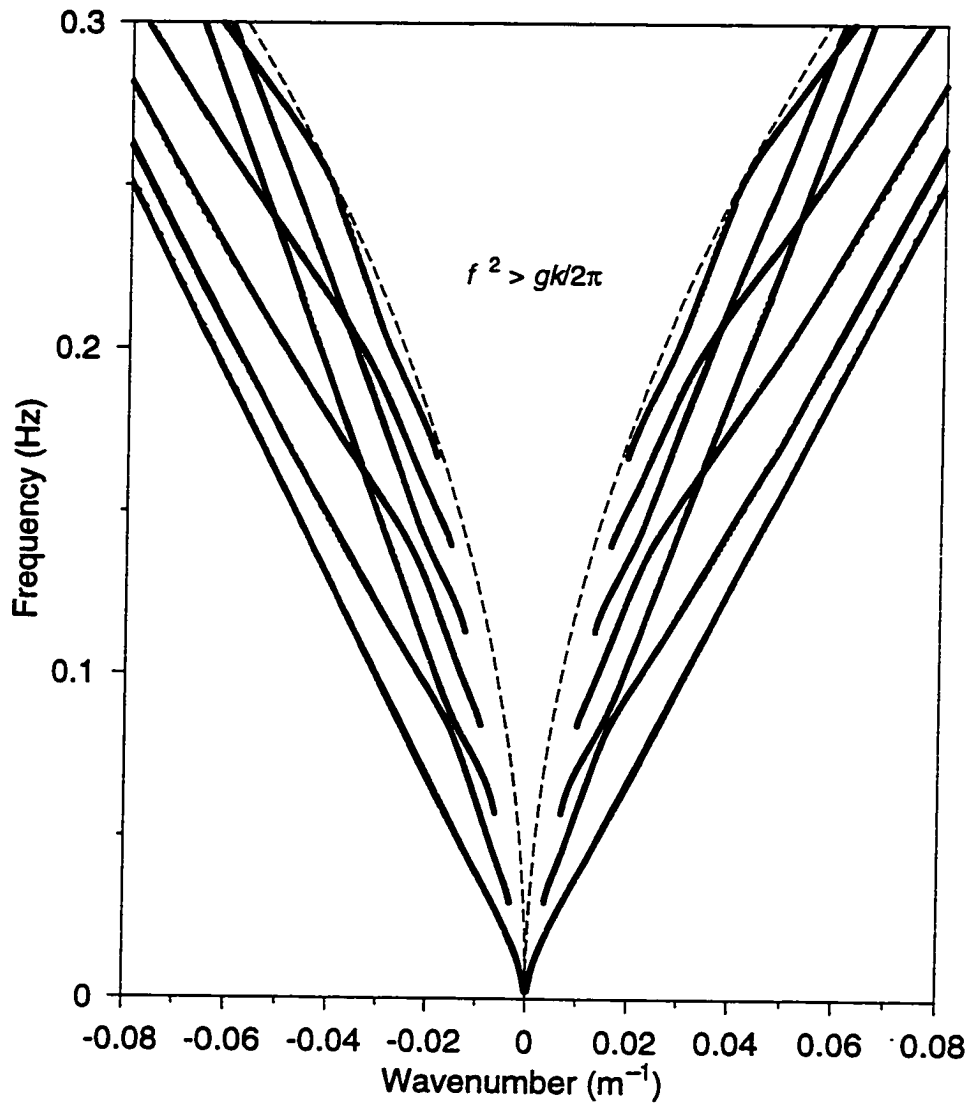


Figure 2.3: Dispersion diagram for the step-barred case, with cyclical longshore wavenumber, $k/2\pi$, plotted against cyclical frequency, solved numerically. Each point on each curve represents a solution. The dashed line is the leaky wave cut-off.

decay in each of the surrounding regions, without creating a discontinuity in sea surface elevation. The only multiples of cross-shore wavelength (i/γ_{bar}) on the bar that satisfy this are $\lambda/4 \times (2, 4, 6, 8\dots)$ corresponding to a 0,1,2,3... “bar” mode wave, respectively. Similar to the step wave in case 2, when the phase speed approaches $\sqrt{gh_{\text{bar}}}$, in order to maintain a finite cross-shore wavelength on the bar, both k and frequency must tend to infinity as $C(= \sigma/k) \rightarrow \sqrt{gh_{\text{bar}}}$. Along each of the $C \rightarrow \sqrt{gh_{\text{bar}}}$ asymptotes the bar mode (or shape over the bar) is approximately constant, but the actual or total mode changes, because the total mode combines the mode number over the step and the mode number over the bar. In these bar-trapped modes the relevance of defining an overall modal number when the wave exists separately on the bar is questionable. Along the $\sqrt{gh_{\text{bar}}}$ asymptote on Figure 2.4, the actual modal lines touch but do not cross (technically called kissing modes). When the wave exists over the bar and over the step but not over the trough, the amplitude of the wave over the bar can become large relative to the amplitude of the wave over the step, as it is governed by the size of the exponential in the trough. In Figure 2.4 the relative amplification becomes larger at higher frequencies and also for phase speeds closer to $\sqrt{gh_{\text{bar}}}$. As the trough becomes wider, the exponential growth from the shore toward the bar (or decay from the bar toward the shore) becomes indefinitely large. The amplification becomes extreme. In practice, this implies that the edge wave is effectively trapped on the bar and shoreline behavior is negligible. The edge wave is not necessarily large in any absolute sense.

4. When the phase speed is greater than $\sqrt{gh_{\text{trough}}}$ and still less than $\sqrt{gh_{\text{sea}}}$, oscillating solutions exist in the trough, step, and bar regions. The magnitude of the wave on the bar is controlled by the magnitude of the wave in the trough and therefore does not become particularly amplified relative to the shore, as in case 3.

5. Finally, when the phase speed is greater than $\sqrt{gh_{\text{sea}}}$, an oscillating solution exists in all regions. This final case is no longer an edge wave with energy trapped at the shoreline but, rather, a leaky wave, as the energy can “leak” out to sea.

These cases are summarized in a schematic in Figure 2.5. In Figure 2.5, Case 1 is

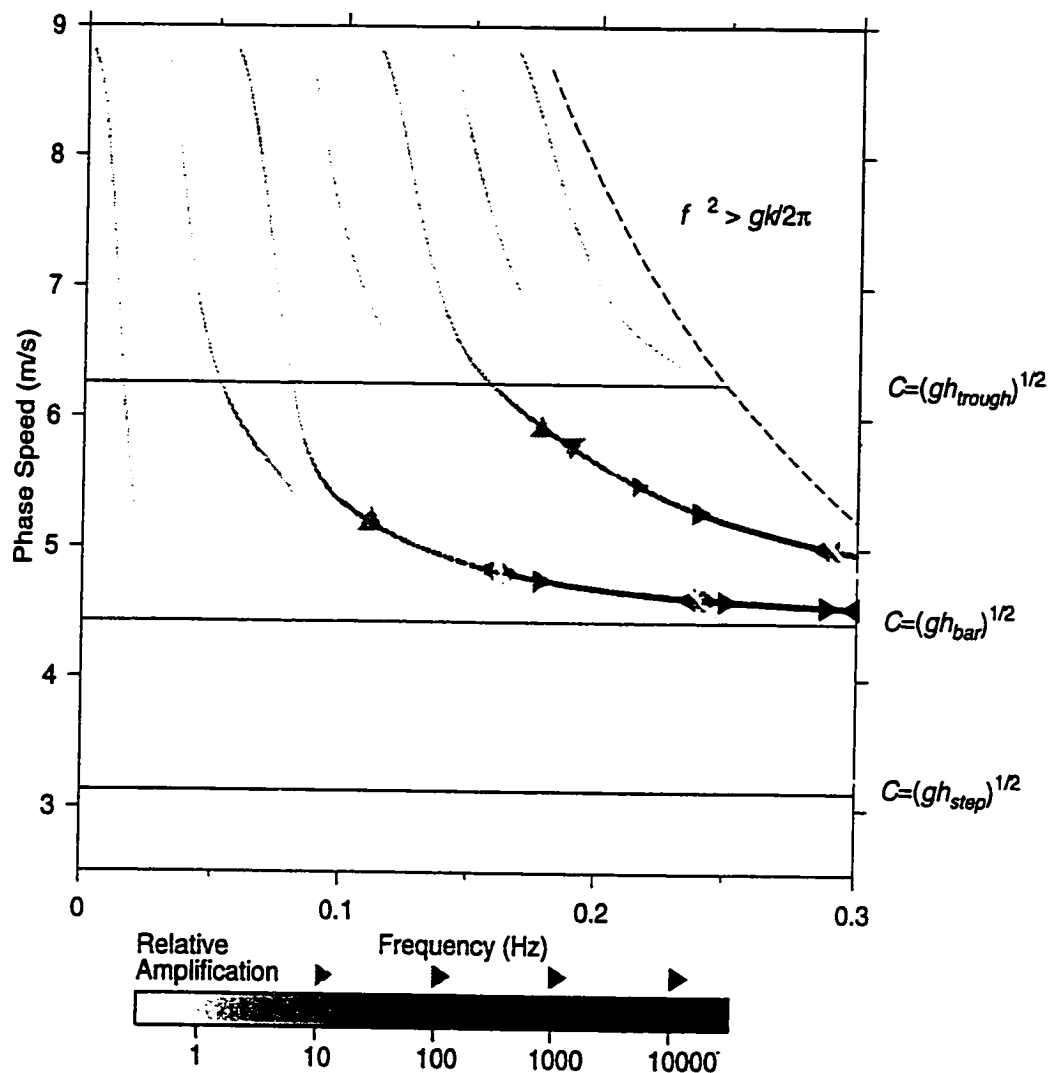


Figure 2.4: Same as in Figure 2.3, except with phase speed plotted against frequency. The leaky wave cutoff is marked with a dashed curve; the limits $C = (gh_{\text{step}})^{1/2}$, $C = (gh_{\text{bar}})^{1/2}$, and $C = (gh_{\text{trough}})^{1/2}$ are marked with labeled lines. Again, each point is a solution to the dispersion relation. The intensity of the point refers to the amplitude of the wave over the bar relative to the shoreline and is defined by computing the cross-shore shape of the edge wave corresponding to that frequency and that wavenumber. For clarity, arrows point to directions of greater amplification.

exponential everywhere, Case 2 shows a mode 3 wave on the step only, Case 3 shows a mode 3 wave which is a combination of a mode 1 wave on the bar and a mode 2 wave on the step, Case 4 is a mode 9 wave, and case 5 is a leaky wave. In Case 3, the solution shown corresponds a position on the second bar-trapped asymptote in Figure 2.4, and is a wave of which one multiple of cross-shore wave length fits on the bar. The first asymptote would correspond to a mode zero bar-trapped wave, or no zero crossings on the bar. Case 3 outlines the physical basis of bar-trapping: the relative amplification on the bar occurs when the phase speed approaches $\sqrt{gh_{\text{bar}}}$ from above.

The possibility of edge wave amplification over the bar has been noted by Kirby *et al.* (1981) and also by Schönfeldt (1991). Schönfeldt (1991) also stressed that amplification occurred at the location of the bar when the phase speed was $\sqrt{gh_{\text{bar}}}$. In general, the number of modes that exist at frequencies below the leaky wave cutoff frequency and also the degree of relative amplification depend on the cross-shore dimensions of the depth profile. Thus a wide trough allows for large relative amplification (or very effective trapping), and a wide bar allows for longer wavelengths and, consequently, modes at lower frequencies. The frequency asymptotes in the dispersion diagram (when the phase speed approaches $\sqrt{gh_{\text{bar}}}$) are inherent with edge wave profiles containing bars (they are absent on plane beach dispersion diagrams (Figure 2.1)) and correspond to dispersion of the waves travelling separately on the bar. Along this asymptote the modes again only touch, though they appear to cross. In the broader sense, this asymptote occurs anytime there is a local minimum in depth where a wave solution can exist somewhat independently on the minimum from the conditions at the shoreline. Schönfeldt (1991, 1995) only show amplification on the outer bar or their two-barred profile, but these results show that amplification could occur on either bar. Buchwald (1968) made similar calculations for the case of a submarine ridge. The wave is trapped on the ridge when exponentially decaying solutions exist on each side of the ridge, and the ridge then acts as a waveguide. The asymptote of frequency and wavenumber to infinity occurs when the phase speed approaches $\sqrt{gh_{\text{ridge}}}$ from above and the group speed $\partial\sigma/\partial k$ approaches $\sqrt{gh_{\text{ridge}}}$

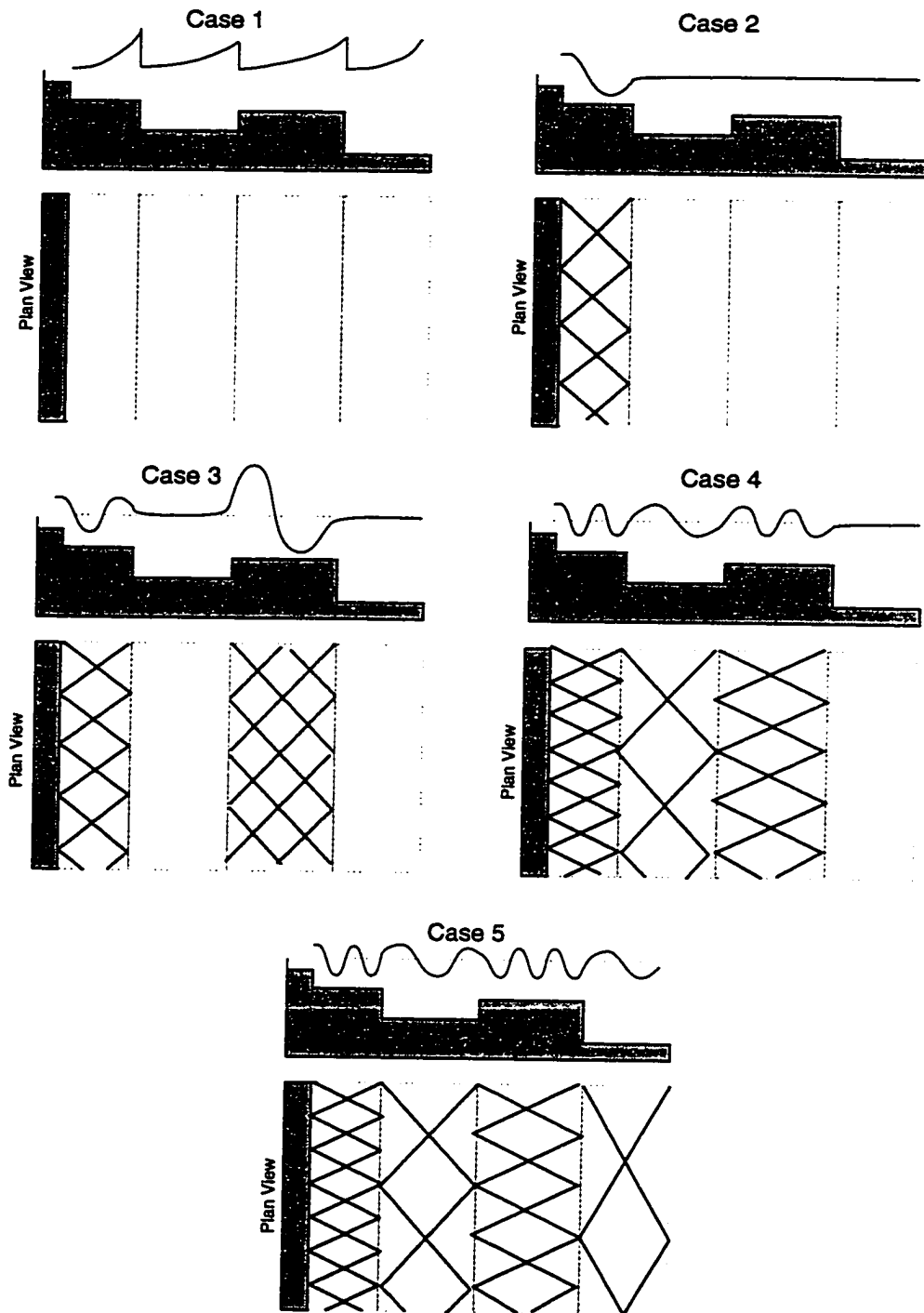


Figure 2.5: A simple schematic of the cases outlined in Section 2.1.2. In each panel shows a cross sectional view of the wave, and a plan view of the wave rays.

from below; the waves are non-dispersive in this limit. The asymptote as the phase speed approaches $\sqrt{gh_{\text{bar}}}$ in Figure 2.4 also appears to correspond to the group speed approaching $\sqrt{gh_{\text{bar}}}$ from below.

The analytic solution for this simple topography identifies the parameters that indicate the possibility of trapping and amplification over bars. In summary, a trough allows a wave-like solution to exist separately on the bar and an exponential solution to exist in the trough, when $\sqrt{gh_{\text{bar}}} < C < \sqrt{gh_{\text{trough}}}$, Case 3. The degree of relative amplification then depends on the width of the trough. These solutions are very different from solutions of edge waves on plane beaches, in which the amplitude generally decays with distance from the beach. The waves that exist somewhat separately on the bar can have a number of different shapes, regardless of the shape of the wave on the step. The simplest shape corresponds to solutions which asymptote closely to the $\sqrt{gh_{\text{bar}}}$ line in Figure 2.4. Higher order shapes correspond to higher asymptotes. The actual mode number changes along the $\sqrt{gh_{\text{bar}}}$ asymptote, so that the modal lines never actually cross, only touch.

2.2 Properties of bar trapped edge waves

2.2.1 The kissing modes

When the modal lines appear to cross, the dispersion lines which asymptote to the $\sqrt{gh_{\text{bar}}}$ line appear to cross with the dispersion lines which asymptote to the $\sqrt{gh_{\text{step}}}$. The latter lines are large over the step and very small over the bar. At the kissing point, the wave that is large over the step has essentially the same frequency and longshore wavenumber as the wave which is large over the bar. The frequency-wavenumber combinations at which this occurs depend on the dimensions of the step and the bar (2.10), and so the spacing of the kissing points depends on the cross-shore dimensions of the bar and step. The degree to which the lines touch depends on the degree to which the wave decays in the trough region. At low frequencies the wave decays minimally in the trough region, and the lines are far apart at the kissing

point. At higher frequencies, the waves decay strongly in the trough region, and the dispersion curves come very close to touching. The degree to which the dispersion curves touch, depends on the degree to which the step wave and the bar wave are coupled or connected in the trough region.

2.2.2 The non-dispersive property

When the phase speed approaches the constant $\sqrt{gh_{\text{bar}}}$, the edge waves are quasi-non dispersive. This property of bar-trapped waves, means that the longshore component of orbital velocity is not significantly diminished at high frequencies and high mode numbers relative to the cross-shore component of orbital velocity, as in the case for the plane beach solutions. For plane beach solutions, it was reasoned that high mode edge waves would be less evident than low mode edge waves in the longshore component of orbital velocity data because of the edge wave dispersion properties, (2.6). Replacing (2.6) into (2.3) and (2.4), the components of orbital velocity for plane beaches are

$$u(x) = \frac{-i\sigma}{k(2n+1)\tan\beta}\eta_x(x), \quad (2.11)$$

$$v(x) = \frac{\sigma}{(2n+1)\tan\beta}\eta(x). \quad (2.12)$$

The longshore component decreases with decreasing frequency and, particularly, with increasing mode number. This is not the case for bar trapped edge waves. In the limit of $C = \sqrt{gh_{\text{bar}}}$, the components of orbital velocity from (2.3) and (2.4) are

$$u(x) = \frac{-ig}{k\sqrt{gh_{\text{bar}}}}\eta_x(x), \quad (2.13)$$

$$v(x) = \frac{g}{\sqrt{gh_{\text{bar}}}}\eta(x).$$

So for a given modal shape, the longshore component of orbital velocity will not decrease with increasing phase speed, but remain simply proportional to the sea surface elevation. The relatively large longshore component of velocity may allow the detection of edge waves at higher frequencies than edge waves have traditionally been observed.

2.3 Numerical solutions for more complex topographies

It is desirable to investigate more realistic topographies to test the robustness of the conclusions drawn from the analytic solutions in Section 2.1.2. We proceeded using the numerical model outlined by Howd *et al.* (1992) to calculate numerical solutions for the idealized and observed beach profiles in Figure 2.6. The model employs a Runge-Kutta scheme to calculate the edge wave shape on a particular topography. A search scheme is used to find the σ and k values for which solutions do not diverge as x gets large. These solutions define a set of edge wave modes for this topography.

Model calculations for a topography similar to that used in the analytical solution (Figure 2.6a) again show relative amplification of sea surface elevation occurring when the phase speed approaches $\sqrt{gh_{\text{bar}}}$ (Figure 2.7). Again, to find the amplification, the sea surface elevation has been calculated for each combination of wavenumber and frequency which lie on the dispersion curve. Differences between the solutions for idealized topography and those for more realistic topography occur in the scale and definition of the bar and the trough. The profile in Figure 2.6a has very wide bar and trough, allowing for very extreme amplification. The analytic solution indicates that the edge wave exists separately on the bar when the phase speed is between $\sqrt{gh_{\text{bar}}}$ and $\sqrt{gh_{\text{trough}}}$, where in the corresponding numeric case, h_{trough} is the deepest part of the trough and h_{bar} is the shallowest part of the bar; therefore the effective length scale of the bar is large, as it includes all the inclined area on either side of the bar. Consequently, at any given phase speed the wider bar in the numeric case will allow larger cross-shore wavelengths, and therefore longshore wavenumber and frequency must be smaller (from (2.10)) than in the analytic case. At any particular phase speed, edge waves on wider bars will exist at lower frequencies. A direct consequence is that more solutions are represented in Figure 2.7, and more of the $\sqrt{gh_{\text{bar}}}$ asymptotes corresponding to higher order bar-trapped modes are shown.

Figures 2.8 and 2.9 show that similar conclusions can be drawn from numerical

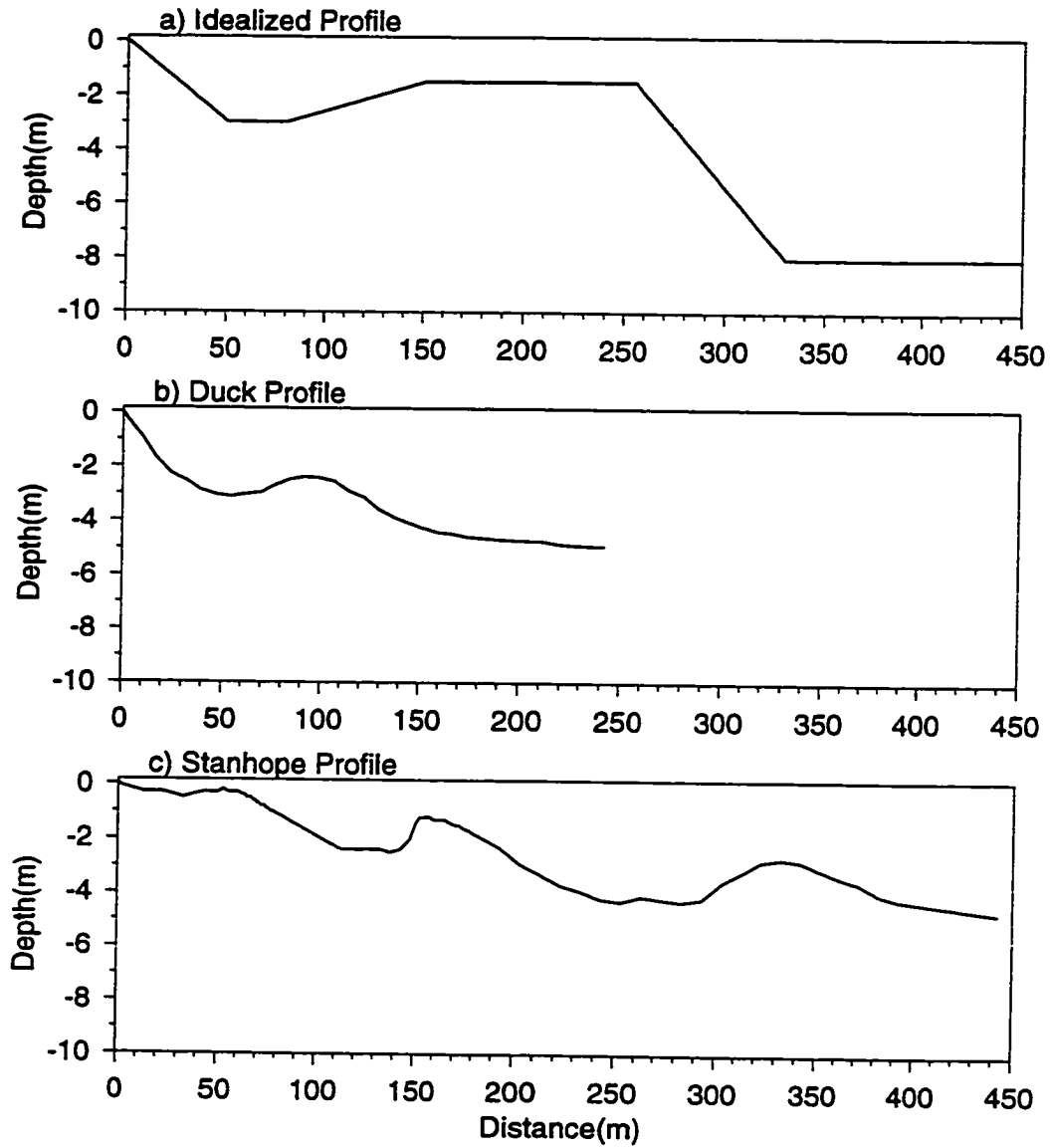


Figure 2.6: Topographies used in numerical calculations (a) idealized (b) Duck, North Carolina, and (c) Stanhope, Prince Edward Island.

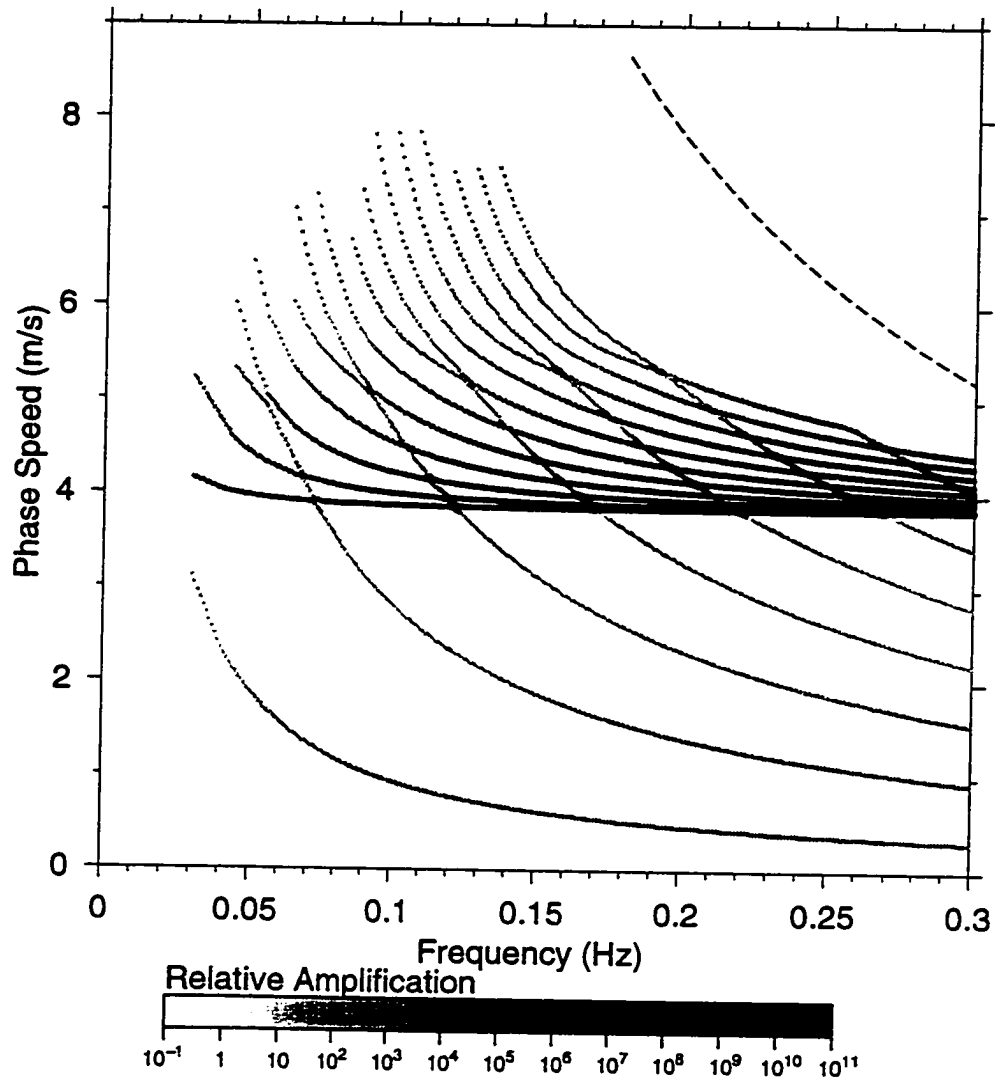


Figure 2.7: Dispersion diagram from numerical calculations over idealized topography (Figure 2.6a). The extreme amplification caused by this topography makes it difficult to calculate the cross-shore shapes of edge waves that have solutions on the dispersion curves which cross the bar trapped line. Closer examination of these solutions show them to be very small over the bar relative to the shoreline, which is not evident in this figure, but is evident in Figure 2.8, and 2.4.

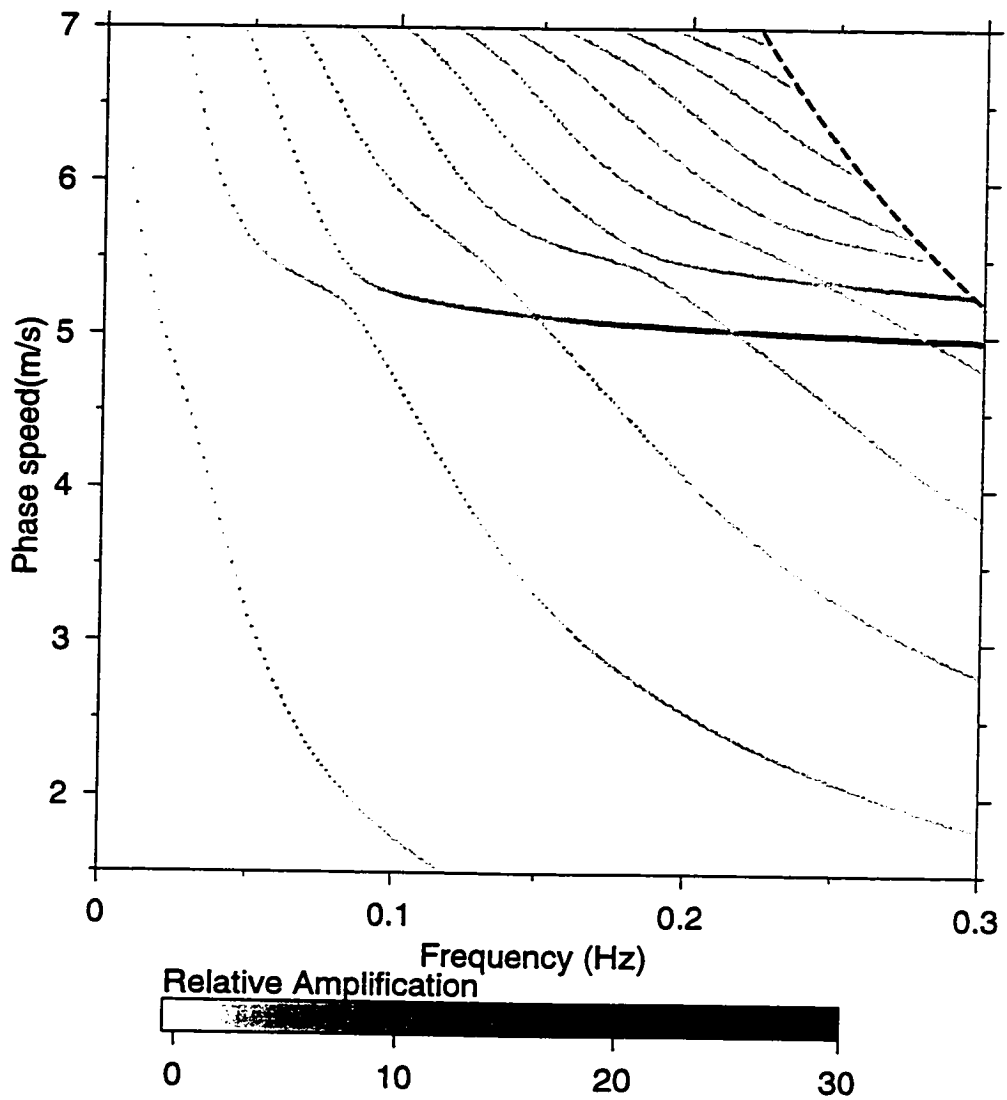


Figure 2.8: Dispersion diagram for Duck, North Carolina, a simple one-bar beach (Figure 2.6b).

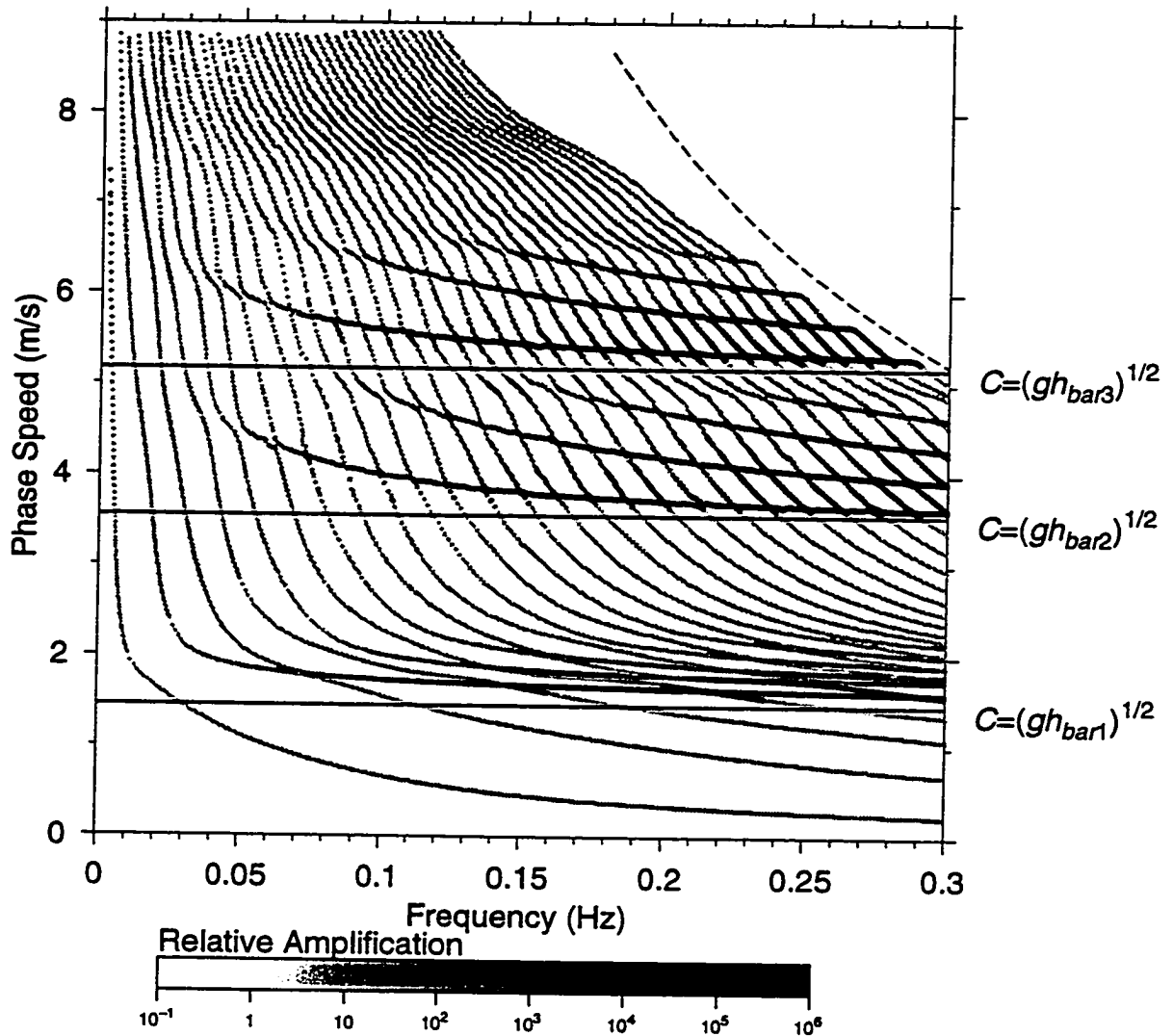


Figure 2.9: Dispersion diagram for Stanhope, Prince Edward Island, a complex three-barred beach system (Figure 2.6c). The extreme amplification caused by this topography makes it difficult to calculate the cross-shore shapes of edge waves that have solutions on the dispersion curves which cross the bar trapped line. Closer examination of these solutions show them to be very small over the bar relative to the shoreline, which is not evident in this figure, but is evident in Figure 2.8, and 2.4.

results over topographies widely different in nature. Two extremes are represented by Duck, North Carolina (Figure 2.6b), which has a small-scale, single-barred topography, and Stanhope Beach, Prince Edward Island (Figure 2.6c), which has complex topography with three large scale bars. On Stanhope Beach, edge waves become amplified over a bar when the phase speed approaches $\sqrt{gh_{\text{bar}}}$ on that bar. As the phase speed approaches $\sqrt{gh_{\text{bar}1}}$, the wave will exist on the inside bar and will decay seaward over the outer two bars. As the phase speed approaches $\sqrt{gh_{\text{bar}2}}$, the wave will exist on the first and second bars, then decay in the trough between the first and second bar and seaward of the second bar over the third bar. The same will be true of the third bar when the phase speed approaches $\sqrt{gh_{\text{bar}3}}$. It would be possible for waves to exist separately on two or more bars at once, if the outer bar is shallower and the outer troughs are of equal depth or shallower than the inner troughs. Stanhope Beach has wider troughs and bars than Duck beach, and, consequently, has greater amplification, the modes existing at comparatively lower frequencies than at Duck. Again, differences from the analytical solutions occur due to the definition of what constitutes a bar.

The numerical calculations illustrate well the conclusions drawn from the analytic solutions: all edge waves on beaches with bars (where obviously the trough must be deeper than the bar) have their greatest maxima over the location of the bar, when the phase speed approaches $\sqrt{gh_{\text{bar}}}$. When this occurs on a particular bar, a separate wave exists on the bar with an exponential solution on the inshore trough. The flattening out of the dispersion diagram at $\sqrt{gh_{\text{bar}}}$ occurs when the cross-shore wavelength on the bar is restricted to decaying on either side of the bar, as noted in the discussion of the analytical solution (Section 2.1.2). Beaches with large length scales such as Stanhope will have larger amplifications and modes of lower frequency than beaches of smaller cross-shore length scales such as Duck.

Figure 2.10: Center panel: the same dispersion diagram as given in Figure 2.8. Each of the surrounding panels: sea surface elevation (m), cross shore velocity (m/s) and longshore velocity (m/s) and depth (m) profiles corresponding to each of the solution ranges marked in the center dispersion diagram, assuming $\eta(0) = 1$. Darker grey lines corresponds to higher frequency.

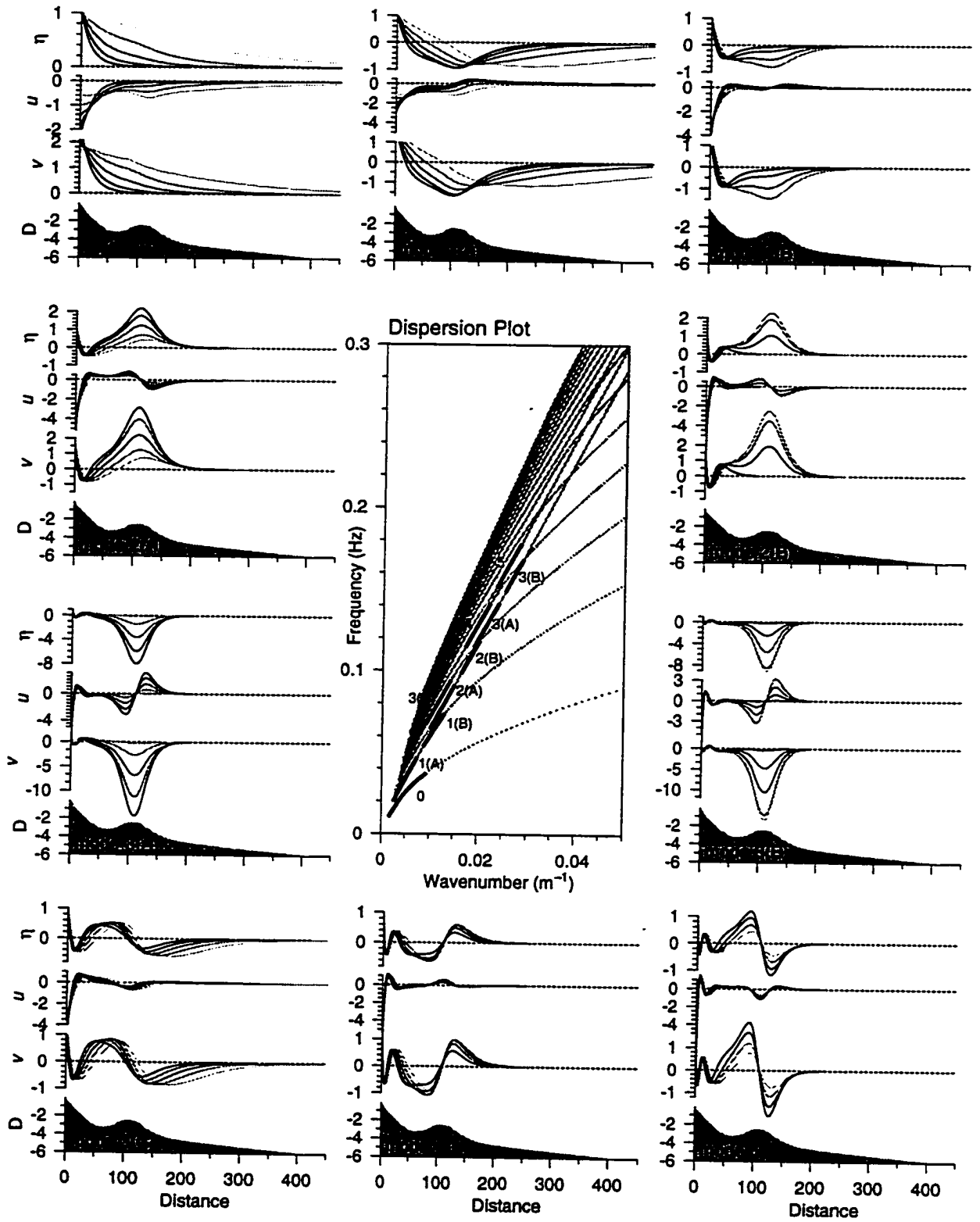


Figure 10

2.4 Cross-shore shapes of bar-trapped edge waves

Each frequency-wavenumber pair defines the coordinates on the dispersion diagram corresponding to one particular edge wave shape, unique to that specific pair. The pair lying along the asymptotes where $C \rightarrow \sqrt{gh_{\text{bar}}}$ are bar trapped edge waves; the lowest asymptote corresponds to the simplest shapes over the bar, the higher asymptotes to more complex shapes, as discussed in Section 2.1.2, Case 3. Though the discussion in Section 2.1.2 and dispersion diagram in Figure 2.4 summarize the fundamentals of the bar trapping mechanism, examining the cross-shore shapes over one of the more realistic topographies, for example the topography in Figure 2.6B, in more detail will prove useful when comparing theoretical solutions to data, in Chapter 3.

Figure 2.10 shows examples from different regions in the dispersion diagram from Duck, N.C., plotted in Figure 2.8 (here, and from now, on the dispersion diagram will be plotted as a function of wavenumber, in preparation for data analysis in Chapter 3). The shapes that are amplified (Figure 2.10, surrounding panels) correspond to the frequency and wavenumber which have phase speeds along the asymptotes $C \rightarrow \sqrt{gh_{\text{bar}}}$ (Figure 2.10, Center Panel), or the solutions discussed in Case 3 in Section 2.1.2. The greyscale in surrounding panels in Figure 2.10 corresponds to increasing frequency. Along the first (lowest) asymptote, the trapping is minimal for mode 0 waves, where only the lowest frequency waves lie along the $C \rightarrow \sqrt{gh_{\text{bar}}}$, and are affected by the bar (Figure 2.10, mode 0). Similarly, low frequency mode 1 waves have phase speeds which are too high to be affected by the bar, but as the frequency increases, edge wave amplification occurs over the bar (Figure 2.10, mode 1A). As the frequency continues to increase (Figure 2.10, mode 1B), the amplification diminishes, until the phase speed drops below $\sqrt{gh_{\text{bar}}}$, in which case the wave exists primarily in the shallow regions in-shore of the bar, Case 2 in Section 2.1.2. The cross-shore component also has zero crossing at the top of the bar corresponding to maxima in v and η . Continuing along the same asymptote, Mode 2A and B have the same shapes over the bar as mode 1A and B (Figure 2.10), but the amplification relative

to the shore is greater; the wave on the bar is more effectively trapped at higher frequencies. Similarly, the trapped mode 3A and B waves have the same shape over the bar as modes 1 and 2; in the absence of a beach, all these shapes correspond to a bar trapped wave of mode 0, or a wave lacking zero crossings in v and η over the bar. This simple bar trapped mode shape becomes more defined for increasingly high modes along the lowest $C \rightarrow \sqrt{gh_{\text{bar}}}$ asymptote. Solutions corresponding to the second asymptote have shapes over the bar with one zero crossing (Figure 2.10, mode 3C), (corresponding to bar-trapped mode 1 in Section 2.1.2, Case 3). Again, this more complex mode becomes more pronounced, as the the frequency increases along this second asymptote (Figure 2.10, mode 4 and mode 5).

2.5 Bar trapping and longshore currents

Longshore currents affect the edge wave as though they were a change in the bottom topography (Howd *et al.*, 1991b, 1992). Edge waves travelling with the longshore current have the same effect as a deeper depth profile and edge waves travelling against the current have the same effect as a shallower depth profile, with the magnitude of the change proportional to the current at that location. It can be seen immediately, that if the effect of the longshore current shear was strong enough, it might change the depth profile to which the edge wave responds, to the point of having the same effect as a bar.

Edge wave behaviour over topography and longshore currents which are variable in the cross-shore direction, but constant in the longshore direction, can be examined mathematically by assuming the cross-shore velocity u and the sea surface elevation η are wave-like in the longshore direction (as in (2.1)), and the longshore velocity v is a combination of a wave-like solution and a mean current $V(x)$ in the longshore direction (Howd *et al.*, 1992)

$$\begin{aligned}\eta &= \eta(x)e^{i(ky-\sigma t)}, \\ u &= u(x)e^{i(ky-\sigma t)},\end{aligned}\tag{2.14}$$

$$v = v(x)e^{i(ky-\sigma t)} + V(x).$$

Substituting (2.14) into the irrotational, inviscid shallow water equations of momentum and continuity and retaining only the terms which are linear in u , v and η gives

$$\left[\frac{gh\eta_x}{(-\sigma + kV)^2} \right]_x + \eta \left[1 - \frac{k^2gh}{(-\sigma + kV)^2} \right] = 0, \quad (2.15)$$

$$u = \frac{ig\eta_x}{(-\sigma + kV)},$$

$$v = \frac{-kg\eta + iuV_x}{(-\sigma + kV)}$$

where the variables are now solely dependent on x . In the case of $V = 0$, (2.15) reduces to the classic edge wave equation, (2.2). Howd *et al.* (1992) defined a new “effective” depth by substituting

$$h' = \frac{h}{(1 - V/C)^2} \quad (2.16)$$

where C is the edge wave phase velocity, σ/k , which gives

$$\left[\frac{gh'\eta_x}{\sigma^2} \right]_x + \eta \left[1 - \frac{k^2gh'}{\sigma^2} \right] = 0 \quad (2.17)$$

which is the classic edge wave (2.2). This substitution shows that the effect of a longshore current on the edge wave shape is mathematically analogous to a change in the bottom topography.

When a local minimum in h' occurs (other than at the shoreline), the edge wave can be trapped and amplified relative to the shore at the location of the minimum in the same way as edge waves are trapped on bars. This introduces the possibility of edge waves which are trapped on longshore currents on plane beaches. On barred beaches, the longshore current can act to enhance or diminish the amplification which already exists due to the effect of bars (Schönfeldt, 1995).

2.5.1 The longshore current waveguide on plane beaches

To discuss the interaction of topography and longshore current in (2.17) in more detail, it is useful to look at the simple case of a longshore current on a plane beach. A local minimum in h' will occur on a plane beach when there is a negative slope somewhere in the effective depth profile, h' , i.e. when the derivative of the effective depth is negative. Taking the derivative of (2.16) gives

$$\frac{dh'}{dx} = \frac{1}{(1 - V/C)^2} \frac{dh}{dx} + \frac{2h}{C(1 - V/C)^3} \frac{dV}{dx}.$$

So the criterion for the existence of an effective bar is

$$\frac{dh}{dx} + \frac{2h}{C - V} \frac{dV}{dx} \leq 0. \quad (2.18)$$

Here we define h and therefore dh/dx to be positive on a plane beach. Since dh/dx and $2h/(C - V)$ are always positive on a plane beach (for edge waves, $V \ll C$; solutions for $V \approx C$ are shear waves), dV/dx must be negative to satisfy (2.18). The existence of an effective bar will depend on the relative magnitudes of dh/dx and dV/dx , the depth at which they occur, and the phase speed. The combination of a strong current shear and a gentle bottom slope is then likely to produce an effective bar, especially if the current is in deeper water.

The longshore current profiles which might realistically occur on plane beaches are determined by the gradient of the radiation stress caused by incident wave breaking (Bowen, 1969; Thornton and Guza, 1986). Radiation stress is conserved outside the surf zone, where the incident waves have not yet broken, and the gradient is maximal where the incident waves break intensively. The distance over which the radiation stress gradient changes from zero to maximal depends on the incident wave height variability (Thornton and Guza, 1986), and can be quite small; this can create a strong shear seaward of the longshore current maximum. Inside the initial breaking zone, the radiation stress diminishes approximately linearly as the saturation wave height diminishes (Thornton and Guza, 1986). Therefore the current shear seaward of the maximum current is generally much larger than the current shear landward

of the current maximum (Figure 2.11A). With these restrictions, a strong longshore current (for example $V_{max} = 1.2m/s$ at $120m$, on a beach with aspect ratio 0.02) will have a landward shear which is insufficient to generate an effective trough when the longshore current is negative, in opposition to the direction of edge wave propagation (Figure 2.11B). In this case, the strong seaward shear is positive and creates an positive slope in effective depth, the seaward face of an terrace in h' (Figure 2.11B). Note the terrace is most extreme at low phase speeds. The cross-shore shapes of the edge wave solutions will be affected by the terrace, but the solutions will not be amplified relative to their shoreline values, as could occur over barred topography (Figure 2.11C). The top of the terrace in Figure 2.11B corresponds to the location of V_{max} .

When the same current is flowing in the positive direction (when the edge waves are travelling with the longshore current), the current will create an effective bar (Figure 2.12A and B). In this case, the stronger seaward current shear allows $dh'/dx < 0$ and an effective trough exists. The size of the trough decreases with increasing phase speed, but for the strong longshore current shown here, still exists at a phase speed $> \sqrt{gh'_{min}}$. When the phase speed approaches $\sqrt{gh'_{min}}$, the solutions are amplified over the effective bar, relative to the shoreline, in exactly the same way as edge waves are amplified over real bars (Figure 2.12C). Amplification relative to the shoreline is mild in the case of the longshore current in Figure 2.12A.

In both Figures 2.11 and 2.12, the phase speed of the edge wave determines both whether an effective bar occurs and whether the edge wave is trapped on that effective bar (i.e. trapping only occurs when $C \rightarrow \sqrt{gh'_{min}}$). For example, though small phase speeds are more likely to make effective bars, if $C < \sqrt{gh'_{min}}$, the edge wave is exponentially decaying over the bar and will not be trapped and amplified relative to the shoreline. Including the dependence of the effective depth (2.16) on phase speed, the bar trapping limit $C \rightarrow \sqrt{gh'_{min}}$ can be written as

$$C \rightarrow \sqrt{gh(x_{min})} + V(x_{min}) \quad (2.19)$$

where x_{min} is the location at which h'_{min} occurs. The trapping limit is greater for

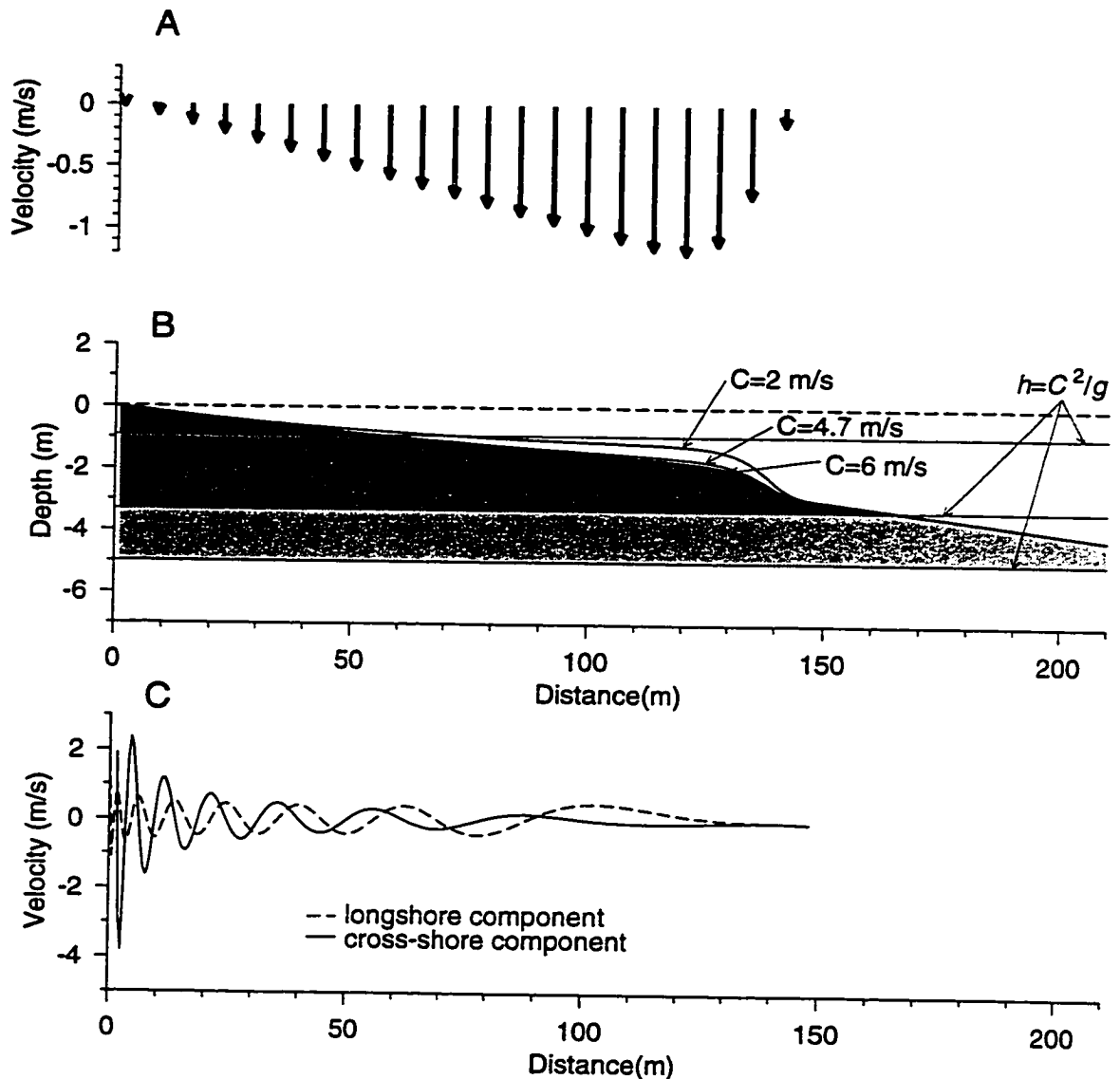


Figure 2.11: A. Idealized longshore current profile on a plane beach (plan view). B. Effective depth profiles for waves travelling against the longshore current for various phase speeds. Shading corresponds to the area for which the edge wave solution is sinusoidal for each phase speed given. C. Calculated edge wave cross-shore and longshore current profiles for $f=0.192\text{Hz}$, $C=3.57\text{m/s}$, mode 14.

waves travelling with the current than against.

The effect of the local minimum in h' is exactly the same as the effect of the local minimum discussed in Section 2.1.2. So the dispersion properties of these longshore current-trapped edge waves are different than those of edge waves on plane beaches, because they are limited to travelling at $C \rightarrow \sqrt{gh'_{min}}$. As a result, the dispersion diagram for a beach with an effective bar is very different from that for a plane beach (Figure 2.1); the effective bar trapped modes occur along a diagonal line in frequency-wavenumber space corresponding to a near constant phase speed (Figure 2.13).

This simple case on a plane beach shows that it is possible to qualitatively examine the effect of the longshore current on the trapping of edge waves, without solving (2.15), but calculating the effective depth profile (2.16). These examples are for a longshore current profile which has a steep seaward shear, but the principle applies to cases with less extreme seaward shear, expected on days with very variable incident wave height. Trapping and amplification of edge waves will occur if the current shear is strong relative to the slope of the bottom.

2.5.2 The combined effect of longshore currents and bars

When bars and longshore currents coexist on a beach, the resulting edge wave shape will depend on some combination of bar effect and the longshore current effect. Schönfeldt (1995) shows an example of a current on a beach with two bars in which the current covers the entire region inshore of the outer bar (Figure 2.14). Such a strong longshore current localized over the trough, causes enhanced trapping of edge waves when waves travel with the longshore current, but no trapping when waves travel against the longshore current. This is a specific example of one of many different cases, which depend, in general, on the position of the minimum in effective depth, h'_{min} , which, in turn, will depend (as in the plane beach case) on the strength and location of the longshore current shear relative to the varying bottom slope, as indicated by (2.16) and (2.18).

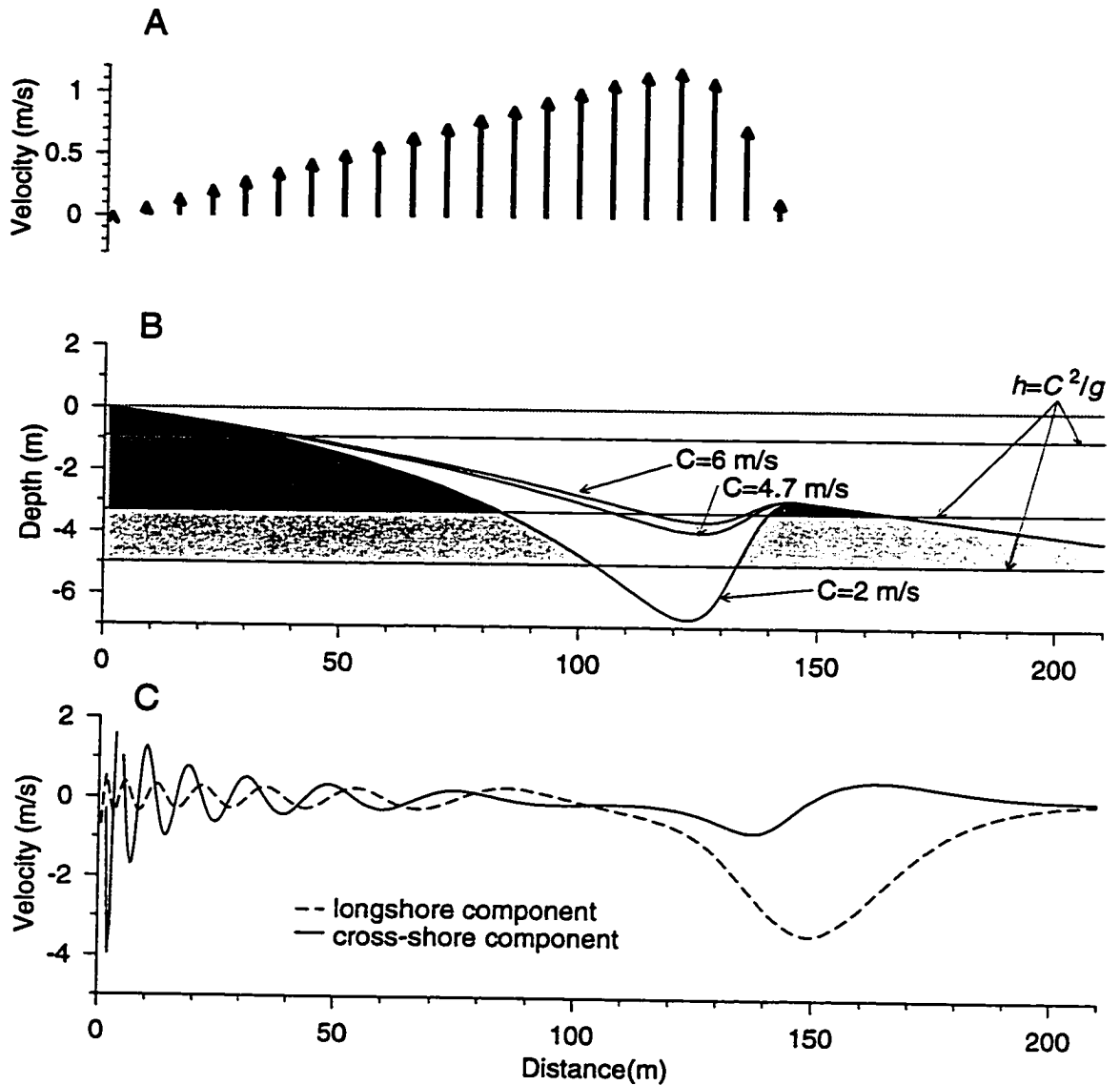


Figure 2.12: A. Idealized longshore current profile on a plane beach (plan view). B. Effective depth profiles for waves travelling with the longshore current for various phase speeds. Shading corresponds to the area for which the edge wave solution is sinusoidal for each phase speed given. C. Calculated edge wave cross-shore and longshore current profiles for $f=0.192\text{Hz}$, $C=5.7\text{m/s}$, mode 14.

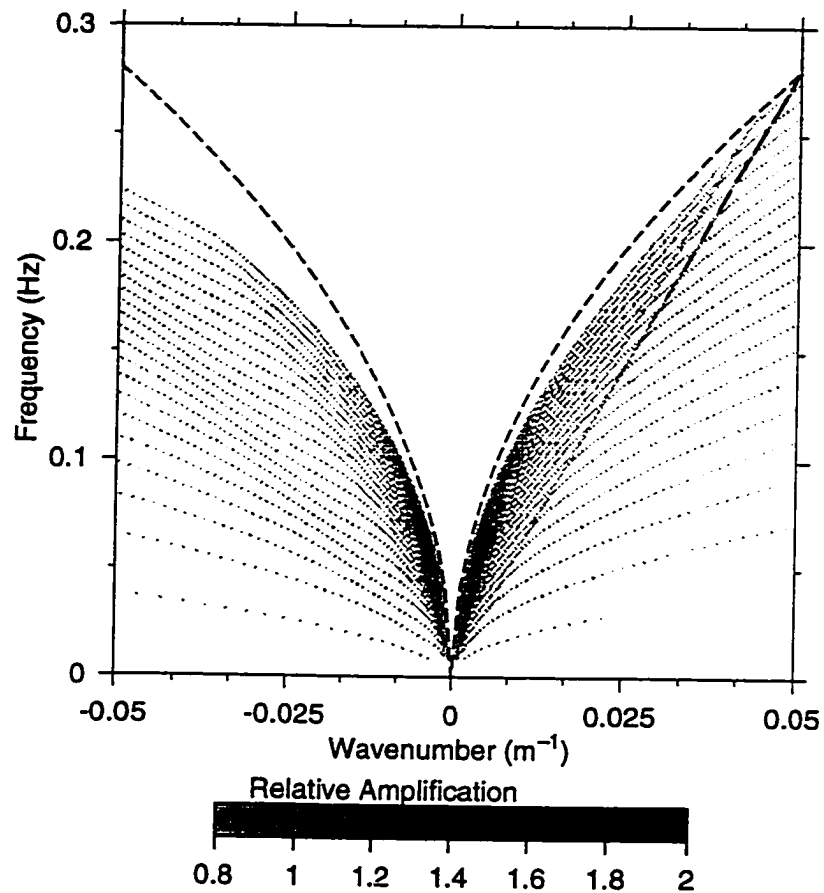


Figure 2.13: Dispersion diagram for edge waves on a plane beach with a longshore current. The grey scale is the amplification of sea surface elevation over the bar relative to the shoreline values. The waves are most amplified when the phase speed C approaches $(gh'_{\text{bar}})^{1/2}$, where h' is the effective depth as defined in (2.16).

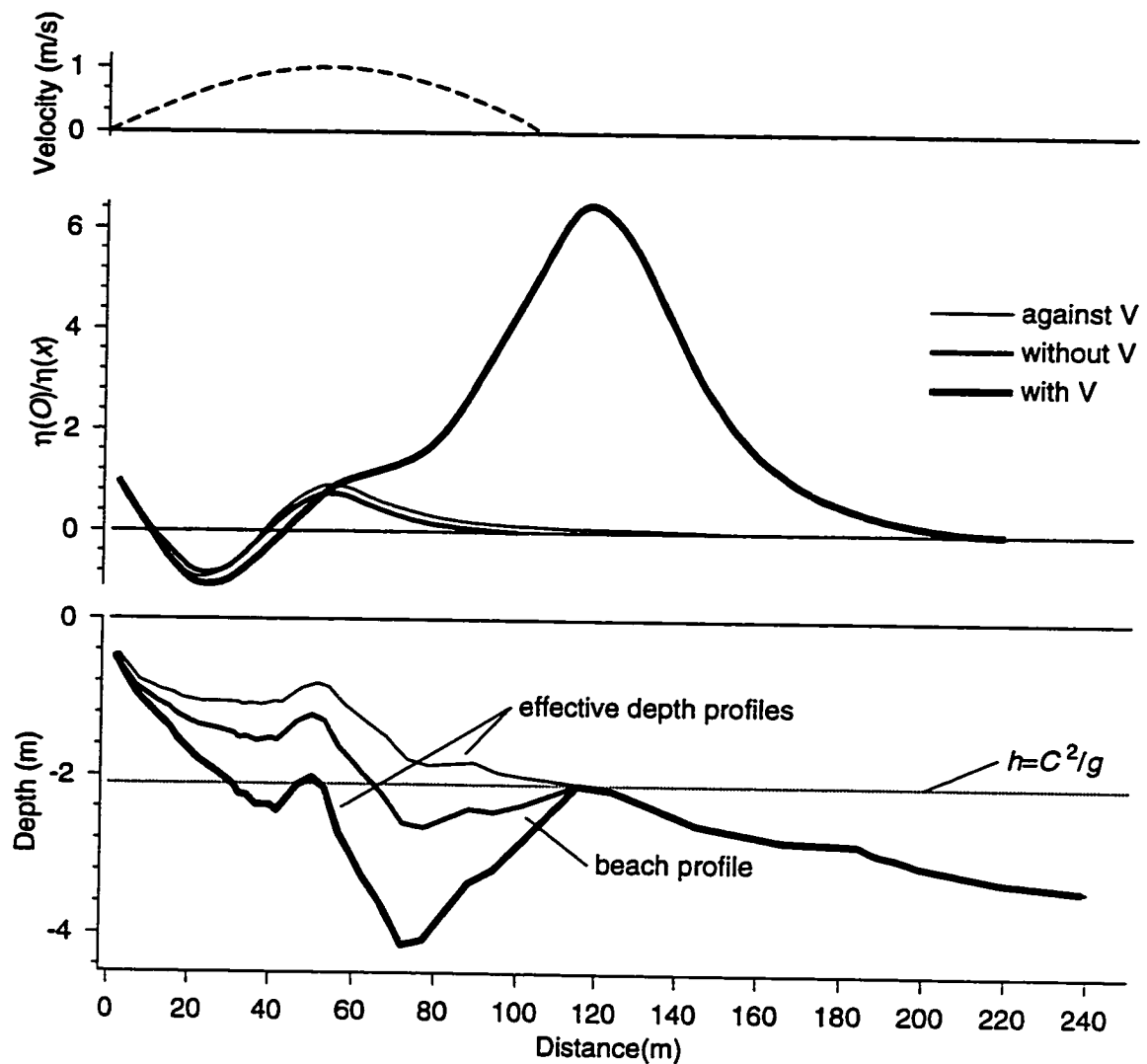


Figure 2.14: Longshore current profile (top), sea surface elevation of a mode 2 edge wave (middle), and bottom profile (bottom) after Schönfeldt (1995). The sea surface elevation was calculated numerically with and without the longshore current. Added to the depth profile, are our calculations of the effective depth for this current profile. Thickest lines are for the edge wave propagating with the longshore current, thinnest lines are for edge waves propagating against the longshore current.

When the longshore current or longshore current shear is weak relative to the bottom slope, the trapping which already occurs due to the bar, will be relatively unaffected by the longshore current. With weak shear, the longshore current peak may cover the bar and the trough, resulting in an overall effective profile which is deeper when waves travel with the longshore current and shallower when waves travel against the longshore current. In this case, the cross-shore location of the effective bar will be similar to the actual bar and the trapping criterion from (2.19) is $C \rightarrow \sqrt{gh_{bar}} + V(x_{bar})$ (a Taylor expansion of (2.16) around $\sqrt{gh_{bar}}$ will give this result to the first order if $(x_{bar} - x_{min})$ is small). When the current is very weak, the bar trapping effect is unaffected and $C \rightarrow \sqrt{gh_{bar}}$, as on a beach with no current. These type of effective depth profiles are dominated by the effect of the bar or “bar-dominated”.

Conversely, if the longshore current has a narrow peak (with a strong shear relative to the bottom slope), the longshore current can determine if and where an effective bar exists on a barred profile. For example, a hypothetical longshore current with a narrow, large, suitably-located peak (Figure 2.15A and B), can completely change the character of the depth profile, at least for edge waves travelling in particular direction; a trough current can remove the effect of the bar when waves travel against the longshore current (Figure 2.15B) and a bar current can completely remove the effect of the bar when waves travel with the longshore current (Figure 2.15A). In Schönfeldt’s (1995) trough current (Figure 2.14), the effect of the outer trough is eliminated for edge waves travelling against the longshore current (the result is a profile where amplification can only occur on the inner bar), and the trough is enhanced when edge waves travel with the longshore current. If the longshore current shear is very strong relative to the topography, it could make a new effective bar at a different location or create an effective bar such as on a plane beach (Figure 2.12). In these cases the current is equally or more important than the bar, a “current-dominated” situation.

In this extreme current dominated case, the pattern of drift velocities may no longer enhance the bar, but might move material to a new location dictated by the

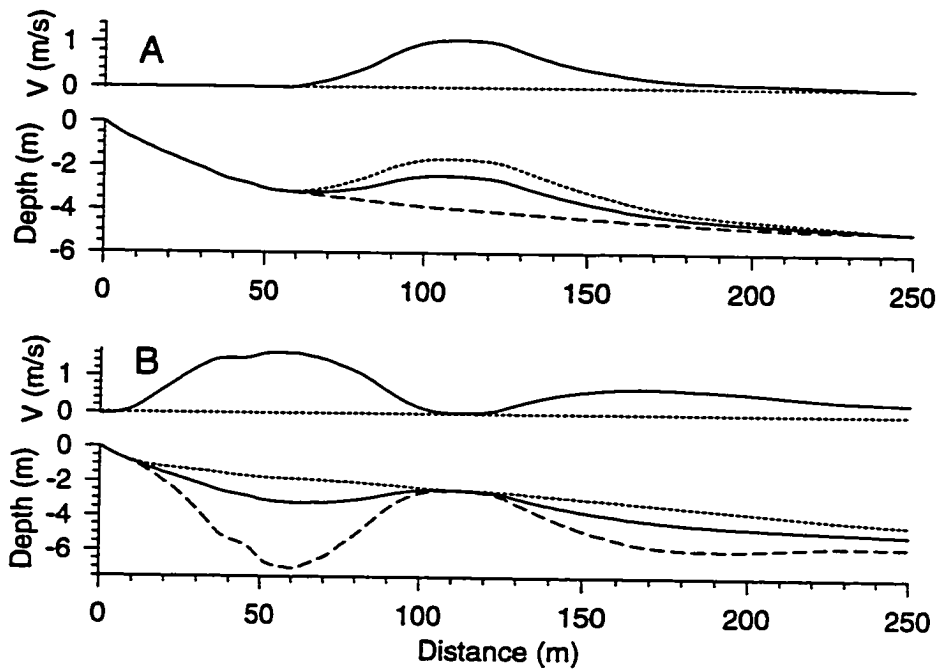


Figure 2.15: A. Idealized longshore current profile for a current over a bar, actual depth profile (solid line), effective depth profile, for waves moving with (long dash) and against (short dash) the longshore current. B. Idealized longshore current profile for a current in the trough, and associated effective and actual depth profiles.

longshore current profile. In reality, longshore bars have frequently been observed to move seaward during storms (Wright and Short, 1983; Sallenger *et al.*, 1985; Howd and Birkemeier, 1987). Howd *et al.* (1991b) showed some preliminary evidence suggesting that during a storm on a barred beach, the bar moved seaward to a location determined by the longshore current profile. The trapping effect of the longshore current could be a mechanism for bar movement. This would depend on whether the effect of the longshore current profile on the edge wave in real beach situations substantially modifies the effect of the bar. In reality the longshore current profiles are not independent of the depth profiles. The current profiles which actually occur are limited by the character of incident wave breaking over the bar. For example, modeling studies show currents on barred beaches should have two maxima: one at, or slightly shoreward, of the bar and one near the shoreline, caused by incident wave breaking patterns (Larson and Kraus, 1991). Field data suggest that the longshore current maximum is often more evenly distributed across the trough (Smith *et al.*, 1993). Though these studies give a general indication of the longshore current profiles one might expect, only detailed examination of the location and strength of naturally occurring current shear relative to real depth profiles, will show whether these current-modified effective depth profiles occur, and consequently whether longshore currents do play a significant role in determining edge wave shape on barred beaches as well as on plane beaches.

2.6 Summary

The results presented in this Chapter generalize the numerical observations made by Schönfeldt (1991, 1995) and Falques and Iranzo (1992) on specific beach profiles. Analytic and numerical solutions show that when $\sqrt{gh_{\text{bar}}} < C < \sqrt{gh_{\text{trough}}}$, edge waves exist on the bar separately from edge waves at the shoreline. When the phase speed and the group speed approach $\sqrt{gh_{\text{bar}}}$, the bar-trapped modes are amplified relative to waves at the shoreline, with the size of the amplification related to the width

of the trough. On beaches with multiple bars, edge waves can be amplified on each bar when the phase speed approaches $\sqrt{gh_{\text{bar}}}$ for that bar. Extreme amplifications indicate mainly that shoreline edge waves are negligible, not that sea surface elevation is large over the bar. On a particular profile, amplification is most extreme for high frequencies and wavenumbers.

The non-dispersive behaviour of these bar-trapped solutions allows the longshore component of orbital velocity to be directly proportional to the sea surface elevation. This is in sharp contrast to plane beaches, where the longshore orbital velocity diminishes with increased frequency and mode number. This property may allow detection and identification of bar trapped edge waves in longshore component of orbital velocity data of higher mode and frequency than in other edge wave field studies (for example, Oltman-Shay and Guza (1987)).

Longshore currents have the potential to seriously modify the effect of the bar on theoretical solutions of bar-trapped edge waves. The effective depth profile provides a convenient way to assess this effect. Longshore currents can cause edge wave trapping, if they cause the effective depth profile (2.16) to have a local minimum or an effective bar. On a plane beach, this is most likely to occur when edge waves travel with the longshore current, in which case trapping occurs at $C \rightarrow \sqrt{gh(x_{\text{min}})} + V(x_{\text{min}})$. When bars and currents coexist, trapping will depend on whether the two effects act to enhance or diminish each other. For example, a trough (bar) current would diminish (enhance) the trough (bar) if edge waves propagated against the longshore current. The longshore current will have greatest affect in changing the effective depth profile when the shear is strong relative to the bottom slope. In extreme cases, it is possible for a longshore current to totally remove the effect of a bar or trough, at least for waves travelling in one direction.

The implications of bar trapping for the design of instrument arrays to observe edge waves are numerous. Shoreline values of edge waves can no longer be seen as indicative of the general edge wave climate, but only of the edge waves that are relatively unaffected by the bar. Edge wave solutions on or close to the bar may be

dominated by the bar trapped waves (but are still affected by nodal structure). Edge waves observed in deep water may not be trapped at the shoreline, but may originate at some deeper bar or bump, previously unconsidered. The edge waves observed at any one location will depend on their distance from the bar crest. Overall, bar trapped edge waves add an increasing level of complexity in the interpretation of edge wave signals. However, the trapped wave on the bar will be limited to travelling at a minimum phase speed governed by the depth of the bar. Significant energy travelling at or close to this speed in data could be attributed to bar-trapped edge waves.

Frequency-wavenumber spectra of the measured longshore component of velocity from alongshore arrays of electro-magnetic current meters have proved useful in identifying edge waves in field data in the past (Oltman-Shay and Guza, 1987). Using such frequency-wavenumber spectra we can assess the dominance and directionality of bar trapped edge waves and also their sensitivity to changes in the longshore current and depth profiles. Observations made during the DELILAH experiment, Duck, N.C., October 1990, are used in the next Chapter to show that bar trapped edge waves are almost always present and frequently dominate edge wave spectra of the longshore component of orbital velocity obtained by instruments located on top of and close to a longshore bar, though they vary in intensity and bandwidth with the incident wave conditions.

Chapter 3

Field Observations of Bar-Trapped Edge Waves

The apparent distribution of energy between edge wave modes in observations of the longshore component of orbital velocity from the nearshore environment depends on the off-shore location at which the observations are taken (Huntley, 1976; Huntley *et al.*, 1981; Holman, 1981; Holman and Sallenger, 1993). Low mode edge waves are relatively more important at, or close to, the shore line (Huntley *et al.*, 1981; Holman, 1981; Oltman-Shay and Guza, 1987; Aagaard, 1990; Bauer and Greenwood, 1990 and many others) and high mode edge waves tend to dominate in deeper (8-13m) water (Okiihiro *et al.*, 1992; Elgar *et al.* 1992; Herbers *et al.*, 1995b), where the lower modes have decayed. In observations from shallow water, the nodal structure may make the edge wave spectra appear peaky (Wright *et al.*, 1986), and provide an incomplete picture of the edge wave field (Holman, 1981). Researchers have tried to correct for this by extrapolating the values obtained at an instrument array to their theoretical value at the shoreline, using the plane beach solutions (Holman, 1981). Shoreline run-up observations should not have this problem, and have been considered ideal for investigating the edge wave field (on plane beaches, edge waves decay with increasing distance from the shoreline). Observations in deeper water are more representative of the overall energy distribution of the edge waves as it is possible to ignore the higher

mode edge wave nodal structure as the anti-nodes are closely spaced and observations can be averaged over a frequency bandwidth to remove this nodal structure (Herbers *et al.*, 1995b). In general, observations of edge waves have assumed that the solutions decay from the shoreline, with the slope of the beach, the frequency and the mode number dictating the rate of decay, and the topography affecting the shape of the solutions in a minor way. This gives a simple model in which higher frequency modes are trapped more closely to the shore than lower frequencies and lower modes are trapped more closely to the shore than higher modes.

However, the analysis in Chapter 2 has shown that edge waves can be strongly modified by surf zone morphology (also see Kirby *et al.*, 1981; Wright *et al.*, 1986; Schönfeldt, 1991; Falques and Iranzo, 1992; Schönfeldt, 1995). These solutions were shown to be very different from the plane beach solutions. Interpretations of field observations of edge waves have suggested that longshore bars do trap edge wave energy in the surf zone (Huntley *et al.*, 1980; Schönfeldt, 1994). Preferential bar-trapping of the higher frequency edge wave antinodes has been used to explain general differences between the ranges of infragravity frequencies excited on bar-trough beaches and ranges of those excited on plane beaches (Wright *et al.*, 1986). These isolated studies suggest that the effect of the bar on the edge wave might be important, but in general, previous analyses have ignored the possibility of strongly bar-trapped modes, resulting in an incomplete description of the edge wave climate. The observations presented in this Chapter, from the DELILAH experiment, Duck, N.C., show how significant and persistent bar trapping of edge wave energy may be, at least at Duck, N.C.

Diagonal lines of variance in frequency-wavenumber spectra of the longshore component of orbital velocity have been observed (i.e. Howd *et al.* 1991a) in the DELILAH data (and also in data from the Superduck experiment at Duck, 1986), however people were puzzled as to their origin. The analysis presented here clearly shows that these lines lie exactly on the dispersion line for bar-trapped edge waves. Moreover, Chapter 2 gives the theoretical basis needed to predict of existence of these

lines and their slopes. The identification of this new type of edge wave is the most significant finding of this thesis. The convincing evidence presented in this Chapter will demonstrate that the effect of bar-trapping on edge waves cannot be ignored in field studies.

Specifically, the objective of Chapter 3 is to clearly demonstrate that the frequency-wavenumber coordinates of diagonal lines of variance in DELILAH frequency-wavenumber spectra correspond to calculated solutions for bar-trapped edge waves, to examine the frequency with which these modes dominate the longshore component of current spectra and to discuss the cause of variability in the diagonal lines of variance. Following a discussion on the experimental conditions, methods used and problems encountered in analyzing the data, the Chapter is divided into two large sections and one small section. The first large section is a general discussion of the bar-trapped edge waves which were observed in the data and their dependence on instrument location and incident wave conditions. The second large section discusses the role of effective depth profiles in bar-trapped variability, and the final small section deals with the directional preference of bar-trapped edge waves. It is difficult, in some places, to separate issues related to the data into specific sections. For example the effect of incident wave variability and instrument location are mentioned in several places.

3.1 Experimental conditions

DELILAH was a large experiment at the US Army Corps of Engineers Field Research Facility (FRF) in Duck, N.C. in October, 1990. Details of the experiment are reported by Birkemeier (1991) and details of the longshore current profiles are described in Smith *et al.* (1993) and Thornton and Kim (1993). Two longshore arrays (one in the trough, one seaward of the bar) and one cross-shore array of electro-magnetic current meters and pressure gauges (Figure 3.1) make the data good for investigating edge waves (an ideal location for bar-trapped edge waves would be on top of the bar). Frequency-wavenumber spectra were calculated using the iterative maximum

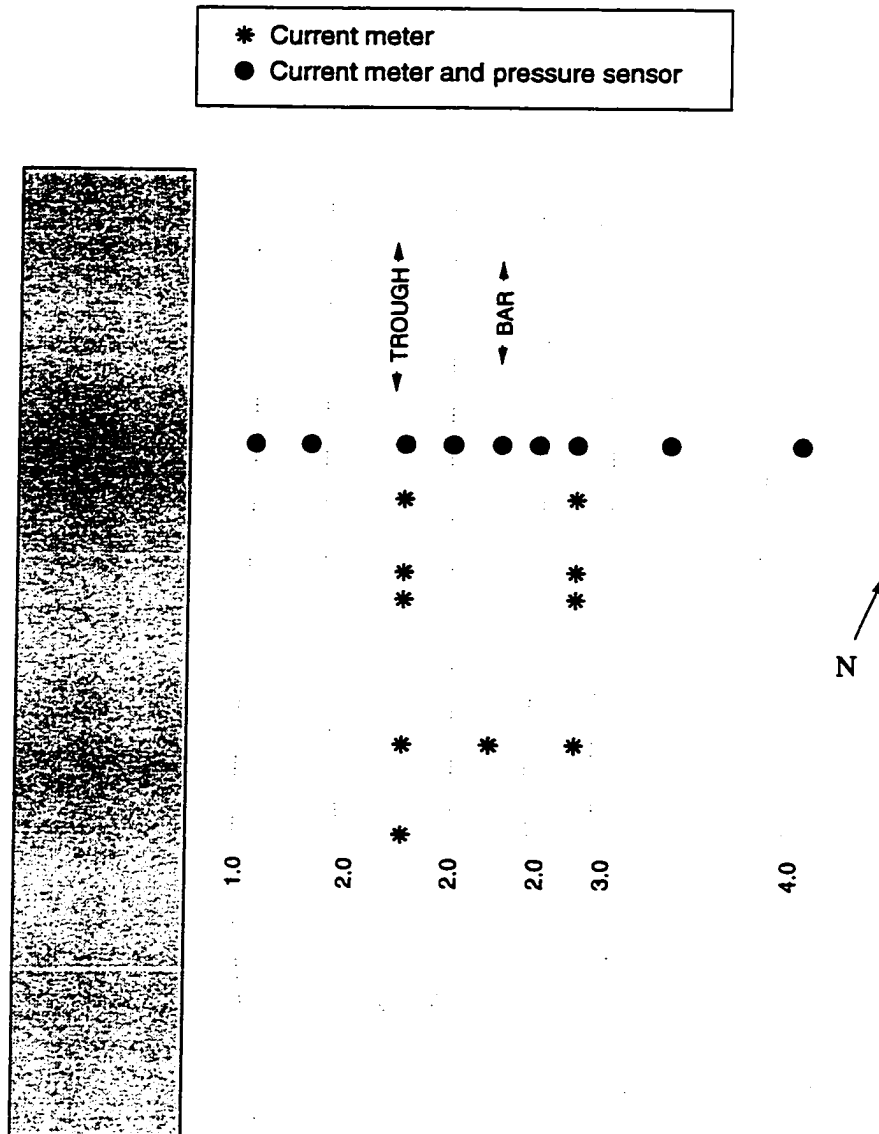


Figure 3.1: A simple schematic of the geometry of the array of current meters and pressure sensors during DELILAH. The depth contours are in metres, and approximately representative of the bottom profile toward the end of the experiment.

likelihood estimator developed by Pawka (1983), tested by Oltman-Shay (1985), and previously applied to nearshore data (Oltman-Shay and Guza, 1987; Oltman-Shay et al. 1989; Howd et al., 1991a; Howd et.al., 1991b (for the same data set used in this paper); Oltman-Shay and Howd, 1993, among others). A discussion of the spectral estimator is offered in the Appendix. Data from the outer array were problematic because the current meters with which they were observed were of different design, which was more susceptible to biofouling. The phase relationships between the waves should be useful, but the amplitudes are somewhat doubtful (Birkemeier, 1991). Therefore we will mainly concentrate on data from the inner array for detailed discussion.

Incident wave conditions during DELILAH were measured by the FRF with an array of pressure sensors in eight meters of water and are summarized in Figure 3.2. The incident wave direction was mainly from the southeast, with three northeast events, one at the beginning, and two toward the end of the experiment. In general, the southeast waves were mostly swell and the northeast waves were mostly locally generated sea. Two main events occurred in the incident wave field: a storm on October 10, and waves from hurricane Lili on October 12. These generated low frequency waves with large significant wave heights.

In order to identify the energy in the observed edge wave regime, it was necessary to calculate the theoretical frequency-wavenumber coordinates for which there are edge wave solutions and also the cross-shore and longshore velocity components corresponding to these solutions. A key data set for calculating these solutions, was the longshore sequence of the daily depth profiles provided by the FRF (Figure 3.3). The profiles used were averages of the six or seven profiles contained within the confines of the longshore array (unless indicated). Profiles during the storm were incomplete, and were estimated from adjacent days when needed. Though the beginning of the experiment had less than ideal conditions for bar-trapped edge waves (no well defined bar), the inner instrument array was ideally located on top of the bar. At the end of the experiment when the bar was well developed, the crest had moved offshore and

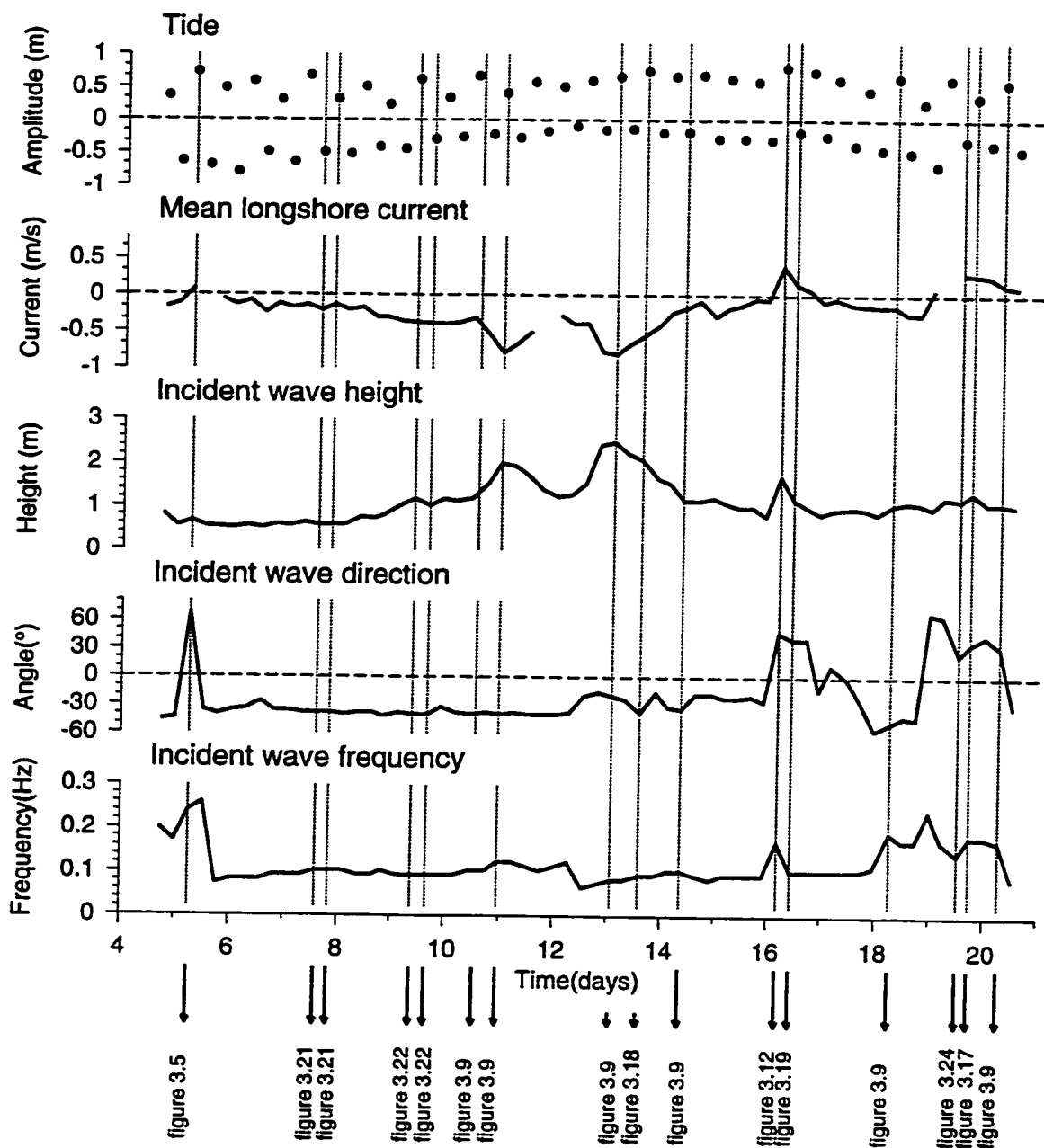


Figure 3.2: Environmental conditions during DELILAH. The mean longshore current was the mean of the longshore component of all the working current meters in the cross-shore array. The longshore current is mostly negative. Incident wave height, direction and frequency were measured at the FRF 8 meter array (courtesy of the FRF). Times at which the data presented in Chapter 3 are taken, are marked.

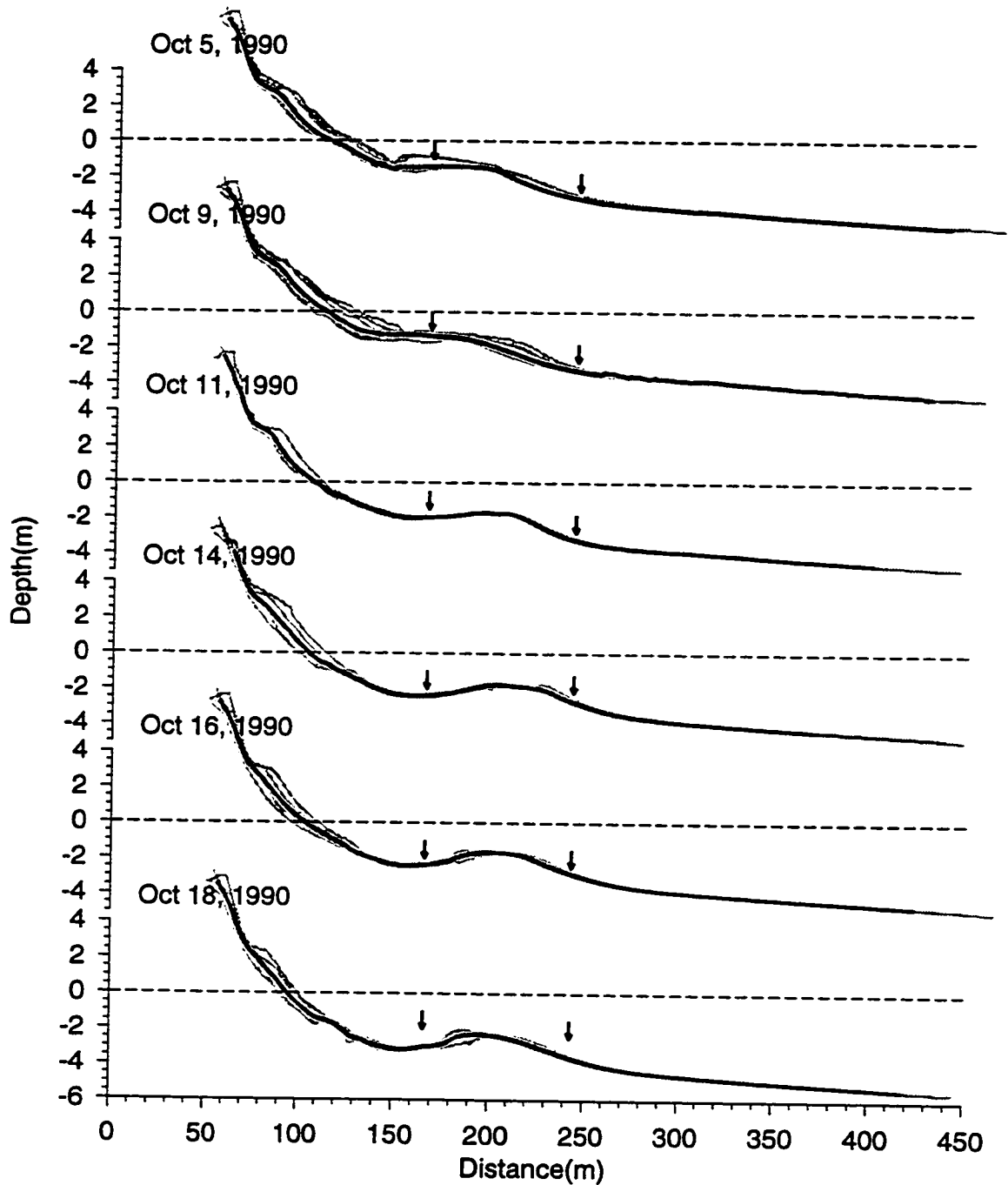


Figure 3.3: Representative depth profiles during the DELILAH experiment (courtesy of the FRF). The black line is the average of the grey lines which are all the profiles taken within the limits of the longshore array. Arrows mark the location of both longshore arrays. Conditions range from an ill-defined bar with the inner array on top of the bar, to a well defined bar, with the inner array in the trough.

the inner array was in the trough.

The cross-shore current meter array was needed to define the cross-shore structure of the mean longshore current, to correctly estimate the longshore current profiles and hence the effective depth profiles (equation 2.16). The mean longshore currents were calculated from three hours of longshore current data at high and low tide; the mean using all the cross-shore current meters is shown in Figure 3.2. Changes in the direction of the longshore current, from northward to southward, occurred when the incident waves changed their direction of approach from southeast to northeast. The longshore current speed increased dramatically during the two high wave events. With an estimate of the depth profile and a longshore current profile, solutions for the edge wave modes could then be obtained numerically using the methods in Section 2.3 (Holman and Bowen, 1979; Howd *et al.*, 1992).

3.2 Evidence of bar-trapped edge waves during DELILAH

Field observations of longshore component of current from sixteen data sets (marked on Figure 3.2) taken during DELILAH, are selected for discussion in this Chapter. They are chosen in order to represent the varying incident wave and depth profile conditions (Figures 3.2 and 3.3). The most notable feature of nearly all of the frequency-wavenumber spectra of the longshore component of velocity from DELILAH, was the persistent diagonal lines of variance below the leaky wave cut off and moving at phase speeds too great for shear waves. These lines existed in every spectrum during the experiment which had a barred effective depth profile. Moreover, the slopes of these lines had phase speeds approaching $\sqrt{gh'_{\text{bar}}}$, a convincing indication that they must be caused by bar-trapped edge waves. (The exact slope of the lines of variance depends both on the magnitude of the bar-trapped waves and the location of the instrument array relative to the bar). These diagonal lines of variance are evident also in longshore array data from other experiments (for example Howd *et al.*, 1991a), but until

now, their origin has not been identified.

The diagonal lines of variance were only obviously present in the longshore component of orbital velocity frequency-wavenumber spectra. Model calculations for the Duck geometry show that, in general, the longshore component of orbital velocity at the location of the arrays is much larger than the cross-shore component (Figure 3.4 shows the ratio of longshore and cross-shore orbital velocity for the inner array along the bar-trapped line, as a function of frequency). There are a few isolated exceptions, at frequencies where there is a node in the longshore component, but in general it would be unlikely to find evidence of bar-trapped edge waves in cross-shore component of velocity spectra.

3.2.1 Observations from near the bar crest

The frequency-wavenumber spectrum from October 5 (Figure 3.5), calculated from three hours of longshore component of current data over high tide, shows examples of this diagonal line of variance (the dashed line in Figure 3.5 is the leaky wave cut-off, above which two broad peaks of incident wave energy are evident). In Figure 3.5 the diagonal line of variance dominates in the positive direction, in the same direction as the longshore current. Theory shows that the largest anti-node for the simplest bar-trapped wave is expected at the top of the bar (Figure 2.10). Therefore the ideal place to measure η and v is on top of the bar. Figure 3.5 is a good introduction to these diagonal lines of variance, because on October 5, the instrument array is on top of the bar, so the problem of solutions decaying on either side of the bar can be temporarily ignored.

Bar-trapped waves with one zero crossing over the bar (corresponding to solutions along the second asymptote in Figure 2.10, modes 3(C), 4 and 5) should be less evident in Figure 3.5, as they have a node in v velocity on top of the bar. Though the ridges of variance in Figure 3.5 are centered around the simplest bar trapped mode line, the width of the peaks in the frequency-wavenumber spectra are greater than the separation of the solutions of simple and more complex bar-trapped modes in

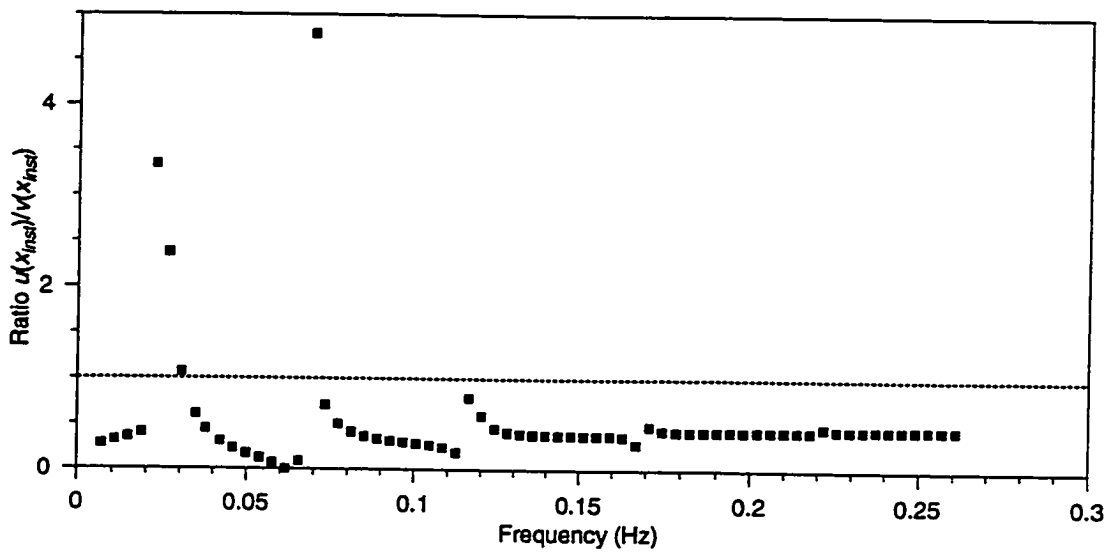


Figure 3.4: Ratio of the cross-shore component of orbital velocity to the longshore component of orbital velocity at the location of the inner instrument array during DELILAH, for selected frequencies along the diagonal bar-trapped line, assuming the sea surface elevation at the shoreline is the same for all frequencies and modes (as in Chapter 2). Calculations are for one of the profiles from toward the end of DELILAH.

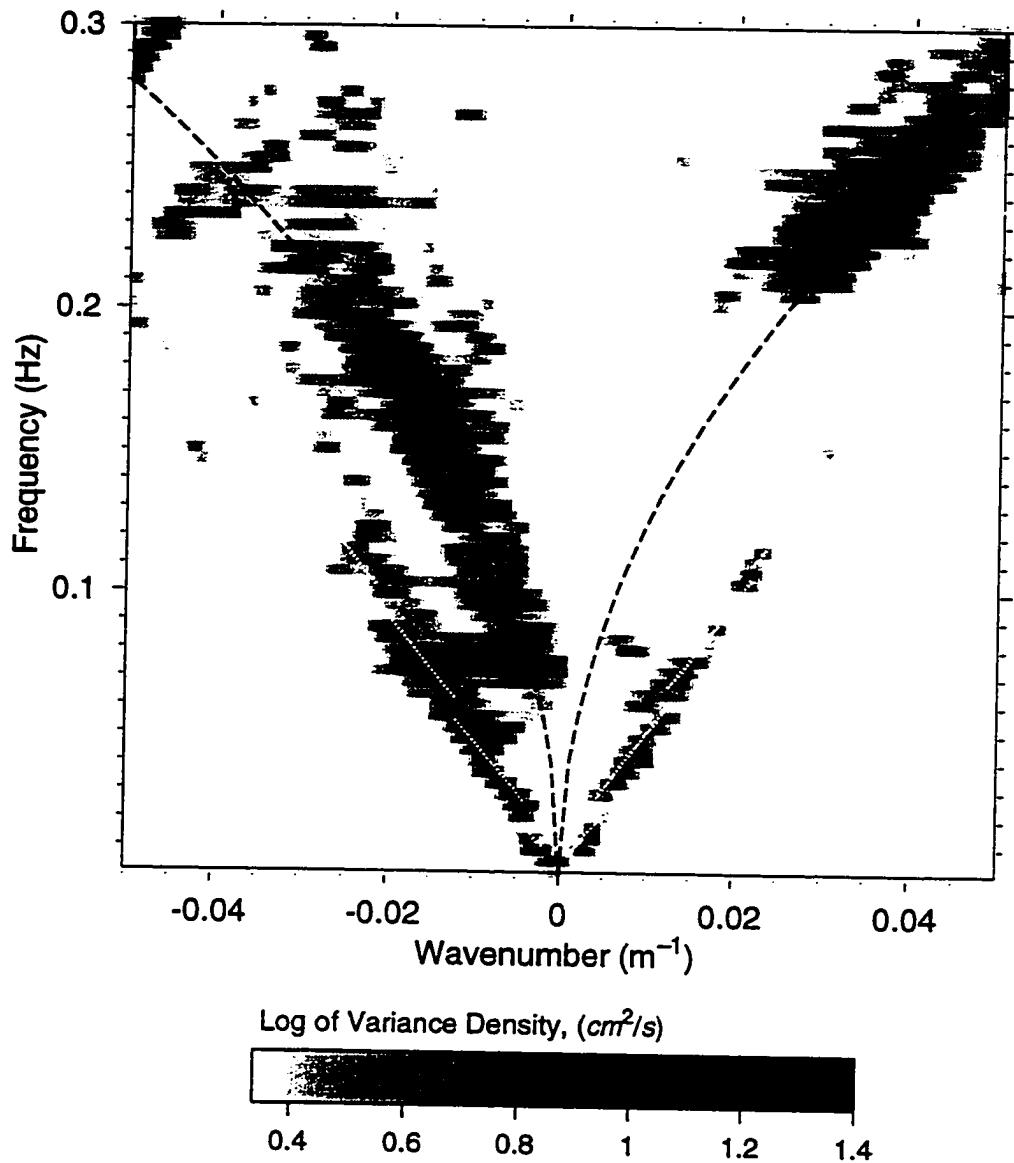


Figure 3.5: Variance density plotted as a function of frequency and wavenumber of longshore component of orbital velocity from the inner array at DELILAH on October 5, when the array was close to the top of the bar. Calculated bar-trapped solutions for this location are plotted with white dots, the leaky wave cut-off is plotted with a black dashed line. White areas contain peaks below the mean variance of the whole spectrum within the ranges shown.

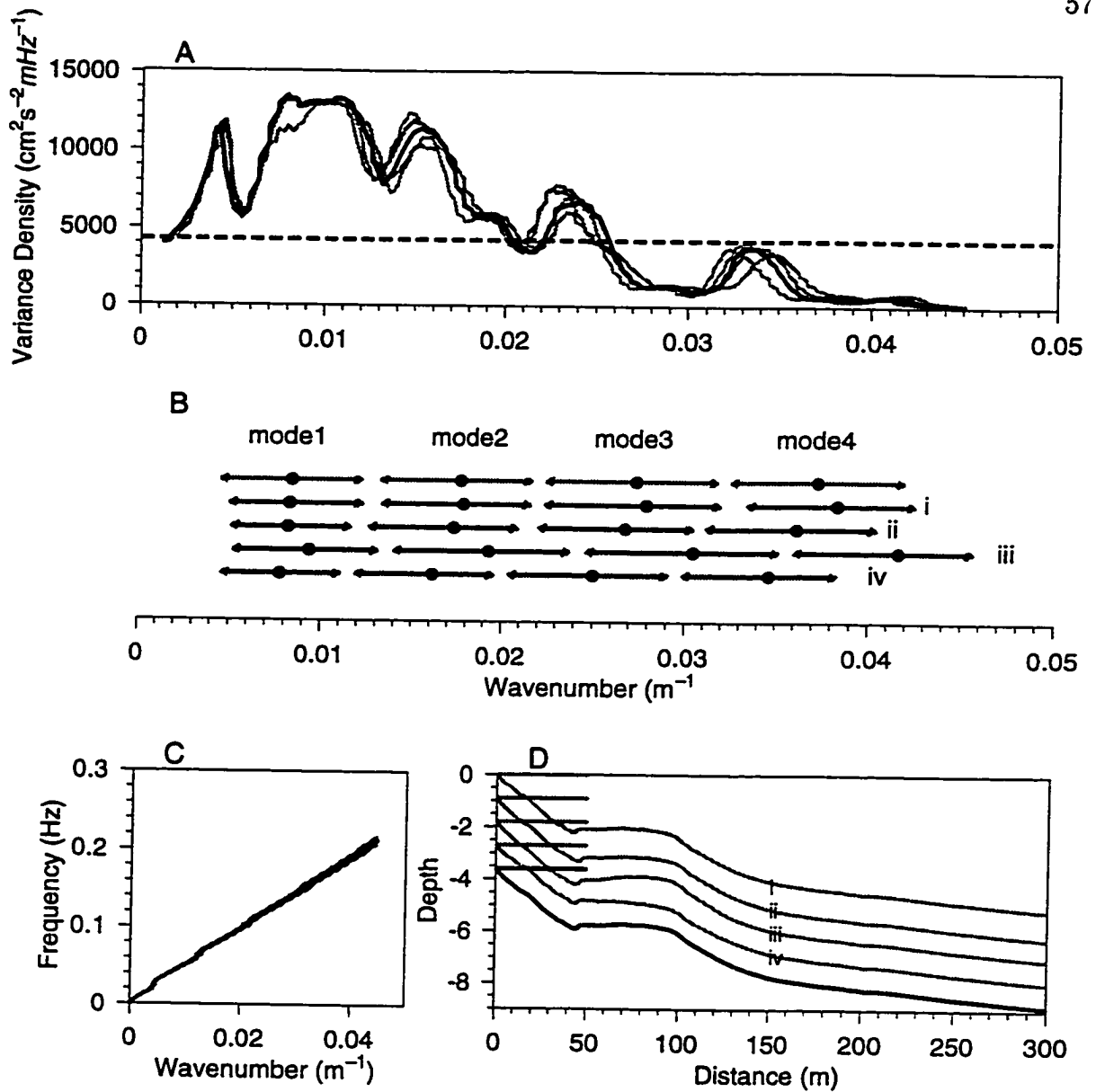


Figure 3.6: A. Variance density along the positive bar-trapped line in Figure 3.5, October 5, plotted against wavenumber. The dark line is the original, the grey lines show variations in the variance caused by varying the depth as in D. The mean variance density for the whole spectrum in Figure 3.5 is marked by a dashed line. B. The location of the modes along the same line, again plotted against wavenumber, for each depth profile in D. The grey lines correspond to the width of the modes, with the most amplified marked with a black dot. C. The variation of the slope of the bar-trapped line given the bottom variations in D. D. The original depth profile for October 5 (black), and variations of that depth profile (grey) corresponding to i) a shallower bar and trough, ii) deeper bar and trough, iii) shallower bar, deeper trough and iv) a shallower trough and deeper bar.

frequency-wavenumber space (Figure 2.10). Neither the resolution of the frequency-wavenumber spectra nor the resolution of the calculated solutions is sufficient to determine how energetic the more complex bar-trapped modes are compared to the simplest bar-trapped modes; minor deviations from the true locations of peaks are caused by the statistical uncertainties inherent in the frequency-wavenumber plots (Oltman-Shay, 1985, and the Appendix). In addition, deviations of the calculated bar trapped solutions from the actual location the line, $C \rightarrow \sqrt{gh_{\text{bar}}}$, are expected, due to the many possible sources of error, such the position of the bar crest, the form of the longshore current, and the particular assumed distribution of the modal energy and the longshore inhomogeneity of the profiles. Despite these details, dominant ridges of variance in the spectrum below the leaky wave cut-off, have the same signature frequency-wavenumber pairs as bar-trapped waves. This clearly shows that on top of the bar, bar-trapped edge waves are the dominant edge waves in the longshore component of velocity spectra. The spectrum shows little energy in the region of frequency wavenumber space below ($C < \sqrt{gh_{\text{bar}}}$), where the edge waves are likely to have decayed by the time they reach the bar. The low level energy spread in the space between the bar-trapped modes and the leaky wave cutoff, suggests that higher mode edge waves would only be dominant far from the bar, where the bar-trapped edge waves have decayed. On October 5, the energy along the bar-trapped line is limited to lower frequencies: less than 0.12 Hz for waves travelling against the longshore current, and below 0.18 Hz for waves travelling with the current.

Figure 3.6A shows the smoothed variance density along the theoretical bar-trapped line projected on to the wavenumber plane (for convenience). Four distinct peaks occur above the mean variance level. Figure 2.10 shows that one might expect valleys or nodes in the spectrum along the $\sqrt{gh_{\text{bar}}}$ asymptote, where the solutions pass through the kissing points in the dispersion diagram.

On first glance the pattern of peaks and valleys does not line up well with the locations of the nodes. The depth profile on October 5 (Figure 3.3) had some longshore variability. Sensitivity of the calculated solutions to variations in the bottom

topography was tested using four variations, Figure 3.6D, (i) whole profile deeper by 10 cm, (ii) whole profile shallower by 10 cm, (iii) trough deeper by 5 cm and bar shallower by 5 cm (iv) trough shallower by 5 cm and bar deeper by 5 cm (which was most similar to the variability on October 5). Though the slope of the amplification line varies minimally (Figure 3.6C), the location of the modes along the amplification line varies considerably, Figure 3.6B. Using an over-all-deeper or shallower profile makes little difference, but changing the relative depths of the trough and the bar changes the distribution of modes along the line. The distribution of modes occurs over a wider range of wavenumbers, when the trough is deeper and bar shallower; the region encompassing the bar is then larger, allowing bar-trapped waves of greater wavelength to exist. Likewise, when the bar is deeper, and the trough is shallower, the horizontal region defined by the bar is smaller and the spread of modes along the line is diminished. The difference between the calculated location of peaks and the actual location of peaks is within the variability caused by the longshore inhomogeneity, but establishing the direct effect of longshore inhomogeneity cannot be addressed with our one-dimensional model.

The peakiness of the modal structure along the line does not show that the edge wave climate is peaky in any general sense. If there is edge wave energy at frequencies given by the valleys between the peaks, the theoretical calculations (i.e. Figure 2.10) show that, due to the nodal structure and the offshore decay scale, energy will not be evident at that particular array location.

3.2.2 Observations from the outer array

The changing magnitudes of different modes with cross-shore distance shown in Figure 2.10, underlines the fact that the relative dominance of particular edge waves modes is a function of the location at which edge waves are observed. An instrument array seaward of the bar will be located in the region of seaward decay of the bar-trapped waves; in general the magnitude of observations of bar-trapped waves is strongly dependent on the distance to the bar crest. Observations from array in the trough

will depend on how much the wave has decayed toward a node in the trough. The dispersion diagrams in Figures 2.4, 2.7, 2.8 and 2.9, on which the greyscale represents the greatest amplification anywhere in the profile, will be significantly modified if plotted from a perspective of an instrument array located in a trough (Figure 3.7A) or an array located outside the bar (Figure 3.7B). (These Figures are calculated using the depth profile on October 16 during the DELILAH experiment, Duck, N.C., including the effect of the appropriate longshore current). The amplification still is strongly evident in the inner array, but some of the waves which are strongly amplified over the bar have decayed at the location of the outer array. In Figure 3.7, the longshore component of orbital velocity squared is plotted to allow comparison with current data, but the pattern of amplification is the same as would be observed from plotting sea surface elevation, because the longshore component of current and the sea surface elevation have the same shape, equation 2.13.

Dominant ridges of variance are evident in the spectra of the longshore component of current from the outer array (Figure 3.8) on October 5. In this case, the dominant ridge of variance corresponds to more complex bar-trapped modes, which have greater phase speeds than the simplest bar-trapped shapes (Figure 2.10). The outer instrument array is seaward of the bar, and the simplest bar-trapped waves (corresponding to the asymptote which is closest to $C \rightarrow \sqrt{gh_{\text{bar}}}$ in Figure 2.10) have decayed somewhat. Even including this effect, the diagonal lines of variance have a somewhat greater phase speed than expected from the model results. This is possibly an artifact of normalizing the calculated solutions to the shoreline. These higher modes are more closely spaced, and do not show the structure of maxima and minima associated with the inner array (Figure 3.6).

3.2.3 Significance levels of spectra estimators

In Figures 3.5, 3.8 and in subsequent spectra, a noise floor is identified arbitrarily as the mean variance over the domain ($f = 0 \rightarrow 0.3\text{Hz}$, $k = -0.05 \rightarrow 0.05\text{m}^{-1}$). In synthetic tests, Oltman-Shay (1985) noted the existence of a number of low level

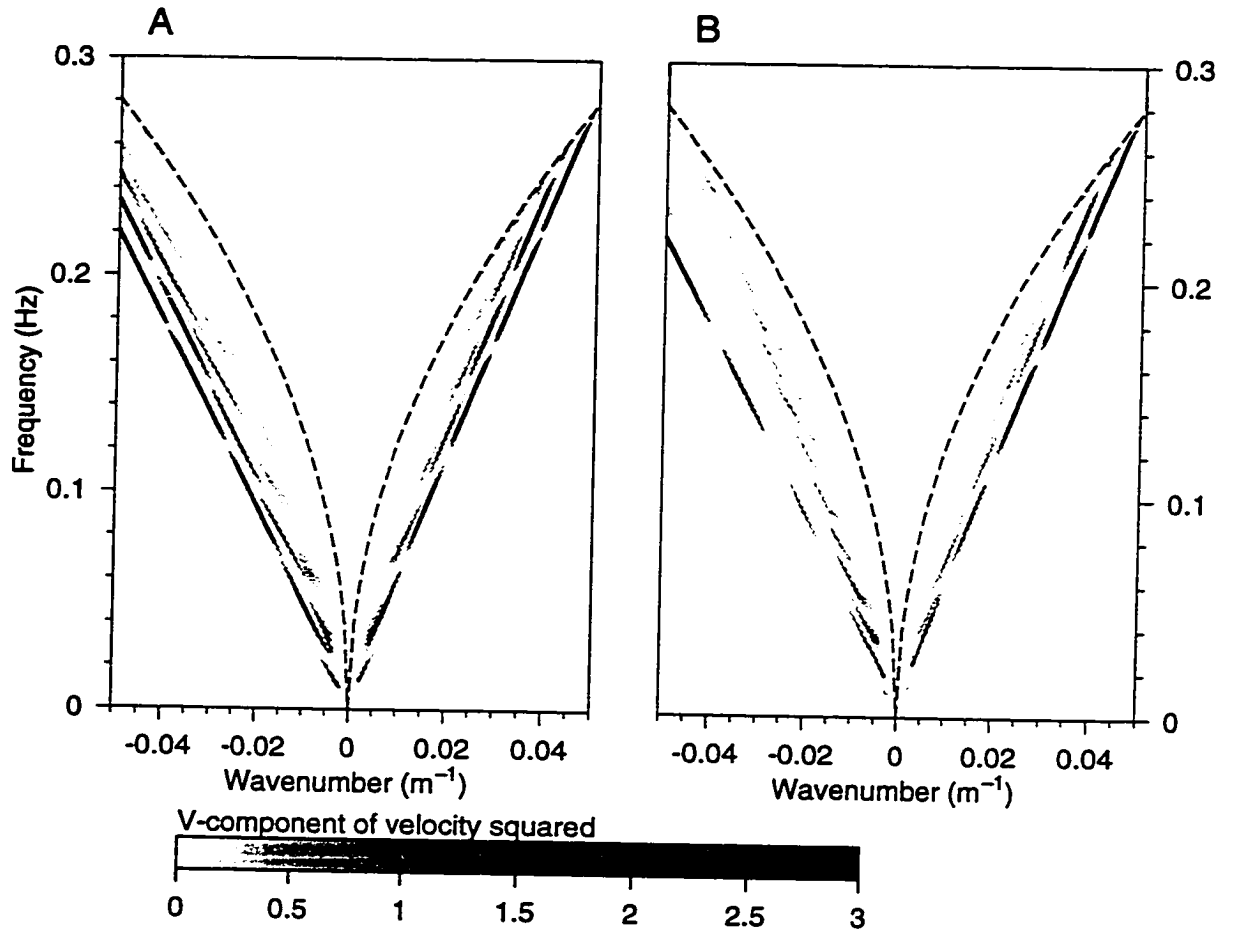


Figure 3.7: Dispersion diagram for the same profile as in Figure 2.8, but the grey scale corresponds to the variance of the longshore component of orbital velocity at the location of the array in the trough (A) and seaward of the bar (B). Some decay of the most amplified modes has occurred, in particular at the outer array. Note the difference between positive and negative solutions, which is due to the longshore current, discussed in more detail in the Chapter 2, Section 2.5.

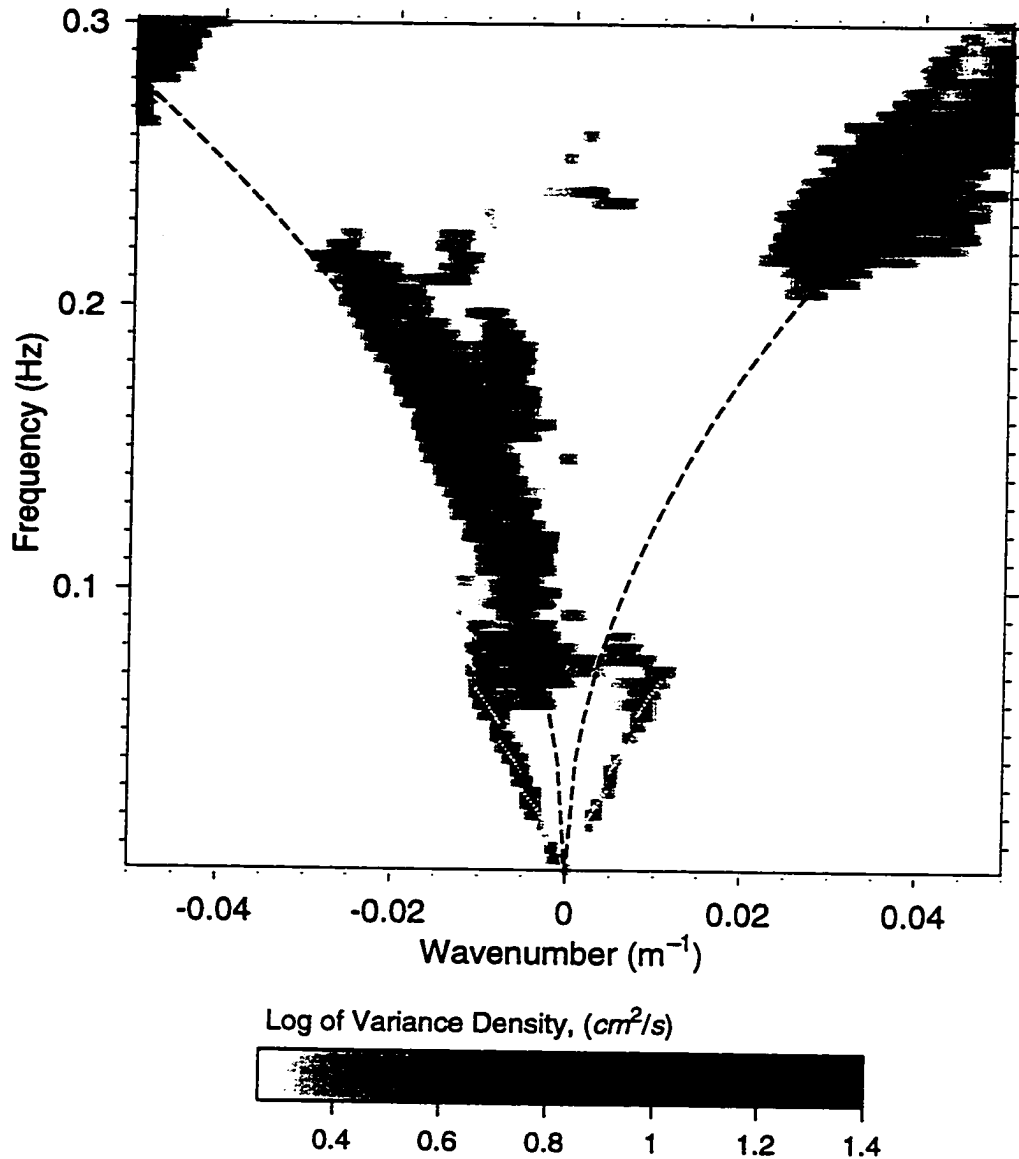


Figure 3.8: Variance density plotted as a function of frequency and wavenumber of the longshore component of current data from the outer array taken on October 5, when the array is far from the top of the bar. The slope of the diagonal line of data corresponds to higher mode bar-trapped waves, as the most amplified ones seen in Figure 3.5 have decayed at this distance. Calculated bar-trapped solutions for this location are plotted with white dots (using the bar-normalization scheme, Section 3.2.5), the leaky wave cut-off is shown by with a black dashed line.

peaks which cannot be confidently identified as real, resulting from energy leakage from more energetic peaks. Oltman-Shay uses a different definition of noise floor. She arbitrarily takes the mean of all the peaks, and then a second mean of all the peaks below the first mean, and then defines the noise floor as one standard deviation above this second mean. (The justification is that if the primary peaks are large, more energy will leak into secondary peaks). We feel that our noise floor is simpler, though peaks close to large incident wave peaks should be regarded with caution. Even with the noise floor, Figure 3.5 has a number of such peaks. However, we are confident that the main peaks are real, based on our own synthetic tests of the DELILAH longshore array geometry, and on the successful use of the estimator with data from DELILAH (Howd *et al.*, 1991; Howd *et al.*, 1992) and other nearshore experiments (Oltman-Shay and Guza, 1987; Oltman-Shay *et al.*, 1989; Howd *et al.*, 1991; Oltman-Shay and Howd, 1993). Further discussion of the the problems associated with the estimator are given in the Appendix. Moreover the conclusions we draw are based on general observations common to most of the spectra, such as the existence of diagonal lines of variance, and the slopes of these lines.

3.2.4 Variability of diagonal lines of variance, and edge wave forcing

Dominant lines of variance are seen, to different degrees, in all of the days for which data exist (Figure 3.9 shows selected examples). This suggests that most incident wave conditions excite these bar-trapped modes, and the density and the band width of the observed energy vary with incident wave conditions. Frequency-directional spectra from the eight meter array (courtesy of Chuck Long, FRF) reveal variations in the range of frequencies and directions over which the incident wave energy is spread, not evident in Figure 3.2.

Though edge waves are obviously related to the incident wave field, the mechanism which forces edge waves has not been clearly demonstrated, despite considerable effort. In general, edge waves will grow when their shape corresponds to the shape

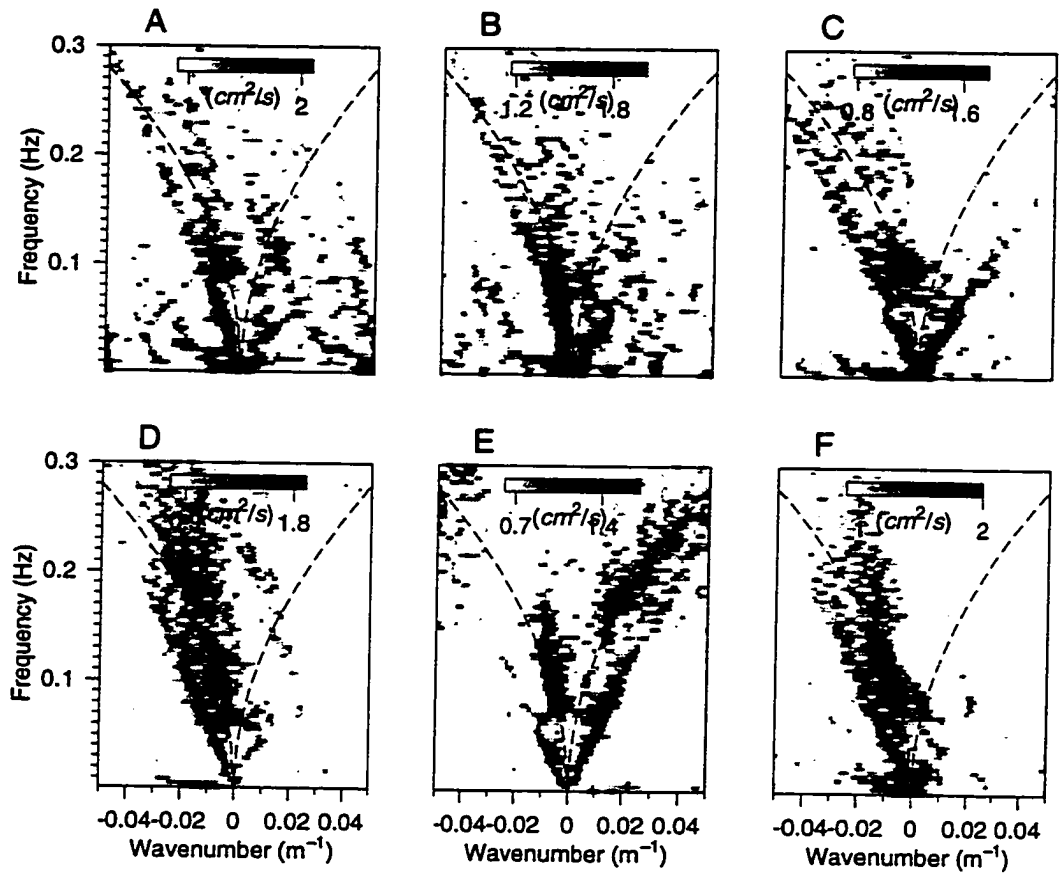


Figure 3.9: Variance density plots of v-component current data taken from the inner array on A. October 10, 22:57 B. October 13, 1:37 C. October 14, 8:39 D. October 18, 6:25 E. October 20, 6:40 F. October 9, 9:19. The leaky wave cut-off is plotted with a black dashed line.

of the forcing function (Bowen and Guza 1978; Holman, 1981). Edge waves cannot be directly resonantly excited by incident waves because the frequencies and wavenumbers of the incident waves must be the same as the edge wave, and the leaky-wave cut-off (equation 2.7) clearly precludes this. So most mechanisms for edge wave forcing involve non-linear interactions between incident waves which result in frequency-wavenumber combinations which are the same as those of an edge wave for that particular topography. Exact correspondences drive resonant responses, but off resonant responses can be driven if the coordinates are nearly correct. If the correct frequency and wavenumbers can be generated, then the response will depend (at least in the one dimensional case treated here) on how well the cross-shore shape of the edge wave corresponds to the cross-shore shape of the forcing and how strong the effect of friction is.

Suggested forcing functions can be categorized into those derived from modulations in radiation stress occurring from the groupiness in the incident wave amplitude (Longuet-Higgins and Stewart, 1962; Gallagher, 1971; Bowen and Guza 1978) and those generated from modulations in the momentum flux caused by variation in the incident wave break point (Symonds *et al*, 1982; Symonds and Bowen, 1984). Recent studies have included both sources (Foda and Mei, 1981; Schaffer, 1993 and Lippmann *et al*, in press). The variable radiation stress forcing occurs outside the surf zone, but can also occur inside the surf zone if the wave amplitude variations are not completely removed by saturation (i.e. if all the waves do not break). It is also possible for edge waves to non-linearly combine together to force other edge waves. This could be relevant to bar-trapped edge waves which have similar shape over the bar, which may facilitate energy transfer between edge waves, and may explain the broad forcing of bar-trapped edge waves, even in cases where the incident wave spectrum is very narrow such as on October 13, Figure 3.9B. The break point mechanism obviously only occurs inside the surf zone. As suggestion in Chapters 1 and 2, the break point mechanism might be particularly relevant to bar-trapped edge waves, as both the forcing and response are large over the bar. Moreover, Lippmann *et al*. (in press)

found the forcing close to the break point to be much more significant in generating edge waves on a plane beach than forcing off-shore.

Mathematically, the forcing problem is addressed in Lippmann *et al.* (in press) by starting with the forced linearized shallow water equations

$$\begin{aligned}\frac{\partial u}{\partial t} + g \frac{\partial \eta}{\partial x} &= \left[-\frac{1}{\rho h} \frac{\partial S_{xx}}{\partial x} + \frac{\partial S_{xy}}{\partial y} \right] - \Lambda u, \\ \frac{\partial v}{\partial t} + g \frac{\partial \eta}{\partial y} &= \left[-\frac{1}{\rho h} \frac{\partial S_{xy}}{\partial x} + \frac{\partial S_{yy}}{\partial y} \right] - \Lambda v, \\ S_{ij} &\approx \rho \int_{-h}^0 \bar{u}_i \bar{u}_j + \delta_{ij} \bar{\eta}^2\end{aligned}$$

where ρ is density, Λ is a friction coefficient and $\mathbf{u} = (u_{inc}, v_{inc})$ are the incident wave orbital velocities. S_{ij} is the excess momentum flux due to waves, or the radiation stress assuming shallow water and $\bar{\eta} \approx 0$ (Longuet-Higgins and Stewart, 1962). Combining these with continuity (and ignoring friction) gives an equation in η

$$\frac{\partial^2 \eta}{\partial t^2} - g \frac{\partial}{\partial x} \left(\frac{\partial \eta}{\partial x} \right) - g \frac{\partial}{\partial y} \left(\frac{\partial \eta}{\partial y} \right) = F$$

where F is the forcing dependent on the S_{ij} . For an edge wave

$$\eta_n(x, y, t) = a_n N_n(x) e^{i(ky - \sigma t)}$$

where $N_n(x)$ represents the cross-shore shape of the wave. Allowing a_n to vary with time, but ignoring the acceleration of growth in a_n , multiplying both sides by $N_n(x)$ and integrating in the cross-shore, gives an expression for the initial edge wave growth rate (Lippmann *et al.*, in press)

$$i2\sigma \frac{\partial a_n}{\partial t} e^{i(ky - \sigma t)} \int_0^\infty N^2(x) dx = \int_0^\infty F N_n(x) dx.$$

This shows how the response depends on how well the forcing is coupled with the edge wave shape. Resonant forcing will occur when $\sigma = \sigma_1 - \sigma_2$ and $k = k_1 - k_2$, where the subscripts refer to any two incident wave trains. The incident wave orbital velocities will change with cross-shore distance due to shoaling, but will also be completely

different inside and outside of the breaker zone. The breaker zone also oscillates with the longshore groupiness of the incident wave field, so the integral must be evaluated separately inside and outside the break point.

Though a detailed examination of forcing is beyond the scope of this thesis, some particular points about the forcing of edge waves by non-linear interactions between incident waves are useful to the interpretation of field data. Given two incident waves with longshore wavenumbers and frequencies (k_1, σ_1) , (k_2, σ_2) and with $\sigma_1 > \sigma_2$ ($\sigma > 0$), then the edge wave will have a wavenumber of

$$\Delta k = k_1 - k_2 = \kappa_1 \sin \alpha_1 - \kappa_2 \sin \alpha_2 = \frac{1}{g}(\sigma_1^2 \sin \alpha_1 - \sigma_2^2 \sin \alpha_2) \quad (3.1)$$

where α_1, α_2 are the angles of approach of the two incident waves in deep water, κ is the wavenumber and the longshore wavenumber is conserved when the incident waves shoal. Suppose k_1 , and therefore α_1 , is positive, if one were to consider a range of values of α_1 and α_2 , (3.1) will give a positive Δk for most cases, in particular when α_1 is large (because σ_2 is greater than σ_1). (In order for Δk to be negative, α_2 must be significantly larger). For a more comprehensive discussion see Bowen and Guza (1978) or Herbers *et al.* (1994). It follows a) that there should be a tendency for edge waves to propagate preferentially in the same longshore direction as incident waves, and b) that increasing the directional spread of the incident waves will increase the range of possible edge wave wavenumbers ($k_1 - k_2$). Herbers *et al.* (1995a,b) have observed the directional spread of infra-gravity waves is correlated to the directional spread of swell, Herbers *et al.* (1995a) show this observation is consistent with nonlinear forcing theory.

The first storm, on October 10 and 11, had a low frequency peak (0.12Hz) on the bar-trapped line with many multiple peaks trailing off at higher frequencies, all coming from the southeast (negative wave angles). Bar-trapped edge waves travelling with the longshore current (in the same direction as the incident waves) are excited (Figure 3.9A). These conditions are very similar to conditions with similar frequency ranges of bar-trapping near the end of the experiment, on October 18 (Figure 3.9D), except that the main incident peak on October 18 was higher (0.19Hz). Both these

days have bar-trapped edge waves excited over a broad range of frequencies and negative wavenumbers, which is consistent with incident wave forcing from a broad range of frequencies and negative wave directions. During the second storm, on October 13, the incident wave conditions had one very narrow low frequency peak (0.083 Hz, maximum directional spread 0 to -30°). Despite this, bar-trapped waves are forced (Figure 3.9B), again in the same direction as the incident waves. (Note the estimator has difficulty in resolving the bar-trapped edge waves from incident waves in the 0.083Hz frequency band, as expected from the discussion in the Appendix). Later this day, the directional spread increased to include waves coming from positive directions (a directional spread of -30° to 30°). This resulted in more edge waves forced at positive wavenumbers (Figure 3.9C). The strongly bi-modal conditions on October 20, with higher frequency waves coming from positive wavenumbers and low frequency waves coming from negative wavenumbers, forced bar-trapped waves in the same directions as the higher frequency incident waves (Figure 3.9E).

Most interesting in Figures 3.9 B and C, is the spread of energy into frequencies greater than the well-contained low frequency incident wave band. (These high frequency peaks are small, but significant using the Oltman-Shay noise floor definition). This cannot be explained in terms of the simple non-linear interaction of incident waves, which results in frequencies which are lower than the two incident frequencies (Bowen and Guza, 1978). Low frequency (swell) waves, such as encountered on October 13 and 14, have been observed to be more effective at exciting infragravity waves than high frequency (sea waves) (Elgar *et al.*, 1992), consistent with forcing theory predictions (Herbers *et al.*, 1995a). Perhaps this low frequency swell transfers energy to higher edge wave frequencies more efficiently than the higher frequency incident waves in Figure 3.5, where the edge waves do not extend to very high frequencies. There is also the possibility of secondary transfer of energy from edge wave to edge wave, mentioned earlier. Bar-trapped edge waves are even evident in Figure 3.9F, data from October 9, when there is no real bar, only an effective bar due to the presence of a mean longshore current, though the variance in the bar-trapped region

does not dominate to the extent that it does on other days.

3.2.5 The normalization problem

Calculating the numerical solutions for the profiles in Figure 3.9, many of which were observed when the instrument array was not located on top of the bar, showed that some of the diagonal lines had slightly higher phase speeds than predicted using the simple scheme of normalizing all the solutions to the shoreline introduced in Chapter 2.

The shoreline normalization used in Figures 2.4, 2.7-2.9 and 3.7 is not necessarily the most appropriate scheme to use when comparing these theoretical solutions to data. The basic difficulty is that edge wave solutions, calculated for a given beach profile, are merely the shapes which that topography will support. Without a full calculation of the theoretical forcing patterns, energy transfer and dissipation for each run, there is no realistic way to theoretically estimate the expected relative amplitudes of the various possible modes. Some previous studies have made the simple assumption that the shoreline amplitudes of these modes are equal (Oltman-Shay and Guza, 1987; Oltman-Shay and Howd, 1993), or that they decrease in some regular fashion with increasing mode number. This has proved useful in illustrating specific points, such as the location of the edge wave nodes in surf zone measurements. Normalization of the edge wave solutions at the shoreline (“shoreline normalization scheme”) may be useful on plane beaches where the shoreline amplitudes are greatest, but makes little sense when the waves are strongly amplified over the bar; the strongly amplified modes completely dominate the predicted spectrum (for example Figure 2.7 or 2.9). Amplification is really only an indication of trapping efficiency over the bar; the more amplified modes decay more rapidly on either side of the bar, and therefore are more efficiently trapped. For example, a mode 3 bar trapped wave in Figure 2.10 has a steeper decay on either side of the bar than a mode 1 bar-trapped wave from Figure 2.10. Normalizing the solutions to the shore causes the longshore component of mode 3 wave to be larger than the mode 1 wave, when observed on either side of

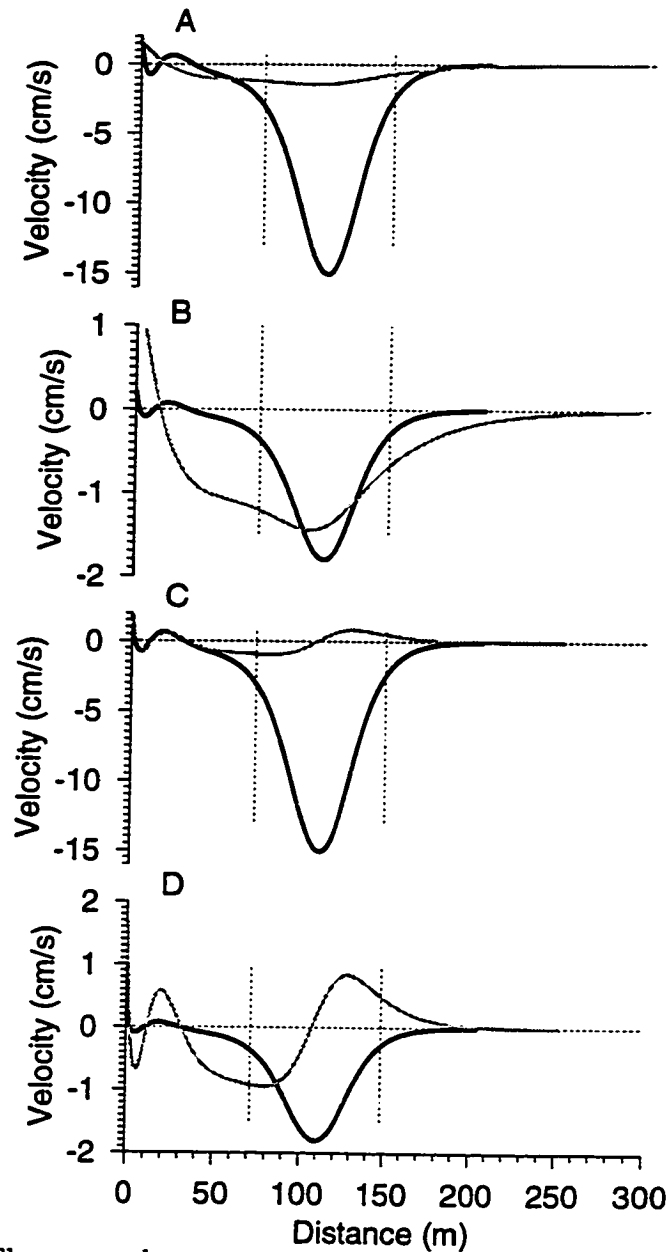


Figure 3.10: The cross-shore structure of the longshore component of orbital velocity, A. a strongly amplified wave (mode 3 from Figure 2.10) versus a less amplified wave (mode 1 from Figure 2.10), normalized so the sea surface elevation is one centimetre at the shoreline. B. The same waves, only the mode 3 wave which was strongly amplified relative to its shoreline value has been renormalized to a sea surface elevation of 1 centimetre at the bar. C. The shore normalized mode 3 wave (a simple bar-trapped shape) versus the less amplified mode 4 wave (a more complex bar-trapped shape). D. The same waves, renormalized to a sea surface elevation of one centimetre at the bar. The more complex bar-trapped mode will be more evident at the location of arrays in the trough or seaward of the bar.

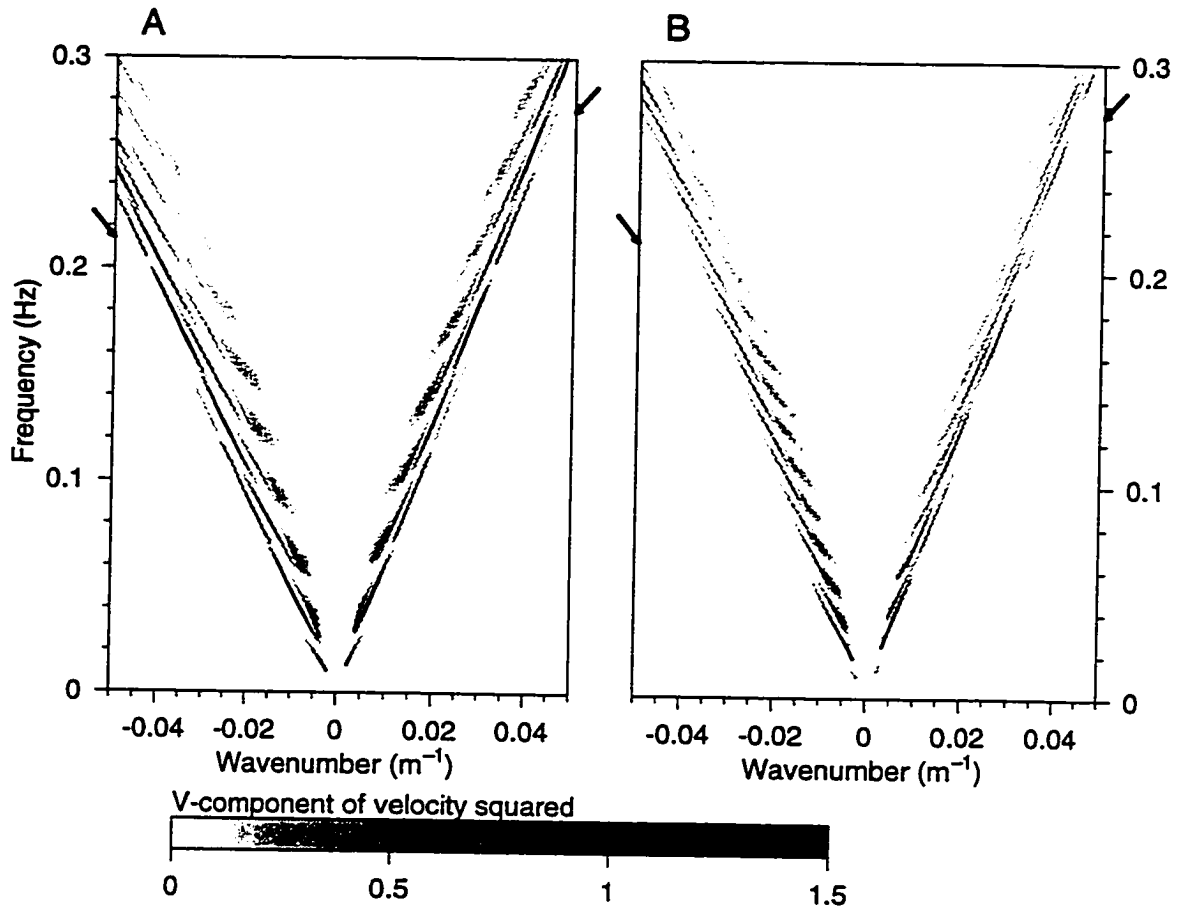


Figure 3.11: The dispersion diagram given in Figure 3.7 renormalized so the amplified waves have a maximum sea surface elevation of one unit anywhere in the cross-shore profile, A. is from the instrument array in the trough B. is from the instrument array seaward of the bar. Note that the amplified line has a greater slope than in Figure 3.7, because the most amplified modes have decayed at the location of the instrument array. Arrows mark the location of the line of most amplified waves.

the bar (Figure 3.10A). However, normalizing the solution to the bar causes the mode 3 wave to appear smaller than the mode 1 wave. Similarly, on plane beaches, higher frequency solutions will decay more rapidly than lower frequency solutions; the higher frequency solutions appear smaller than lower frequency solutions, when observed at a distance from the shoreline, but only if they are normalized at the location of their maximum amplitude (the shoreline).

The same observation can be made of solutions corresponding to the higher $C \rightarrow \sqrt{gh_{\text{bar}}}$ asymptote discussed in Section 2.1.2, where the asymptote closest to the $C \rightarrow \sqrt{gh_{\text{bar}}}$ corresponds the simplest bar trapped shapes, and higher asymptotes correspond to more complex bar-trapped shapes (Figure 2.10). With a shore normalization scheme, bar trapped solutions along the simplest bar-trapped asymptote (for example mode 3) are larger than bar-trapped solutions for higher bar trapped asymptotes with the same frequency (for example mode 4), Figure 3.10C. If these waves are renormalized to have a unit sea surface elevation over the bar, the most amplified wave will be smaller at the location of instrument arrays both in the trough, and outside the bar (Figure 3.10D). The choice of normalization scheme changes the appearance of the predicted spectrum, as the most amplified waves with the simplest shapes over the bar decay more quickly on either side of the bar.

Normalizing the most amplified waves to their values at the location of the bar rather than at the shore, is useful because it deals more realistically with the rapid decay of the most amplified modes on either side of the bar, relative to their less amplified counterparts. However, normalization of all the solutions on top of the bar is problematic as some solutions decay or have nodes on top of the bar. Therefore we choose a scheme in which only the solutions which are exactly larger over the bar than at the shoreline are normalized to the bar, the remaining solutions are normalized to the shoreline as before (“bar normalization scheme”). So this objective normalization criterion limits the maximum amplitude of any solution. The result is the bar-trapped line ($C \rightarrow \sqrt{gh_{\text{bar}}}$) in Figure 3.7 appears to have a higher slope (Figure 3.11) as the most strongly amplified modes have decayed before reaching the

instruments in the trough (Figure 3.11A) and seaward of the bar (Figure 3.11B). The slope of the variance ridges, found repeatedly in the frequency-wavenumber spectra of current data from DELILAH, will determine whether either of these schemes is appropriate and how large the most amplified modes become on top of the bar.

During most of the experiment, when the arrays were not located at the top of the bar, diagonal lines of variance corresponded better to solutions calculated using the bar normalization scheme, rather than the shore normalization scheme. The bar normalization scheme essentially emphasizes that the simplest bar-trapped shapes (the most amplified shapes (Figure 2.10)), decay faster on either side of the bar and thus may not be energetic at array locations on either side of the bar. In which case, only the higher bar-trapped waves may be evident in much of the data. With the introduction of the bar-normalization scheme to Figure 3.8, the data and diagonal lines of variance correspond well. It must be emphasized that the bar normalization scheme and the shore normalization scheme are two limits depicting the size of the waves over the bar. In practice, unless the instrument array is very far from the bar (i.e. Figure 3.8), the resulting lines are not very different. If the resolution of the peaks were better, it may have been possible to determine exactly the size of the waves over the bar, and design a proper normalization scheme, but for the broad conclusions drawn here, it is sufficient to note that there may be some variability in the slope of the line due to this effect.

3.2.6 Remarks on optimal observing conditions

There were some incident wave conditions that appeared to excite particularly distinct diagonal lines of variance, extending up to high frequencies. These conditions consisted of two incident wave peaks, at different frequencies coming from different directions. A spectrum, where these favourable conditions occur, October 16 (Figure 3.12), is discussed in some detail in this Section because it will be used to normalize the drift velocity calculations in Chapter 4.

The theoretical solutions plotted in Figure 3.12, are not the solutions calculated

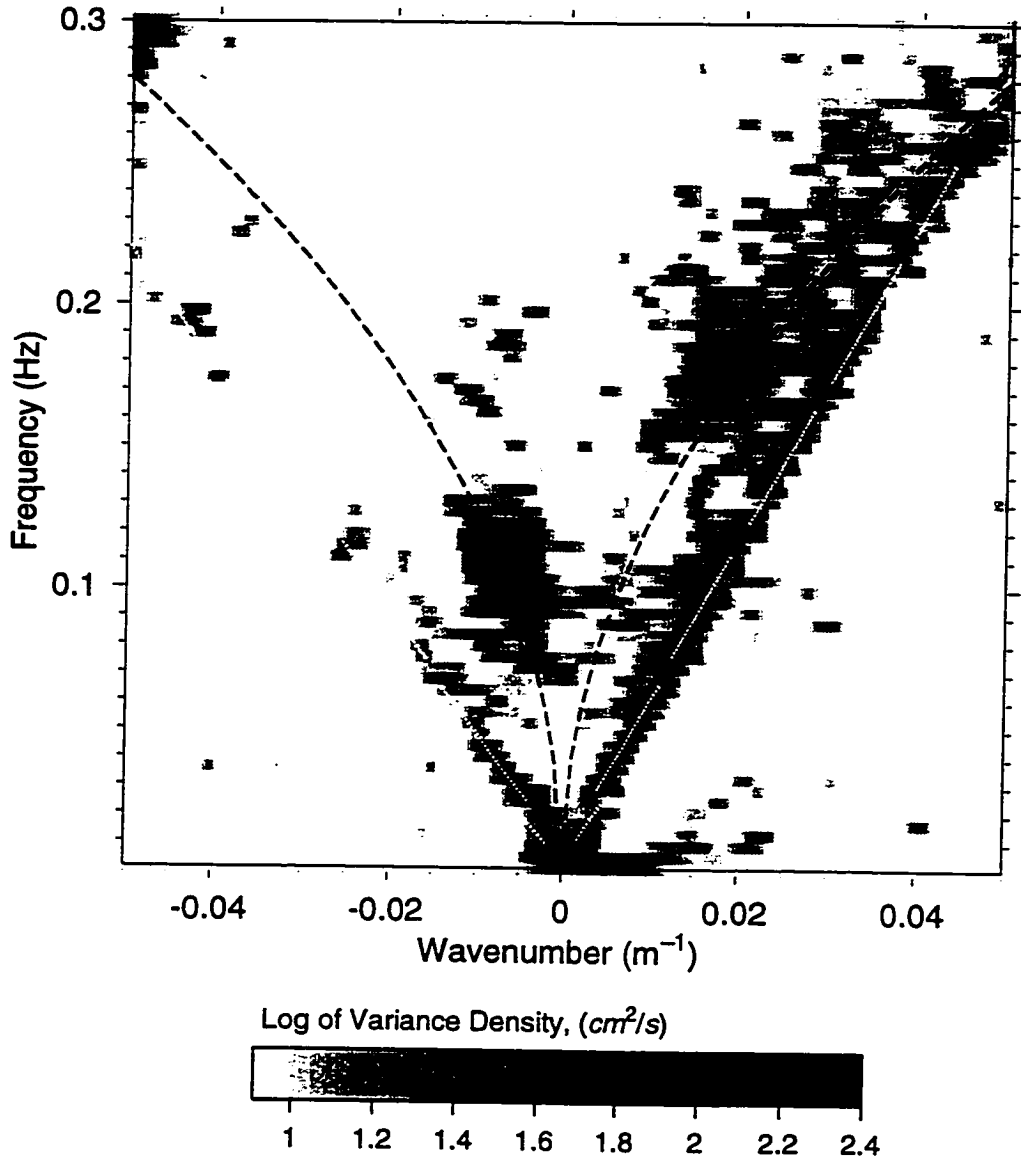


Figure 3.12: Variance density of the longshore component of orbital velocity from the inner array taken when the array is in the trough, on October 16. Though the array is not ideally located, the slope of the line of variance is for the lowest mode bar-trapped waves. This suggests that the lowest mode bar-trapped waves, are larger than other bar-trapped waves at the location of the array for this day. Calculated bar-trapped solutions for this location are plotted with white dots, the leaky wave cut-off is plotted with a black dashed line.

using the bar normalization scheme, as was appropriate for the other spectra observed in the trough (for example, Figure 3.9), but the shore normalization scheme. The bar-trapped line generated using this constraint fits the slope of the variance ridges in data better than the bar normalization scheme: the diagonal line of variance corresponds to the simplest shape for bar-trapped modes (with no zero crossings over the bar). Extrapolating the solutions to the top of the bar, implies that the bar-trapped edge waves with the simplest shapes are in fact considerably larger than more complex bar-trapped modes on top of the bar (if the simple shapes were the same size, they would have decayed by the location of the inner array and the line of variance would correspond to the bar normalization scheme, Figure 3.12). Figure 3.12 also shows that the incident wave field was strongly bi-modal, with high and low frequency peaks coming from different directions. Theoretically, a broad directional range of the incident waves is needed to generate edge waves at high wavenumbers by simple non-linear interactions. When incident waves arrive from different directions, the higher frequency peak dictates the direction of edge wave propagation (Herbers *et.al.*, 1995a), which is true in this case. (The concentration of variance at high wavenumbers and very low frequencies moving in the direction of the longshore current, is probably evidence of shear waves.)

The diagonal line of variance from the outer array on October 16 is slightly above the bar-trapped line corresponding to the simplest bar-trapped modes; if there were any simplest bar-trapped waves, they have decayed (Figure 3.13). If one could be sure of the data quality collected by open frame current meters on the outer array, one could in principle match the solutions on either side of the bar, and estimate the energy on top of the bar as a function of frequency and longshore wavenumber. Rough calculations of the variance contained in a peak corresponding to a mode two wave, with the simplest bar-trapped shape, (using spectra averaged over a frequency band width of $0.0137 Hz$, and a half power wavenumber band width of the peak), show this small part of the spectrum to have an average, root mean squared velocity of $2.5 cm/s$. Assuming all this energy were attributable to the mean shape (of the

same frequency wavenumber range) of a mode two wave which is trapped over the bar (with the simplest shape), this wave would have a longshore velocity of 5.5 cm/s on top of the bar (with a wave height of 3 cm). This is small, but is only a small portion of the total variance along the diagonal line of variance, attributable to bar-trapped waves.

In data from a longshore array of 8 wave gauges on top of a bar on a beach in the Baltic Sea, Schönfeldt (1994) observed that a significant proportion of variance of sea surface elevation appeared to propagate alongshore at phase speeds of about $\sqrt{gh_{\text{bar}}}$. Though the energy contributed from each mode may be small, the sum of variance from all the modes may contribute a significant portion of the sea surface elevation variance on top of the bar. The quasi non-dispersive nature of the bar-trapped modes shows that for a given amplitude, the longshore component of velocity is large relative to the solutions for edge waves not effected by the bar. So a large longshore component velocity signal may not necessarily mean that the sea surface elevation is large, as it might in the case of edge waves on a plane beach. Further observations of sea surface elevation such as Schönfeldt's (1994) results are needed to determine how frequently bar-trapped waves are dominant in an absolute sense (i.e. in terms of elevation). The problem is complex, as always with these model solutions, in that only the simplest bar-trapped waves and the higher even numbered modes, have maxima at the bar crest. Higher odd-numbered modes have nodes at the crest (Figure 2.10) and will not be evident in sea surface elevation measurements from on top of the bar.

Although there is strong signal which appears to be bar-trapped waves in the longshore velocity component data, the cross-shore velocity (Figure 3.14) does not show a similarly strong signal; it is instead dominated by energy from other sources such as incident waves, leaky waves etc., as previous edge wave studies have also noted (Huntley *et.al.*, 1981; Oltman-Shay and Guza, 1987; Howd *et al.*, 1991b, among others). This is sensible, as the model calculation show that the cross-shore component of velocity should not be large compared to the longshore component of velocity (Figure 3.4). Also the longshore component of velocity is less likely to be dominated by

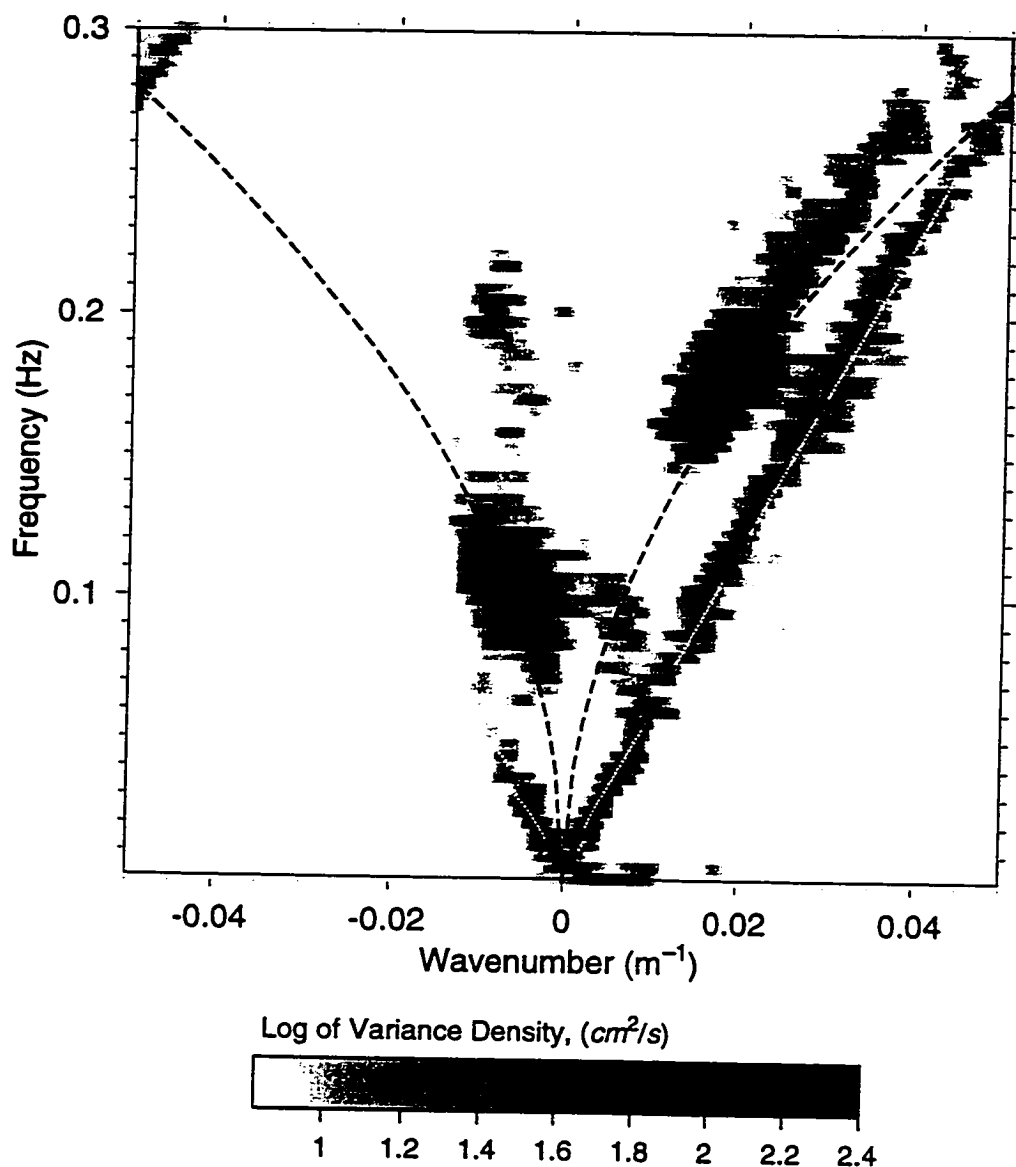


Figure 3.13: Variance density as a function of frequency and wavenumber of the longshore component of orbital velocity from the outer array taken when the array is far from the top of the bar, on October 16. The lowest mode bar-trapped waves are large on this particular day. Calculated bar-trapped solutions for this location are plotted with white dots, the leaky wave cut-off is plotted with a black dashed line.

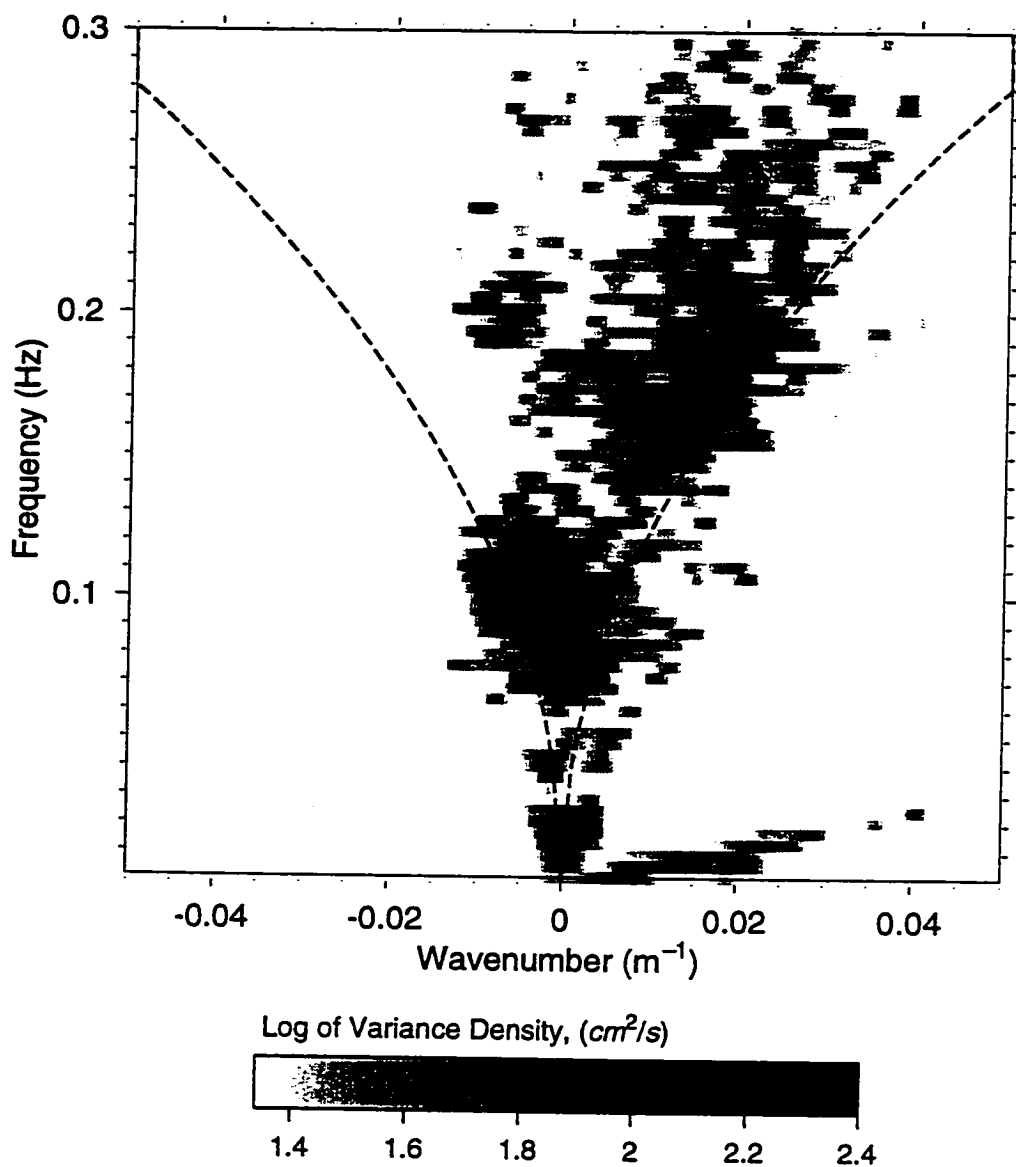


Figure 3.14: Variance density as a function of frequency and wavenumber of cross-shore component of orbital velocity from the inner array from the same time as Figures 3.12 and 3.13. Though bar-trapped modes are large on this day, there is little signal in the cross-shore component of velocity. Shear waves are present at low frequencies, high positive wavenumber.

incident waves, which tend to have small longshore components. Both the longshore component and the cross-shore component spectrum show evidence of shear waves at phase speeds less than the maximum longshore current (positive on this day), Figures 3.12, 3.13 and 3.14.

The diagonal ridge of variance density in the inner array on October 16, corresponds to the line of bar-trapped waves of the simplest shape. Mode zero, one and two peaks in variance density along this bar-trapped line for the inner array on October 16, are clearly present (and significant using the Oltman-Shay noise floor), with locations corresponding to the expected nodal structure of a bar-trapped edge waves (Figure 3.15), calculated assuming shore normalization. This does not imply that edge waves do not exist at the frequency-wavenumber coordinates between the peaks; calculated solutions corresponding approximately to these valleys show that these edge waves might be energetic close to the shore, but not at the bar. The calculated solutions match the peaks more exactly than in Figure 3.6, perhaps because of the longshore homogeneity in depth profiles from the latter part of the experiment. Mode 3 seems to be lower and mode 4 is only just significant using the Oltman-Shay noise floor (variations on the spectrum represented by multiple lines are to indicate possible uncertainties in the exact depth of the bar; these do not affect the significance of the fourth mode, just the location). In this case, the Oltman-Shay noise floor is large, because mode 4 lies in the same frequency band as a strong incident wave peak. The frequency of the mode 2 peak (at about 0.08Hz), which is larger than the others, is close to that of the lower frequency incident wave peak (at about 0.09 Hz), and the mode four peak (at about 0.18Hz) is near the higher frequency incident peak (at about 0.17 Hz); these are edge wave modes at incident frequencies.

The excellent agreement between the calculated dispersion curves and the observed distribution in frequency-wavenumber space of longshore component of edge wave velocity allows conclusive identification of bar-trapped energy. When the array was located in the trough or seaward of the bar, the simplest bar-trapped waves may have decayed, and only higher modes may be evident. The signature of this type of

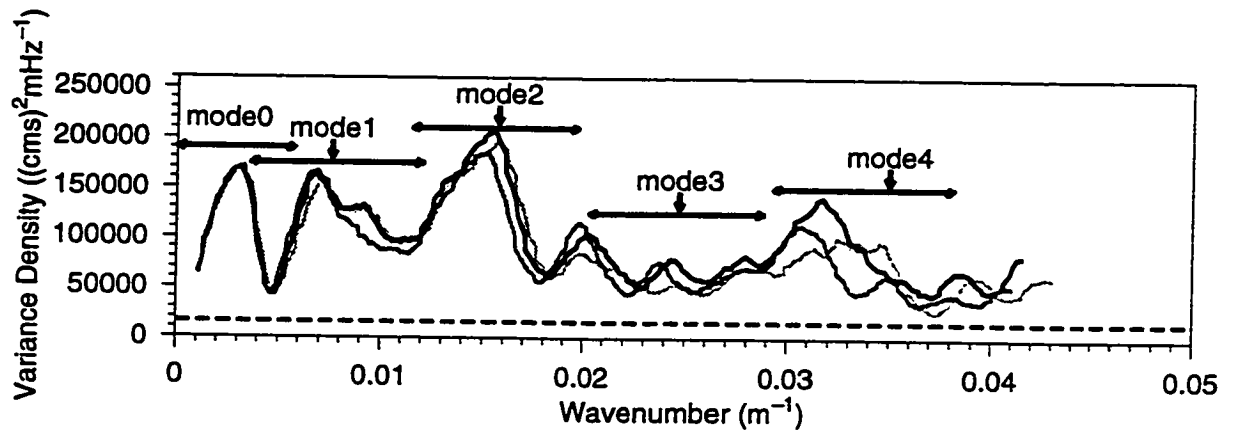


Figure 3.15: Variance density along the positive bar-trapped line in Figure 3.12. Variations correspond to changes in the slope of the line caused by a change in phase speed associated with a 20 cm change in the depth of the bar. The peak mode locations and the breadth of these peaks is marked. The mean variance density of the whole spectrum within the ranges of Figure 3.12 is marked with a dashed line

edge wave energy was persistent throughout the experiment, with energy extending from very low frequencies, to frequencies higher than incident. Higher frequency bar-trapped edge waves are evident because the longshore component of orbital velocity does not diminish with frequency as for plane beach solutions. The bandwidth of the energy along the bar-trapped line depends somewhat on the directional spread of the incident waves. Bar trapped edge waves were very clearly defined when the incident waves had two separate peaks of different frequency arriving from opposite directions. The bar-trapped waves that are generated seemed to travel preferentially in the same direction as the incident wave peak, and in the same direction as the higher frequency peak when more than one existed. Clear identification of these lines allows for a more detailed examination of edge wave response to different depth and longshore current profiles in the following section.

3.3 Bar-trapped edge waves and effective depth profiles during DELILAH

In Section 3.2.4 the importance of variable incident wave conditions in determining variability in the diagonal lines of variance was briefly discussed. However changes in the diagonal line of variance will also be a function of the effective depth profile which changes with the longshore current and depth profiles (Section 2.5). In fact, there were cases at the beginning of the DELILAH experiment where the incident wave conditions remained nearly constant, but the diagonal line of variance appeared and disappeared. The variety of effective depth profiles experienced during DELILAH can be reconstructed from the beach surveys and the longshore current profiles collected during the experiment. These profiles are a function of the bottom topography and the mean longshore current, and consequently vary with the tide as well as the incident wave conditions.

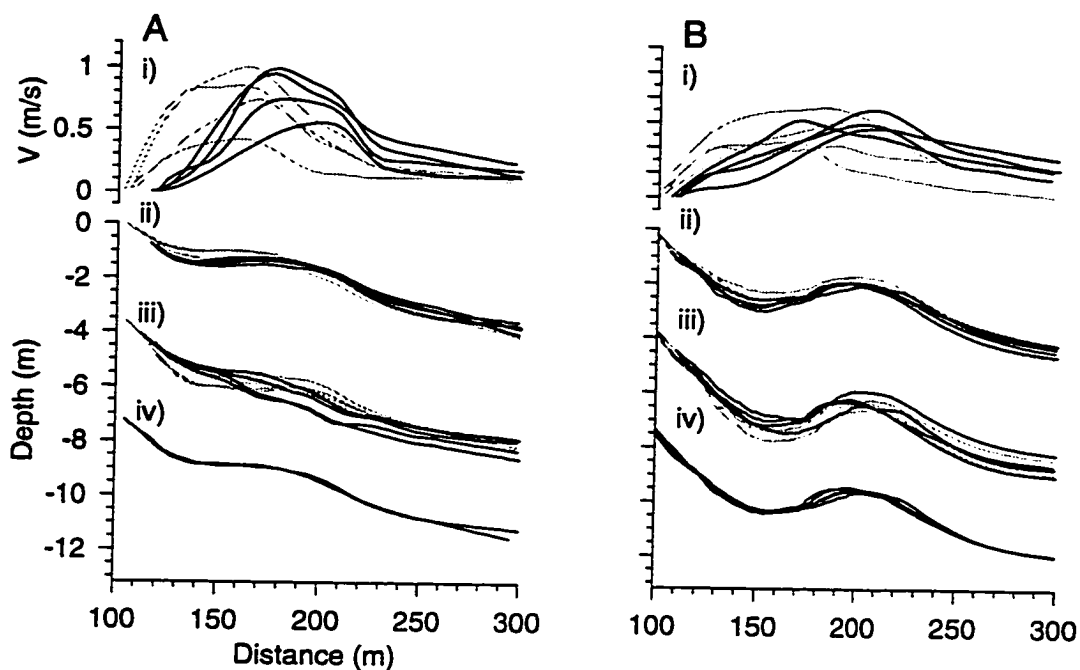


Figure 3.16: A.(i) Longshore current profiles at high tide (grey) and low tide (black) from October 7-9. (ii) Effective depth profile for the same times for edge waves travelling against the longshore current and (iii) for waves with the longshore current. (iv) Actual depth profile. B.(i) Eight of the larger longshore current profiles at high tide (grey) and low tide (black) from October 14-20. (ii) Effective depth profiles for edge waves travelling against the longshore current and (iii) with the longshore current. (iv) Actual depth profile.

3.3.1 Effective depth profiles during DELILAH

The cross-shore shape of the mean longshore current during DELILAH were characterized by a broad peak over the trough (Smith *et al.*, 1993), which was modulated both in size and location by the tide (Thornton and Kim, 1993). At low tide the current increased, and the current peak moved seaward with the increase in incident wave breaking over the bar, conversely at high tide the profiles moved shoreward and the current strength diminished. Some examples of longshore current profiles at high tide (grey line) and low tide (black line), for the beginning and the end of the experiment, when the bottom profiles were relatively stable, are shown in Figure 3.16A(i) and 3.16B(i) respectively. In general, when the bottom profile was gently sloping with a small bar or terrace, the longshore current had a small well defined peak, exemplified in Figure 3.16A(i). Numerical simulations of this current show it to be similar to the longshore current expected on a plane beach, with disturbances in the profile shape caused by the non-planar part of the topography (Thornton and Kim, 1993). When the bar was well defined, the longshore current had a very broad peak (Figure 3.16B (i))

The longshore current profiles and depth profiles during DELILAH combined to give examples of both current dominated, and depth dominated effective depth profiles. (Chapter 2, Section 2.5.2). The poorly defined bar, with gentle bottom slope, characteristic of the beginning of the experiment combined with a longshore current with a narrow peak to make a current-dominated effective depth profile (Figure 3.16A). In these cases, when the current was located over the bar at low tide, the effective depth was near planar, the current effect essentially eliminating the bar (Figure 3.16A(iii)) for waves travelling with the longshore current. When the current was located in the trough at high tide, the bar was enhanced (Figure 3.16A(iii)) for waves travelling with the longshore current (or in the case where there was a terrace, the terrace became a bar). Toward the end of the experiment, the longshore current profile was too weak and broad relative to the well defined bar, to significantly alter the effective depth profile (Figure 3.16B). The effective depth profiles both with and

against the longshore current, both had a well defined bar similar to the bar in actual depth (Figure 3.16B(ii) and 3.16B(iii)). Minor differences exist in the depths of the bar and trough, which affect the degree of edge wave amplification over the bar. Trapping occurs at x_{bar} , when $C \rightarrow \sqrt{gh_{bar}} + V_{bar}$ (Figures 3.17(B,C), 3.19(B,C) and 3.24(B,C), show the effective depth profiles from selected bar-dominated examples toward the end of the experiment).

During the high wave events, the longshore current profiles were broader than in the early part of the experiment, but stronger than in the latter part of the experiment. The current profiles were not narrow enough to completely change the character of the effective depth profile, but the existence of a strong longshore current peak in the trough made a large difference between the effective depth profiles for waves travelling with the longshore current and those travelling against, which strongly affected both the degree of trapping and the slope of the $\sqrt{gh'_{min}}$ line, for example Figure 3.18B,C. The shoreward increase of the longshore current over the bar resulted in the creation of a consistently seaward effective depth profile for waves travelling with the longshore current and an effective bar slightly landward of the actual bar for waves travel against the longshore current. Howd *et al.*(1991) calculated the effective depth profiles during the first storm at DELILAH, and showed the effective bar for waves travelling with the longshore current to be consistently seaward of the actual bar. The same was probably true of the second storm, though the depth records were incomplete.

3.3.2 Edge wave response to effective depth profiles.

In Section 3.2, the diagonal lines of variance were shown to be present, to varying degrees, in spectra of the longshore component of current from most days during DELILAH, and the lines of variance corresponded well to calculated solutions for bar-trapped edge waves. In Section 3.3.1 it was shown that the effective depth profiles could vary considerably not only with the changing bottom, but also with the changing longshore current, suggesting that some of the variability in the diagonal lines of variance could be explained by variability in the effective depth profiles.

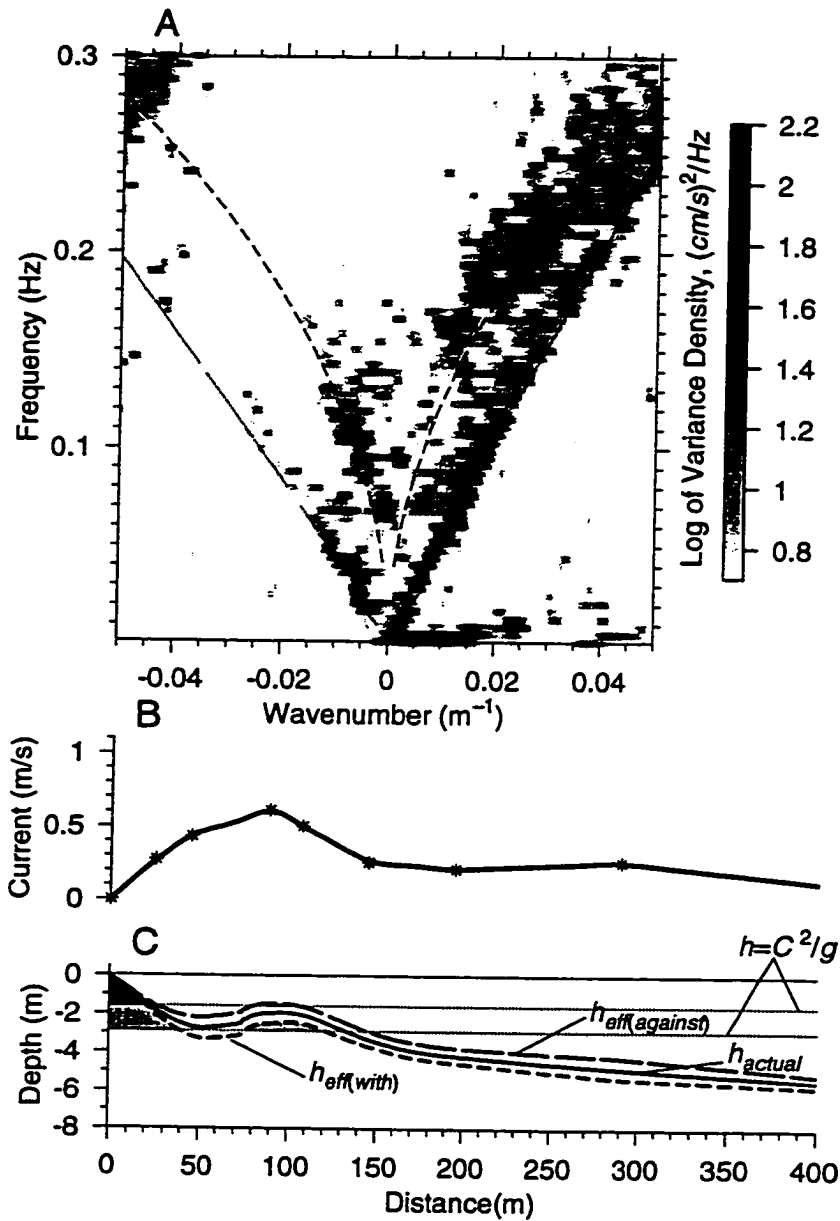


Figure 3.17: A. Frequency-wavenumber spectra of the longshore component of orbital velocity from the inner array for three hours over high tide on October 19, starting at 17:36. The dashed line is the leaky wave cut off, dotted lines are numerically calculated solutions for the most amplified bar trapped modes. Variance is normalized by frequency, as is usual. B. The mean longshore current profile over this same time period. C. The actual depth (solid line) and effective depth profiles both with (small dashes), and against (large dashes) the longshore current. Shaded areas are the depth below which the edge wave is sinusoidal for the phase speed chosen for each effective depth profile.

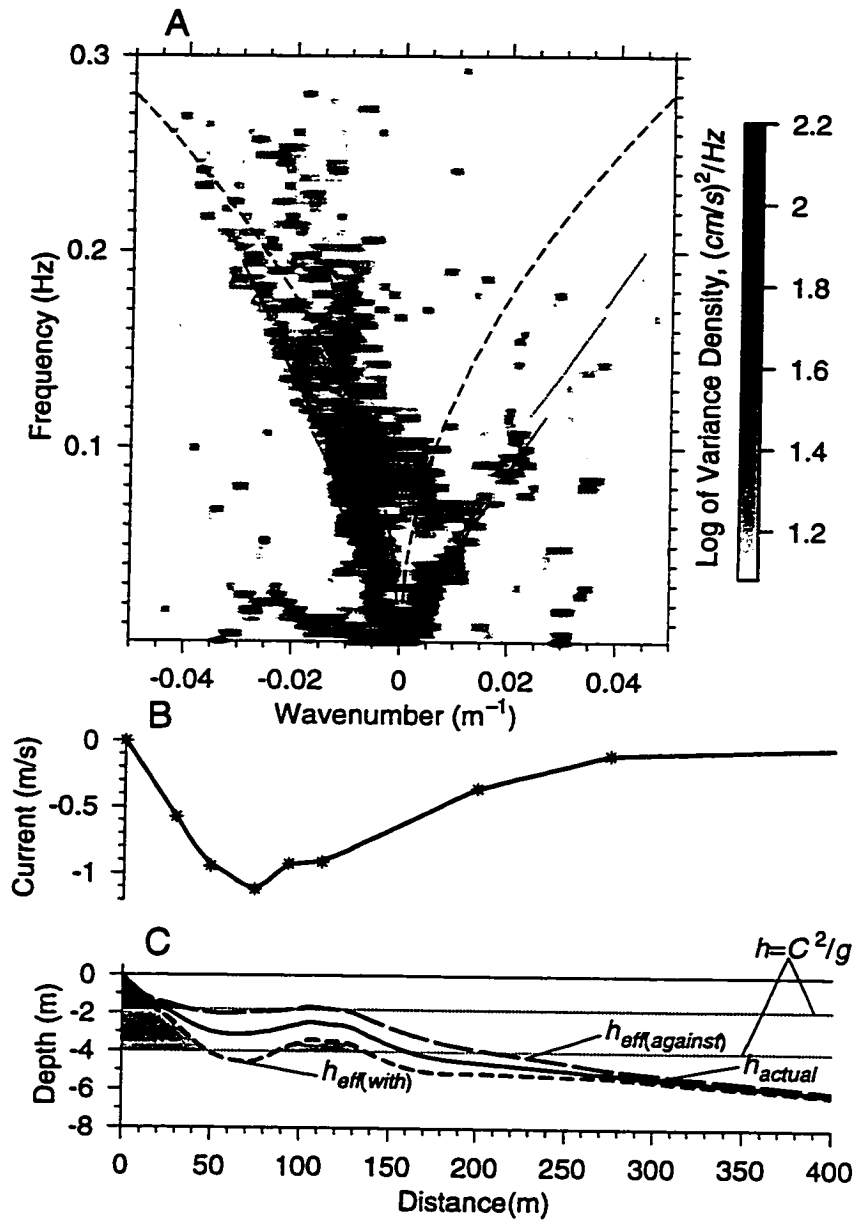


Figure 3.18: Same as Figure 3.17, but for October 13, starting at 13:57

The slope of the diagonal lines of variance corresponded well to predictions made using equation 2.19 and the effective depth profiles, particularly if one considers that the instrument array is fixed, and not usually located near x_{min} . The diagonal line of variance corresponds well to the frequency-wavenumber coordinates of edge waves trapped over the effective depth profiles measured at the same time (Figure 3.17 B and C). In this case, the bar is well defined and the longshore current has a broad peak, resulting in an effective depth profile which is dominated by the bar; the diagonal line of variance occurs at a phase speed approaching $\sqrt{gh'_{min}}$, or $\sqrt{gh_{bar}} + V_{bar}$. For example, frequency-wavenumber spectra from October 13 (Figure 3.18), during the second storm, show a diagonal line of variance corresponding to solutions which are bar trapped (but these are not the solutions which approach $\sqrt{gh'_{min}}$ the most closely, as those have decayed at the location of the instrument array (Section 3.5.2)). The two diagonal lines of variance in Figure 3.18 have strongly asymmetric slopes, corresponding to the strong difference in the depth of effective bars for waves travelling with and against the current (Figure 3.18C). (Depth profiles from October 14 are used in Figure 3.18C). Conversely, on days with little current, the two diagonal lines of variance are almost completely symmetric (Figure 3.19).

3.3.3 The sensitivity of bar-trapped waves to current dominated profiles

When the effective depth profile is current dominated, the effective bar, and changes in the effective bar, are often quite small (Figure 3.16A), and it is questionable whether the bar is large enough to cause substantial trapping of edge wave rays.

Numerical experiments using idealized effective depth profiles show the sensitivity of the longshore component of orbital velocity at the bar crest, to six different profiles with a bar or terrace of varying intensity (Figure 3.20). These profiles are chosen to mimic the subtle changes in the effective depth profile occurring early in the experiment. The calculated edge wave solutions are amplified over the bar relative to their shoreline values, only in the last three cases (Figures 3.20 D-F) when a bar exists.

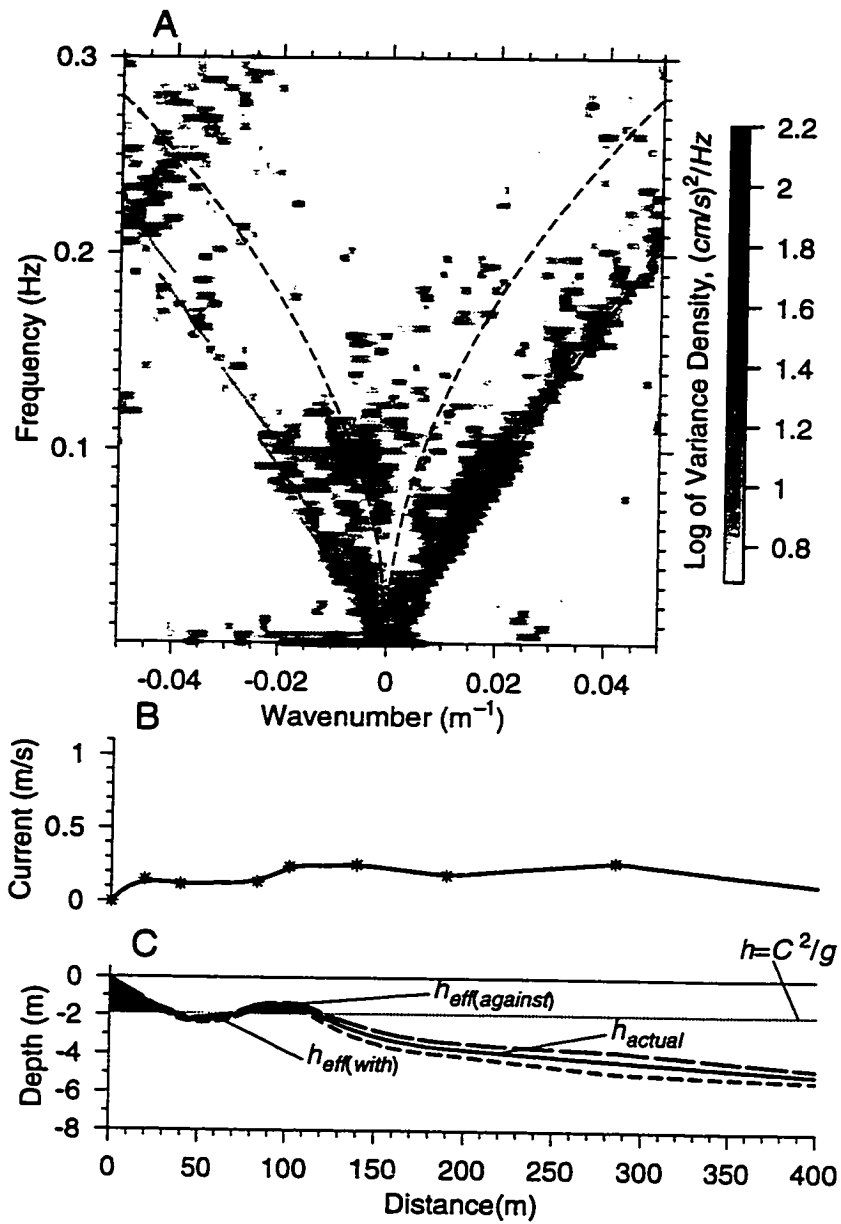


Figure 3.19: Same as Figure 3.17, but for October 16, starting at 10:20

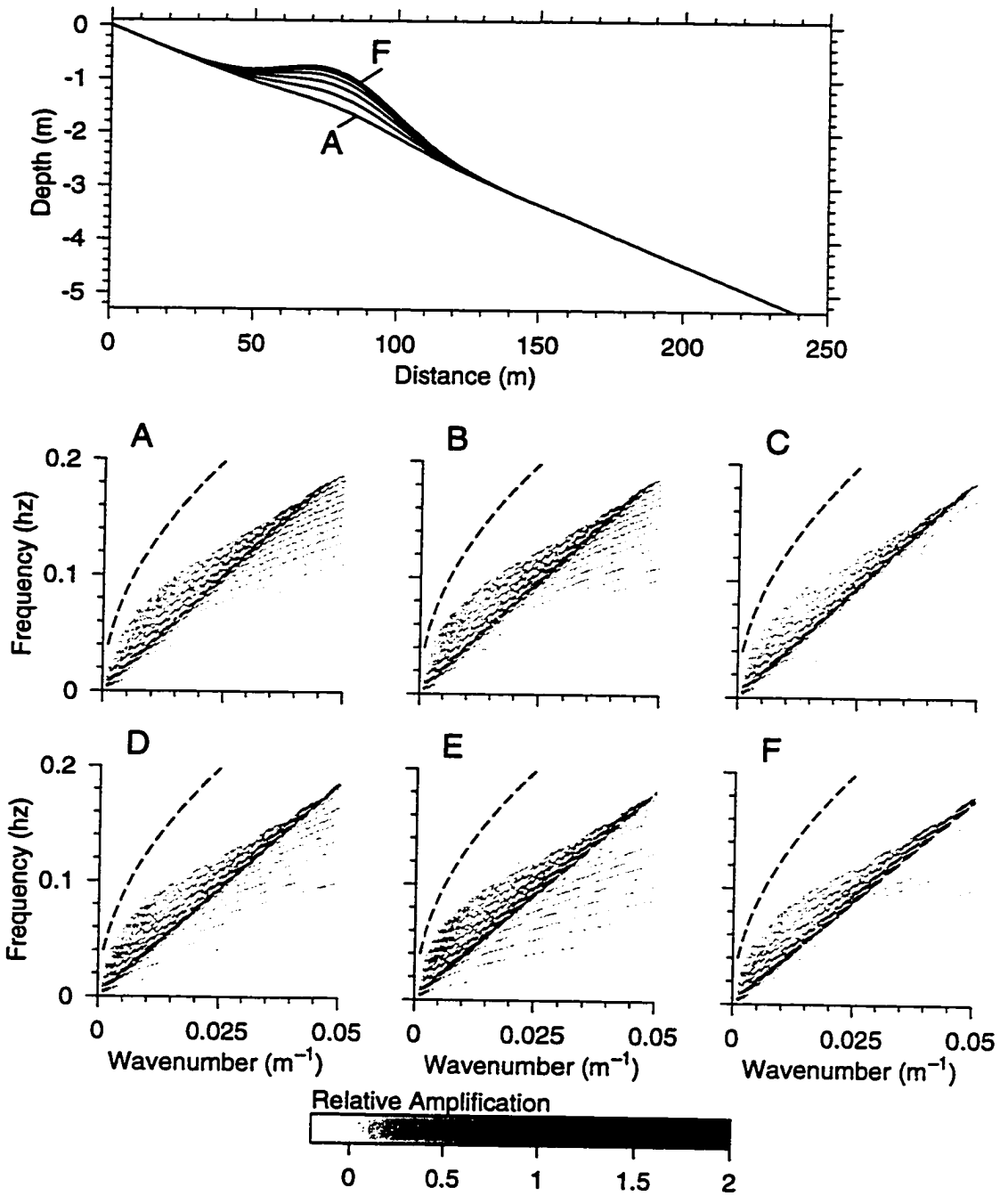


Figure 3.20: Upper panel: Six artificial depth profiles created to test the sensitivity of edge waves to small bottom perturbations. Lower panels: Numerically calculated dispersion diagrams for the same profiles. The greyscale corresponds to the magnitude of longshore component of velocity squared over the location of the bar.

However, in the first three cases, the existence of even a slight terrace, will cause the velocity of edge waves travelling at a phase speed similar to the depth of the terrace, to be slightly larger than surrounding modes (Figures 3.20 A-C). Theoretically, a small bar or even a terrace (effective or not), representative of the conditions early in the experiment, will cause an edge wave anti-node to get mildly trapped on the terrace or bar, at phase speeds approaching $\sqrt{gh'_{terrace}}$.

Frequency-wavenumber spectra from the early part of the experiment show that edge waves shapes are affected by a very small bar, and also by small changes induced by tidal variability in the longshore current, as suggested by the theoretical examples in Figure 3.20. When the effective bar is small, frequency-wavenumber spectra still show the diagonal lines of variance characteristic of bar-trapped edge waves (Figure 3.21B, 3.22A). Generally, during the early part of the experiment, these diagonal lines of variance are observed to respond to the changes predicted in effective depth, disappearing at low tide, when the effective bar disappears, and reappearing at high tide, when the effective bar reappears (for waves travelling with the longshore current). For example, on October 7, the actual depth profile has a small bar, the effective depth profile at low tide has a terrace, and the effective profile at high tide has an enhanced bar (Figure 3.21 C and D). The frequency-wavenumber spectrum at high tide has a clearly observable diagonal line (Figure 3.21B, where as the spectrum from low tide is diffuse with little evidence of a line (Figure 3.21A). Similarly, a few days later, the actual profile has a terrace, the effective profile at high tide has a bar and at low tide it is almost a plane beach (Figure 3.22 C and D). The spectrum at high tide has a diagonal line of variance (Figure 3.22A), but six hours later at low tide the dominance of this diagonal line is clearly diminished (Figure 3.22B). These conditions continued, until the storm began on October 9, when a more distinct bar formed and migrated seaward.

Though the bars are small in these two examples, they show the ability of the longshore current to change the effective depth from barred to non-barred and vice versa, and consequently to noticeably modify the character of the edge wave solutions. In

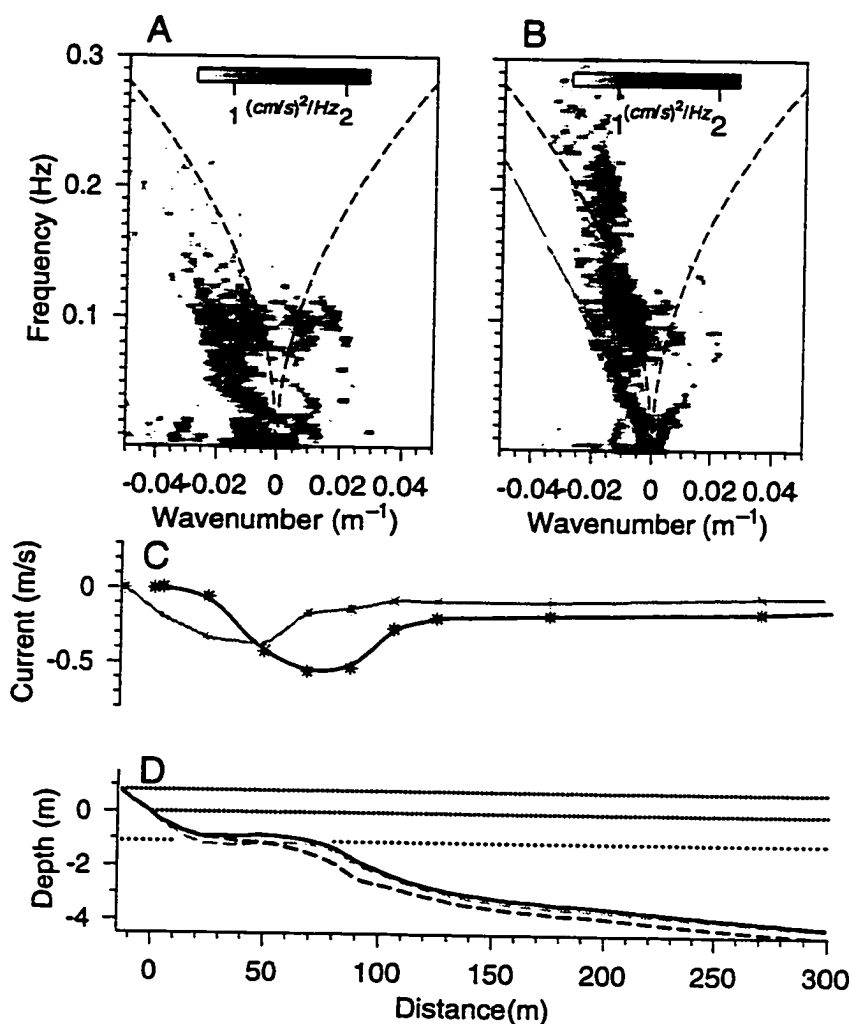


Figure 3.21: A. Frequency-wavenumber spectrum of the v-component of velocity from the inner array on October 7, over low tide, starting at 14:04. B. Frequency-wavenumber spectrum at high tide on the same day (starting at 19:54). C. The mean longshore current profiles for low tide (black line) and high tide (grey line). D. The actual depth profile (black line) and the effective depth profile at low tide (black dashed line) and at high tide (grey dashed line), for waves travelling with the longshore current. The depth at which the cross-shore solution goes from sinusoidal to exponential is marked, using the same phase speed as for the effective depth profiles. The water line for high tide and low tide are marked.

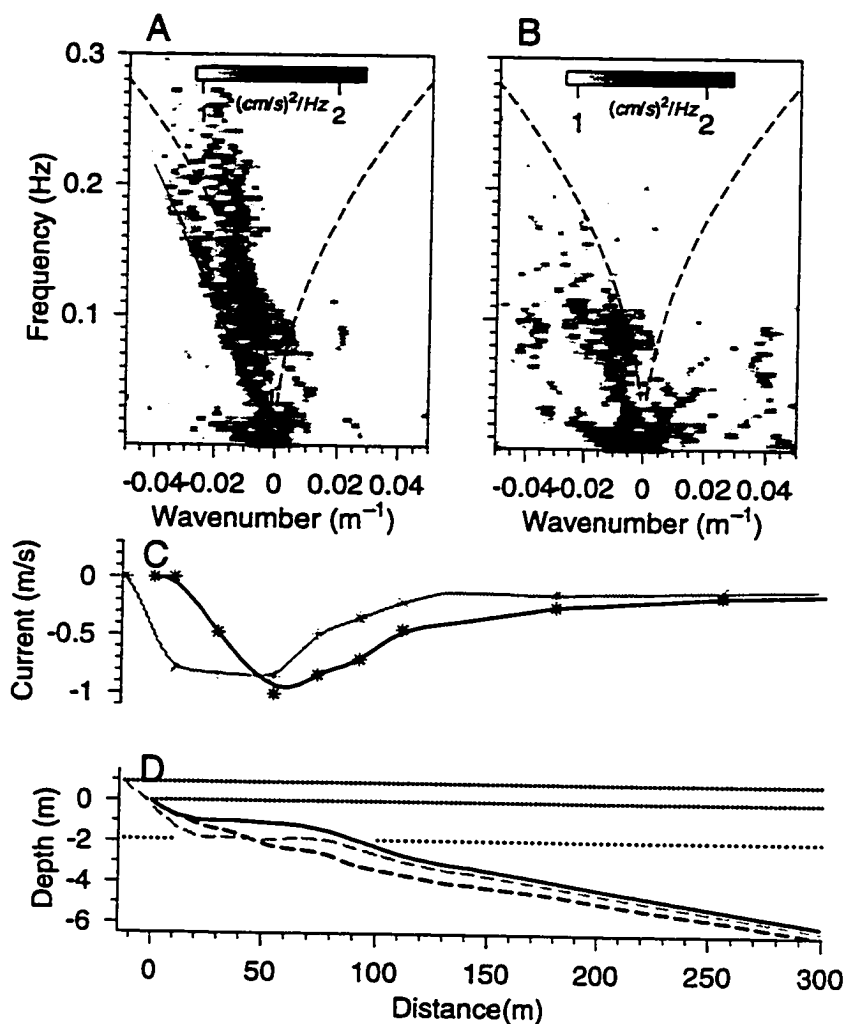


Figure 3.22: A. Frequency-wavenumber spectrum of the v -component of velocity from the inner array on October 9, over high tide, starting at 9:19. B. Frequency-wavenumber spectrum at low tide on the same day (starting at 16:03). C. The mean longshore current profiles for low tide (black line) and high tide (grey line). D. The actual depth profile (black line) and the effective depth profile at low tide (black dashed line) and at high tide (grey dashed line), for waves travelling with the longshore current. The depth at which the cross-shore solution goes from sinusoidal to exponential is marked, using the same phase speed as for the effective depth profiles. The water line for high tide and low tide are marked.

these current-dominated effective depth profiles, the longshore current dictates where the effective bar occurs, as on plane beaches. For example, in Figure 3.21, the trapping criterion is governed approximately by the location and depth at which the seaward longshore current shear occurs as is the case in Figure 2.12. Figure 3.23 shows the location of the actual bar (black line), the location of the effective bar for edge waves travelling both with (black bullet) and against (grey bullet) the longshore current, with the mean longshore current from Figure 3.2 plotted for reference. Though the exact location of the effective bar will depend on the accuracy and resolution of the longshore current measurements, Figure 3.23 shows a general trend in the variability of the location of the effective bar relative to the location of the actual bar during the experiment. For most of the early part of the experiment, the location of the effective bar is determined by the location of the seaward longshore current shear, and therefore modulates with the tide. This is in sharp contrast to the latter part of the experiment when the weak current shear (relative to the bottom slope) has little effect on the location of the effective bar.

The high and low tide effective depth profiles in Figure 3.21, 3.22 and 3.23 are end points. The effective profile would in reality move continuously from its high tide shape to its low tide shape, with the modulation in sea level. Clearly, the effective bar created by the longshore current would move shoreward and seaward with the tide on plane beaches. Consequently, when the effective depth profile is strongly current dominated, the net effect on the beach is some complex average over the tidal period. When Howd *et al.* (1992) introduced the idea of effective depth, they hypothesized that this could be a mechanism for bar growth on a plane beach. However, they add that this will occur if the effective bar is stationary. As with all models for bar generation, the fluctuating tidal elevation considerably complicates any simple prediction.

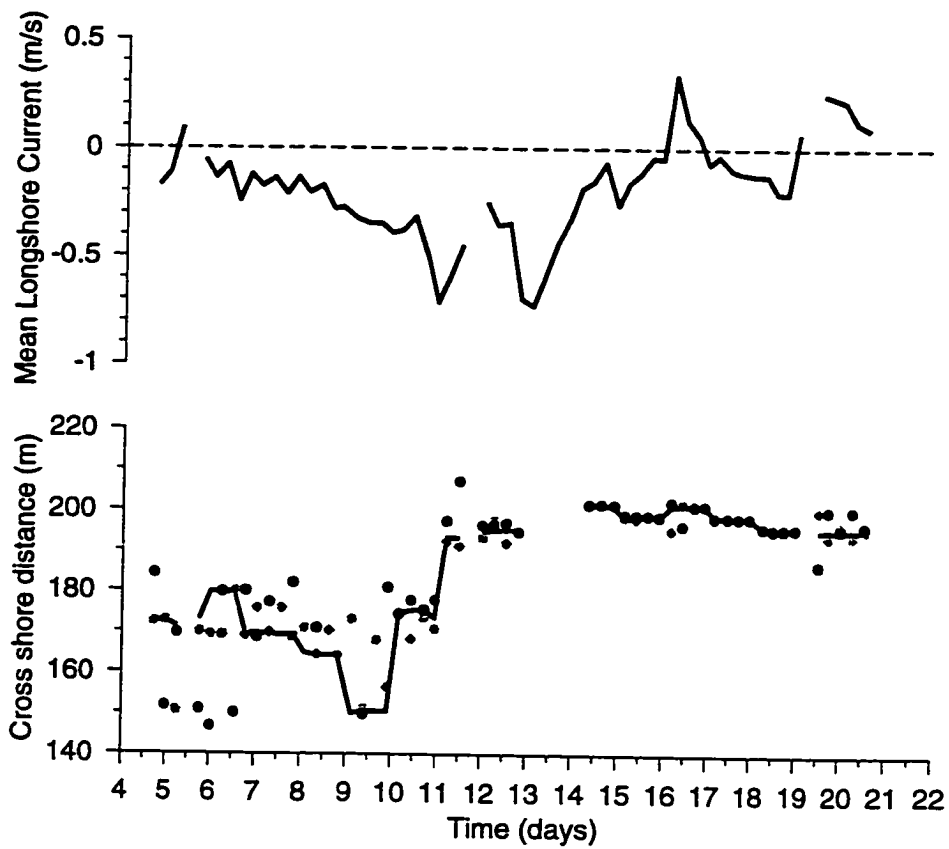


Figure 3.23: A. Mean longshore current profile during the whole experiment (same as in Figure 3.2). B. Cross shore location of the actual (black line) and effective bars for waves travelling with (black dots) and against (grey dots) the longshore current.

3.4 Directionality of bar-trapped edge waves during DELILAH

In general, during the DELILAH experiment, the edge waves travelling with the mean longshore current had greater variance than edge waves travelling against the current, as assumed by Howd *et al.* (1992) and Schönfeldt (1995). Directionality is particularly significant when the profile is current-dominated. For example, on plane beaches, edge wave trapping is only likely to occur when waves travel with the longshore current (Figure 2.12). The effect of current in equation 2.18, dV/dx , is greatest when V and C are the same sign. During DELILAH, when the current dominates the effective depth profile, radical changes such as from a barred profile to a near-planar effective depth profile (Figures 3.16, 3.21, and 3.22) only occur when waves travel with the longshore current. On days when the bar is more important (and the current can have a strong effect in both directions), the dominance of edge waves travelling with the current suggests that the net effect of current is to enhance amplification. For example, in Schönfeldt's case (Figure 2.14), the trough is significantly deepened for waves travelling with the longshore current. Similarly, on October 13, a stormy day with a strong longshore current in the trough (Figure 3.18C), the effective depth profile is more extreme when edge waves travel with the longshore current. In addition the effective bar is very slightly seaward of the actual bar (Howd *et al.*, 1991). Obviously, toward the end of the experiment, when the effective depth is bar dominated, directionality makes relatively little difference (Figure 3.16B).

Edge waves may tend to travel in the same direction as the longshore current because generation theories for both longshore currents and edge waves depend on the directionality of the incident wave field. The longshore current is forced mainly by the longshore momentum flux, or radiation stress, associated with the incident waves and (assuming longshore homogeneity) the longshore current direction is necessarily that of the longshore component of mean incident wave approach. For an edge wave where $k = k_1 - k_2$, equation 3.1 shows that for a range of angles of incident wave

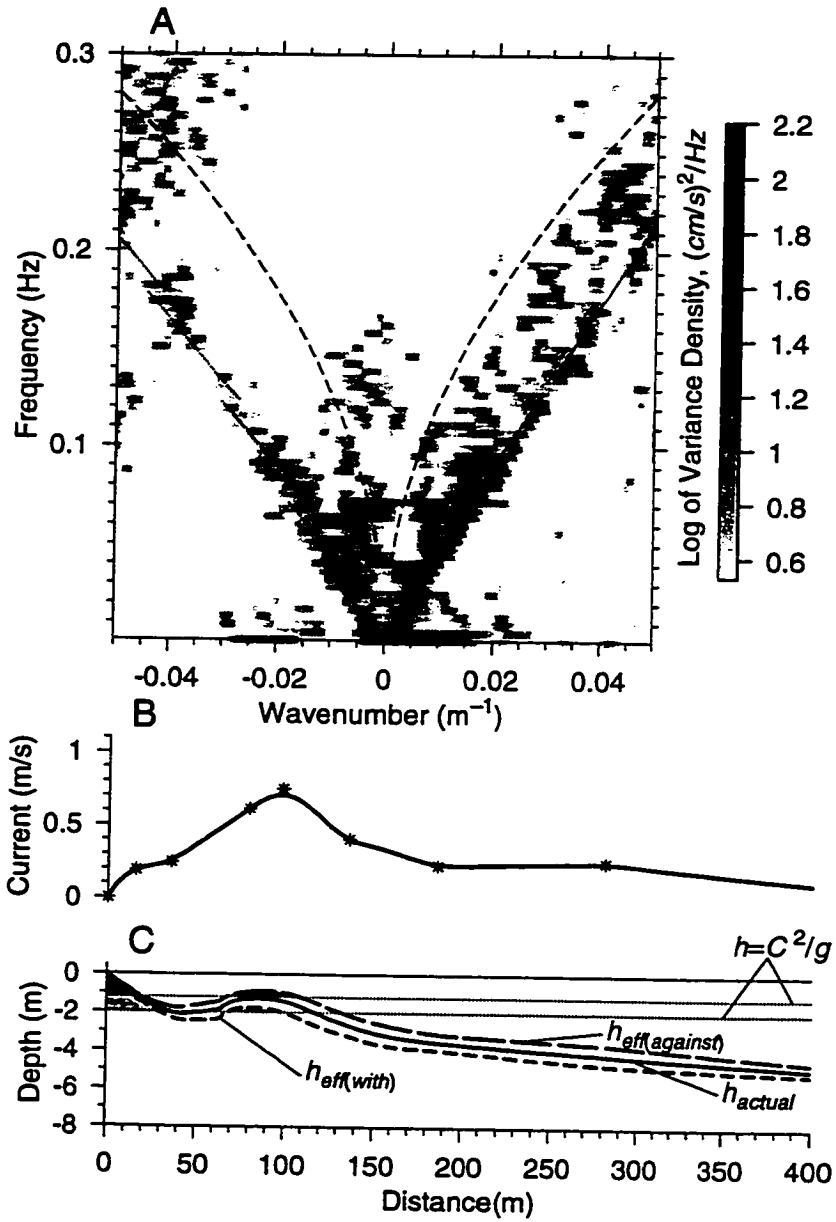


Figure 3.24: Same as Figure 3.17, but for three hours over low tide on October 19, starting at 12:25

approach, it is more likely for edge waves to be forced in the same direction as the incident wave direction. The expectation is then for most, but not necessarily all, of the edge wave energy to be in the direction of the longshore component of the incident waves. In most cases during DELILAH, combinations of incident waves preferentially forced edge waves in the same direction as the longshore current. For example, around October 13, the incident waves were characterized by low frequency, uni-directional swell from hurricane Lili. The edge waves were predominantly in the same direction as the incident waves, and the longshore current (Figure 3.18).

The marked difference between the effective depth profile for edge waves travelling with the longshore current and waves travelling against the current shown in Figure 3.18, suggests the possibility that edge waves could be preferentially forced over one bottom shape rather than another. Since the mean longshore current at Duck quite often has a peak in the trough (Smith *et al.*, 1993) or a peak on the bar which increases toward the trough, the effective bar for edge waves travelling with the longshore current is often more extreme than those travelling against the longshore current, which results in more extreme amplification. Some theories suggest that strong edge wave forcing occurs over the bar (Symonds *et al.*, 1982), so that coupling between the forcing and response might be superior for the most amplified bar-trapped modes. However, there is a marked dominance in edge waves travelling with the longshore current in the spectra shown in Figure 3.17, even though the dimensions of the effective bar and trough are not dependent on the longshore current in this case. The asymmetry in the edge wave variance seems to be associated with the incident wave forcing. Figure 3.17 shows two incident wave peaks above the leaky wave cut-off, one broad higher frequency peak in the positive (southeast) direction and a smaller, lower frequency peak at negative wavenumber. Again, in this case, the longshore current is in the same direction as the high frequency incident wave peak, and the observed bar-trapped edge waves are dominant in that direction. Six hours earlier at low tide, the edge waves travelling with the longshore current are less dominant than in Figure 3.17, but the effective depth profiles are similar (Figure 3.24).

This change in edge wave dominance seems to be related to the increased directional spread of the incident waves. Finally, on days when the longshore current is so small, as to have almost no effect on the effective depth profiles, there is still a dominance of edge waves travelling with the longshore current (Figure 3.19). Again, this seems to be related to the direction of the incident waves, which in this case have a broad high frequency incident wave peak in the same direction as the longshore current (which is not evident on Figure 3.19, but is evident in the frequency-wavenumber spectrum measured with the eight-metre array).

Though the enhanced effective depth profile, which increases amplification for wave propagating in a particular direction, may result in increased coupling between forcing and edge wave response, the dominant process determining the directionality of the edge wave response seems to be the directionality of the incident wave forcing. Though edge waves are dominant in the direction of the longshore current, this is only because both their respective forcing mechanisms depend on the incident wave directionality.

3.5 Summary

Diagonal lines of variance in the longshore component of orbital velocity spectra existed when an effective bar existed throughout the DELILAH experiment. Though these diagonal lines have been observed in past experiments, their likely cause has never been identified. The correspondence of these lines to predicted frequency-wavenumber coordinates, conclusively shows these lines to be bar-trapped edge waves. These bar-trapped waves were persistently energetic over a wide range of incident wave conditions throughout the experiment. Conditions ranged from low frequency uni-modal peaks (both narrow and broad in directional spread), to high and low frequency bi-modal peaks (again narrow and broad in directional spread), to multiple peaks spread out over a large range of frequencies and wavenumbers. Despite the variability in forcing conditions, bar-trapped waves are continually excited at all the

frequencies and wavenumbers obeying the bar-trapped phase speed, $C \rightarrow \sqrt{gh_{\text{bar}}}$.

Theoretically, the forcing should be enhanced when the cross-shore shape of the forcing function and the shape of the response function are well coupled. Bar trapped edge waves have their greatest maxima at the location of the bar, and some theories predict maximal edge wave forcing on the seaward face of the bar (Symonds and Bowen, 1984). This potential coupling could preferentially force bar-trapped waves, and explain why they are so dominant in these observations. The frequency-wavenumber spectra during DELILAH also showed a clear dominance of edge waves travelling with the longshore current over edge waves travelling against the longshore current, an effect probably due to the dependence of the directions of both edge wave forcing and longshore current forcing on the incident wave direction. Though there were days when the effective depth profile remained constant and the incident wave conditions changed, there were no days where the converse was true; therefore there is insufficient evidence to determine the exact cause of edge wave variability.

Edge waves have traditionally been observed at low frequencies ($f < 1/60$ Hz) (Huntley and Bowen, 1975) or sub harmonic frequencies. These are some of the few observations of edge waves at incident wave frequencies. It has always been assumed that edge waves exist at incident wave frequencies, though without a longshore array, these high frequency edge waves are difficult to discern among the incident wave noise. These bar-trapped edge waves are clearly not incident waves, because they exist below the leaky wave cutoff. The non-dispersive nature of bar-trapped edge waves partially causes this dominance of bar-trapped edge waves in the longshore component of orbital velocity at higher frequencies. Previously, it was assumed that the higher mode edge waves would not be evident in longshore component of velocity data, as the longshore component of orbital velocity diminishes strongly with mode number on plane beaches.

Since it is possible to attribute much of the observed variance to bar-trapped edge waves, the DELILAH data set provided a variety of different conditions with which to test the importance of realistic longshore current profiles in determining

the location, depth and shape of effective bars, and also the degree to which edge waves in field data, respond to the longshore current. The character of the effective depth profile toward the end of the experiment, when the bar was well developed, was rarely significantly altered by the longshore current; in these cases, the current merely enhanced the bar trapping mechanism. Conversely, when a small bar or terrace exists, or on a plane beach, the longshore current can significantly alter the effective depth profile and change the theoretical edge wave solutions, for example Figures 3.21,3.22. Modulations in the longshore current cause subtle changes in the effective depth profile which can determine the existence of an effective bar, and the existence of dominant lines of variance in frequency-wavenumber spectra. When a profile is current dominated (and when an effective bar exists) it can occur at a significantly different location than the actual bar. However, tidal modulations in the longshore current make it difficult to predict the effect that edge waves trapped on such an effective bar might have on the bottom morphology.

When a well defined bar and a strong current co-exist, the current could, if contained in the trough, remove the effect of that trough, as Schönfeldt (1995) shows with his numerical experiments with idealized longshore currents. However the observations made during DELILAH show that the broad longshore current peaks covered not only the trough but also the bar, diminishing the depth of both the bar and the trough when waves travel against the longshore current. The increase of the longshore current over the bar toward a peak in the trough caused an effective bar which is slightly shoreward (seaward) of the actual bar when waves travel against (with) the longshore current leading to a current-dominated situation, but not to the extent of Schönfeldt's rather artificial example.

The identification and predictability of persistent bar-trapped energy at Duck strongly suggests that studies of any barred beach, or plane beach with a longshore current, should not neglect the contribution of these bar-trapped modes to the overall hydrodynamic response. On beaches with bars and minimal longshore current, the diagonal line of variance will reflect edge waves amplified over the location of the bar.

On beaches with strong longshore currents, the situation is more complicated and the amplified edge waves may shift position or disappear with changes in the tide.

Chapter 4

Mass Transport by Bar-Trapped Edge Waves

4.1 Introduction

In addition to the time varying orbital velocities, waves possess a time-invariant second order velocity, called a drift velocity or mass transport velocity. A single progressive wave train in shallow water generates a drift in the bottom boundary layer, in the direction of wave propagation, which has no variation in the longshore direction (Longuet-Higgins, 1953). The combination of two or more wave trains, such as in a standing wave, may have a spatial pattern of drift convergences and divergences above the sea bed, if the two wave trains are phase locked. For example, a simple two dimensional standing wave has convergences at sea surface elevation nodes at the bottom of the boundary layer and at sea surface elevation antinodes at the top of the boundary layer (Longuet-Higgins, 1953). Particles rolling or saltating on the bottom (bed load) may be transported to nodes, and particles in suspension (suspended load) at the top of the boundary layer may move toward antinodes. Deposition under standing waves could theoretically occur under either nodes or anti-nodes. The question of whether deposition occurs under nodes or antinodes has been the source of much discussion (Short, 1975); some laboratory evidence shows deposition

under antinodes. For example, Carter *et al.* (1973) show, that when there is a large degree of reflectivity sediment accumulates at the peak of a wave envelope, suggesting that deposition may occur at antinodes.

On a beach, the overall pattern of second order steady flow will depend on the types of wave that are present. The progressive incident waves will move sand shoreward against the gravitational effect of the sloping beach. When a wave reflects on the beach, the cross-shore spatial pattern of convergences and divergences causes a mass transport velocity which is, in places, opposite to the progressive incident wave drift; deposition may occur at half wave wavelength intervals in longshore bars (Short, 1975). Progressive edge waves, which are standing in the on-offshore direction may cause accumulation in a similar way to reflected waves (Bowen, 1980), and standing edge waves may generate both a longshore and a cross-shore repeating pattern (Bowen and Inman, 1971). Phase locking of two or more progressive edge waves will produce various sorts of both irregular and regular longshore patterns which may lead to, for example, welded bars (Holman and Bowen, 1982).

The standing wave drift theory provides an interesting hypothesis to account for the existence of bars on beaches (Bowen and Inman, 1971; Carter *et al.*, 1973; Short, 1975; Bowen, 1980; Schönfeldt, 1989; Howd *et al.*, 1991b, 1992; Aagaard, 1990, 1991, among others). In order for a bar to evolve, a standing wave of the correct longshore scale must dominate for sufficiently long time for the bar to evolve. Though there are some isolated examples of edge waves with the "correct" length scales dominating the spectrum (Aagaard, 1988), in general edge waves occupy a broad range of frequencies (Holman, 1981). Though the convergence of drift under standing waves could cause longshore bars, it is difficult to show that drift patterns of appropriate scales dominate on a particular beach.

In Chapters 2 and 3, I have hypothesized, in a similar way, that the drift velocities associated with bar-trapped edge waves may cause bars to grow, based on the observation that the simplest bar-trapped edge waves of various frequencies should all have similar shapes over the bar. The objective of this chapter, is to investigate these

links more thoroughly by calculating the sum of drift velocities of a whole spectrum of edge waves, using data from Chapter 3 to determine the modes that should be included, and the relative magnitude of these modes. Though the results can only be a order-of-magnitude estimate, because of the assumptions and approximations involved, such an estimate is a significant advance on past work. These calculations will determine whether the net effect of bar-trapped edge wave drift around the bar is to enhance the bar, and will also determine the speed at which a parcel of water, moving with the drift, could move from the side of the bar to the top of the bar. The transport of sand particles by a mean drift is a complicated, poorly understood process, involving not only the actual transport of the sand, but the suspension and settling of sediment into and out of the water column. Extending these calculations to the movement of sand particles is beyond the scope of this thesis, however examining the direction and magnitude of drift should provide insights into the possible nature of sediment transport.

The chapter begins with a discussion of the derivation of drift velocities in the whole water column, with calculations of drift of a mode 1 edge wave provided as an example. Then the drift velocities at the top of the boundary layer for edge waves on general topography are calculated, from which the direction of cross-shore drift on the bar is demonstrated. The amplitudes of the cross-shore and longshore components of velocity are calculated for peaks in the frequency-wavenumber spectrum from DELILAH corresponding to bar-trapped edge waves. These velocities are used to normalize calculated edge wave velocity profiles. Finally drift velocities are calculated for each frequency band and summed over the whole spectrum, neglecting interactions between different modes.

4.2 Mass transport in a mode 1 edge wave

The total (Lagrangian) mass transport is comprised of the Stokes drift, or the drift resulting from following a water parcel through the wave orbit, which does not quite

close, and a second order Eulerian streaming, induced by the Reynolds stresses of the first order flow. Mass transport can be calculated directly in Lagrangian coordinates (i.e. Ünlüata and Mei, 1970; Jenkins, 1986) or the Eulerian drift can be calculated and added to the Stokes drift to get the total drift (i.e. Longuet-Higgins 1953; Iskandarani and Liu, 1991; Xu and Bowen, 1994). Here, the Eulerian approach is used.

To calculate the Eulerian drift, the viscid first order solutions are used to calculate the wave induced Reynolds stresses, which are then used to derive the second order drift, with the wave induced surface stress as the top boundary condition and a no-slip bottom boundary condition. To close the last calculation, a second order pressure gradient must be imposed (Longuet-Higgins, 1953).

To simplify the mass transport calculations, it is assumed that the velocity \mathbf{u} can be expanded into an asymptotic series around the small parameter ka (Longuet-Higgins 1953; Stuart 1966; Dore 1976; Iskandarani and Liu, 1991), where a is the wave amplitude. As a result the first order flow can be resolved separately from the second order flow and so on.

$$\mathbf{u} = \mathbf{u}_1 + \mathbf{u}_2 + \dots \quad (4.1)$$

where \mathbf{u}_1 is of order ka and \mathbf{u}_2 is of order $(ka)^2$. The Eulerian streaming velocity is the time average of the second order flow. The Lagrangian velocity \mathbf{u}_L can then be calculated by adding the Eulerian streaming $\overline{\mathbf{u}_2}$ to the Stokes drift \mathbf{u}_s (i.e. Mei, 1989).

$$\mathbf{u}_L = \overline{\mathbf{u}_2} + \mathbf{u}_s, \quad (4.2)$$

$$\mathbf{u}_s = \overline{\mathbf{u}_1 dt' \cdot \nabla \mathbf{u}_1}. \quad (4.3)$$

Other assumptions made in calculating drift under waves are that the time average of the first order flow is zero and that the first order flow is irrotational in the interior. Top and bottom boundaries, of thickness $\sqrt{2\nu/\sigma}$, exist where the flow is viscid, since the no slip conditions must be accommodated at the bottom boundary and the shear stress must be continuous at the surface.

The vorticity generated by the shear in these boundaries provides a driving mechanism for the steady Eulerian drift in the core region. Another way of thinking about this is the viscous boundary layer effects cause the wave velocities to no longer be in quadrature, so the wave induced Reynolds stresses have a mean component when time-averaged. The boundary layer affects the entire fluid eventually, regardless of the magnitude of the viscosity (Longuet-Higgins, 1953). This vorticity is transported into the interior flow either by diffusion or by vortex advection and stretching (Longuet-Higgins, 1953; Dore 1967). The dominance of diffusion over advection will depend on the ratio of the boundary layer thickness to the amplitude of the waves. When the ratio is small, vorticity diffuses into the core region, and if the ratio is large, vorticity advects into the region. In the latter case, advection in a second boundary layer may be set up to counteract the vorticity gradient, and the result is elimination of Eulerian streaming in the core region. This second boundary layer is called Stuart Layer (Stuart, 1966; Riley, 1965), and is larger than the wave bottom boundary layer. The calculations of drift velocity caused by advecting vorticity from the boundary are complicated (Mei, 1989). So, in the case of small amplitude edge waves, to simplify the calculations, the Stuart boundary layers are assumed to be relatively unimportant and vorticity diffusion dominates the core region flow. This assumption is valid if the amplitude of the edge waves is small compared to the size of the boundary layer.

Other assumptions made are the neglect of Coriolis force (which has been shown to be important in deeper water by Hasselmann (1970) and Xu and Bowen (1994)) and the use of an eddy viscosity which is constant in space and in time. The neglect of Coriolis force (for example Longuet-Higgins, 1953), should give a reasonable result, when a steady state is reached in which a return flow is superimposed to insure no net mass transport (Ünlüata and Mei, 1970). Moreover, Xu and Bowen (1994) show that the bottom streaming terms are relatively unaffected by the Coriolis force. The assumption of constant eddy viscosity is necessary to simplify the calculations; it is only recently that a time and space varying eddy viscosity has been included in drift calculations (Trowbridge and Madsen, 1984a,b; Jenkins 1987). Time varying

eddy viscosity can change the direction of drift. However, for these calculations, the temporal changes in the eddy viscosity are assumed to be associated with the larger incident waves, and do not vary on edge wave time scales. Spatial variations in the eddy viscosity will only change the size of the boundary layer.

In this section, the mass transport throughout the water column of a mode 1 edge wave is examined. A mode 1 edge wave on a plane beach is used for these calculations, to simplify the solutions, while still examining the interesting behavior around a node. Extension to higher order modes is straight forward. The first order solutions to the inviscid shallow water equations of motion for a mode 1 edge wave are

$$u_{inv} = \frac{akg}{\sigma}(-3 + 2kx)e^{-kx} \sin \phi, \quad (4.4)$$

$$v_{inv} = \frac{akg}{\sigma}(1 - 2kx)e^{-kx} \cos \phi, \quad (4.5)$$

$$\eta = a(1 - 2kx)e^{-kx} \cos \phi \quad (4.6)$$

where $\phi = ky - \sigma t$. For a wave travelling in the opposite direction, $\phi = -ky - \sigma t$, and the sign of the v velocity changes.

4.2.1 Free surface boundary layer

The free surface boundary condition is that the tangential stress must equal zero at the boundary (see Batchelor, 1967). The free surface boundary layer is problematic because the direction of normal and tangential stresses changes with the moving sea surface. To solve the problem, curvilinear (Longuet-Higgins, 1953), or Lagrangian (i.e. Ünlüata and Mei, 1970) coordinates are used, but these methods are hard to follow. Xu and Bowen (1994) derived the tangential stress (virtual wave stress) of a surface gravity wave with a more transparent method, which is used here to calculate the tangential stress at the bottom of the top boundary layer, of a mode 1 edge wave on a plane beach.

The free surface S of a mode 1 edge wave from (4.6) is

$$S = z - a(1 - 2kx)e^{-kx} \cos \phi \equiv 0. \quad (4.7)$$

The surface boundary condition (assuming surface tension is small, and the overlying medium is a vacuum) is zero tangential stress. According to Batchelor [1967], this condition gives

$$\begin{aligned}\epsilon_{ij}t_i n_j &= 0, \\ \epsilon_{ij}s_i n_j &= 0, \\ \epsilon_{ij} &= \frac{\mu}{2} \left(\frac{\partial u_i}{\partial x_j} + \frac{\partial u_j}{\partial x_i} \right)\end{aligned}\tag{4.8}$$

where ϵ is the stress tensor, t_i, s_i and n_j are the unit vectors which are tangent (in both directions) and normal to the free surface respectively, and $u_{i,j,k} = u, v, w$; $x_{i,j,k} = x, y, z$ are used interchangeably. The normal and tangential vectors are given by

$$\begin{aligned}\mathbf{n} &= \frac{1}{\|\mathbf{n}\|} (S_x, S_y, S_z), \\ \mathbf{t} &= \frac{1}{\|\mathbf{t}\|} (-S_z, 0, S_x), \\ \mathbf{s} &= \frac{1}{\|\mathbf{s}\|} (0, -S_x, S_y)\end{aligned}\tag{4.9}$$

where the subscripts x, y, z are the partial derivatives of the surface in the x, y and z direction respectively

$$\begin{aligned}S_x &= (3 - 2kx)ake^{-kx} \cos \phi, \\ S_y &= (1 - 2kx)ake^{-kx} \sin \phi, \\ S_z &= 1.\end{aligned}\tag{4.10}$$

Expanding (4.8) for the tangential stress in the cross-shore direction gives

$$\begin{aligned}& \frac{\mu}{2} \left[\frac{\partial u}{\partial z} + \frac{\partial w}{\partial x} \right] \\ & - \mu(ak)e^{-kx} \left[(3 - 2kx) \left[\frac{\partial w}{\partial z} - \frac{\partial u}{\partial x} \right] \cos \phi - \frac{(1 - 2kx)}{2} \left[\frac{\partial u}{\partial y} + \frac{\partial v}{\partial x} \right] \sin \phi \right] \\ & + O(ak)^2 = 0\end{aligned}\tag{4.11}$$

and for the tangential stress in the longshore direction

$$\begin{aligned} & \frac{\mu}{2} \left[\frac{\partial v}{\partial z} + \frac{\partial w}{\partial y} \right] \\ & - \mu(ak)e^{-kx} \left[(1 - 2kx) \left[\frac{\partial w}{\partial z} - \frac{\partial v}{\partial y} \right] \sin \phi - \frac{(3 - 2kx)}{2} \left[\frac{\partial v}{\partial x} + \frac{\partial u}{\partial y} \right] \cos \phi \right] \\ & + O(ak)^2 = 0. \end{aligned} \quad (4.12)$$

These two equations can be separated into their first and second order components according to (4.1). To the first order the tangential stresses are

$$\mu \left[\frac{\partial u_1}{\partial z} + \frac{\partial w_1}{\partial x} \right] = 0, \quad (4.13)$$

$$\mu \left[\frac{\partial v_1}{\partial z} + \frac{\partial w_1}{\partial y} \right] = 0 \quad (4.14)$$

and the second order stresses are (where the horizontal change of w_2 in the boundary layer has been considered small enough to be ignored (Xu and Bowen, 1994))

$$\mu \frac{\partial u_2}{\partial z} \quad (4.15)$$

$$\begin{aligned} = & \mu(ak)2e^{-kx} \left[(3 - 2kx) \left[\frac{\partial w_1}{\partial z} - \frac{\partial u_1}{\partial x} \right] \cos \phi - \frac{(1 - 2kx)}{2} \left[\frac{\partial u_1}{\partial y} + \frac{\partial v_1}{\partial x} \right] \sin \phi \right] \\ & \mu \frac{\partial v_2}{\partial z}, \end{aligned} \quad (4.16)$$

$$= \mu(ak)2e^{-kx} \left[(1 - 2kx) \left[\frac{\partial w_1}{\partial z} - \frac{\partial v_1}{\partial y} \right] \sin \phi - \frac{(3 - 2kx)}{2} \left[\frac{\partial v_1}{\partial x} + \frac{\partial u_1}{\partial y} \right] \cos \phi \right].$$

These are very similar results to Xu and Bowen(1994). The term $\partial v_2/\partial z$ corresponds to the tangential stress in the direction of wave propagation, which, if the horizontal decay part and the term caused by the three dimensional nature of the wave, $(\partial v_1/\partial x + \partial u_1/\partial y)$, are ignored, reduces to Xu and Bowen's results for a wave propagating in the y direction.

Assuming the first order inviscid solution is much larger than the viscid solution (Ünlüata and Mei, 1970; Xu and Bowen, 1994), so that the viscid solution can be

ignored, and using continuity and (4.4) and (4.5) gives

$$\begin{aligned}\frac{\partial w_1}{\partial z} - \frac{\partial u_1}{\partial x} &= -2\frac{\partial u_1}{\partial x} - \frac{\partial v_1}{\partial y} = (-9 + 2kx)e^{-kx}\frac{ak^2g}{\sigma}\sin\phi, \\ \frac{\partial w_1}{\partial z} - \frac{\partial v_1}{\partial y} &= -2\frac{\partial v_1}{\partial y} - \frac{\partial u_1}{\partial x} = (-3 - 2kx)e^{-kx}\frac{ak^2g}{\sigma}\sin\phi, \\ \frac{\partial u_1}{\partial y} + \frac{\partial v_1}{\partial x} &= (-6 + 4kx)e^{-kx}\frac{ak^2g}{\sigma}\cos\phi.\end{aligned}\tag{4.17}$$

Replacing these in the equations for tangential stress (4.11) and (4.12) and time averaging to find the steady second order tangential stress results in (where the stress is given in terms of the dynamic kinematic ν rather than the viscosity μ)

$$\nu\frac{\partial u_2}{\partial z} = 0,\tag{4.18}$$

$$\nu\frac{\partial v_2}{\partial z} = (6 - 8kx + 8k^2x^2)e^{-2kx}\frac{\nu a^2 k^3 g}{\sigma} = \tau_y.\tag{4.19}$$

The second order tangential shear in the cross-shore direction is always zero because the first order shear is always in quadrature with the surface in this direction. However, there is a second order shear stress in the direction of edge wave propagation.

4.2.2 The interior flow and the bottom boundary layer

Longuet-Higgins (1953) showed that no matter how small the the viscosity is, the effect of the boundary still diffuses into the inviscid core to cause steady streaming. For shallow water waves this can be illustrated simply: u_1 and v_1 in shallow water waves have no vertical dependence. However, the vertical velocity must equal zero at the bottom, but still satisfy continuity with u_1 and v_1 simultaneously. Without allowing for a small boundary layer, these two conditions are impossible to satisfy. Allowing for a small boundary layer below u_1 and v_1 generates a small phase shift in w_1 which extends well into the inviscid core. With this phase shift, u_1 and v_1 are no longer in quadrature with w_1 in the core for plane waves (for edge waves u_1 and w_1 are no longer completely in phase). The result is that the $\overline{u_1 w_1}$ and the $\overline{v_1 w_1}$ Reynolds

stress terms are both non zero and can drive the second order viscous streaming in the core. In an edge wave there will also be a Reynolds stress component in the cross-shore due to the $\overline{u_1 u_1}$ stress term.

To derive the first order velocity in the boundary layer the inviscid velocity is opposed by a viscous velocity, so the total velocity is $u_1 = u_{inv} + u_{vis}$. This first order viscous velocity must satisfy

$$\begin{aligned}\frac{\partial u_1}{\partial t} &= \nu \frac{\partial^2 u_1}{\partial z^2}, \\ \frac{\partial v_1}{\partial t} &= \nu \frac{\partial^2 v_1}{\partial z^2}\end{aligned}\quad (4.20)$$

with boundary conditions

$$\begin{aligned}(u_{vis}, v_{vis}) &\rightarrow 0 & z'/\delta \gg 1, \\ (u_{vis}, v_{vis}) &\rightarrow (-u_{inv}, -v_{inv}) & z' = 0,\end{aligned}$$

where $\delta = (2\nu/\sigma)^{1/2}$ is a natural scale for the size of the boundary layer, and since the z coordinate is defined as zero at the surface, $z' = z + h$. The total solution for the first order velocity (including the inviscid solution) is (by extension from Mei, 1989)

$$u_1 = \frac{akg}{\sigma}(-3 + 2kx) \left[e^{-kx} \sin(\phi) - e^{-kx - \frac{z'}{\delta}} \sin\left(\phi + \frac{z'}{\delta}\right) \right], \quad (4.21)$$

$$v_1 = \frac{akg}{\sigma}(1 - 2kx) \left[e^{-kx} \cos(\phi) - e^{-kx - \frac{z'}{\delta}} \cos\left(\phi + \frac{z'}{\delta}\right) \right]. \quad (4.22)$$

These expressions are only valid when the depth of the water ($h = x \tan \beta$) is much greater than the size of the boundary layer δ . Using (4.21) and (4.22) in the continuity equation gives the desired expression for w_1

$$\begin{aligned}w_1 &= -\frac{4ak^2g}{\sigma} e^{-kx} \int_0^{z'} \left[\sin \phi - e^{-\frac{z'}{\delta}} \cos\left(\phi + \frac{z'}{\delta}\right) dz' \right] \\ &= -\frac{2ak^2g}{\sigma} e^{-kx} \left[2z \sin \phi + \delta e^{-\frac{z'}{\delta}} \left(\cos\left(\phi + \frac{z'}{\delta}\right) + \sin\left(\phi + \frac{z'}{\delta}\right) \right) - \delta \cos \phi - \delta \sin \phi \right].\end{aligned}\quad (4.23)$$

Away from the shoreline w_1 is approximately $\partial\eta/\partial t$ at the sea surface, but close to the shoreline, the bottom boundary gets closer to the surface, and causes a phase

shift so that $w_1 \neq \partial\eta/\partial t$ at the surface. w is a sine function, so is in phase with u and in quadrature with v , (but recall the effect of the bottom boundary layer causes a slight shift in the phases, so that v and w are no longer completely in quadrature).

From the expressions for u_1, v_1 and w_1 , the wave driven Reynolds stresses are

$$\begin{aligned}
 \overline{u_1 u_1} &= \left(\frac{a k g}{\sigma}\right)^2 e^{-2kx} (-3 + 2kx)^2 \frac{1}{2} A(z'), \\
 \overline{v_1 v_1} &= \left(\frac{a k g}{\sigma}\right)^2 e^{-2kx} (1 - 2kx)^2 \frac{1}{2} A(z'), \\
 \overline{v_1 u_1} &= 0, \\
 \overline{u_1 w_1} &= -k \left(\frac{a k g}{\sigma}\right)^2 e^{-2kx} (2kx - 3) B(z'), \\
 \overline{v_1 w_1} &= -k \left(\frac{a k g}{\sigma}\right)^2 e^{-2kx} (1 - 2kx) C(z')
 \end{aligned} \tag{4.24}$$

where

$$\begin{aligned}
 A(z') &= \left(1 + e^{-2\frac{z'}{\delta}} - 2e^{-\frac{z'}{\delta}} \cos \frac{z'}{\delta}\right), \\
 B(z') &= \left(2z' - \delta - \delta e^{-2\frac{z'}{\delta}} + 2(\delta - z')e^{-\frac{z'}{\delta}} \cos \frac{z'}{\delta}\right), \\
 C(z') &= \left(2z' e^{-\frac{z'}{\delta}} \sin \frac{z'}{\delta} + 2\delta e^{-\frac{z'}{\delta}} \cos \frac{z'}{\delta} - \delta - \delta e^{-2\frac{z'}{\delta}}\right).
 \end{aligned}$$

The gradient of the Reynolds stress drives the second order flow in the momentum equations. The cross-shore derivative of the first term exists, so it can contribute to driving a second order flow in the cross-shore direction. The second term has no longshore dependence, and therefore will not contribute to longshore second order drift. The longshore and cross-shore velocities are in quadrature, and therefore the third term does not cause a Reynolds stress. The fifth term adds to the Reynolds stress because the bottom boundary causes v_1 and w_1 to be slightly in phase.

Assuming that the main changes in acceleration due to viscosity are in the vertical,

not the horizontal, the second order mean equations of motion are

$$\begin{aligned}\nu \frac{\partial^2 \bar{u}_2}{\partial z^2} &= \frac{1}{\rho} \frac{\partial p_2}{\partial x} + \frac{\partial \bar{u}_1 \bar{u}_1}{\partial x} + \frac{\partial \bar{u}_1 \bar{v}_1}{\partial y} + \frac{\partial \bar{u}_1 \bar{w}_1}{\partial z}, \\ \nu \frac{\partial^2 \bar{v}_2}{\partial z^2} &= \frac{1}{\rho} \frac{\partial p_2}{\partial y} + \frac{\partial \bar{u}_1 \bar{v}_1}{\partial x} + \frac{\partial \bar{v}_1 \bar{v}_1}{\partial y} + \frac{\partial \bar{v}_1 \bar{w}_1}{\partial z}.\end{aligned}\quad (4.25)$$

With the boundary conditions

$$\begin{aligned}\nu \frac{\partial \bar{u}_2}{\partial z} &= 0 & z = 0, \\ \nu \frac{\partial \bar{v}_2}{\partial z} &= \tau_y & z = 0, \\ \bar{u}_2, \bar{v}_2 &= 0 & z = -h = -x \tan \beta\end{aligned}\quad (4.26)$$

where τ_y is the surface stress defined in Section 4.2.1 Replacing (4.24) in (4.25) gives

$$\begin{aligned}\nu \frac{\partial^2 \bar{u}_2}{\partial z^2} &= \frac{1}{\rho} \frac{\partial p_2}{\partial x} + k \left(\frac{akg}{\sigma} \right)^2 (-3 + 2kx) \left[(5 - 2kx) 2e^{-2kx} A(z') - \frac{\partial}{\partial z} B(z') \right], \\ \nu \frac{\partial^2 \bar{v}_2}{\partial z^2} &= \frac{1}{\rho} \frac{\partial p_2}{\partial y} - k \left(\frac{akg}{\sigma} \right)^2 e^{-2kx} (1 - 2kx) \frac{\partial}{\partial z} C(z').\end{aligned}\quad (4.27)$$

Integrating these equations with respect to z , from $z' = 0$ to $z' = z'$ and applying the surface boundary condition gives second order shear in the core of the wave.

$$\begin{aligned}\nu \frac{\partial \bar{u}_2}{\partial z} &= U_{z_{const}} + \frac{1}{\rho} \frac{\partial p_2}{\partial x} z' + k \left(\frac{akg}{\sigma} \right)^2 (-3 + 2kx) e^{-2kx} \\ &\quad \left[(5 - 2kx) \left(z' - \frac{\delta}{2} e^{-2z'/\delta} + \delta e^{-z'/\delta} \cos \frac{z'}{\delta} - \delta e^{z'/\delta} \sin \frac{z'}{\delta} - \frac{\delta}{2} \right) - B(z') \right], \\ \nu \frac{\partial \bar{v}_2}{\partial z} &= V_{z_{const}} + \frac{1}{\rho} \frac{\partial p_2}{\partial y} z' - k \left(\frac{akg}{\sigma} \right)^2 e^{-2kx} (1 - 2kx) C(z').\end{aligned}\quad (4.28)$$

$U_{z_{const}}, V_{z_{const}}$ are chosen in order to satisfy the surface boundary conditions (which also will allow freedom in the choice of second order pressure gradient).

$$\begin{aligned}U_{z_{const}} &= -\frac{1}{\rho} \frac{\partial p_2}{\partial x} h - k \left(\frac{akg}{\sigma} \right)^2 (-3 + 2kx) e^{-2kx} \left[(3 - 2kx) \left(h - \frac{\delta}{2} \right) \right], \\ V_{z_{const}} &= -\frac{1}{\rho} \frac{\partial p_2}{\partial y} h + k \left(\frac{akg}{\sigma} \right)^2 e^{-2kx} (1 - 2kx) \delta + \tau_y.\end{aligned}\quad (4.29)$$

And finally, integrating (4.28) with respect to z gives the second order Eulerian streaming in the core of the wave.

$$\begin{aligned} \bar{u}_2 = & \frac{1}{\nu} U_{z_{const}} z' + \frac{1}{\mu} \frac{\partial p_2}{\partial x} \frac{z'^2}{2} + k \frac{(akg)^2}{\sigma^3} (-3 + 2kx) e^{-2kx} \\ & \times \left[(5 - 2kx) \left(\frac{z'}{\delta} \right)^2 + \frac{1}{2} e^{-2z'/\delta} + 2e^{-z'/\delta} \sin \frac{z'}{\delta} - \frac{1}{2} - \frac{z'}{\delta} \right. \\ & \left. - 2 \left(\frac{z'}{\delta} \right)^2 - e^{-2z'/\delta} + 2e^{-z'/\delta} \cos \frac{z'}{\delta} + 2 \frac{z'}{\delta} e^{-z'/\delta} \left(\cos \frac{z'}{\delta} - \sin \frac{z'}{\delta} \right) - 1 + \frac{2}{\delta} z' \right], \end{aligned} \quad (4.30)$$

$$\begin{aligned} \bar{v}_2 = & \frac{1}{\nu} V_{z_{const}} z' + \frac{1}{\mu} \frac{\partial p_2}{\partial y} \frac{z'^2}{2} - k \frac{(akg)^2}{\sigma^3} e^{-2kx} (1 - 2kx) \\ & \times \left(e^{-2z'/\delta} - \frac{2z'}{\delta} e^{-z'/\delta} \left(\cos \frac{z'}{\delta} + \sin \frac{z'}{\delta} \right) - 4e^{-z'/\delta} \cos \frac{z'}{\delta} + 2e^{-z'/\delta} \sin \frac{z'}{\delta} + 3 - \frac{2}{\delta} z' \right) \end{aligned} \quad (4.31)$$

where $\mu = \nu\rho$. Above the bottom boundary layer, these reduce to

$$\begin{aligned} \bar{u}_2 = & \frac{1}{\mu} \frac{\partial p_2}{\partial x} \left(\frac{z^2}{2} - \frac{h^2}{2} \right) + k \frac{(akg)^2}{\sigma^3} (-3 + 2kx) e^{-2kx} \\ & \left[(3 - 2kx) \frac{1}{\delta^2} (z^2 - h^2) - \frac{1}{2} (7 - 2kx) \right] \\ \bar{v}_2 = & \frac{\tau_y}{\nu} z' + \frac{1}{\mu} \frac{\partial p_2}{\partial y} \left(\frac{z^2}{2} - \frac{h^2}{2} \right) - k \frac{(akg)^2}{\sigma^3} e^{-2kx} 3(1 - 2kx). \end{aligned} \quad (4.32)$$

To solve (4.32), a second order pressure gradient is needed. Longuet-Higgins (1953) stipulates that the mass flux integrated throughout the water column must be zero. Integrating (4.32) from $z = -h$ to $z = 0$ and solving for the pressure gradient gives (using $\delta^2 = 2\nu/\sigma$)

$$\begin{aligned} \frac{1}{\rho} \frac{\partial p_2}{\partial x} = & k \frac{(akg)^2}{\sigma^2} e^{-2kx} \left((-3 + 2kx)^2 - \frac{3\nu}{2\sigma h^2} (-3 + 2kx)(7 - 2kx) \right), \\ \frac{1}{\rho} \frac{\partial p_2}{\partial y} = & -k \frac{\nu(akg)^2}{h^2 \sigma^3} e^{-2kx} 9(1 - 2kx) + \frac{3}{2h} \tau_y. \end{aligned} \quad (4.33)$$

The expressions derived here for \bar{u}_2 \bar{v}_2 are similar to those derived by Hunt and Johns (1963) and Carter *et al.* (1973). They derive the first order flow in the boundary

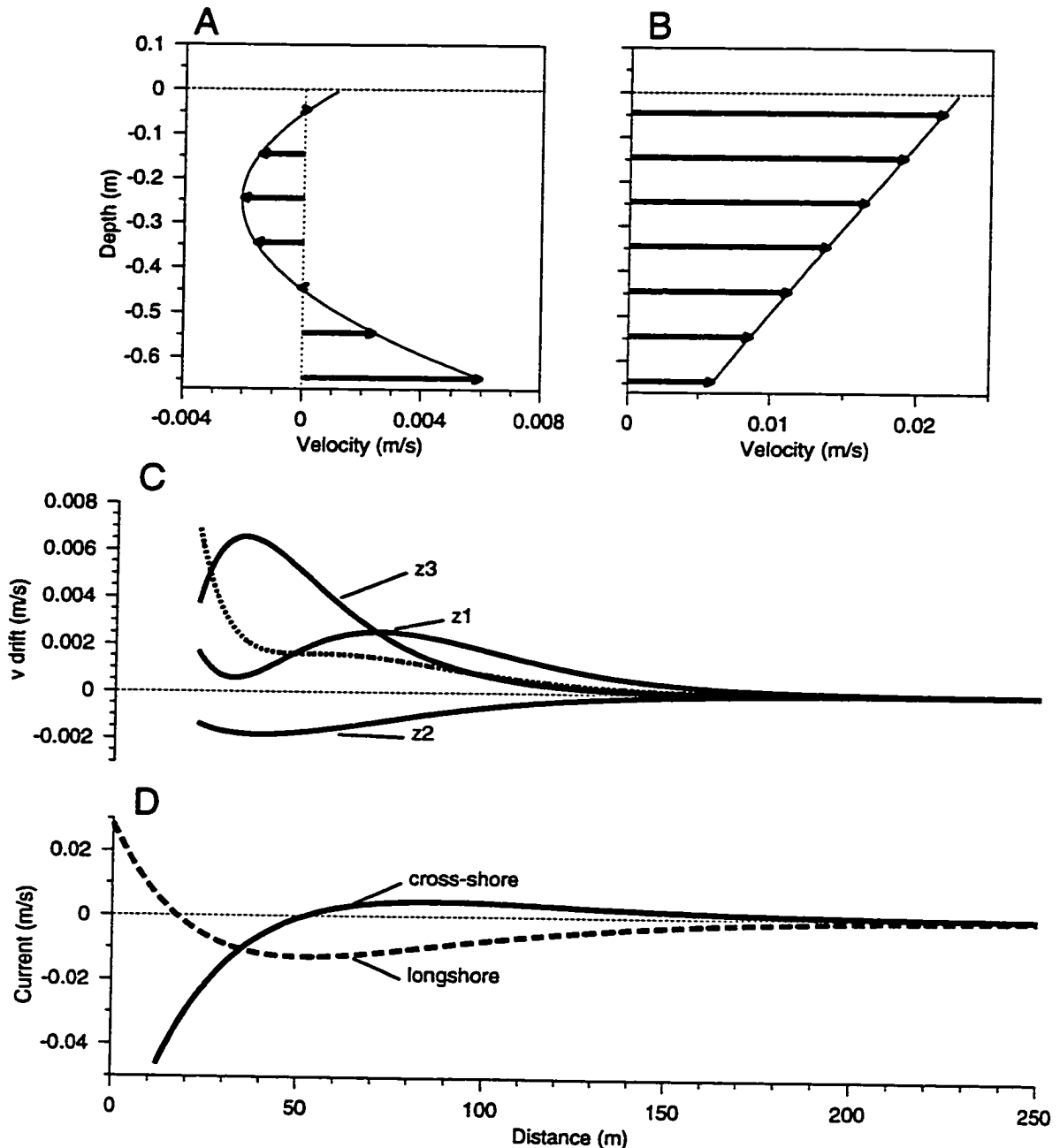


Figure 4.1: A. Depth profile at the location of the v_1 antinode ($x = 43m$) of the longshore drift velocity of a mode 1 edge wave (positive is the direction of wave propagation), $f = 0.018Hz$, slope = 0.015, assuming the net mass flux through the water column is zero. B. The same depth profile of drift, assuming no net second order pressure gradient, note scale difference. C. Cross-shore distribution of longshore drift (assuming no net mass flux) at the surface (z_1), at half the total depth (z_2) and at the top of the boundary layer (z_3). Dashed line is Stokes drift in the inviscid core. D. Cross-shore distribution of the first order cross-shore and longshore component of orbital velocity.

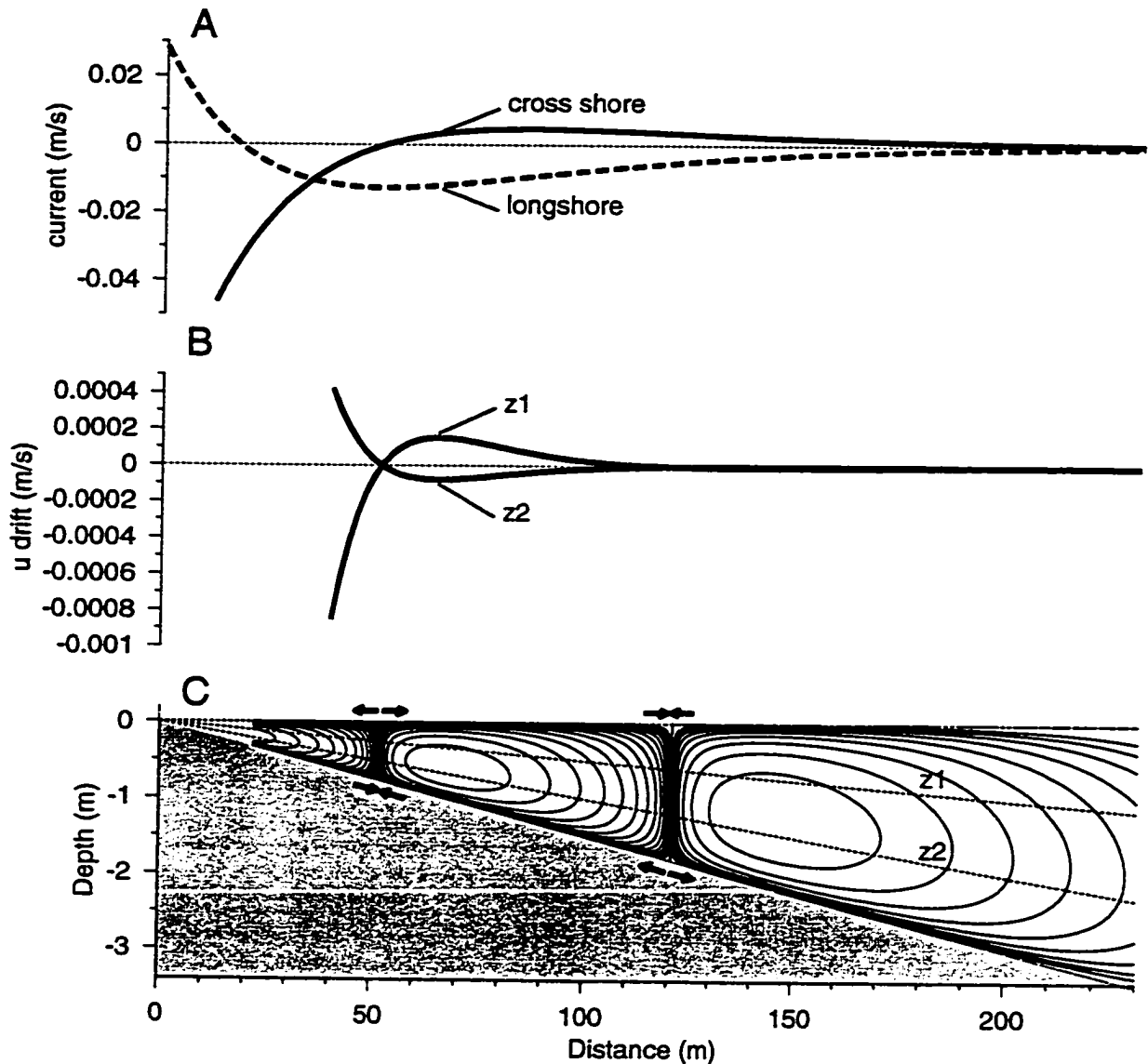


Figure 4.2: A. Cross-shore distribution of the first order cross-shore and longshore component of orbital velocity of a mode 1 edge wave, $f = 0.018\text{Hz}$, $\tan \beta = 0.015$. B. Cross-shore distribution of cross-shore drift at two thirds of the depth (z_1) and one third of the depth (z_2). C. Stream function of the cross-shore drift, z_1 and z_2 are marked.

layer in the same way as (4.30) and (4.31) were derived, (but assuming the shear stress disappears away from the boundary layer or $\tau_y = 0$) and then use the second order pressure gradient induced by the first order flow in the irrotational core to drive the second order flow in the boundary layer. The second order pressure in the boundary layer is assumed to be hydrostatic, in which case its value in the boundary layer is not significantly different from its value in the inviscid flow just above the boundary layer. Therefore the second order pressure field in the boundary layer can be approximated by the second order pressure in the inviscid region above the boundary layer.

$$-\frac{1}{\rho} \frac{\partial \bar{p}_2}{\partial x} = \overline{u_{inv} \frac{\partial u_{inv}}{\partial x}} + \overline{v_{inv} \frac{\partial u_{inv}}{\partial y}}, \quad (4.34)$$

$$-\frac{1}{\rho} \frac{\partial \bar{p}_2}{\partial y} = \overline{u_{inv} \frac{\partial v_{inv}}{\partial x}} + \overline{v_{inv} \frac{\partial v_{inv}}{\partial y}}.$$

Hunt and Johns can make these assumptions because they are only interested in the flow in and near the bottom boundary layer. If we also make these assumptions, (4.31) are exactly the same as those derived by Hunt and Johns (1963) and Carter *et al.* (1973).

The cross-shore and longshore drift above the boundary layer (4.31 and 4.32) are shown in Figures 4.2 and 4.1. The longshore drift is in the direction of wave propagation at both the surface and the bottom boundary layer. In the interior region, a return flow in the opposite direction is a result of insisting upon no net mass flux (Figure 4.1A). These results, without the cross-shore decay, are similar to the Longuet-Higgins (1953) solution. If the pressure gradient is assumed to be zero there is a flow in the direction of the wave throughout the water column (Figure 4.1B). The value of the drift at the top of the bottom boundary layer is independent of the assumption for $\partial p_2 / \partial y$. The bottom drift, and the drift in the core region is greatest underneath the sea surface elevation antinode; conversely the surface drift is greatest under the cross-shore velocity antinode.

The cross-shore drift at the surface is in the opposite direction to the top of the bottom boundary layer, also a result of insisting upon no net mass flux (Figure 4.2C). There is a cross-shore pattern of convergences and divergences, where the bottom

boundary layer convergence corresponds to the antinode in sea surface elevation as predicted by Longuet-Higgins (1953). The locations where the flow changes directions are marked in Figure 4.2C. The overall cross-shore drift pattern has three circulation cells, each in opposition to its neighbour (the one closest to the shore is anti-clockwise on Figure 4.2C). Obviously the drift patterns shown in Figures 4.2 and 4.1 are violated at the shore line, when the water is shallow. Moreover, the drift velocities were calculated assuming the bottom slope was negligible at the bottom boundary (but with depth changing as on a beach).

4.2.3 Stokes drift

To obtain the Lagrangian drift from (4.30) and (4.31), the Stokes drift must be superimposed. Stokes drift is the time averaged velocity following a particle of water, (4.3). See Mei (1989) for a derivation.

$$\begin{aligned} u_s &= \overline{\left(\int^t u_1 dt'\right) \frac{\partial u_1}{\partial x}} + \overline{\left(\int^t v_1 dt'\right) \frac{\partial u_1}{\partial y}} + \overline{\left(\int^t w_1 dt'\right) \frac{\partial u_1}{\partial y}}, \\ v_s &= \overline{\left(\int^t u_1 dt'\right) \frac{\partial v_1}{\partial x}} + \overline{\left(\int^t v_1 dt'\right) \frac{\partial v_1}{\partial y}} + \overline{\left(\int^t w_1 dt'\right) \frac{\partial v_1}{\partial y}}. \end{aligned} \quad (4.35)$$

For example, in the center core region of the wave, where $\partial u_1/\partial z = 0$ and $\partial v_1/\partial z = 0$, where the first order velocity is irrotational, replacing (4.4) and (4.5) in (4.35), the Stokes drift for a mode 1 edge wave is simply

$$\begin{aligned} u_s &= 0, \\ v_s &= \left(\frac{akg}{\sigma}\right)^2 \frac{k}{\sigma} (5 - 8kx + 4k^2x^2)e^{-2kx}. \end{aligned} \quad (4.36)$$

This can also be obtained from the Stokes drift for arbitrary two dimensional flow which is harmonic in time given in Mei (1989). Not surprisingly, there is only a component of Stokes' drift in the direction of wave propagation (Figure 4.1).

4.3 Mass transport at the top of the boundary layer in bar trapped edge waves

The equations governing mass transport in the bottom boundary layer caused by an arbitrary two dimensional flow which is oscillatory in time, $u_{inv} = U_o(x, y)e^{-i\sigma t}$, $v_{inv} = V_o(x, y)e^{-i\sigma t}$, have been derived by Hunt and Johns (1963) and subsequently by Carter, *et al.* (1973). Replacing (4.34) in (4.25) and integrating with respect to z , with the boundary conditions that there is no flow through the bottom, and no stress at the outer edge of the boundary, gives equations for the second order Eulerian flow in the boundary layer (Hunt and Johns, 1963), in a similar fashion to the derivation in Section 4.2.2, only without the wave-induced surface stress. At the top of the boundary layer these equations can be simplified considerably to

$$\begin{aligned}\bar{u}_2 &= -\frac{1}{4\sigma} \Re \left[(3 - 3i)U_o \frac{\partial U_o^*}{\partial x} + V_o \frac{\partial U_o^*}{\partial y} + (2 - 3i)U_o \frac{\partial V_o^*}{\partial y} \right], \\ \bar{v}_2 &= -\frac{1}{4\sigma} \Re \left[(3 - 3i)V_o \frac{\partial V_o^*}{\partial y} + U_o \frac{\partial V_o^*}{\partial x} + (2 - 3i)V_o \frac{\partial U_o^*}{\partial x} \right]\end{aligned}\quad (4.37)$$

where * is the complex conjugate. For an edge wave, u_{inv}, v_{inv} must have the form $-iU_o(x)e^{i(ky-\sigma t)}$, $V_o(x)e^{i(ky-\sigma t)}$, so that the Eulerian drift due to an edge wave at the top of the boundary layer is

$$\begin{aligned}\bar{u}_2 &= -\frac{1}{4\sigma} \left[3U_o \frac{\partial U_o}{\partial x} - kU_o V_o \right], \\ \bar{v}_2 &= +\frac{1}{4\sigma} \left[3kV_o^2 - 3V_o \frac{\partial U_o}{\partial x} \right].\end{aligned}\quad (4.38)$$

The terms in \bar{v}_2 are due only to the $\overline{v_1 w_1}$ Reynolds stress terms. The \bar{u}_2 term is due to the $\overline{u_1 w_1}$ and the $\overline{u_1 u_1}$ Reynolds stresses. The $\overline{u_1 v_1}$ term does not contribute in either velocity component in an edge wave. For waves traveling in the opposite direction, the cross-shore drift is the same, but the longshore is negative.

This solution is completely analogous to the solution derived for the flow at the top of the boundary layer of a mode 1 edge wave. To confirm this, using (4.4) and

(4.5) in (4.38), the drift for a mode 1 edge wave is

$$\begin{aligned}\bar{u}_2 &= -\frac{k(kag)^2}{2\sigma^3}(-3 + 2kx)(7 - 2kx), \\ \bar{v}_2 &= -\frac{k(kag)^2}{\sigma^3}3(1 - 2kx)\end{aligned}\quad (4.39)$$

which is exactly the same result as would be obtained by setting the pressure gradient in (4.33) to (4.34), and having no longshore wave stress.

The Stokes' drift in the boundary layer for a general two dimension flow can be calculated using (4.35). The result at the top of the boundary layer is (Hunt and Johns, 1963)

$$\begin{aligned}\bar{u}_2 &= \Re \frac{i}{2\sigma} \left[U_o \frac{\partial U_o}{\partial x} + V_o \frac{\partial U_o}{\partial y} \right], \\ \bar{v}_2 &= \Re \frac{i}{2\sigma} \left[V_o \frac{\partial V_o}{\partial y} + U_o \frac{\partial V_o}{\partial x} \right].\end{aligned}\quad (4.40)$$

For a general edge wave solution, this reduces to

$$\begin{aligned}\bar{u}_2 &= 0 \\ \bar{v}_2 &= \frac{1}{2\sigma} \left[kV_o^2 + U_o \frac{\partial V_o}{\partial x} \right]\end{aligned}\quad (4.41)$$

There is only a Stokes drift in the longshore direction, or in the direction of wave propagation, as was shown to be true for a mode one edge wave. When the mode 1 edge wave solutions are substituted into (4.41), the same result is obtained as in (4.36).

Adding the Stokes drift term to the Eulerian streaming term, will give the total mass transport at the top of the boundary layer

$$\begin{aligned}\bar{u}_2 &= -\frac{1}{4\sigma} \left[3U_o \frac{\partial U_o}{\partial x} - kU_o V_o \right], \\ \bar{v}_2 &= \frac{1}{4\sigma} \left[5kV_o^2 + 2U_o \frac{\partial V_o}{\partial x} - 3V_o \frac{\partial U_o}{\partial x} \right].\end{aligned}\quad (4.42)$$

These equations are generally used to provide the link between edge wave shape and the direction of the sediment transport they may induce. For example, Bowen and Inman (1971) used Hunt and Johns (1963) to theoretically calculate the drift induced by a standing edge wave on a plane beach, as did Holman and Bowen (1982), to theoretically calculate the drift due to phase locked edge waves. Howd *et al.* (1992) used (4.42) to calculate the cross-shore drift velocity for an edge wave on a plane beach with a longshore current. In this manner, (4.42) can be used to calculate the drift velocity induced by bar-trapped edge waves.

4.4 Boundary layer drift during DELILAH

The ultimate goal of studying the drift velocity patterns of bar-trapped edge waves, is to estimate the magnitude and direction of the drift velocities that occur on a real beach with bar-trapped edge waves such as during DELILAH. The direction of edge wave drift for individual modes can be calculated using (4.42). To calculate the direction of a spectrum of edge wave modes, the relative magnitudes of edge wave modes are needed. The magnitude of edge wave variance, relative to other sources of nearshore variance (i.e. incident waves, shear waves) has been estimated using frequency-wavenumber spectra, such as Figure 3.12 in Chapter 3, by Howd *et al.* (1991a) and also by Oltman-Shay and Guza (1987).

Howd *et al.* partitioned the total variance over the whole spectral domain (in this case $k = -0.05 \rightarrow 0.05m^{-1}$ and $f = 0 \rightarrow 0.25Hz$) between incident waves (including high frequency edge waves and leaky waves), infragravity waves, and shear waves, summed the energy contained in the significant peaks in each area, and calculated the percent energy contained in each respective area. In the infragravity wave category they include all waves below $0.05Hz$ and above the theoretical mode 0 edge wave dispersion curve. Conversely Oltman-Shay and Guza were more interested in the total energy which could be identified as edge wave energy of a particular type (either low mode or high mode), and added up only the peaks which existed on the edge wave

dispersion curves.

In both cases, only peaks which were considered significant by the Oltman-Shay criterion (see Chapter 3) and only the energy contained within the half-power wavenumber bandwidth were considered. Since the spectral estimator calculates wavenumber spectra separately for each frequency, the peaks are identified based on their half power bandwidth in wavenumber space. Oltman-Shay and Guza point out that the result of this is a conservative estimate of edge wave bandwidth because the average effect (or the effect of smoothing) of a true spectral peak which follows the edge wave dispersion curve almost diagonally through a frequency-wavenumber region (or pixel) will result in artificially wide peak.

In most cases during DELILAH, it is possible to identify specific peaks, in the longshore component of velocity spectra, which lie on the dispersion line for bar trapped edge waves, with the same definition of a peak as used in Oltman-Shay and Guza (1987) and Howd *et al.* (1991). Fortunately, in the cases we use for drift velocity calculations (October 16, 1990) the variance due to bar trapped edge waves is distinct because very little energy exists in regions of the spectrum above and below the line of bar-trapped edge waves (this is evident in Figure 3.12). In fact, October 16 was chosen because the diagonal line of variance due to bar trapped edge waves was very distinct. Assuming that all the energy lying on the bar-trapped dispersion line is attributable to bar-trapped edge waves, the variance contained in each of these peaks can be used to estimate the magnitude of induced boundary layer drift, at the location of the instrument array. Each pixel in the frequency-wavenumber plot represents the average variance density of a wave train with frequency and wavenumber values of that pixel. The amplitude of the waves in that pixel is then

$$\frac{1}{2}a^2 = \int_{k-\Delta k}^{k+\Delta k} \int_{f-\Delta f}^{f+\Delta f} h(f, k) df dk. \quad (4.43)$$

We use the term variance density rather than power spectrum to emphasize the assumptions made when estimating energy at a particular frequency (see Appendix). Using the peaks lying along one line, as Oltman-Shay and Guza have done, rather than attempting to sum energy in the whole region where edge waves exist (similar

to Howd *et al*), will minimize the energy from other sources mistakenly included in the bar-trapped total.

In order to use (4.42), the cross-shore shear is needed, which is clearly unavailable from data collected at only one cross-shore location. To solve this problem, the shear is numerically calculated using the correct topography and longshore current for October 16, and the frequency-wavenumber coordinate in the dispersion line which is closest in frequency-wavenumber space to the center of the spectral peak (for a peak to be acceptable as bar trapped variance, one part of that peak must contain the frequency-wavenumber coordinate within its half power band width). The implicit assumption is that the edge wave shape of that coordinate is representative of the entire peak. The assumption is to some extent unavoidable when associating model results (which are for a point in frequency-wavenumber space with infinitesimally small frequency-wavenumber area) and spectral estimates, where the peak has a finite width in frequency-wavenumber space (naturally occurring, or due to smoothing and uncertainties in the spectral techniques). This assumption is problematic when the dispersion curves of more than one mode exist close to, or within this peak. Though the dispersion curves are relatively more separated at bar-trapped mode frequencies and wavenumbers than at higher modes (Figure 3.7, in Chapter 2), confusion in identifying modes is not ruled out. To overcome this problem somewhat, three edge wave solutions are averaged, evenly spaced throughout each frequency band. The theoretical cross-shore shape of a mode can also change considerably within the confines of a particular peak, though bar-trapped modes with the simplest shapes have similar shapes, at least over the bar. If variance in a pixel in reality represents two peaks in close proximity, the result is obviously the average amplitude of the group. To obtain the average amplitude for a whole region, the variance must be summed first and then (4.43) used.

The outcome of numerically calculating a representative shape for each bar-trapped edge wave, is that the model results can be used to extrapolate the variance measured at the instrument location not only to make a prediction of variance over the bar, as

was roughly made in Chapter 3, but also to make a prediction of the drift velocities over the bar, and on either side of the bar. The estimate of drift velocity can only be a rough approximation due to the uncertainties inherent in the spectral estimators (the results early in the experiment have less errors than late in the experiment, as all the instruments were operational). However, given that these drift velocities may be a key link between edge waves and topographical features, some order of magnitude estimates are badly needed.

4.4.1 Patterns of boundary layer drift due to bar-trapped edge waves

Using the numerical calculations for an edge wave on depth and longshore current profiles observed during the DELILAH experiment, October 16, 1990, (4.42) are used to calculate the drift velocities associated with an edge wave trapped on a bar from the latter part of the experiment. Figure 4.3 shows the cross-shore profiles of cross-shore and longshore drift of five edge wave shapes (mode 0 to 4), all with phase speed approaching $\sqrt{gh'_{bar}}$. Since the drift velocity calculations are made assuming the boundary layer is small compared with the depth of the water, the solutions are unreliable near the shoreline.

For all the modes, except mode 0 (where the wave is not strongly affected by the bar), the longshore drift velocity is relatively large over the bar and in the direction of wave propagation. In most cases the drift was less than a millimetre per second. The cross-shore velocity was off-shore inside of the bar and on-shore on the seaward face of the bar, converging on top of the bar. In this case the drift was relatively large close to the shore, but the magnitude over the bar was very small (on the order of $10^{-5}m/s$). The mode 0 drift velocity was the only velocity which did not have a convergence on top of the bar, and was nearly always seaward.

In Figure 4.4 the drift velocities for the second asymptote approaching the $C \rightarrow \sqrt{gh_{bar}}$ limit (for example modes 4 and 5 in Figure 2.10 are plotted). The cross-shore drift converges on either side of the bar, but diverges strongly on top of the bar. The

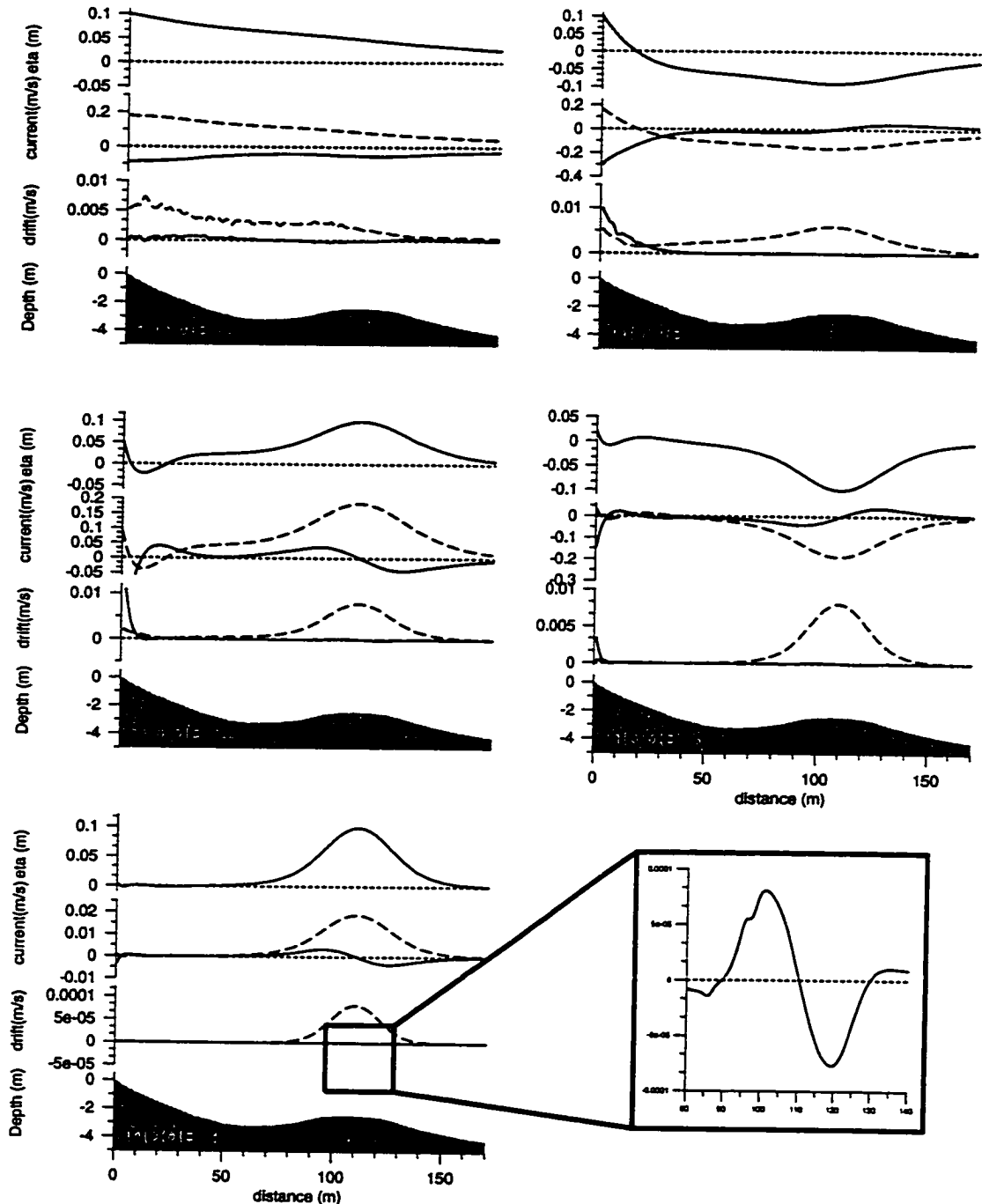


Figure 4.3: Each panel shows sea surface elevation at the top, u and v (dashed) components of orbital velocity at the middle top, u and v (dashed) drift at the bottom middle, depth at the bottom, for a mode 0,1,2,3,4 edge wave calculated with the DELILAH (October 16) depth and longshore current profiles. All values are calculated considering a maximum sea surface elevation of 10 cm. These modes lie along the first bar trapped asymptote.

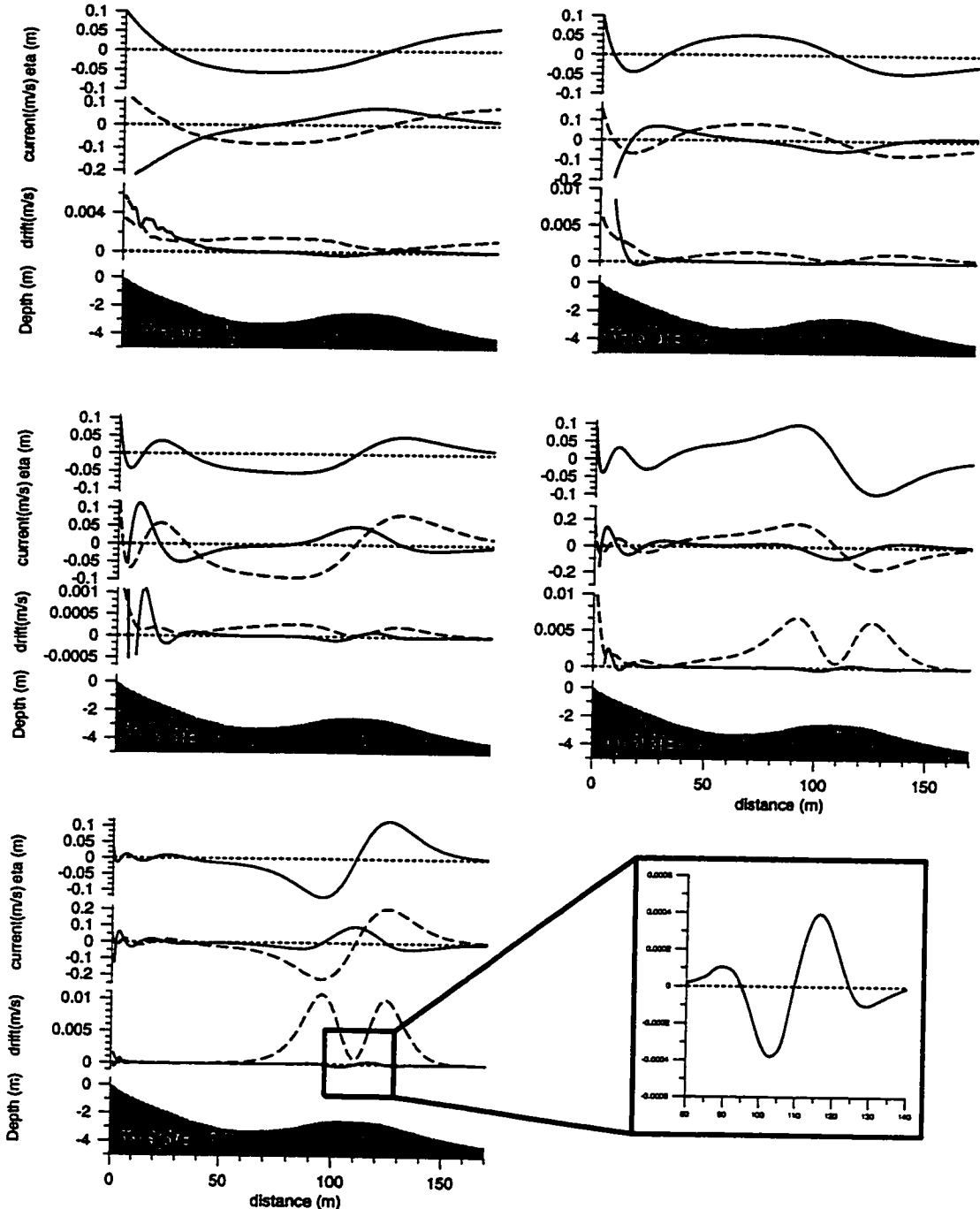


Figure 4.4: Each panel shows sea surface elevation at the top, u and v (dashed) components of orbital velocity at the middle top, u and v (dashed) drift at the bottom middle, depth at the bottom, for a mode 2,3,4,5,6 edge wave calculated with the DELILAH (October 16) depth and longshore current profiles. All values are calculated considering a maximum sea surface elevation of 10 cm. These modes lie along the second bar trapped asymptote.

longshore drift is large on either flank of the bar. Though the drift pattern is more complicated than that for the simplest bar-trapped shapes, there is still a general convergence near the bar (though not on top). If some of the more complex modes were part of the source of the bar-trapped variance in data, the estimates of drift would probably be over-predicted, but the drift would still converge in the general vicinity of the bar.

Though these drift velocities are very small, the modes in Figure 4.3 were selected as examples of the different shapes that exist on October 14. If the whole spectrum of bar-trapped edge wave drift is integrated, these waves may still cause a significant drift.

4.4.2 Magnitude of boundary layer drift during DELILAH

The strong diagonal line of variance in the frequency-wavenumber spectrum of October 16, 1990, is a good example of variance attributable to bar-trapped edge waves, which can be used to estimate the real size of the calculated solutions of edge waves. The amplitude derived from the longshore component of velocity variance peak (using (4.43)) is used to estimate the real size the calculated solutions for the longshore orbital velocity at the location of the instrument array.

Calculating the variance of peaks in the spectrum lying along the $C \rightarrow \sqrt{gh_{bar}}$ line from October 14, 1990 shows that the v component of variance of edge waves travelling from the north, contributes 16% of the total variance of the spectrum. Conversely the cross-shore variance contributes only 2% of the total variance over the whole spectrum. Some of the very low frequency peaks in the cross-shore spectrum are questionable, as they were wide enough to incorporate leaky wave energy. Only 5% of the total variance from the longshore component of velocity was due to waves travelling in the negative direction. There was no significant cross-shore variance travelling in the negative direction.

Figure 4.5 shows the distribution of variance with the frequency of bar trapped waves travelling both in the positive and negative directions. Note there are two

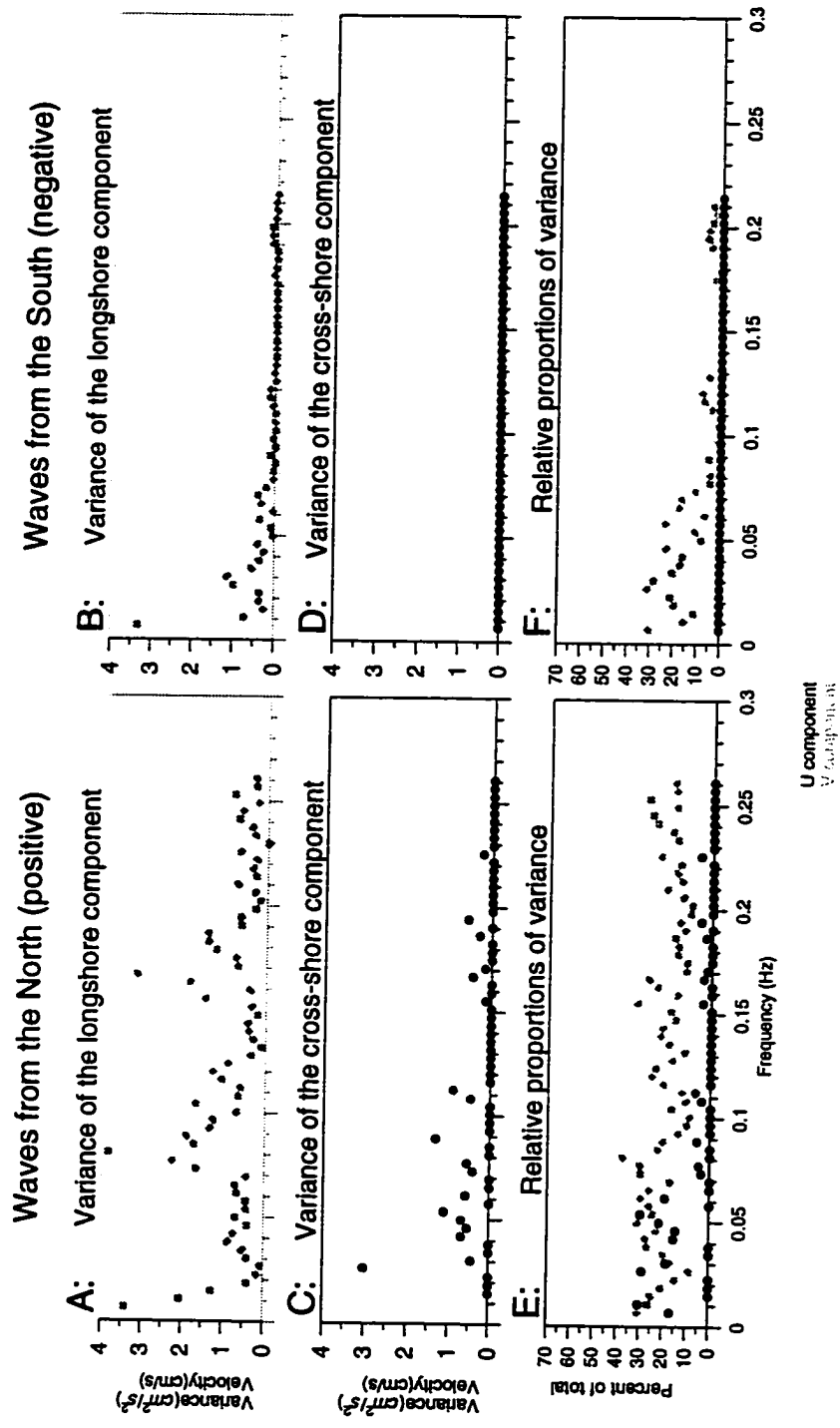


Figure 4.5: A-D: Total variance of peaks attributable to bar trapped waves along the diagonal line of variance in Figure 3.12, from October 16, at 4:00, high tide. E-F: percent of total variance of peaks attributable to bar trapped edge waves for the same peaks.

Figure 4.6: A: ratio of u amplitude to v amplitude (from model results) B-E: Values of cross-shore and longshore orbital velocities projected to locations at the shoreline and over the bar using from model results, which were normalized at the location of the array using the variances in Figure 4.5, from October 16, 4 am, high tide. Modes that are not amplified over the bar are theoretically extremely small at the location of the instrument array, so despite the averaging of several modes together, extrapolation to the shoreline of these modes will cause unrealistically high shoreline orbital velocities.

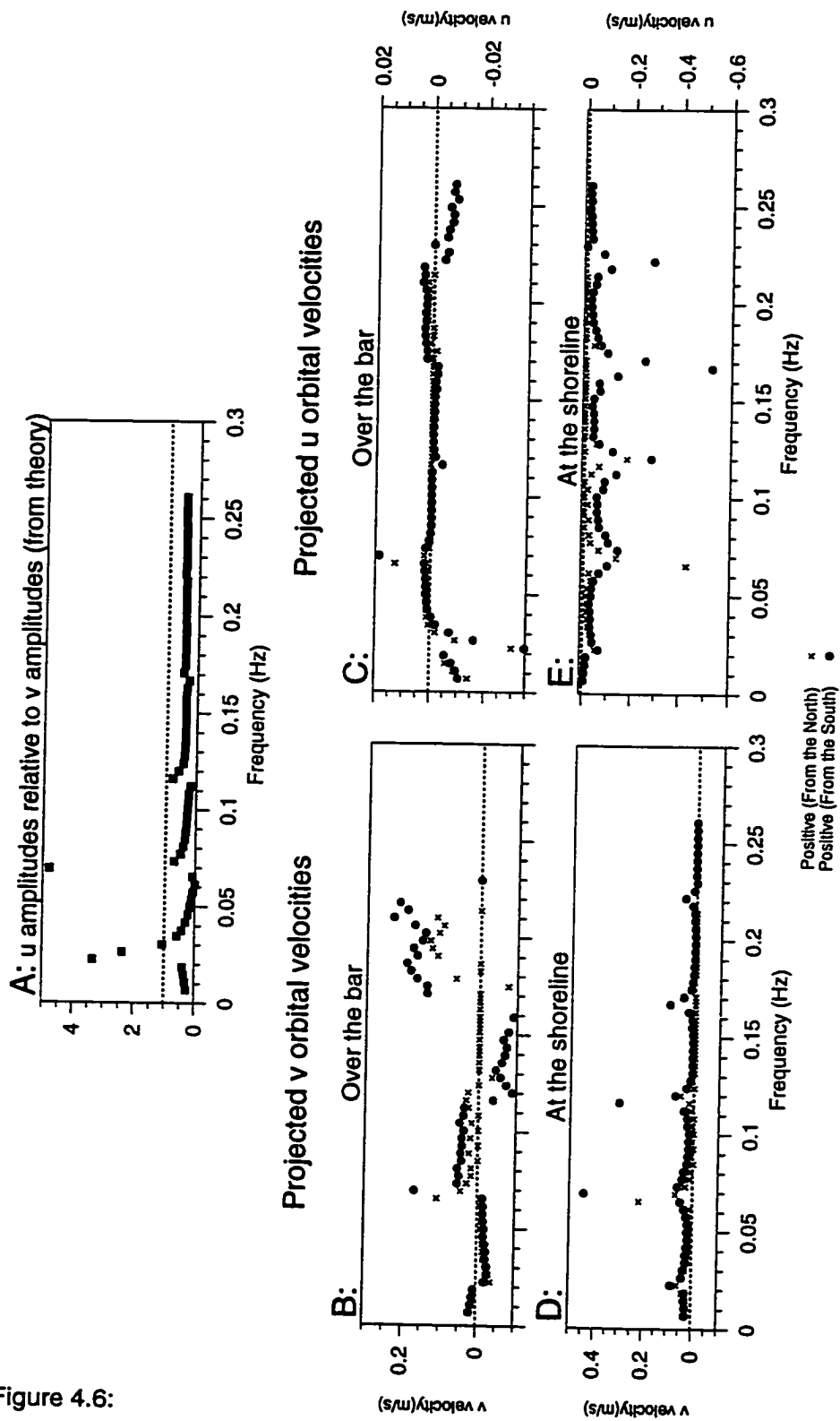


Figure 4.6:

peaks in the distribution of variance of the longshore component of velocity, which correspond to principal incident wave frequencies. As mentioned in Chapter 3, these peaks may be real, but also may be somewhat a result of leakage from the very energetic, incident wave frequencies.

Note in Figure 4.5, that the cross-shore component is significantly smaller than the longshore component. Model calculations show, that unless one is in close proximity to a node in the longshore component, the cross-shore component in bar-trapped edge waves is significantly smaller than the longshore component (Figure 4.6A), a property of bar-trapped edge waves which was introduced in Chapter 3. The smaller the secondary peak is relative to the incident waves, the more likely the signal is to be swamped by energy leaking from the more energetic peaks. Considering this and the problems in identifying lower frequency cross-shore peaks mentioned earlier, only the longshore spectra will be used to normalize the drift calculations.

Normalized model calculations can be used to extrapolate velocities to other parts of the beach profile. For example, Figure 4.6 B-E shows the projected magnitudes of the cross-shore and longshore orbital velocities over the bar and at the shoreline as a function of frequency (summed over each frequency band). The magnitude of longshore orbital velocity of the most amplified bar trapped waves, may reach a magnitude of 20cm/s over the bar, conversely the cross-shore component at high frequencies is very small over the bar, on the order of 1cm/s. However the opposite trend is expected at the shoreline. The v velocities are generally less than half a centimetre per second, whereas the cross-shore velocities can be on the order of 5cm/s. The extreme velocities shown at the shoreline are the product of extrapolating when the solution is close to a node at the instrument array. Despite averaging together several solutions within the frequency band, the variance attributed to these solutions is probably much too high. The higher frequency waves appear to be much larger over the bar relative to their value at the instrument array. Since the instrument array is at a location where calculations show that these high frequency waves should have decayed considerably, a small amount of noise at the instrument array will extrapolate

to cause a large signal over the bar. Therefore the values obtained at high frequencies should be viewed with caution.

Using the variance of the longshore component of velocity from Figure 4.5 to normalize the drift velocity calculations, the cross-shore and longshore drift velocities for waves travelling in the positive and negative directions are shown in Figure 4.7. At the location of the array, the longshore velocity is of the order of a half a millimetre per second, the cross-shore velocity is at least an order of magnitude less. Projecting the drift velocities to a location on top of the bar, the longshore drift for the most amplified waves could reach a magnitude of 3 cm/s. The cross-shore drift is symmetrical on either side of the bar as expected from Figure 4.3, with a maximum for the most amplified modes of around 1mm/s. Again, the higher frequency extrapolations are very sensitive to noise and should be viewed with caution. Though the projections depend on correctly identifying the mode of the bar trapped edge wave, the calculations of drift at the location of the instrument array only depend on model results for estimates of the cross-shore shear.

Though these drifts seem small, the combined effect of the normalized drift velocities for all the modes (not including interactions between modes,) calculated by summing the contribution from all frequency bands, gives a maximum drift near the bar which is on the order of 40cm/s in the longshore and 1-2cm/s in the cross-shore. This is clearly too large, probably because of the amplification of noise when extrapolating in the higher frequency bands, mentioned earlier. Summing the contribution of drift at the instrument array location, which should be less sensitive to noise, gives a total cross-shore drift of approximately 0.2mm/s and a total longshore drift of approximately 2mm/s. Clearly the drift over the bar should be larger and converge on top of the bar in the cross-shore, but the magnitude is difficult to determine from an instrument array located in the trough.

A cross-shore drift of 0.2mm/s may appear small, but if a parcel of water were to start at the velocity maximum on the side of the bar, it could travel to the center of the bar in a day or two. Considering that the frequency-wavenumber spectrum show

Figure 4.7: Drift velocities calculated using (4.42). The cross-shore shear and the projections of the longshore and cross-shore component of orbital velocity are calculated numerically, and all the first order velocities are normalized at the location of the array by the variance of the longshore component of orbital velocity in Figure 4.5, from October 16, 1990, 4am, high tide. A-B: at the instrument array. C-H: velocities projected to locations on either side of the bar, and on top of the bar.

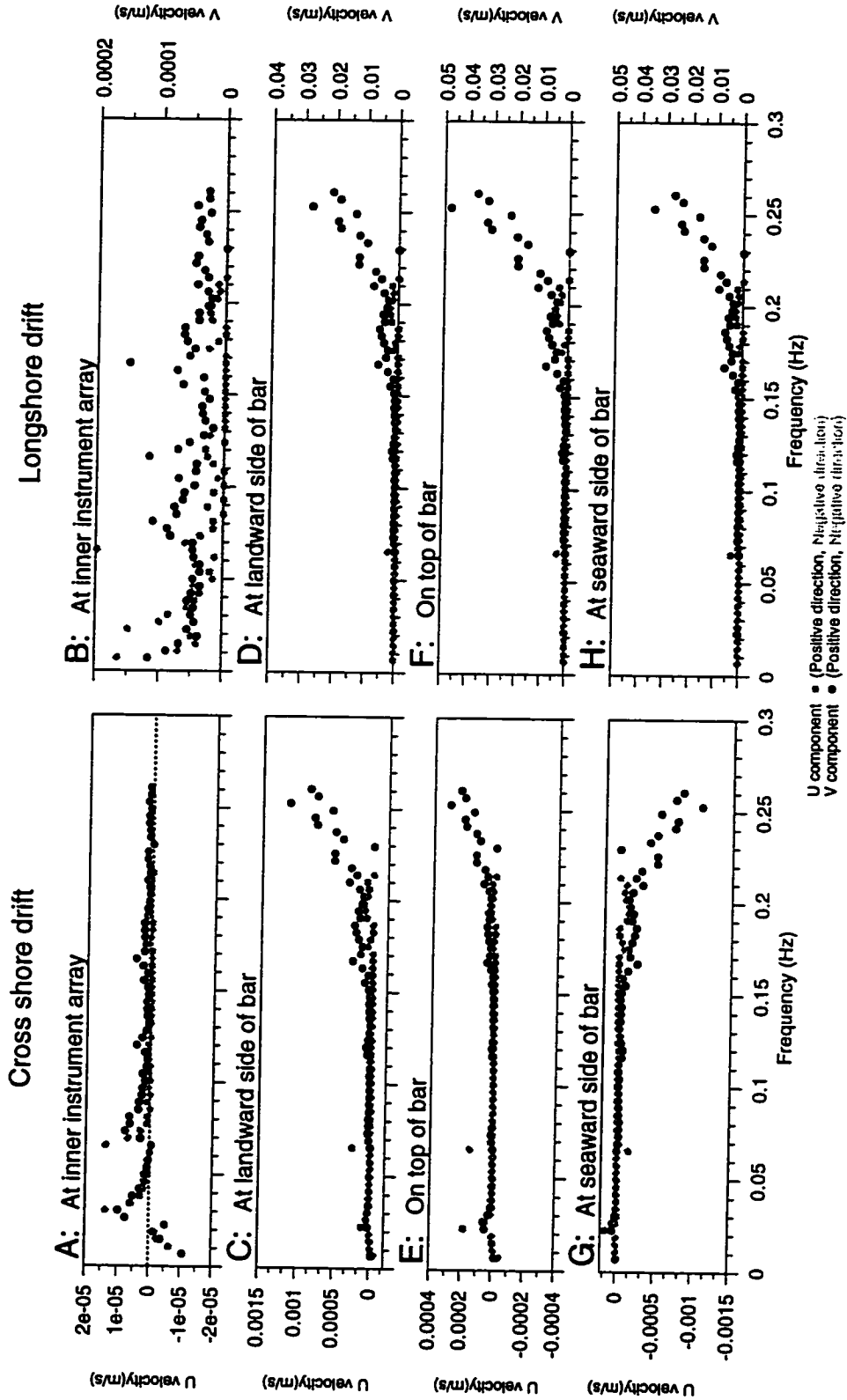


Figure 4.7:

bar-trapped waves existing for weeks at a time, the duration of the edge wave would probably leave enough time for sediment to accumulate at the node, if a significant portion of the sediment is in suspension at the top of the boundary layer. Determining the fate of a water parcel on the flank of a bar on a real beach is a far more difficult, since the bar-trapped edge wave drift is just one of many mean flows on the beach, for examples, the progressive incident wave causes a shoreward drift, there is a seaward drift due to undertow inside the surf zone and higher mode non-bar-trapped edge waves and leaky waves cause a drift which may not converge on the bar.

The actual response of sediment to the presence of a mean drift or a combination of mean drifts, is again even more complicated. The movement of sediment depends not only on the direction of transport (which depends on whether the sediment is transported as bedload or suspended load), but also on the erosion and deposition process. The laboratory evidence shown in Carter *et al* (1973) does give us confidence that depositions may occur under the anti-node of the standing wave, but to what degree the standing wave must dominate over the many other sources of mean flow to allow sediment to move to the antinode, remains to be studied.

4.5 Conclusions

Example calculations of the second order drift associated with a mode one edge wave, show that the longshore drift is similar to that of a progressive wave, but decays in the cross-shore direction. This Eulerian drift is partially induced by the bottom boundary layer, and partially by the surface virtual wave stress. In addition to the Eulerian contribution to the drift, there is Stokes' drift, related to the asymmetry in the wave orbital motion. The cross-shore drift, on the other hand, has no Stokes component, and no virtual stress. The drift is entirely induced by the bottom boundary layer. Though these calculations are for a mode 1 edge wave, calculations for higher modes can be done with the same method, as the general behaviour is dependent not on the cross-shore exponential structure of the wave, but on the phase relationships between

u,v, and w and how they are affected by the boundary layers. Clearly the results are not valid in very shallow water, where the boundary layer approaches the depth of the water.

Extending these results for a plane beach solution, using Hunt and Johns' 1963 formulation, to an edge wave on arbitrary topography and longshore currents, the observations from DELILAH shows that the amplification of the edge wave over the bar causes a strong longshore drift in the direction of edge wave propagation, and a cross-shore drift which is toward the bar, strong on either side of the bar and converges at the crest, at least for the bar-trapped waves with the simplest shapes.

Isolated peaks in frequency-wavenumber spectra of the longshore component of current measured at Duck, N.C. on October 14, have the same frequency-wavenumber coordinates as bar trapped edge waves, and can be used to estimate the real magnitude of theoretically calculated edge wave shapes. These calculations show that bar trapped edge waves may make up approximately 18 percent of the total variance of the longshore component of current measured at the location of the instrument array. Projections using calculated shapes show that the longshore component of orbital velocity due to bar trapped waves may be considerably larger over the bar. Conversely theoretical calculations suggest that the cross-shore component of orbital velocity due to bar trapped waves may be insignificant relative to the incident wave signal, except perhaps at the shoreline.

Normalized drift velocity calculations show that though the contribution to drift of each individual frequency band may be small, the integrated drift may be significant over the bar. A cross-shore drift of the magnitude predicted could cause movement of particles within the time frame of the duration of the edge wave. Unfortunately the predicted magnitudes over the bar are strongly influenced by extrapolating noise at high frequencies from the location of the instrument array. The only definite conclusion that can be drawn, is that the drift over the bar is likely to be significantly more than the drift at the instrument array. On days when the effective depth profile was strongly dominated by current, the location of the convergence underneath the

bar-trapped antinode would modulate with the tide. It is unclear where sediment would deposit on such a day.

A spectrum from October 16 was chosen to normalize calculations of drift velocity because the diagonal line of variance attributable to bar trapped edge waves was well defined and extended into higher frequencies. Choosing a particularly good day for bar trapped edge waves was necessary to minimize error in attributing spectral peaks to particular modes. Though the spectra in Chapter 3 show many days with diagonal lines of variance which were nearly as well defined as on October 16, these calculations should still be viewed as a best case scenario. The strong convergence behaviour of the cross-shore drift is less likely on days when the diagonal line of variance in spectra does not extend to high frequencies such as in Figure 3.12. Days with evidence of considerable energy from higher edge wave modes will have a more complicated pattern of drift, though the solutions which correspond to higher bar-trapped edge waves will still have convergences in the vicinity of the bar (Figure 4.4), (but divergences on the top of the bar).

Though these calculations are based on extrapolations from data which is from less than an ideal location, the results strongly suggest that the drift velocities associated with bar trapped edge waves may play an important role in maintaining the bar.

Chapter 5

Conclusions

5.1 Summary of ideas

Both the cross-shore shapes and dispersion relationships of edge waves which are affected by longshore currents and bars can significantly differ from those on plane beaches. The bars and longshore currents act as wave guides, and the edge wave solutions may be strongly amplified over the location of the bar, relative to their shoreline values. Field measurements of the longshore component of orbital velocity show that these bar-trapped solutions clearly exist, and may be the dominant edge wave shape near the bar.

Specific conclusions are:

1. Edge waves are trapped and amplified, relative to the shoreline, on longshore bars when the phase speed is between $\sqrt{gh_{\text{bar}}}$ and $\sqrt{gh_{\text{trough}}}$, with the extreme amplification occurring when phase speed approaches $\sqrt{gh_{\text{bar}}}$. The cross-shore shapes of edge waves change from sinusoidal to exponential when the water depth is greater than C^2/g ; amplification occurs when the cross-shore shape is sinusoidal close to the shore and on the bar and exponential in the trough and out to sea. Amplification is greater at higher frequencies, when the wave tends to exist separately on the bar. Beaches with large-scale, multiple bars, such

as Stanhope Beach, P.E.I., will have more amplified edge wave solutions than beaches with smaller scale bars such as Duck, N.C. and solutions will exist for each bar in turn, as the phase speed approaches $\sqrt{gh_{\text{bar}}}$ on each bar. These bar-trapped modes are quasi-non dispersive, a property which allows the longshore component of orbital velocity to be larger for higher modes and frequencies than on plane beaches.

2. On a beach with both longshore currents and bars, the degree of edge wave amplification depends on the strength and location of the longshore current shear relative to the steepness of the bottom slope, and also on the direction of edge wave propagation relative to the current. Weak longshore current shear, in particular over well developed bars, does not alter edge wave trapping over bars significantly, simply enhancing or reducing the existing bar-trapping effect. Conversely, strong current shears over gentle topography can govern the existence and location of edge wave trapping, the extreme example being edge wave trapping on plane beaches where the amplification is entirely due to the existence of mean longshore currents.
3. The most significant result presented here is the observation of bar-trapped edge waves. Spectral analysis of field data from two longshore instrument arrays, one in the trough, and one seaward of the bar, showed continuous, distinct, diagonal lines of variance, extending into incident wave frequencies. These lines of variance have the same frequency-wavenumber coordinates as theoretical calculations of bar-trapped edge waves, and changes in these lines can be predicted from the longshore current and depth profiles.
4. Instrument location, and detailed pictures of edge wave calculated solutions are extremely important when interpreting spectra. When the instrument array is on the top of the bar, the bar-trapped waves with the simplest shape are dominant, however when the array is further from the bar, more complex bar-trapped waves may dominate. In the latter case, the simplest bar trapped edge

waves will exist on top of the bar, but not be observed, if they have decayed to an insignificant size at the instrument location. Spectra measured at the shoreline and far seaward of the bar may show very little evidence of bar-trapping.

5. In cases where the effect of current shear is strong relative to the effect of bottom slope, the location of edge wave trapping changes as the the longshore current profile changes with the tide. When the bar is well defined, the longshore current shear is rarely strong enough to influence the existence or location of edge wave trapping, but could have an enhancing effect, at least at Duck, N.C.. While past work has suggested that edge waves, trapped and amplified on longshore currents, may cause bars to form on plane beaches, and bars to move on barred beaches, the DELILAH observations suggest that under most conditions, edge wave trapping on longshore currents is a subtle effect, modulated by sea level changes, and is unlikely to produce significant morphological change unless the current is very strong.
6. Though bar-trapped edge waves are unlikely to move bars or create bars, they may play a strong role in the growth or maintance of bars. The cross-shore drift velocity converges at or near the bar crest. Using variance data from DELILAH to estimate the real size of the drift velocity, shows this effect (not even including the between-mode contributions) is a minimum of a few millimetres per second on either side of the bar, and probably much larger. These bar-trapped modes can provide the spatially and temporally coherent flow patterns necessary to maintain an existing bar.
7. These results are also the first clear identification in field measurements of edge wave energy at incident wave frequencies. Edge waves at incident frequencies have always been theoretically plausible, but field studies have focused on edge waves at infra-gravity frequencies (Oltman-Shay and Guza, 1987; Howd *et al.*, 1991). As a consequence, there is minimal evidence of edge wave energy at periods below about 30s, at frequencies other than the subharmonic.

It is clear from these findings that the plane beach solutions are not even remotely adequate for modeling edge wave behaviour on barred beaches, except perhaps at low and high phase speeds. The DELILAH data shows that, at least near the bar, the dominant edge wave modes are bar-trapped. The potential contribution of bar-trapped edge waves to nearshore hydrodynamics needs to be addressed in all future studies of barred beaches.

5.2 Related research possibilities

The variability in the dominance of bar-trapped edge waves on different days during DELILAH, shows that the incident wave forcing plays an important role. Edge wave forcing theories have been studied sufficiently, that introducing bar-trapped edge wave solutions may not be too difficult. The existence of incident wave spectra during the DELILAH experiment and the possibility of identifying, to some degree, bar-trapped edge wave peaks in spectra, allows for the possibility of investigating the transfer of energy between incident wave and bar-trapped shapes in much more detail. There are many unanswered questions that can be addressed with such a model. For example, do bar-trapped edge waves have shapes which are optimal for transferring energy between incident waves and edge waves, as was suggested in Chapters 2 and 3? In view of their similarity of shape, phase and group speed, do bar-trapped edge modes exchange energy efficiently between themselves? For example, do the kissing points connecting bar-trapped solutions of different mode have any special properties (i.e. do they facilitate the transfer of energy between bar-trapped modes?). Finally there is also the unresolved issue of how edge waves are forced at incident wave frequencies, when traditional edge wave forcing theories are for edge waves at lower frequencies.

During the early part of DELILAH, the bar had some longshore variability. The calculated solutions for edge waves used a mean depth profile, which seemed adequate in identifying diagonal lines of variance, though there was some variability on the degree to which diagonal lines of variance matched calculated solutions. Though the

variability in fit may be partially an effect due to the instrument not being located on top of the bar, it may also be due to longshore variability. A potential project is the effect of longshore variability on edge wave solutions, both horizontal variability (for example crescentic bars), and vertical variability. It would seem reasonable that lower wavenumber solutions may respond to an average of the depth profile, because of their large cross-shore scales, whereas higher wavenumber, higher frequency solutions may follow the topography. Again, one would expect a $\sqrt{gh_{\text{bar}}}$ dependence as in the case of the one dimensional model.

There are numerous other possibilities: some examples are looking at the duration of different edge wave regimes versus the duration of incident wave conditions, looking at the edge wave drift in more detail by including between-mode interaction, also looking at the temporal variability in edge wave drift, especially the magnitude of drift during storms when the bar was observed to move seaward. Though bar-trapped waves have been clearly identified, longshore current-trapped waves have not been demonstrated to exist on plane beaches. The observations of edge waves on plane beaches in Oltman-Shay and Guza (1987) are at frequencies below $0.05Hz$, and some of the frequency-wavenumber spectra from their experiments, show evidence of what might be the lower part of a diagonal line of variance. Perhaps re-examination of some of these spectra in light of longshore current-trapped edge waves is in order.

Bar-trapping of edge wave has been demonstrated to be one of the dominant hydrodynamic processes in the neighbourhood of a bar on a barred beach, and since this is a new consideration, many interesting questions arise.

Appendix A

A.1 The maximum likelihood spectral estimator for a longshore array

Spectral estimators are needed to examine the directional distribution of wave energy, because the wave field is generally inadequately sampled in the spatial dimension. For example, during the DELILAH experiment the velocity is only sampled at six locations in the longshore direction. There are many ways to estimate the directional distribution of energy depending not only on the type, number and distribution of instruments, but also on the type of wave field that is being measured. To identify bar-trapped edge waves, the estimator must be able to distinguish edge wave energy from incident wave energy which can occur at the same frequency. The MLE (Maximum Likelihood Estimator) spectral estimator used in Chapter 3 is one of many kinds of spectral estimators. It has been chosen to examine the DELILAH data for bar-trapped edge waves, because past work has shown that it is very good at estimating wave energy in complex environments that have many waves, all of different spectral signatures (Huntley *et al.*, 1981; Oltman-Shay and Guza, 1984; Pawka 1983).

In general, spectral estimators work by modeling the frequency-wavenumber spectrum; they assume the spectrum at a given frequency (σ_w) is some weighted sum of cross spectra of the velocity time series (or sea surface elevation) between each instrument location in the longshore array. An example of the velocity time series from

each of the instruments is given in Figure A.1. This is the same as viewing the true spectrum through a window, which depends on the weighting and on the instrument spatial separation. The estimator assumes that some of the measured cross spectrum is due to energy of the wavenumber of interest (k_w), and some is due to random or statistical noise, and energy at wavenumbers other than the one of interest (k_{other}). The weighting function is then derived by minimizing the amount of noise and other energy included, and imposing the constraint that if there are no other contributions, the true spectrum must equal the estimated spectrum. An ideal window would be like a Dirac δ -function, which would only let energy through of the desired wavenumber. The result is an estimate of the energy distribution at a given frequency as a function of wavenumber. The estimate will have a strong peak at the true wavenumber(s), but also may have a number of low level peaks which are a result of energy leakage from the main peak. These occur because the window has a limited ability to remove the effect of energy at other wavenumbers. These low level peaks cannot be interpreted as real.

The MLE differs from other estimators because it uses the data to construct the window. This gives added information and consequently better estimates, but it makes the statistical properties (for example the error) difficult to characterize because they depend on the data. Thus, there is no way to determine the estimator behaviour for a particular instrument array, other than to perform numerous tests with synthetic spectra. This is an essential step in using this estimator with particular data sets. Since the estimator will create more peaks than exist in the data, the probability that a particular peak is real should be assessed in order to be confident in the results. Another problem of the MLE, the original version of the estimator, is that it flattens out the original peak. The IMLE is a recent addition which recovers some of the variance lost when the peak is flattened out by the MLE in a predictable manner.

In this appendix, the necessity of employing a such complex spectral estimator is demonstrated, the derivation of the estimator is briefly discussed, and finally the

results of a series of tests using synthetic spectra are summarized. The estimator has been tested with the DELILAH instrument array (since some of the resulting spectral estimates are published in Howd *et al.* (1991)); to judge the limitations of my conclusions, I have performed some of my own tests.

A.2 Some simple statistical properties of longshore array data

Before resorting to a complex spectral estimator, it is possible to derive information about the waves travelling in the along shore direction by examining the way in which the time series decorrelates between instruments in the alongshore array. The cross-correlation between instruments from the array at DELILAH on October 16, from Figure 3.12, shows several peaks that increase in lag as the spatial separation between instruments increases (Figure A.2). These peaks are consistent with the two incident wave peaks which travel at about 10m/s for the high frequency peak, and 20 m/s for the low frequency peak (marked on Figure A.2 with asterisks) and two bar-trapped edge wave peaks travelling at 5.9 m/s in the positive direction and 4.4m/s in the negative direction (marked on A.2 with bullets). These peaks are evidence of bar-trapped edge waves, but the distribution of bar-trapped energy with frequency is impossible to discern from the correlation coefficients. Note the low correlations between instruments.

It is also possible to examine the time series in the frequency domain. Calculating the coherence between instruments, shows some coherent energy at the expected incident wave frequencies (around 0.09Hz and 0.16Hz) but only at very small separations or spatial lags (Figure A.3). At low frequencies there are a number of low level peaks. Some of the nodes in the coherency suggest that longshore standing edge waves may exist. This is consistent with the frequency-wavenumber spectra, Figure 3.12, which would show a standing wave as two progressive edge waves going in the opposite directions. The phases between the instruments generally show a progressive trend

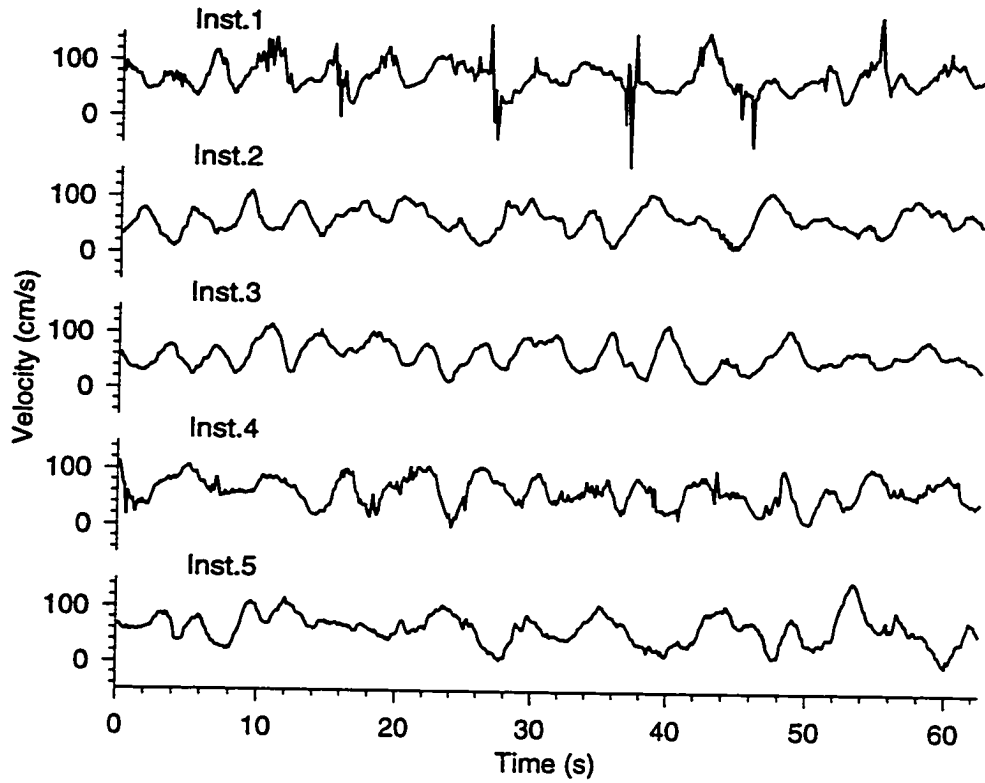


Figure A.1: Time series of the longshore component of orbital velocity from each sensor location on October 16, 1990, 4:00am

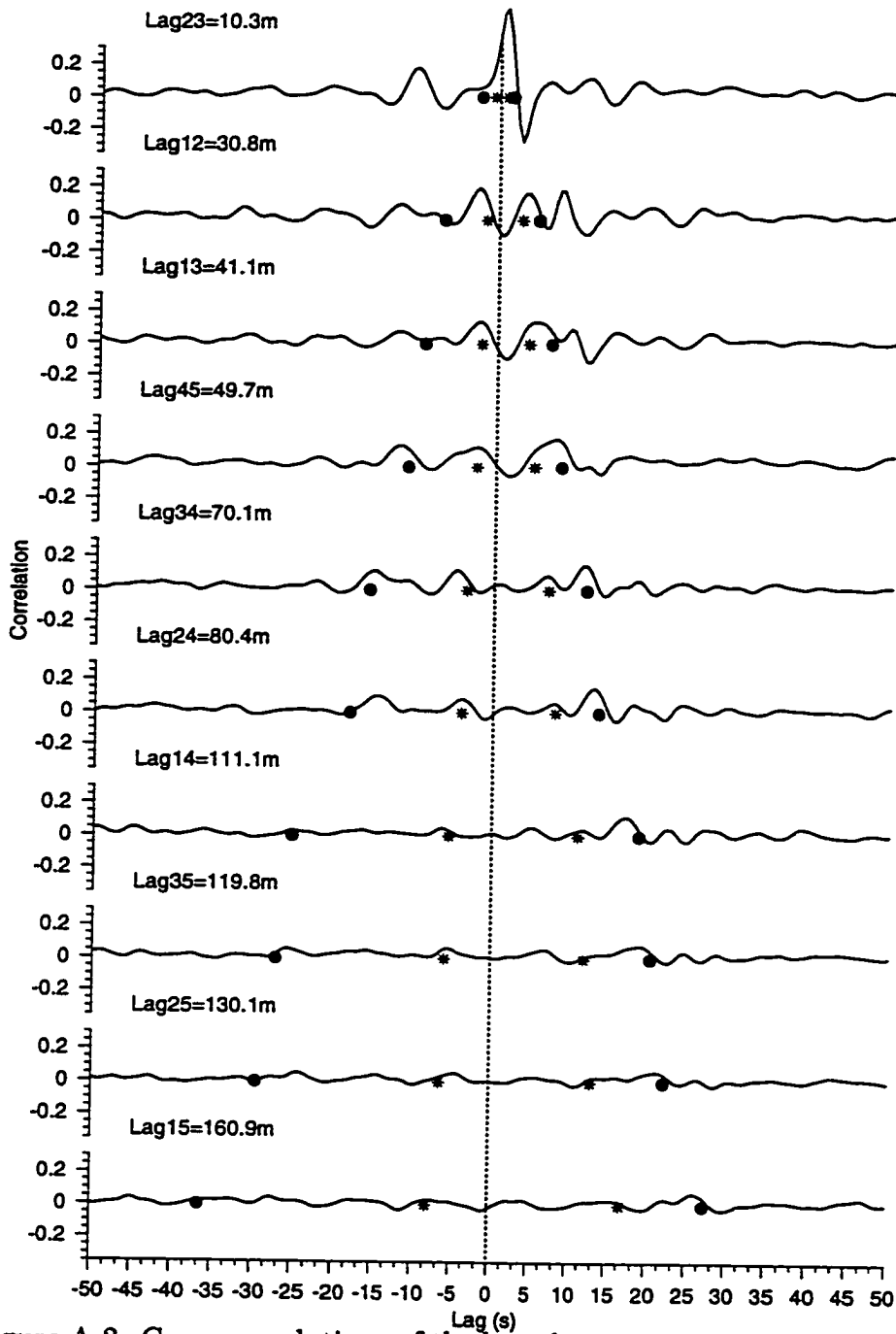


Figure A.2: Cross correlations of the longshore component of orbital velocity between all sensor combinations on October 16, 1990, 4:00am (same day as Figure 3.12). The time waves travelling at 5.9m/s in the positive and 4.4m/s in the negative take to propagate from sensor to sensor are marked with a bullet for scale. Waves travelling at 10m/s and 20m/s are marked with asterisks.

(in which phase changes linearly with frequency), with energy at higher frequencies progressing alongshore in one direction, and some energy at about 0.1 Hz progressing alongshore in the other direction (Figure A.4). In this case only the phases above the significance level are plotted. The progressive signal at high frequencies disappears quickly with spatial lag. At lower frequencies, the energy is again progressing alongshore in the same direction as the higher frequency energy. This energy could be edge wave energy. The phase relations at 0.1Hz are confused, possibly because there are edge waves and incident waves both at this frequency.

These approaches allow the main incident peaks to be identified, and the phase speed, and frequency measured. Unfortunately the secondary peaks (which are of interest here) are identifiable, but information about wavenumber is difficult to obtain because waves of several different wavenumbers exist at the same frequency. The necessity of resorting to a more complex spectral estimators, is evident.

A.3 The relationship between the frequency-wavenumber spectrum and the covariance.

A.3.1 Frequency-wavenumber spectrum

The frequency-wavenumber spectrum can be derived assuming that the wave is adequately sampled both in time and in space. In this case, a spectrum of one spatial dimension is derived (the longshore direction), because we will eventually use it to estimate the variance due to waves travelling in the longshore direction. However, extension to two or more dimensions is straight forward (Davis and Regier, 1977). A time-space series of a stochastic process can be represented as the inverse Fourier-Stieltjes integral of that series (by direct analogy to the representation of a times series given in Priestley (1981))

$$X(y, t) = \int_0^{2\pi} \int_{-\infty}^{+\infty} e^{i(ky - \sigma t)} dZ(k, \sigma) \quad (\text{A.1})$$

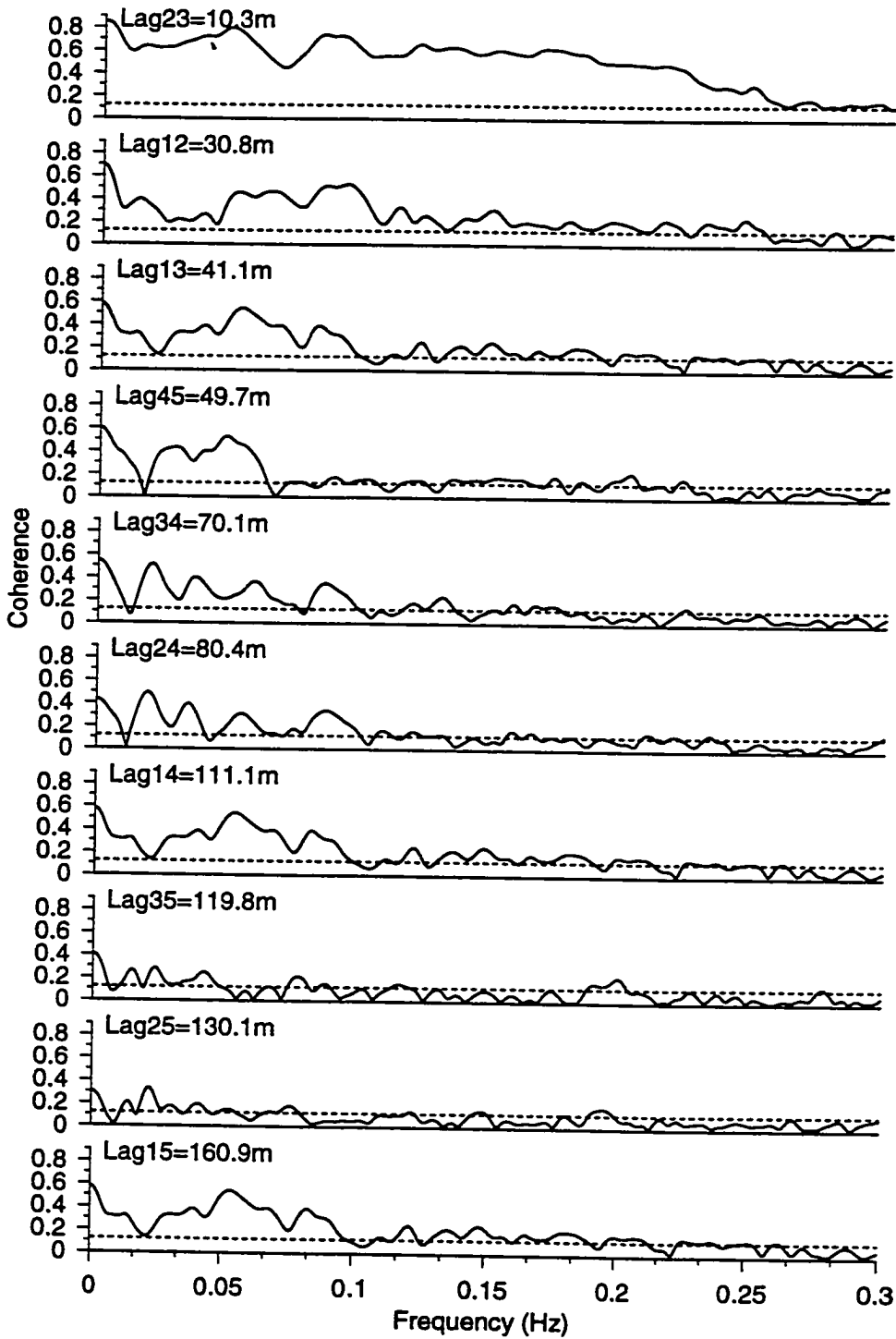


Figure A.3: The coherence of the longshore component of orbital velocity between all sensor combinations on October 16, 1990, 4:00am. Significance levels are marked with dashed lines.

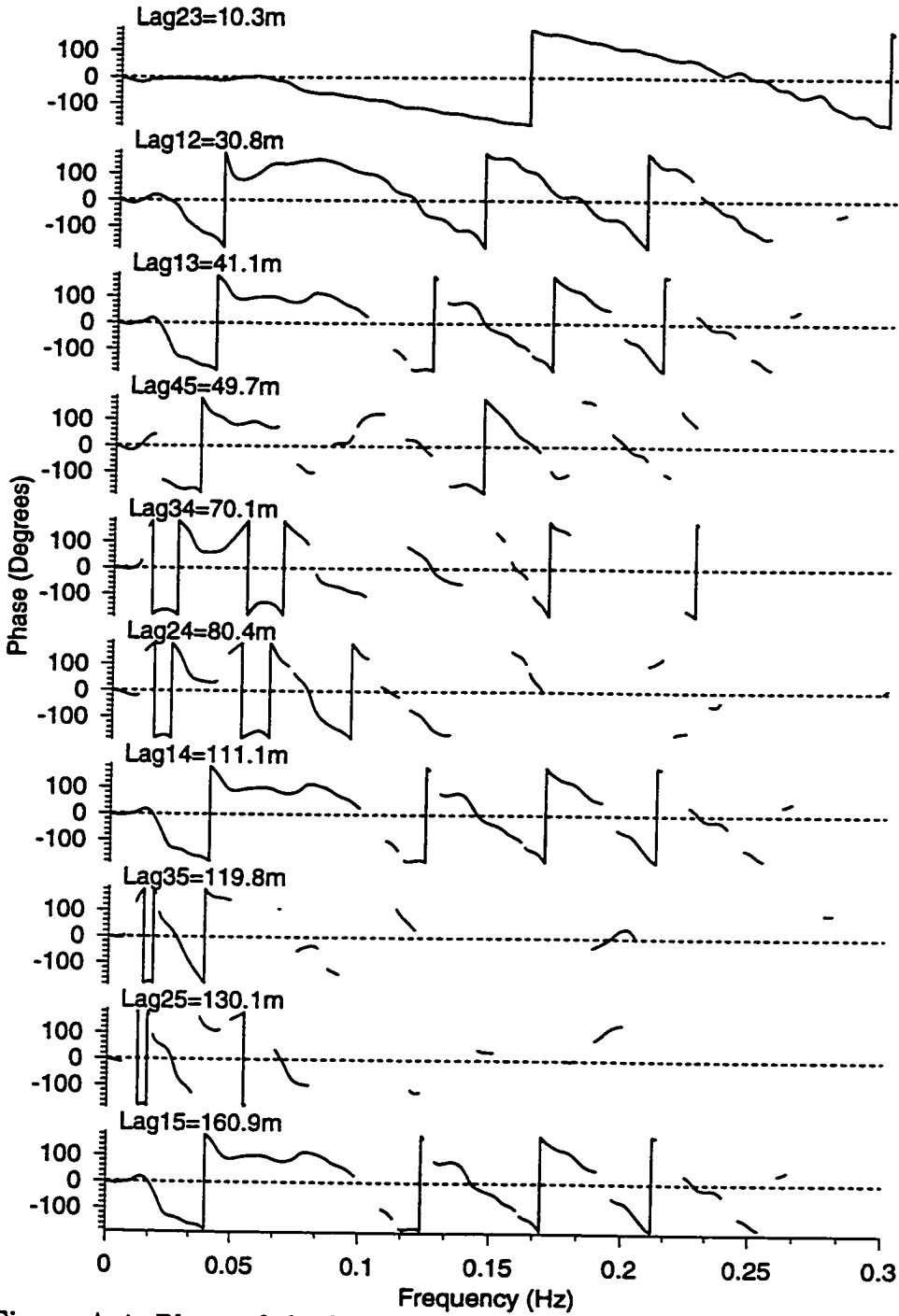


Figure A.4: Phase of the longshore component of orbital velocity between all sensor combinations on October 16, 1990, 4:00am. Only phases above the significance level are marked.

where the magnitude of $dZ(k, \sigma)$ is the roughly the amplitude of the component at frequency σ and longshore wavenumber k . Multiplying the space-time series, by the space-times series at time lag T and space lag Y and taking expectations, gives the covariance function $R(Y, T)$ as a function of the frequency-wavenumber power spectrum, $h(k, \sigma)$,

$$R(Y, T) = E[X(y, t), X(y + Y, t + T)] = \int_0^{2\pi} \int_{-\infty}^{+\infty} e^{i(-kY + \sigma T)} h(k, \sigma) dk d\sigma \quad (\text{A.2})$$

where

$$h(k, \sigma) dk d\sigma = E[dZ(k, \sigma), dZ^*(k, \sigma)] \quad (\text{A.3})$$

where $*$ is the complex conjugate. The inverse Fourier transform of (A.2) will give the frequency-wavenumber spectrum

$$h(k, \sigma) = \frac{1}{(2\pi)^2} \int_{-\infty}^{+\infty} \int_{-\infty}^{+\infty} e^{i(kY - \sigma T)} R(Y, T) dT dY. \quad (\text{A.4})$$

For random, white noise the frequency-wavenumber spectrum can be found by direct analogy to the frequency spectrum derived in Priestley (1981, p234)

$$h_N(k, \sigma) = \frac{1}{(2\pi)^2} \int_{-\infty}^{+\infty} \int_{-\infty}^{+\infty} e^{i(kY - \sigma T)} \delta(Y) \delta(T) s_N^2 dt dY = \frac{s_N^2}{2\pi^2} \quad (\text{A.5})$$

where s_N^2 is the variance of the noise, and δ is the Kronecker-delta function. For the case where the signal is a deterministic harmonic process $X(y, t) = a_w \cos(k_w y - \sigma_w t)$, there is a problem because the covariance function does not disappear for infinite lag, and the integral in (A.4) is infinite. This follows from $h(k, \sigma)$ in (A.2) being the power spectral density, or the power per unit wavenumber, per unit frequency, so if the unit of wavenumber tends to zero then the power tends to infinity. Priestley (1981, p242) shows that if one assumes that the measurements have a finite maximum spatial lag, we can represent the spectrum of a wave as the amplitude times a delta function in the same way as the covariance of random noise was represented (A.5). By direct analogy to the frequency spectrum given in Priestley, the frequency-wavenumber spectrum of a harmonic process is

$$h(k_w, \sigma_w) = \frac{a_w^2}{2} \delta(\sigma - \sigma_w) \delta(k - k_w) \quad (\text{A.6})$$

so that $a_w^2/2$ is the variance of the wave. For practical purposes, we can define the total amplitude of waves with wavenumber and frequency between $\sigma_w \pm \Delta\sigma, k_w \pm \Delta k$ as the total power contained in a small bandwidth $\Delta\sigma, \Delta k$ over which the power spectral density does not change appreciably

$$\frac{a_w^2}{2} \approx h(k_w, \sigma_w) \Delta\sigma \Delta k \quad (\text{A.7})$$

A.3.2 Cross-spectral matrix

In practice, we cannot calculate the inverse Fourier transform to get the frequency-wavenumber spectrum in (A.4), because we have inadequate spatial lags. What we can get is the cross-spectrum between different instrument locations which can be defined from (A.2) as

$$M(Y, \sigma) = \int_{-\infty}^{+\infty} e^{-ikY} h(k, \sigma) dk \quad (\text{A.8})$$

so

$$R(Y, T) = \int_0^{2\pi} M(Y, \sigma) e^{i\sigma T} d\sigma.$$

The cross spectrum can also be defined as the inverse Fourier transform of the covariance function

$$M(Y, \sigma) = \frac{1}{2\pi} \int_{-\infty}^{+\infty} e^{-i\sigma T} R(Y, T) dT.$$

$M(Y, \sigma)$ can be roughly interpreted as the spatially-lagged covariance function at a particular frequency. So if one had a very large number of closely spaced lags, one could sum all the components of the estimated cross-spectral matrix at a particular frequency σ_w , weighted by $e^{ik_w Y_i}$ to get the estimate of the frequency-wavenumber spectrum at a particular frequency σ_w and wavenumber k_w .

$$\hat{h}(\sigma_w, k_w) = \frac{1}{2\pi} \left[M(\sigma_w, Y_1) e^{ik_w Y_1} + M(\sigma_w, Y_2) e^{ik_w Y_2} + M(\sigma_w, Y_3) e^{ik_w Y_3} + \dots \right]$$

However, since you have very few lags in practice, you would get a very bad estimate. This is where a spectral estimator is needed.

A.4 Derivation of the maximum likelihood estimator

When deriving the estimator, the spectrum is assumed to have so much better resolution in the frequency dimension, than in the wavenumber dimension, as to have nearly perfect frequency resolution. The derivation here follows the derivation given in Davis and Regier (1977), but for an array in one dimension only. I have also put their derivation of the MLE in matrix notation.

Let us assume there are N spatial lags available in the instrument array. This will result in N estimates of the cross spectral matrix. At any one frequency σ_w , these must be made up of the energy at the desired wavenumber k_w plus the energy from other wavenumbers and some noise

$$\begin{aligned}\hat{M}(Y, \sigma_w) &= M(Y, \sigma_w) + q_N(Y, \sigma_w), \\ &= M_w(Y, \sigma_w) + M_{other}(Y, \sigma_w) + q_N(Y, \sigma_w)\end{aligned}\tag{A.9}$$

where $\hat{\cdot}$ means estimate. We assume that the estimate is unbiased, in that

$$E[q_N(Y, \sigma_w)] = 0, \quad E[\hat{M}(Y, \sigma_w)] = M(Y, \sigma_w).\tag{A.10}$$

Since M is like a covariance function, there are some combinations of spatial lag that give greater percentages of our desired wavenumber, k_w , and though we do not know the contribution from other wavenumbers, k_{other} , we do know the lags which the contribution from the desired wavenumber will be largest. Therefore is sensible that the estimator be constructed by adding up the cross spectral matrices unevenly, or by taking the weighted average

$$\hat{h}(\sigma_w, k_w) = \sum_{i=1}^N w_{Y_i}(k_w, \sigma_w) \hat{M}(Y_i, \sigma_w).\tag{A.11}$$

For simplicity, the notation will be changed to represent the spatial lag as subscript mn , rather than $(Y_i) = (y_n - y_m)$, where n and m are the indices of the each instrument, and dropping the reference to σ_w as the estimate is done on a frequency by

frequency basis. In this case (A.11) will be

$$\hat{h}(k_w) = \sum_{mn=1}^N w_{mn}(k_w) \hat{M}_{mn}. \quad (\text{A.12})$$

My interpretation of M_{mn} from (A.12), considering (A.6), is that it is roughly equal to

$$M_{mn} = \frac{a_w^2}{2} e^{ik_w Y_{mn}} + \frac{a_{\text{other}}^2}{2} e^{ik_{\text{other}} Y_{mn}} + \delta(Y_{mn}) s_N^2 \quad (\text{A.13})$$

from which one can directly see that some lags will have greater proportions of a_w^2 than other lags (but this assumes that all the energy is due to plane waves and that all the noise is uncorrelated between instruments).

On average, since the estimates are assumed to be unbiased, A.12 becomes

$$E[\hat{h}(k_w)] = \sum_{mn=1}^N w_{mn}(k_w) M_{mn}. \quad (\text{A.14})$$

Substituting A.8 into A.14

$$E[\hat{h}(k_w)] = \sum_{mn=1}^N w_{mn}(k_w) \int_{-\infty}^{+\infty} h(k) e^{-ik Y_{nm}} dk, \quad (\text{A.15})$$

$$= \int_{-\infty}^{+\infty} W(k_w, k) h(k) dk, \quad (\text{A.16})$$

$$W(k_w, k) = \sum_{mn=1}^N w_{mn}(k_w) e^{-ik Y_{mn}}. \quad (\text{A.17})$$

W is the window with which we look at our real spectrum. Ideally, our window should look like a Dirac δ -function and only let energy pass from the true spectrum to the estimated spectrum when $k = k_w$. Though we may not quite be able to accomplish this with our choice of weights w_{mn} , we can minimize W subject to the constraint that it must equal 1 at $k = k_w$. This is the same as minimizing the contribution of energy from all other wavenumbers. This is one of the main forms of estimator commonly used, and it deals only with creating a suitable window W . It is called an *a priori* estimator, because the window can be designed before the data is collected.

To illustrate this, Figure A.5 shows a schematic of the types of window that would result from three array geometries and a window constructed by minimizing

$$\int_{k=-\pi}^{k=\pi} W^2(k_w, k + k_w) dk \quad (\text{A.18})$$

subject to constraint

$$W(k_w, k_w) = 1 \quad (\text{A.19})$$

according to Davis and Regier (1977). The different windows shown in Figure A.5, which correspond to different array geometries, let some energy in at the wrong wavenumbers k_{other} , with the amount dependent on the geometry of the array.

Another way of estimating $\hat{h}(k_w)$ in (A.16) is to minimize the cross spectrum and the weights at the same time. Conceptually, this is logical, because what is the sense in having a window which takes out the effect of energy from the wrong wavenumber k_{other} , when there is no energy at that particular wavenumber? This method is called data adaptive, because it uses the data to design the window, in that it attempts to minimize the weights only at the wavenumbers where the spectrum is significant. The constraint is then that the measured spectrum multiplied by the weights should equal the true spectrum at $k = k_w$. It is an *a posteriori* method, because in order to calculate the weights, the cross spectrum must already be measured. Minimizing the noise and the signal simultaneously assumes that the magnitude of the noise is proportional and distributed in the same way as the signal.

In order to design an estimator of this type, some assumptions are made (Davis and Regier, 1977). First of all, assume that the measured spectrum is a single plane wave embedded in noise and signal from other waves

$$h(k_w) = \delta(k - k_w)E(k_w) + h_N(k) \quad (\text{A.20})$$

where $E(k_w)$ is the variance of the plane wave, and is equal to $a_w^2/2$. Though the notation gives the representation of both the plane wave and the noise as continuous spectra, this is in essence the problem discussed in Priestley, Chapter 8, of a mixed

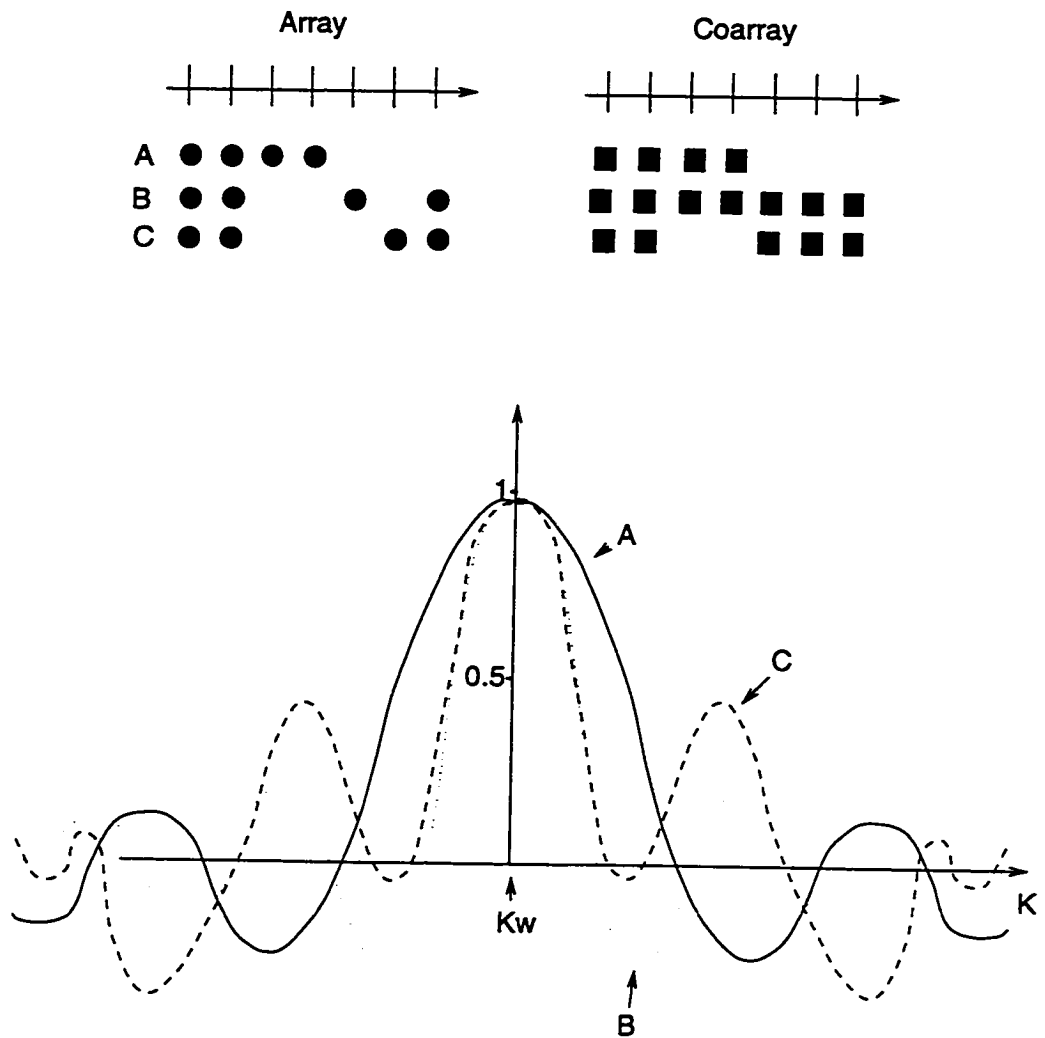


Figure A.5: Schematic of the windows that would be derived from several different array geometries of the same number of windows, after Davis and Regier (1977).

spectrum, or a discrete spectrum (the signal) embedded in a continuous spectrum (the noise). My interpretation of $h_N(k)$ is that it equals $\frac{a_{other}^2}{2}\delta(k - k_{other})$. The assumption is that the estimated spectrum $\hat{h}(k_w)$ will be the variance of a plane wave of wavenumber k_w , so that

$$\hat{h}(k_w) = \hat{E}(k_w)\delta(k - k_w) = \sum_{nm=1}^N w_{nm}(k_w)M_{nm}, \quad (\text{A.21})$$

where M_{nm} is the measured cross-spectrum between instruments.

Since the estimate is an amplitude squared, then the weights must be factorable (Davis and Regier, 1977). (The amplitude is then a linear combination of the Fourier transforms from each instrument location). Factoring these weights gives

$$\sum_{nm=1}^N w_{nm}(k_w) = \sum_{n=1}^M \sum_{m=1}^M w_n(k_w)w_m^*(k_w) = \sum_{m=1}^M w_m(k_w) \sum_{n=1}^M w_n^*(k_w) \quad (\text{A.22})$$

where M is the total number of instruments in the array, and w^* is the complex conjugate of w , and $|w_n(k_w)| = |w_n^*(k_w)|$. The estimated spectrum is then

$$E[\hat{h}(k_w)] = \sum_{n=1}^M \sum_{m=1}^M w_n(k_w)w_m^*(k_w)M_{nm}. \quad (\text{A.23})$$

Incorporating (A.20) in (A.23) gives

$$E[\hat{h}(k_w)] = E(k_w)\delta(k - k_w)W(k_w, k_w) + \int_{-\infty}^{+\infty} W(k_w, k)h_N(k)dk, \quad (\text{A.24})$$

$$W(k_w, k) = \left| \sum_{n=1}^M w_n(k_w)e^{iky_n} \right|^2. \quad (\text{A.25})$$

The essence of this type of estimator is that both the window and the measurement are minimized (A.23), subject to the constraint that if there are no other waves present, then the estimated amplitude should equal the true amplitude, or that $W(k_w, k_w) = 1$. This is equivalent to saying

$$\sum_{m=1}^M w_m(k_w)e^{ik_w y_m} = \sum_{n=1}^M w_n^*(k_w)e^{-ik_w y_n} = 1. \quad (\text{A.26})$$

To minimize (A.23) with a constraint, the method of Lagrange multipliers is used (see Arfkin, 1985). The method combines the constraint (A.26) and the function to be

minimized (A.23) using the Lagrange multiplier λ , as follows (dropping the reference to wavenumber, as (A.27) and (A.28) deal only with k_w)

$$\lambda \left[1 - \sum_{n=1}^N w_n e^{ik_w y_n} \right] = 0, \quad (\text{A.27})$$

$$E \left[\hat{h}(k_w) \right] = \sum_{n=1}^N \sum_{m=1}^N w_m w_n^* M_{nm} + \lambda \left[1 - \sum_{n=0}^N w_n e^{ik_w y_n} \right] = 0. \quad (\text{A.28})$$

This function is minimized by setting the derivative with respect to all the weights to zero, and solving for the estimated spectrum. Moving to matrix notation, and dropping the expectation, for simplicity (A.28) becomes

$$\hat{h}(k_w) = \mathbf{w}^T \mathbf{M}^T \mathbf{w}^* + \lambda \left[1 - \mathbf{w}^T \mathbf{G} \right] = 0 \quad (\text{A.29})$$

where $\mathbf{w}^T = (w_1, w_2, w_3 \dots)$, $\mathbf{M} = (M_{1n}, M_{2n}, \dots)$ (\mathbf{M} is a matrix) where $n = 1, 2, 3 \dots$ and $\mathbf{G}^T = (e^{ik_w y_1}, e^{ik_w y_2}, \dots)$. The minimization takes the form

$$\frac{\partial \hat{h}(k_w)}{\partial \mathbf{w}_R} = 0, \quad (\text{A.30})$$

$$\frac{\partial \hat{h}(k_w)}{\partial \mathbf{w}_I} = 0$$

where

$$\mathbf{w} = \mathbf{w}_R + i \mathbf{w}_I. \quad (\text{A.31})$$

So that

$$\mathbf{w}^T \mathbf{M} \mathbf{w}^* = \mathbf{w}_R^T \mathbf{M} \mathbf{w}_R + \mathbf{w}_I^T \mathbf{M} \mathbf{w}_I + i \mathbf{w}_R^T \mathbf{M} \mathbf{w}_I - i \mathbf{w}_I^T \mathbf{M} \mathbf{w}_R. \quad (\text{A.32})$$

Performing the derivatives in (A.30)

$$\frac{\partial \hat{h}(k_w)}{\partial \mathbf{w}_R} = \mathbf{M} \mathbf{w}_R + \mathbf{M}^T \mathbf{w}_R + i \mathbf{M} \mathbf{w}_I - i \mathbf{M}^T \mathbf{w}_I - \lambda \mathbf{G} = 0, \quad (\text{A.33})$$

$$\frac{\partial \hat{h}(k_w)}{\partial \mathbf{w}_I} = \mathbf{M} \mathbf{w}_I + \mathbf{M}^T \mathbf{w}_I - i \mathbf{M} \mathbf{w}_R + i \mathbf{M}^T \mathbf{w}_R - i \lambda \mathbf{G} = 0. \quad (\text{A.34})$$

Using (A.31) to write these more succinctly

$$\mathbf{M}\mathbf{w} + \mathbf{M}^T\mathbf{w}^* = \lambda\mathbf{G}, \quad (\text{A.35})$$

$$\mathbf{M}\mathbf{w} - \mathbf{M}^T\mathbf{w}^* = -\lambda\mathbf{G}. \quad (\text{A.36})$$

These can be combined in one equation by subtracting (A.36) from (A.35) and dividing by two, which gives

$$\mathbf{M}^T\mathbf{w}^* = \lambda\mathbf{G}. \quad (\text{A.37})$$

Multiplying this results by \mathbf{w}^T gives

$$\begin{aligned} \mathbf{w}^T\mathbf{M}^T\mathbf{w}^* &= \mathbf{w}^T\lambda\mathbf{G}, \\ &= \lambda\mathbf{w}^T\mathbf{G}. \end{aligned} \quad (\text{A.38})$$

From our original equations and constraint respectively, we know the left hand side of this equation is $\hat{h}(k_w)$ and the right hand side of this equation is just λ , so if we solve for λ , we have our minimized estimate of the spectrum.

$$\begin{aligned} \mathbf{M}^T\mathbf{w}^* &= \lambda\mathbf{G}, \\ \mathbf{M}^{-T}\mathbf{M}^T\mathbf{w}^* &= \lambda\mathbf{M}^{-T}\mathbf{G}. \end{aligned}$$

Multiplying by \mathbf{G}^{*T}

$$\begin{aligned} \mathbf{G}^{*T}\mathbf{w}^* &= \lambda\mathbf{G}^{*T}\mathbf{M}^{-T}\mathbf{G}, \\ \mathbf{w}^{*T}\mathbf{G}^* &= \lambda\mathbf{G}^T\mathbf{M}^{-1}\mathbf{G}^*, \\ &= \mathbf{w}^T\mathbf{G} = 1. \end{aligned}$$

where the rule $(AB)^T = (B^T A^T)$ has been used. So finally

$$\lambda = \hat{h}(k_w) = [\mathbf{G}^T\mathbf{M}^{-1}\mathbf{G}^*]^{-1}. \quad (\text{A.39})$$

The estimator performance is strongly a function of \mathbf{G} or the instrument lag e^{ikY} . Since the data is needed to derive the estimator, it is impossible to determine the capability of the estimator in any general sense.

Since the estimator does not conserve the total variance in the spectrum (therefore in practice you cannot retrieve the coherence between sensors from the final estimate), it is necessary to use the Iterative Maximum Likelihood Estimator (IMLE). The IMLE has been proven by Pawka (1983), and Oltman-Shay (1985) to be an improvement on the MLE, because it more closely approximates the total theoretical variance.

Davis and Regier (1977) discuss the fundamental problem with maximum likelihood estimators, which is that they are approximating a continuous spectrum with discrete values of variance. In practice, the variance is smoothed over the whole frequency-wavenumber domain, to give a reasonable approximation of the continuous spectrum, but conceptually this is problematic. For this reason, the power spectra are normally referred to as variance density plots in the literature. Attempts have been made to address this problem, by using a constraint which consists of the integral of the weight over a small wavenumber bandwidth being equal to one, in which case the spectrum is the sum variance of waves contained in a small band width around k_w .

A.5 The iterative maximum likelihood estimator

Every time the true spectrum is passed through the spectral window A.39 to get the estimated spectrum, some of the total variance is lost. Pawka (1983) hypothesized that adding some adjustment term ϵ on the the first estimate $\hat{h}_o(k_w)$ of the true spectrum h and re-passing it through the spectral window will give a new estimate $\hat{T}_1(k_w)$. If $\hat{T}_1(k_w) \approx \hat{T}_o(k_w)$, this must mean that we can retrieve the true spectrum by adding the adjustment ($\hat{T}_o(k_w) \approx h$). Of course it takes many tries or iterations to get the adjustment right; in each case, i , the new $\hat{h}_i(k_w)$ is set equal to $\hat{T}_{i-1}(k_w)$ and re-passed through the window. The adjustment used each time will depend on if

$\hat{T}_i(k_w)$ is greater or smaller than $\hat{h}_o(k_w)$ so

$$\epsilon_i(k_w) = f \left[\hat{h}_o(k_w) / \hat{T}_{i-1}(k_w), \hat{h}_{i-1}(k_w) \right] \quad (\text{A.40})$$

Pawka [1983] derived a suitable form for $\epsilon(\alpha)$.

$$\epsilon_i(k_w) = \frac{|\lambda|^{\beta+1} \hat{h}_{i-1}(k_w)}{\lambda \gamma} \quad (\text{A.41})$$

$$\lambda = 1.0 - (T_{i-1}(k_w) / \hat{h}_o(k_w)) \quad (\text{A.42})$$

To analyse the DELILAH data, $\beta = 1$, $\gamma = 5$ and 50 iterations were used, according to Pawka's (1983) suggestions.

A.6 Limitations of the iterative maximum likelihood estimator

Tests on the spectral estimator with the array geometry used at DELILAH reveal some limitations. These tests were performed on five sensors, as one sensor broke during the storm halfway through the experiment. Using the sixth sensor improves the results shown here considerably. Also the synthetic spectral peaks used in these tests, have small wavenumber bandwidths. So these synthetic tests should be viewed as worst-case scenarios. The estimator was tested using i) noise ii) unimodal signal at different wavenumbers and frequencies iii) bimodal sigma a) the same wavenumber and different frequencies b) at the same frequency and different wavenumbers iv) the signal of October 16, 1990 in which the phases have been randomized, but the amplitudes are the same.

A.6.1 Uni-modal peak

At most frequencies and wavenumbers the estimator reproduced the peak well. Some multiple secondary peaks, spread out over wavenumber space, were produced at the same frequency. These secondary peaks were much smaller and clearly discernible

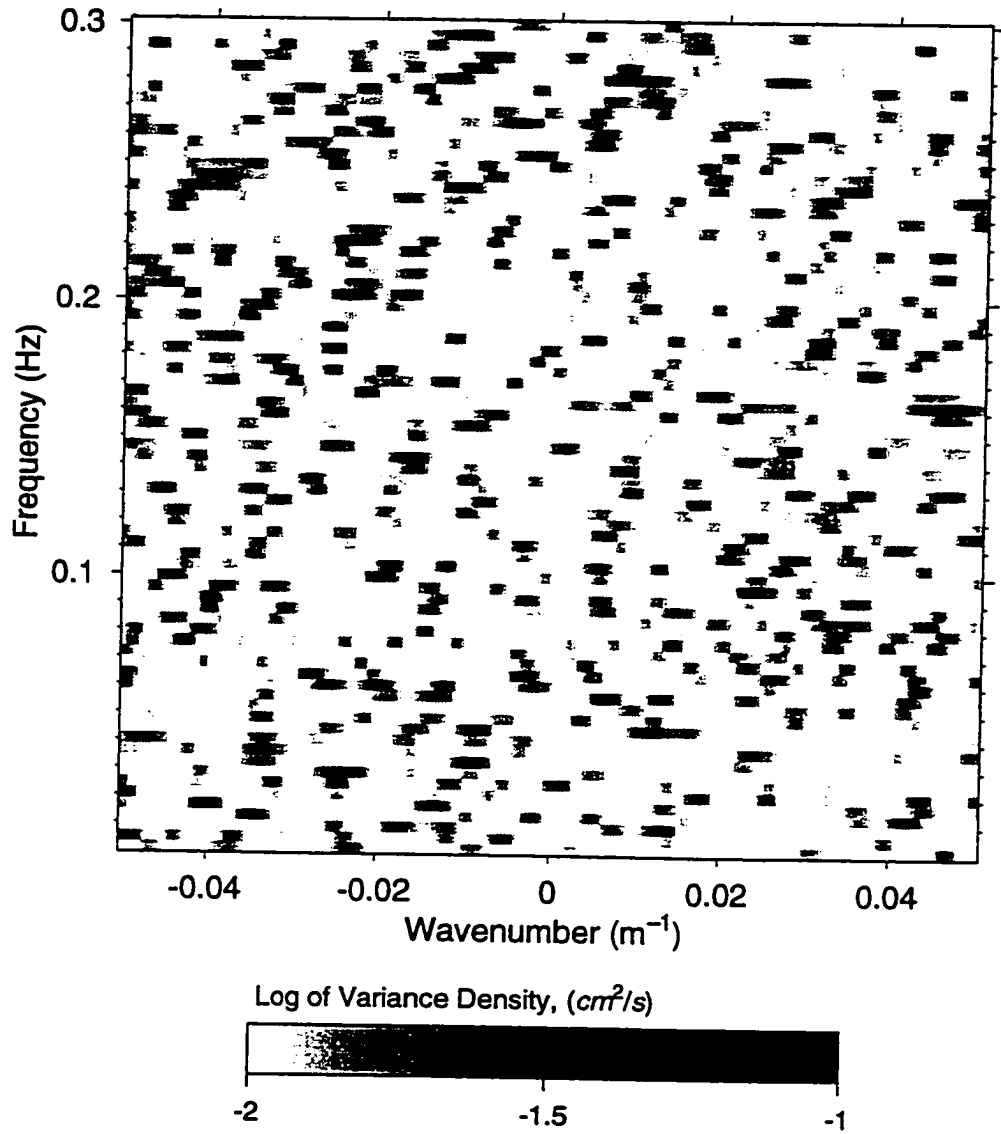


Figure A.6: The spectral estimate of random noise at each instrument location.

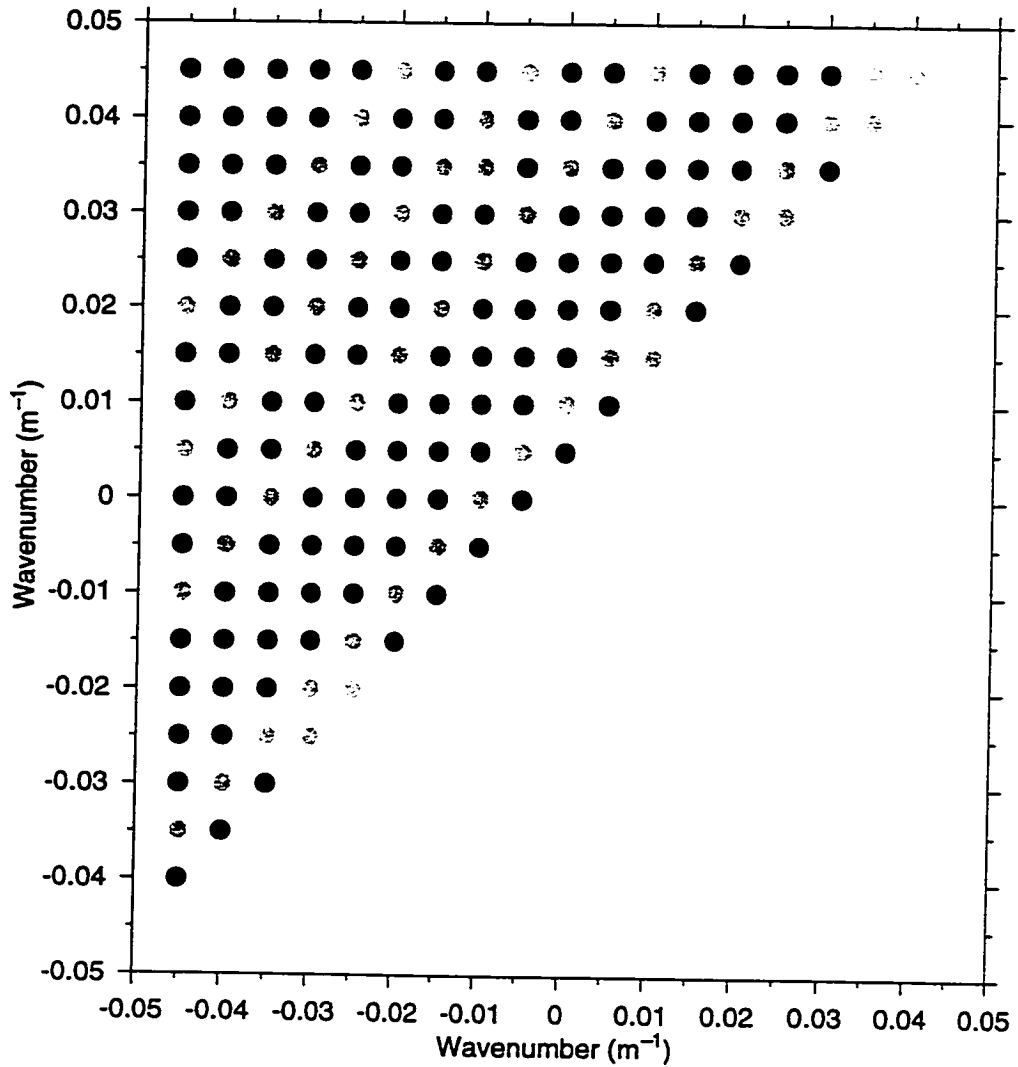


Figure A.7: All combinations of wavenumber with which the spectral estimator was tested for its ability to reproduce a bimodal wavenumber spectrum, for the case when only five out of six sensors are working, on October 16, 1990, 4:00am. Grey bullets are combinations in which unrealistic secondary peaks existed which were as big as or larger than the actual peaks. Black bullets are combinations in which the estimator correctly reproduced the peaks.

from the main wavenumber peak, but they were slightly larger than the peaks due to background noise. The actual noise is suppressed by the estimator in the frequency band where the signal occurs. The secondary peaks (or 'side-lobes') are not random, but were a result of energy leaking from the main peak. The only case where the estimator had problems, was at frequencies lower than 0.005 Hz, when the estimator reproduced the wavenumber correctly, but could not resolve the direction of wave propagation, similar to the findings of Oltman-Shay (1985). This sets the minimum resolvable frequency at about 0.005Hz.

A.6.2 Bi-modal peak

Multiple peaks proved to be more of a problem. The estimator correctly reproduced peaks that were at different frequencies and the same wavenumber, in exactly the same fashion as uni-modal peaks were reproduced. When two peaks at different wavenumbers, but the same frequency were estimated, in some cases, the secondary peaks were very large. In a few cases the secondary peaks were larger than the signal. This occurred when the secondary peaks or side lobes of the two main peaks coincided. Figure A.7 shows the success rate of estimating all the combinations of peaks between -0.045 and $+0.045$ at a resolution of $0.005m^{-1}$. Of all the peaks estimated, 30% were incorrectly estimated. It must be emphasized that these secondary peaks are not random, they are a function of an inadequately sampled spatial dimension. The tests do not say the primary peaks are not reproduced, just that large secondary peaks are also created. Also noted, though, was some shifting of the true peaks when they were close to each other in wavenumber space. Though Oltman-Shay (1985) did different types of synthetic spectral tests, her results yielded similar success with the array geometries she used. In general, these tests explain the number of large peaks which seem random, and are at locations which are not particularly consistent with theory. As a result of these tests, when the spectrum is strongly bimodal, the results must be interpreted with caution. Luckily, in the case of bar-trapped modes which have separations which are symmetric or close to symmetric in wavenumber space, the

estimator success is not unusually bad.

A.6.3 Random phase

Finally the estimator was tested using the data from October 16 in which the phases had been randomized (Figure A.8). The frequency of the two incident wave peaks is evident, but all detail about the wavenumber distribution is lost, as would be expected if there were no phase relationships between sensors.

Despite these shortcomings, the results are a considerable improvement on the cross-spectra between instruments at different lags (Figure A.3), with which it would be impossible to identify bar trapped edge waves, particularly at incident wave frequencies. Though as a precaution, these conclusions should be based on general observations from the frequency-wavenumber spectra, not on observations of the energy contained within specific peaks.

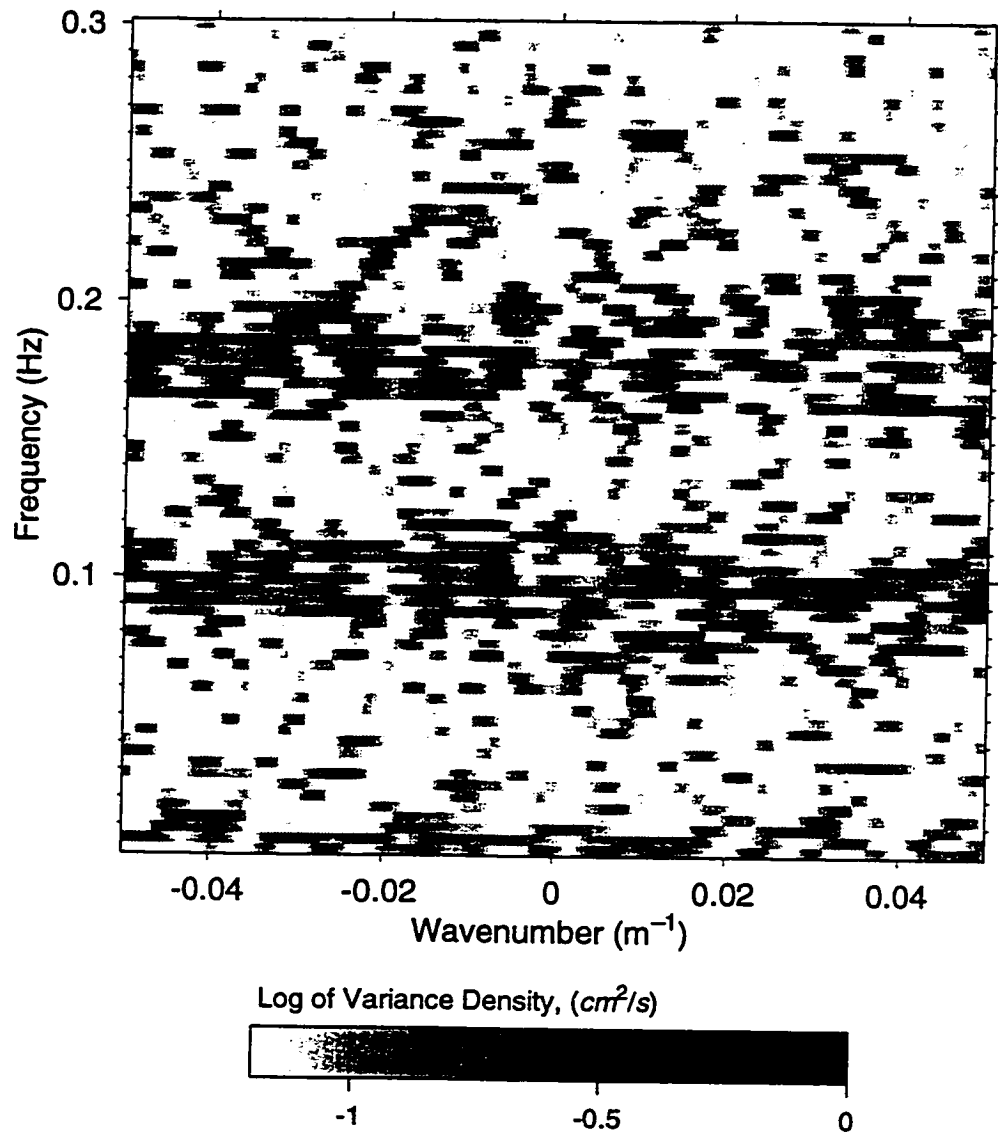


Figure A.8: The spectral estimate of the longshore component of orbital velocity, from October 16, 1990, 4:00am, when the phases of each signal have been randomized.

Bibliography

- Aagaard, T., 1988, A study on nearshore bar dynamics in a low-energy environment; northern Zealand, Demark, *J. Coast. Res.*, 4, 115-128.
- Aagaard, T., 1990, Infra-gravity waves and nearshore bars in protected storm-dominated coastal environments, *Mar. Geol.*, 94, 181-203.
- Aagaard, T., 1991, Multiple-bar morphodynamics and its relation to low-frequency edge waves, *J. Coast. Res.* 7, 801-813.
- Aagaard, T. and B. Greenwood, 1994, Suspended sediment transport and the role of infragravity waves in a barred surf zone, *Mar. Geol.*, 118, 23-48.
- Arfkin, G. ,1985, *Mathematical Methods for Physicists*, Academic Press, 985pp.
- Batchelor, G. K., 1967, *An Introduction to Fluid Dynamics*, Cambridge University Press, Cambridge, 615 pp.
- Ball, F. K., 1967, Edge waves in an ocean of finite depth, *Deep Sea Res.* 14, 79-88.
- Bauer, B. O. and B. G. Greenwood, 1990, Modification of a linear bar-trough system by a standing edge wave, *Mar. Geol.*, 92, 177-204.
- Birkemeier, W. A., 1991, Samson and Delilah at the FRF, *The CERCular*, CERC-91-1, U.S. Army Coastal Eng. Res. Cent., Vicksburg, Miss. 6pp.
- Bowen, A. J., 1969, The generation of longshore currents on a plane beach, *J. Mar. Res.*, 27, 206-215.

- Bowen, A. J. and D. L. Inman, 1971, Edge waves and crescentic bars, *J. Geophys. Res.*, **76**, 8662-8671.
- Bowen, A. J. and R. T. Guza, 1978, Edge waves and surf beat, *J. Geophys. Res.* **83**, 1913-1920
- Bowen, A. J., 1980, Simple models of nearshore sedimentation; beach profiles and longshore bars, in *The Coastline of Canada*, S.B. McCann, editor; Geological Survey of Canada, Paper 80-10, 1-11.
- Buchwald, V. T., 1968, Longwaves on oceanic ridges, *Proc. R. Soc. London A*, **308**, 343-354.
- Buchwald, V. T. and R. A. de Szoeko, 1973, The response of a continental shelf to travelling pressure disturbances, *Aust. J. Mar. Freshwat. Res.* **24**, 143-158.
- Carter, T. G., P. L. F. Liu, and C. C. Mei, 1973, Mass transport by waves and offshore bedforms, *J. Waterways, Harbours Coastal Eng. Div. ASCE* **99**, 165-184.
- Dally, A. J. and R. G. Dean, 1984, Suspended sediment transport and beach profile evolution, *J. Waterway Port Coastal Ocean Eng.* **110**, 15-33.
- Davis E. D., and L. A. Regier, 1977, Methods for estimating directional wave spectra from multi-element arrays, *J. Mar. Res.* **35**, 453-477.
- Dore, B. D., 1976, Double boundary layer in standing surface waves, *Pure and App. Geophys.*, **114**, 629-637.
- Eckart, C., 1951, Surface waves on water of variable depth, *Wave Rep. 100, Ref. 51-12*, Scripps Inst. of Oceanogr., Univ. of Calif., La Jolla, 99 pp.
- Elgar, S., T. H. C. Herbers, M. Okihiro, J. Oltman-Shay and R. T. Guza, 1992, Observations of infra gravity waves, *J. Geophys. Res.*, **97**, 15,573-15,577.

- Falques, A. and V. Iranzo, 1992, Edge waves on longshore shear flow, *Phys. Fluids A* 4, 2169-2190.
- Foda, M. A. and C. C. Mei, 1981, Excitation of long-trapped waves by a group of short swells, *J. Fluid Mech.*, 111, 319-345.
- Gallagher, B., 1971, Generation of surf beat by non-linear wave interactions, *J. Fluid. Mech.*, 49, 1-20.
- Guza, R. T., and D. L. Inman, 1975, Edge waves and beach cusps, *J. Geophys. Res.*, 80, 2997-3012.
- Guza, R. T., and E. B. Thornton, 1985, Observations of surf beat, *J. Geophys. Res.*, 90, 3161-3172.
- Hasselmann, K., 1970, Wave-driven inertial oscillations, *Geophysical Fluid Dynamics* 1, 463-502.
- Herbers, T. H. C., S. Elgar and R. T. Guza, 1995a, Generation and propagation of infragravity waves, *J. Geophys. Res.* 100, 24,863-24,872.
- Herbers, T. H. C., S. Elgar, R. T. Guza, and W. C. O'Reilly, 1995b, Infragravity-frequency (0.005-0.05 Hz) motions on the shelf Part II: free waves, *J. Phys. Ocean.* 25, 1063-1079.
- Holman, R. A. and A. J. Bowen, 1979, Edge waves on complex beach profiles, *J. Geophys. Res.* 84, 6339-6346.
- Holman, R. A., 1981, Infragravity energy in the surf zone, *J. Geophys. Res.* 86, 6442-6450.
- Holman, R. A., and A. J. Bowen, 1982, Bars, bumps and holes: Models for the generation of complex beach topography, *J. Geophys. Res.*, 87, 457-468.
- Holman, R. A., and A. H. Sallenger, 1985, Setup and swash on a natural beach, *J. Geophys. Res.*, 90, 945-953.

- Holman, R. A. and A. H. Sallenger, 1993, Sand bar generation: a discussion of the Duck experiment series, *J. Coast. Res.* 15, 76-92.
- Howd, P. A. and W. A. Birkemeier, 1987, Storm induced morphological changes during DUCK85, *Proceedings Coastal Sediments '87*, ASCE, 834-847.
- Howd, P.A., J. Oltman-Shay, R. A. Holman, 1991a, Wave variance partitioning in the trough of a barred beach, *J. Geophys. Res.*, 96 , 12,781-12,795.
- Howd, P. A., A. J. Bowen, R. A. Holman, and J. Oltman-Shay, 1991b, Infragravity waves, longshore currents and linear sand bar formation, *Proceedings, Coastal Sediments '91*, 72-84.
- Howd, P. A., A. J. Bowen and R. A. Holman, 1992, Edge waves in the presence of strong longshore currents, *J. Geophys. Res.*, 97, 11,357-11,371.
- Hunt, J. N., and B. Johns, 1963, Currents induced by tides and gravity waves, *Tellus XV*, 343-351.
- Huntley, D. A. and A. J. Bowen, 1975, Field observations of edge waves and their effect on beach material, *J. Geol. Soc. London*, 131, 69-81.
- Huntley, D. A., 1976, Long period waves on a natural beach, *J. Geophys. Res.* 81, 6441-6449.
- Huntley, D. A., 1980, Edge waves in a crescentic bar system, in *The Coastline of Canada*, S.B. McCann, ed.; Geol. Surv. Can, Pap., 80-10, 111-121.
- Huntley, D. A., R. T. Guza and E. B. Thornton, 1981, Field observations of surf beat, 1. Progressive edge waves, *J. Geophys. Res.*, 86, 6451-6466.
- Iskandarani, M and P. L. Liu, 1991, Mass transport in two-dimensional water waves, *J. Fluid Mech.*, 231, 395-415.
- Jenkins, A. D., 1987, Wind and wave induced currents in a rotating sea with depth varying eddy viscosity *J. Phys. Ocean.*, 17, 938-951.

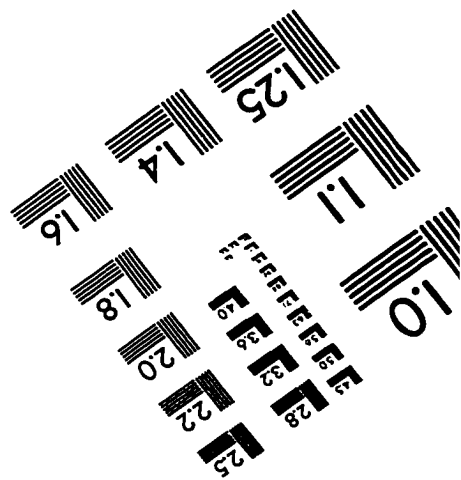
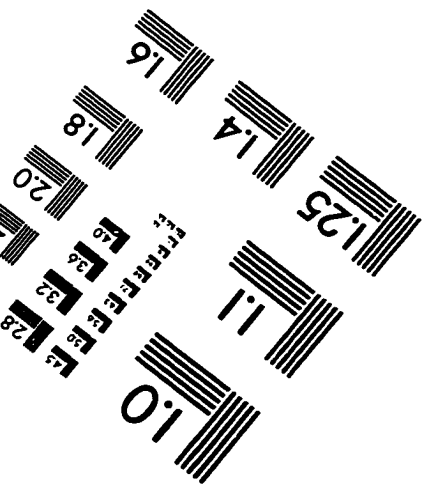
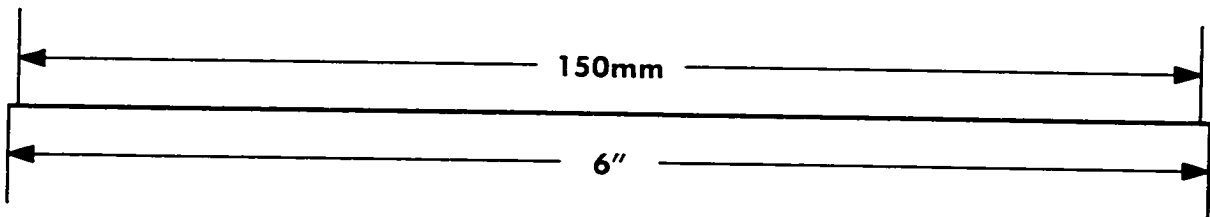
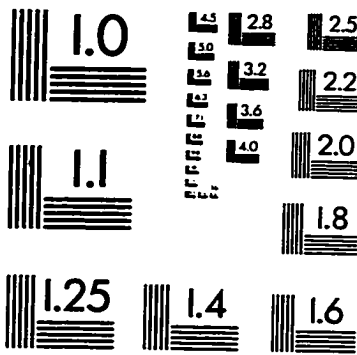
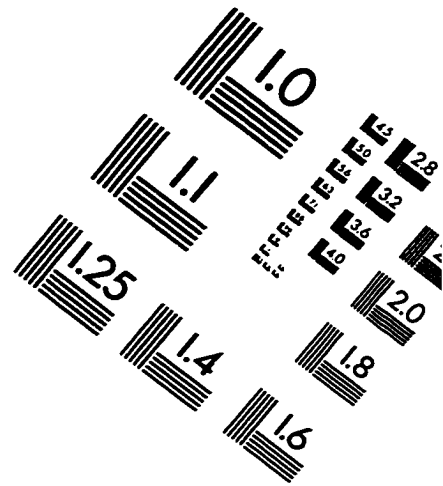
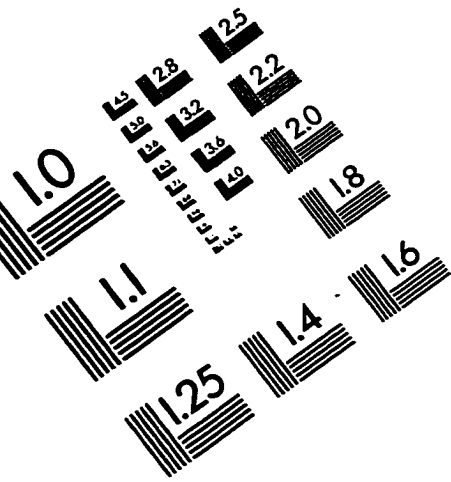
- Kirby, J. T., R. A. Dalrymple and L. F. Liu, 1981, Modification of edge waves by barred-beach topography, *Coastal Eng.*, 5, 35-49.
- Larson, M. and N. C. Kraus, 1991, Numerical model of longshore current over bar and trough beaches, *J. Waterw. Port Coastal Ocean Eng.*, 117, 326-347.
- Lippmann, T. C., R. A. Holman and A. J. Bowen, Generation of edge waves in shallow water, *J. Geophys. Res.*, in press.
- Longuet-Higgins, M. S., 1953, Mass transport in water waves, *Phil. Trans. R. Soc. Lond. A.*, 245, 535-581.
- Longuet-Higgins, M. S. and R. W. Stewart, 1962, Radiation stress and mass transport in surface gravity waves with application to 'surf-beats', *J. Fluid Mech.*, 13, 481-504.
- Mei, C. C., 1989, *The Applied Dynamics of Ocean Surface Waves*, World Scientific, Singapore, 740 pp.
- Okihiro, M., R. T. Guza and R. J. Seymour, 1992, Bound Infragravity waves, *J. Geophys. Res.*, 87, 11,453-11,469.
- Oltman-Shay, J. and R. T. Guza, 1984, A data adaptive ocean wave directional spectrum estimator for pitch and roll type measurements, *J. Phys. Ocean.*, 14, 1800-1810.
- Oltman-Shay, J., 1985, Infragravity edge wave observations on two California beaches, Ph.D. dissertation, Scripps Instit. of Oceanogr. University of California, San Diego, 111 pp.
- Oltman-Shay, J. and R. T. Guza, 1987, Infragravity edge wave observations on two California beaches, *J. Phys. Ocean.*, 17, 644-663.

- Oltman-Shay, J., P. A. Howd and W. A. Birkemeier, 1989, Shear instabilities of the mean longshore current: 2. Field observations, *J. Geophys. Res.*, *94*, 18,031-18,042.
- Oltman-Shay, J., and P. A. Howd, 1993, Edge waves on non-planar bathymetry and alongshore currents. A model and data comparison, *J. Geophys. Res.*, *98*, 2495-2507.
- Pawka, S., 1983, Island shadows in wave directional spectra, *J. Geophys. Res.*, *88*, 2579-2591.
- Priestley, M. B., 1981, *Spectral Analysis and Time Series*, Academic Press, 890pp.
- Riley, N., 1965, Oscillating viscous flows, *Mathematika*, *12*, 161-175.
- Sallenger, A. H., R. A. Holman and W. A. Birkemeier, 1985, Storm-induced response of a nearshore bar system, *Mar. Geol.*, *64*, 237-257.
- Schaffer, H. A., 1993, Infragravity waves induced by short-wave groups, *J. Fluid Mech.*, *247*, 551-588.
- Schönfeldt, H. J., 1989, Are edge waves responsible for the location of sand reefs?, *Beitr. Meereskd.*, *60*, 35-40.
- Schönfeldt, H. J., 1991, Randwellen und Sedimentation, *Geophys. Veroff.*, *4*, 75-81.
- Schönfeldt, H. J., 1994, Edge waves in the Baltic sea and anomalous dispersion in the surf zone, *German Journal of Hydrography*, *46*(1), 81-98.
- Schönfeldt, H. J., 1995, On the modification of edge waves by longshore currents, *Cont. Shelf Res.*, *15*, 1213-1221.
- Short, A. D., 1975, Multiple offshore bars and standing waves, *J. Geophys. Res.*, *80*, 3838-3840.

- Smith, J. M., M. Larson and N. C. Kraus, 1993, Longshore current on a barred beach: field measurements and calculation, *J. Geophys. Res.*, *98*, 22,717-22,731.
- Snodgrass, F. E., W. H. Munk and G. R. Miller, 1962, Long-period waves on the continental borderland, I, Background spectra, *J. Mar. Res.*, *20*, 3-30.
- Stokes, G. G., Report on recent research in hydrodynamics, *Brit. Ass. Rep.*, (Papers, i.167).
- Stuart, J. T., 1966, Double boundary layer in oscillatory viscous flow, *J. Fluid. Mech.*, *24*, 673-687.
- Symonds, G., D. A. Huntley and A. J. Bowen, 1982, Two-dimensional surf beat: Longwave generation by a time-varying breakpoint, *J. Geophys. Res.*, *87*, 492-498.
- Symonds, G. and A. J. Bowen, 1984, Interactions of nearshore bars with incoming wave groups, *J. Geophys. Res.*, *89*, 1953-1959.
- Thornton, E. B. and R. T. Guza, 1986, Surf zone currents and random waves: field data and models, *J. Phys. Ocean.*, *16*, 1165-1178.
- Thornton, E. B. and C. S. Kim, 1993, Longshore current and wave height modulation at tidal frequency inside the surf zone, *J. Geophys. Res.* *98*, 16,509-16,519.
- Trowbridge, J. and O. S. Madsen, 1984a, Turbulent wave boundary layers 1. model formulation and first-order solutions, *J. Geophys. Res.*, *89*, 7989-7997.
- Trowbridge, J. and O. S. Madsen, 1984b, Turbulent wave boundary layers 2. second-order theory and mass transport, *J. Geophys. Res.*, *89*, 7999-8007.
- Ünlüata, Ü and Mei, C.C. 1970, Mass transport in water waves, *J. Geophys. Res.* *75*, 7611-7618.
- Ursell, F., 1952, Edge waves on a sloping beach, *Proc. Roy. Soc., Ser. A* *214*, 79-98.

- Wright, L. D. and A. D. Short, 1983, Morphodynamics of beaches and surf zones in Australia. In P. D. Komar (Ed.), *CRC Handbook of Coastal Processes and Erosion*, CRC Press, Boca Raton, Fla, 35-64 pp.
- Wright, L. D. and A. D. Short, 1984, Morphodynamic variability of surf zones and beaches: A synthesis, *Mar. Geol.* 56, 93-118.
- Wright, L. D., P. Nielsen, N. C. Shi and J. H. List, 1986, Morphodynamics of a bar-trough surf zone, *Mar. Geol.* 70, 251-285.
- Xu, Z. and A. J. Bowen, 1994, Wave and wind-driven flow in water of finite depth, *J. Phys. Ocean.*, 24, 1850-1866.

IMAGE EVALUATION TEST TARGET (QA-3)



APPLIED IMAGE, Inc
1653 East Main Street
Rochester, NY 14609 USA
Phone: 716/482-0300
Fax: 716/288-5989

© 1993, Applied Image, Inc., All Rights Reserved